



KATHOLIEKE UNIVERSITEIT
LEUVEN

Arenberg Doctoral School of Science, Engineering & Technology
Faculty of Engineering
Department of Mechanical Engineering

Model Predictive Control of Ground Coupled Heat Pump Systems for Office Buildings

Clara VERHELST

Dissertation presented in partial fulfillment of the requirements for the degree of Doctor in Engineering

April 2012

Model Predictive Control of Ground Coupled Heat Pump Systems for Office Buildings

Clara VERHELST

Jury:

Prof. dr. ir. P. Van Houtte, chair

Prof. dr. ir. L. Helsen, promotor

Prof. dr. ir. J. Berghmans

Prof. dr. ir. H. Hens

Prof. dr. ir. J. Swevers

Prof. dr. ir. E. Van den Bulck

Dissertation presented in partial fulfillment of the requirements for the degree of Doctor of Engineering

Prof. dr. G. Vandersteen

(Vrije Universiteit Brussel)

Prof. dr. J. Spitler

(Oklahoma State University)

April 2012

© Katholieke Universiteit Leuven – Faculty of Engineering
Celestijnenlaan 300A box 2421, B-3001 Heverlee(Belgium)

Alle rechten voorbehouden. Niets uit deze uitgave mag worden vermenigvuldigd en/of openbaar gemaakt worden door middel van druk, fotocopie, microfilm, elektronisch of op welke andere wijze ook zonder voorafgaande schriftelijke toestemming van de uitgever.

All rights reserved. No part of the publication may be reproduced in any form by print, photoprint, microfilm or any other means without written permission from the publisher.

D/2012/7515/33
ISBN 978-94-6018-497-0

Universe loves simplicity.

Albert Einstein

Preface

During my PhD I have had the chance to work with many great people. I feel very grateful for having had the opportunity to work in such an inspiring environment. I acknowledge the Institute for the Promotion of Innovation through Science and Technology in Flanders (IWT Vlaanderen) for the research funding and the Prof. R. Snoeys Foundation for travelling funding.

First of all, I want to thank my promoter, professor Lieve Helsen. Lieve, I have always felt your support, in all aspects of work and life. Your participative style, openness, trust, sense of humour and – also- sense for adventure, creates a team spirit where one feels confident and rewarded. It is a pleasure working under your guidance.

I gratefully acknowledge my examination committee for their critical reading and valuable feedback. I am aware that this was a considerable task since the volume of this dissertation largely exceeds the limit to be categorized as 'small is beautiful'.

I would not have started a PhD without the inspiring coaching of Dries Haeseldonckx and Geert Van den Branden for my master thesis, under supervision of professor William D'haeseleer. William, you convinced me that the future of our planet can not be saved by changing people's behavior only. Technological break-throughs combined with economical incentives are required; thereby not forgetting "the nonlinearity of real processes". Dries, from you I learned to be more pragmatic. Geert, you learned me that the step prior to all analyses is to check whether the mass balance is correct... You also infected me with the exergy-virus. I would not have started a PhD on heat pumps without being passionate about this concept.

The focus of my PhD on ground coupled heat pump systems I thank to Hans Hoes from Terra Energy and Johan Van Bael from VITO, who discussed the control challenges related to the long term dynamics of the borefield. During the second year I worked some time at VITO. Fjo De Ridder, thank you for all

the expertise you shared. You also brought me into contact with the system identification research group at the VUB. Johan Schoukens, Rik Pintelon, Gerd Vandersteen, Yves Rolain and Griet Monteyne: thank you for the introduction in the frequency domain identification, the vivid discussions on the blackboard and – last but not least - the welcoming atmosphere.

The concepts of optimal control and MPC have been spread by OPTEC, the Centre of Excellence of Optimization in Engineering. My personal experience is that OPTEC is not only an excellent in bringing user-friendly optimization tools to engineers; but also excellent in bringing people together. Moritz Diehl, thank you for creating this enriching research environment. Hereby I also acknowledge Joachim Ferreau, Boris Houska and David Ariens, the developers of the ACADO tool. OPTEC brought me into contact with the research group on model predictive control at ETH Zürich. Prof. Manfred Morari, I am very grateful to have had the opportunity for a research stay at Ifa. It was a wonderful time spending at Ifa. Colin Jones, you learned me to search for the most simple solution. The results of this work confirm this is indeed the way to go. Daniel Axehill, your help with solvers was invaluable. Thanks a lot. Dimitrios Gyalistras, thank you for the opportunity to take part in the OptiControl meetings. Frauke Oldewurtel, without you this stay in Zürich would not have been the same. Thank you for being a wonderful host. The interactions within OPTEC also resulted in a collaboration with the Chemical Engineering department here at KULeuven. Filip Logist, I hope we can continue this fruitful collaboration... Hereby I also want to thank Lukas Ferkl, for inviting us to the Prague to give a workshop on system identification (quite a challenge at that time, I admit) and for the very nice ongoing research together.

Of course, most of the time I have spent at the Mechanical Engineering Department. I do not exaggerate if I say it is a pleasure to work here. Frederik Rogiers, thank you for the five years we shared the same office and being witness/supporters of each others small/big changes in life. Leen Peeters and Tine Stevens, thank you for everything, ranging from our runnings in Heverlee to the 'clear all, close all, clc, start writing!' mails; Anouk Bosmans, Anke Van Campen, Bram Demeulenaere, Friedl De Groote, Goele Pipeleers, Joris De Schutter, Keivan Zavari, Maarten Vanierschot, Maarten Witters, Max Bögli and Wouter Dekeyser... with you the running speed is higher, but this is greatly compensated by the increased intake of home brewed juices, home baked cakes and cheese fondue. And concerning culinary achievements: Tinne De Laet and Paul Van Herck, I will always be proud of our big cross-division wafelbak. Nele Famaey, Han Vandevyvere and Joost Dufflou, I am proud of our initiative to promote a sustainable operation of KULeuven. Dear SySi's (for those unfamiliar to this acronym: it stands for the Thermal systems simulation group), the number of SySi-cups with coffee and cookies have been limited, but the spirit is

invaluable. Maarten Sourbron, I will never forget October 2011 and our famous Montréal paper: now we can tackle any challenge! Stefan Antonov, the internal gains man, we still have some borefield mysteries to unveil; Jan Hoogmartens, with your warmth and calm, you are the ‘rots in the branding’; Roel De Coninck; your expertise and passion for your work are infectious; Dieter Patteeuw, your problem solving skills have helped me a great deal the last year, not to forget your jokes, very powerful in reducing cortisol levels. Bart Saerens, Ruben Gielen and Joris Gillis, I would have struggled even more with Latex without your help. Nico Keyaerts, thank you for having a critical look to the economic evaluation part. Hereby I also want to thank our colleagues of building physics; Dirk Saelens, for building bridges, Wout Parys, for your help with debugging TRNSYS and Ruben Baetens, for taking charge of peak stress reduction at the final stage of writing. Frieda De Coster and Kathleen Coenen, the ‘core’ of TME, thanks for making sure that everything runs smoothly. Kathleen, I am waiting until you become the female counterpart of Alex Agnew. Tine Baelmans, thanks to you I have started the master thermal energy sciences. You convinced me that mechanical engineering is not only for boys. Eric Van den Bulck, you incited me to go beyond simulation-based research. I am afraid I have to leave the analytical solution of the optimal control problems for future research. Stefan Antonov or Damien Picard, are you willing to grasp the opportunity? I also want to mention the colleagues whom I meet daily when going for coffee: Jan Thielemans, Ronny Moreas, Jean-Pierre Merckx, Jan Peirs, Amar Kumar Behera, Eric Demeester, Dirk Vanhooydonck and Alex Hüntemann... Finally, I want to thank all colleagues from TME, Anouk, Asim, Bart, Daniël, Darin, Dieter, Eric, Erik, Filip, Frederic, Frederik N., Frederik R., Frieda, Geert, Ivo, Hans, Jan, Jay, Jeroen, Joachim, Johan, Joris C. and Joris G., Juliana, Kathleen, Kenneth, Lieve, Maarten, Nico, Peng, Roel, Ruben, Sandip, Shijie, Shivanand, Stefan, Tijs, Tine, Tom, Vladimir, William and Wouter for all the nice moments shared. Just as Sara said: I will miss it!

Last but not least, I want to thank my family and friends for creating the best imaginable atmosphere for the final sprint. Julie Verhelst and Karolien Vasseur, now it is your turn to start writing! Enjoy the journey!

Clara Verhelst

Leuven, April 2012

Beknopte samenvatting

Grondgekoppelde warmtepompsystemen (GGWP) in combinatie met lage-temperatuur-afgiftesystemen zoals betonkernactivering (BKA) hebben een primair energiebesparingspotentieel van ruim 50% in vergelijking met klassieke verwarmings- en koelinstallaties. In koudere klimaten zoals België, kan de bodem benut worden als warmtebron voor de warmtepomp (WP) en als koudebron voor passieve koeling (PK). Om de investering in grondwarmtewisselaars te beperken, wordt de GGWP vaak ontworpen voor het dekken van de basislast, met een conventionele back-up installatie voor het opvangen van de piekvermogens.

In de praktijk blijkt het energiebesparingspotentieel van BKA-GGWP systemen met huidige regelstrategieën moeilijk te realiseren. Dit is te wijten aan een statische benadering van het systeemgedrag en een niet-optimale afstemming van de drie subsystemen (gebouw, installatie en bodem). Dit doctoraat stelt het ontwerp van een modelgebaseerde predictieve regelaar (MPC) voor die de werking van het systeem optimaliseert vanuit een integrale systeembenadering, rekening houdend met thermisch comfort, energiekost en thermische balans in de bodem. Een belangrijk aspect hierbij is het definiëren van een zowel nauwkeurig als eenvoudig regelaarmodel voor de drie subsystemen.

De resultaten tonen aan dat MPC een energiekostbesparing van 20% tot 40% kan realiseren in vergelijking met huidige stookcurve/koelcurve regelstrategieën. MPC benut de thermische massa van BKA om optimaal gebruik te maken van variaties in de elektriciteitsprijs en om piekvermogens - en dus het gebruik van de duurdere back-up installatie(s) - tot een minimum te herleiden. De voornaamste beperking op de thermische vermogens van en naar de bodem is hierbij de temperatuursgrenzen in de grondwarmtewisselaars. De bodem fungeert daarom optimaliter als dissipator van warmte en koude, niet als opslagmedium. Reductie van het piekvermogen door MPC laat bovendien een kleinere dimensionering toe, wat leidt tot significante besparingen in de investeringskost.

Abstract

Ground coupled heat pump (GCHP) systems combined with low-temperature heat emission systems such as concrete core activation (CCA) have a primary energy savings potential of more than 50% compared to conventional installations for space heating and cooling. In colder climates, such as in Belgium, the ground is used as a heat source for the heat pump (HP) and as a heat sink for passive cooling (PC). Because of the high investment cost of the ground loop heat exchangers, GCHP systems are often designed for base load operation. A conventional backup installation is added to cover the peak loads.

Currently, however, the energy savings potential of CCA-GCHP systems is rarely realized in practice. This is mainly due to the fact that current control strategies are based on a static system representation and do not optimally combine the different sublevels (building, installation and ground). This work presents a model predictive control (MPC) strategy which optimizes the system operation from an integrated system's perspective with maximization of thermal comfort, minimization of energy cost and a long term sustainable use of the ground as control objectives.

Within the development of MPC the definition of an adequate system controller model is crucial. For each sublevel (building, installation and ground) a controller model is identified which yields good control performance while being as simple as possible.

With respect to building dynamics modeling, we addressed the question how to describe the response of the operative temperature in the presence of solar gains and internal gains. It was found that a simple grey box model structure, combined with an online prediction error compensation method, fits this purpose. This prediction error is found to be highly correlated with the solar and internal gains, indicating that the impact of these gains on the operative temperature can be represented in a rather static way, at least for the investigated landscape office building. Further research is needed to define good excitation signals for

identifying the model parameters, as well as to decrease the sensitivity of the MPC performance towards disturbance prediction errors.

With respect to heat pump characteristics modeling, we addressed the question how to deal with the nonlinearities caused by the temperature dependency of the heat pump coefficient of performance (COP). Since these nonlinearities give rise to a non-convex optimization problem, we investigated the performance loss caused by the use of a simplified COP representation giving rise to a convex optimization problem. Both approaches are found in the literature, but had apparently not been compared before. The comparative study reveals that simplified models can be used if the cost function penalizes power peaks. This way, the control strategy obtained resembles the one found with the accurate COP representations, namely a smooth operation at part load.

With respect to borefield modeling, we addressed the question to which extent the number of states in the model can be reduced while still capturing both the short and long term borefield dynamics. Three approaches, i.e. white-box modeling followed by model reduction, grey-box modeling with parameter estimation and black-box modeling in the Laplace variable s and the Warburg variable \sqrt{s} , have been evaluated. The white-box models are found to best describe the long term dynamics, the gray-box models yield the best validation results for typical borefield operation profiles, evaluated over a time frame of 10 years, and this with very low model orders (3 to 6). The black-box models in s yield inferior validation results which could be explained by numerical artifacts in the identification data sets used. Finally, the black-box models in \sqrt{s} have a better prediction performance than the models in s , indicating that they are effectively better suited for describing thermal diffusion phenomena. For incorporation in the optimal control framework, we selected the low-order grey-box models and the initial white box model. A sensitivity analysis of the control performance as a function of the model order indicates that a 3rd order borefield model, based on parameter estimation, is sufficient. Compared to the initial 11th order white box model, the computation time is reduced by approximately a factor 7.

The final question addressed is how to incorporate both the short and long term objectives in the optimal control problem formulation. The former are related to the thermal comfort requirements, the day-night variations in the electricity price and the diurnal variation of the ambient air temperature which influence the efficiency of the backup chiller. The latter are related to the requirement of a long term sustainable use of the borefield which implies that – after the transient phase after start up – an optimal equilibrium solution should be reached. To this end, as a first step, the optimal control problem was solved open loop, i.e. outside the MPC framework. From the analysis of the optimal long term HyGCHP operation, following insights are gained: first,

as long as the brine fluid temperature remains within its limits, i.e. above 0°C and below the supply water temperature of 20°C for passive cooling, it is more cost effective to use the heat pump than the gas boiler, and more cost effective to use passive cooling than the chiller. In other words, maximizing the COP of the heat pump for heating dominated buildings (by striving towards higher source temperatures), or maximizing the COP for passive cooling for cooling dominated buildings (by striving towards lower source temperatures), is not the driving factor of the optimization. Instead, the optimization tries to maximize the share of heat pump operation and passive cooling within the brine fluid temperature limits. As a natural consequence, this results in a net heat extraction on annual basis for the heating dominated buildings and vice versa for the cooling dominated buildings. At equilibrium, this net heat injection/extraction is compensated by the heat exchange between the borefield and the surrounding ground. From this it is clear that the borefield actually serves as a heat and cold dissipater rather than as a heat and cold storage device. From this point of view, the term ‘seasonal storage’, often used in this context, does not seem adequate. Second, switching between the heat pump/passive cooling on the one hand, and the backup gas boiler/chiller on the other hand, does not seem to be motivated by any long term cost optimization strategy. Switching from the borefield system to the backup system only occurs when the constraints on the brine fluid temperature are active. Third, to maximize the share of the heat pump and passive cooling given the brine fluid temperature limits, the heat injection and extraction rates should be kept as low as possible. The lower the heat transfer rate inside the borehole heat exchanger, the smaller the temperature difference between the brine fluid and the surrounding ground.

These insights have important consequences for the formulation of the MPC strategy. First, we conclude that it is not required to add a long term constraint in the MPC formulation to impose thermal balance of the borefield. Second, a long term horizon to guarantee a cost optimal operation on an annual basis, is not required neither. Third, guaranteeing a cost optimal operation definitely requires incorporating the building dynamics in the optimization. This way, the peak shaving capacity of the building thermal mass in general, and of the CCA in specific, can be exploited to flatten the power profile of the heating and cooling loads. The latter is the key to increase the use of the heat pump and passive cooling while remaining within the brine fluid temperature limits.

The strengths of MPC, being its ability to account for the system dynamics, state and input constraints, suggest that MPC is ideally suited to fulfill this control task. The results in this work confirm this: MPC can realize energy cost savings of up to 20-40% compared to the conventional heating curve/cooling curve-based control strategies. MPC uses the CCA thermal mass to make optimal use of the variations in electricity price (through load shifting) and to minimize the use of

the expensive backup system (through peak load reduction), as discussed above. The upper bound of the cost savings potential of 40% corresponds to HyGCHP designs with very compact borefields. This is explained by the fact that the smaller the borefield size, the smaller the heat pump capacity and the passive cooling capacity. In order to satisfy the thermal comfort requirements with a large share of heat pump and passive cooling operation, a better anticipative behavior of the controller is needed, as well as an accurate estimation of the available heat pump/passive cooling capacity. As indicated by the results, MPC enables us to fully exploit the energy savings potential of very compact – and therefore economically competitive – HyGCHP designs.

Contents

Abstract	ix
Contents	xiii
Nomenclature	xix
1 Introduction	1
1.1 Motivation	1
1.2 Research objectives	6
1.3 Overview of the dissertation	7
2 Concepts	9
2.1 Optimal control	9
2.1.1 General description	9
2.1.2 Classification	10
2.1.3 Solution methods	10
2.2 Model predictive control	11
2.3 System identification	12
2.3.1 Step 1: Model requirements	13
2.3.2 Step 2: Model type	15

2.3.3	Step 3: Model structures	16
2.3.4	Step 4: Identification data	16
2.3.5	Step 5: Parameter estimation	18
2.3.6	Step 6: Model validation	20
2.3.7	Step 7: Model selection	21
3	Literature review	24
3.1	Optimal control at building level	24
3.2	Optimal control at installation level	27
3.3	Optimal control at borefield level	28
3.4	Optimal control at system level	31
3.5	Integration of control and design	32
3.6	Summary	33
4	System description	34
4.1	Introduction	34
4.2	Overview	34
4.2.1	Two zone office building with concrete core activation	34
4.2.2	Heat and cold distribution	38
4.2.3	Heat and cold production	38
4.3	Weather data	40
4.4	Thermal comfort requirements	40
4.5	Reference control strategy	45
4.5.1	Methodology	45
4.5.2	Settings	48
4.6	Reference design	51
4.6.1	Building load calculation	51
4.6.2	Installation sizing	55

4.6.3	Borefield sizing	56
4.6.4	Result	61
4.7	Chapter highlights	61
5	Building level control	63
5.1	Introduction	63
5.2	Literature study	64
5.2.1	Choice of cost function	64
5.2.2	Choice of controller building model	67
5.3	System description	68
5.3.1	System	68
5.3.2	Reference control strategy	69
5.3.3	MPC formulation	70
5.3.4	Control performance criteria	73
5.4	Controller building model	74
5.4.1	Model structure	74
5.4.2	Model equations	76
5.4.3	Parameter estimation	77
5.4.4	Validation results	83
5.4.5	Incorporation of the model in the MPC framework	87
5.5	Control performance evaluation	90
5.5.1	Scenario 1: Perfect disturbance predictions	90
5.5.2	Scenario 2: Imperfect disturbance predictions	99
5.5.3	Scenario 3: Zone-level versus lumped-building-level control	101
5.6	Summary and conclusions	105
5.7	Chapter highlights	109
6	Heat pump level control	112

6.1	Introduction	112
6.2	Physical background	113
6.3	Optimal control problem formulation	114
6.3.1	Cost function	115
6.3.2	Controller building model	116
6.3.3	Initial condition and temperature constraints	117
6.3.4	Controller heat pump model	117
6.3.5	Input constraints	120
6.3.6	Solving the optimal control problem	123
6.3.7	Boundary conditions	123
6.4	Control performance evaluation	125
6.4.1	Case 1: Constant electricity price scenario	125
6.4.2	Case 2: Variable electricity price scenario	129
6.4.3	Modified cost function	130
6.4.4	Influence of boundary conditions and building model parameters	133
6.5	Summary and conclusions	133
6.6	Chapter highlights	134
7	Borefield level control	136
7.1	Introduction	136
7.2	Optimal control problem formulation	137
7.3	Heat transfer processes in borefields	141
7.3.1	Introduction	141
7.3.2	First principle equations	145
7.3.3	Modeling the inner problem	147
7.3.4	Modeling the outer problem	151
7.3.5	Determining the physical parameters	159

7.3.6	Model validation	160
7.3.7	Models for optimal control purpose	160
7.4	Controller borefield model	162
7.4.1	Methodology	162
7.4.2	Modeling approaches	172
7.4.3	Results	179
7.4.4	Sensitivity to non-idealities	191
7.4.5	Summary and conclusions	193
7.5	Control performance evaluation	197
7.5.1	Settings	197
7.5.2	Computational limitations	201
7.5.3	What drives the optimization in the long term?	206
7.5.4	What drives the optimization in the short term?	220
7.5.5	Comparison of weekly versus hourly optimization	225
7.5.6	Computation time	227
7.5.7	Optimization from a system's perspective	228
7.6	Summary and conclusions	229
7.7	Chapter highlights	231
8	MPC of a HyGCHP system	234
8.1	Introduction	234
8.2	Methodology	235
8.3	MPC strategy	241
8.4	Results	245
8.4.1	Overview	246
8.4.2	Tuning of the control parameters	247
8.4.3	Thermal comfort	248

8.4.4	Primary energy consumption	249
8.4.5	Energy cost	250
8.4.6	Long term sustainability of borefield use	251
8.4.7	Economic evaluation	254
8.5	Summary and conclusions	256
8.6	Chapter highlights	258
9	Conclusions	259
	Bibliography	265
	Curriculum Vitae	283
	List of Publications	285

Nomenclature

List of Acronyms

AIC	Aikaike Information Criterion
AHU	air handling unit
1D-FDM	1-dimensional finite difference model
BHE	borehole heat exchanger
CC	cooling curve
CH	chiller
CT	cooling tower
CCA	concrete core activation
COP	coefficient of performance
DC	design case
DST	Duct Storage Model
FD	finite difference
GB	gas boiler
(Hy)GCHP	(hybrid) ground-coupled heat pump
GHE	ground heat exchanger
HC	heating curve
HE	heat exchanger
HP	heat pump
IC	investment cost
ID	identification data
KKT	Karush-Kuhn-Tucker
LDC	load duration curve
LT	long term
MPC	model predictive control
MR	model reduction
N	North
NPV	net present value

OCP	optimal control problem
PC	passive cooling
PE	parameter estimation
PEM	prediction error method
PMV	predicted mean vote
PPD	percentage of people dissatisfied
RBC	rule based control
RC	resistance - capacitance
RMSE	root mean squared error
S	South
SBM	Superposition Borehole Model
SI	system identification
TRT	thermal response test
WWHP	water-to-water heat pump

List of Symbols

Roman symbols

A, B, C, D	system matrices of state space model
B	distance between boreholes in borefield, (m)
c	specific heat capacity, (J/kgK)
c_{gas}	gas price, (€/kWh)
c_{el}	electricity price, (€/kWh)
C	heat capacity, (J/K)
C_e	specific annual energy cost, (€/m ² /y)
D	insulated length of borehole below the ground surface, (m)
d_i	center-to-center distance between tube and borehole, (m)
d_r	nominal discount rate, (-)
E_{prim}	specific annual primary energy consumption (kWh/m ² /y)
E_r	nominal energy price rise, (-)
GEO_c	fraction of total building cooling demand covered by passive cooling, (-)
GEO_h	fraction of total building heating demand covered by the heat pump, (-)
H	active borehole depth, (m)
H_c	control horizon (-)
h	heat transfer coefficient, (W/m ² K)
J_d	thermal discomfort cost in the cost function, (K ² h)
J_e	energy cost in the cost function, (kJ) or (€)
J_{LT}	long term penalty cost in the cost function, (kJ)
k	thermal conductivity, (W/mK)
K	weighting factor in cost function
\dot{m}_f	fluid mass flow rate inside borehole heat exchanger, (kg/s)
\dot{m}_w	water mass flow rate in heat and cold distribution system, (kg/s)
N	model order (-)
n_b	number of boreholes inside a borefield (-)
n_x	number of state variables (-)
n_u	number of input variables (-)
P	electrical power (W)
P_{HP}	heat pump compressor power(W)
P_{CH}	chiller compressor power (W)
$P_{HP,aux}$	primary circulation pumps power in heat pump mode (W)
$P_{PC,aux}$	primary circulation pumps power in passive cooling mode (W)
$P_{CH,aux}$	fan power dry cooling tower (W)
P_{prim}	power consumption primary circulation pumps (W)
Q	thermal energy (J)

\dot{Q}	thermal power (W or W/m^2)
q''	heat flux per unit surface, (W/m^2)
\dot{Q}_{bf}	extracted heat power from a borehole per unit length, (W/m)
\dot{Q}_{bf}	net thermal energy injected to the borefield (W)
$\dot{Q}_{bf,ext}$	thermal energy extracted from the borefield (W)
$\dot{Q}_{bf,inj}$	thermal energy injected to the borefield (W)
\dot{Q}_c	thermal power extracted from the building (cooling) (W)
\dot{Q}_{CH}	thermal power extracted from the building through active cooling (W)
\dot{Q}_{GB}	thermal power supplied to the building by the gas boiler (W)
\dot{Q}_h	thermal power supplied to the building (heating) (W)
\dot{Q}_{HP}	thermal power supplied to the building by the heat pump (W)
\dot{Q}_{int}	internal heat gains (W)
\dot{Q}_{PC}	thermal energy extracted from the building through passive cooling (W)
\dot{Q}_{vs}	ventilation heat gains (W)
\dot{Q}_{sol}	solar heat gains (W)
R	thermal resistance, (K/W)
R_{bf}	thermal resistance of an entire borefield, (K/W)
R_b	thermal borehole resistance, (K/W)
R'_b	thermal borehole resistance (per unit length), (K/(W/m))
r_b	borehole radius, (m)
r_t	tube radius, (m)
Re	Reynolds number, (-)
t	time, (s)
Δt_c	control time step, (s)
T	temperature, ($^{\circ}C$)
T_a	zone air temperature ($^{\circ}C$)
T_a	indoor air temperature ($^{\circ}C$)
T_{amb}	ambient temperature ($^{\circ}C$)
T_{bf}	mean borefield temperature, ($^{\circ}C$)
T_c	concrete core temperature, ($^{\circ}C$)
T_{cv}	control variable used as feedback for reference control strategy, ($^{\circ}C$)
$T_{comf,min}$	lower bound on operative temperature, ($^{\circ}C$)
$T_{comf,max}$	upper bound on operative temperature, ($^{\circ}C$)
T_f	mean fluid temperature through borehole heat exchanger, ($^{\circ}C$)
$T_{f,av}$	week average mean fluid temperature, ($^{\circ}C$)
$T_{f,i}$	fluid temperature entering a borefield, ($^{\circ}C$)
$T_{f,o}$	fluid temperature leaving a borefield, ($^{\circ}C$)
$T_{g,\infty}$	undisturbed ground temperature, ($^{\circ}C$)
T_g	ground temperature in the borefield, ($^{\circ}C$)
T_{mrt}	mean radiative temperature ($^{\circ}C$)
T_{op}	zone operative temperature, ($^{\circ}C$)

T_{rm}	running mean ambient temperature, ($^{\circ}\text{C}$)
T_{vs}	ventilation air supply temperature, ($^{\circ}\text{C}$)
T_{wr}	water return temperature, ($^{\circ}\text{C}$)
T_{ws}	water supply temperature, ($^{\circ}\text{C}$)
$T_{ws,set}$	set point water supply temperature, ($^{\circ}\text{C}$)
T_z	lumped zone temperature, ($^{\circ}\text{C}$)
$T_{z,ref}$	reference zone temperature, ($^{\circ}\text{C}$)
UA	heat exchange coefficient (W/K)

Subscripts

b	building <i>or</i> borehole
bf	borefield
c	cooling
h	heating
N	north
$prod$	at heat and cold production level
S	south
$schad$	with solar shading
set	setpoint

Superscripts

*	value determined by optimization <i>or</i> resulting from modified cost function (Chapter 6)
\wedge	estimated value

Greek symbols

α	thermal diffusivity, (m^2/K)
α_d	weighting factor thermal discomfort in cost function, ($\text{€}/\text{K}^2\text{h}$)
α_e	weighting factor energy cost in cost function, ($\text{€}/\text{kWh}$ <i>or</i> $\text{€}/(\text{kWh})^2$)
β	update factor, (-)
δ	relative difference, (-)
Δ	absolute difference
ρ	density, (kg/m) ³

Chapter 1

Introduction

1.1 Motivation

The building sector represents about 30-40% of the total end energy consumption in Europe, 50% of which is related to heating and cooling [129]. Climate change concerns and shrinking fossil fuel reserves push governments to work on demand side management. Rising electricity prices incite end users to lower their energy consumption as well. The first and most important step remains the quality of the building design with attention to the compactness of the building, air tightness and degree of insulation of the building envelope. Most often, the heating, cooling and ventilation systems are selected at the end of the design phase of the building. Incorporating the design of the installation at an early phase, however, can be very interesting to achieve very low-energy buildings. The integration of concrete core activation (CCA) or other so-called 'low-exergy heat emission systems' makes low-temperature heating and high-temperature cooling possible. This yields the potential to deliver this low-exergy heat or cold with a minimal amount of external work [58].

The three operation modes of a ground coupled heat pump (GCHP) system, i.e. heating, active cooling and/or passive cooling, are presented in Figure 1.1. In the heating mode, a heat pump is used to extract heat from the ground through ground loop heat exchangers. In the cooling mode, heat can be injected to the ground by an active cooling device or by a heat exchanger. The latter way of cooling, referred to as 'passive cooling', requires the ground temperature around the ground loop heat exchangers to be relatively low and is therefore mainly restricted to the moderate and colder climates. The primary energy

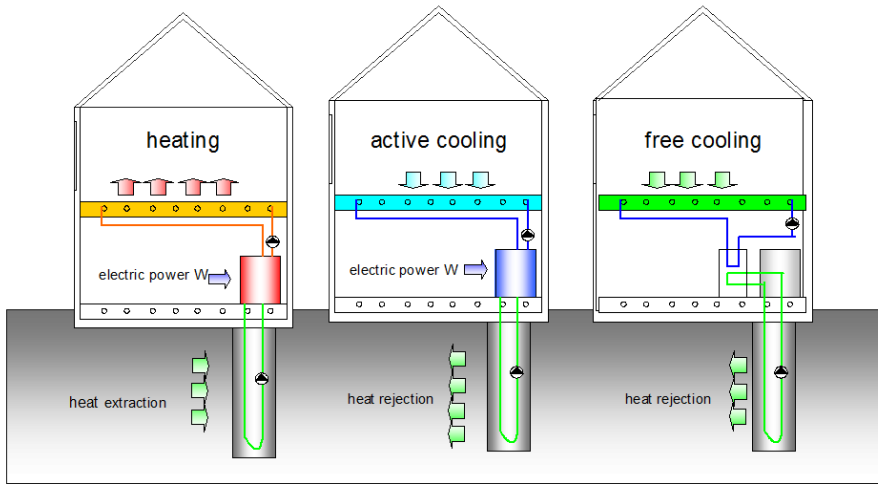


Figure 1.1: Operation modes of a ground coupled heat pump system

savings of the combination of a CCA system with a GCHP system compared to conventional systems may reach 50% [1]. To achieve these savings in practice, a good integration of the building design, installation design and system control is needed.

In the early '70s heat pumps started to enter the European market due to the high oil prices after the first oil crises. The heat pump market boomed, especially in Sweden and also in the United States [112, 151]. Huge research budgets were allocated to the field of energy technologies, which resulted in substantial research efforts, not only in the field of solar thermal power but in the field of heat pumps as well. However, once the oil prices stabilized in the early '80s, the heat pump sales figures dropped quickly. The main reason for this collapse was the poor actual heat pump performance. This was due to both low performance of the heat pump component itself, and to the lack of knowledge on the side of architects and installers about how to integrate the heat pump in the building.

The tendency to install large glazing areas has resulted in increased need for cooling in summer. The sales of air conditioning units grows exponentially [34]. In countries like the United States, this causes peaks in the electricity demand in summer, with electricity black outs as a result. By incorporating thermal energy storage in the design of the heating and cooling installation, the peak electricity demand for cooling can be reduced and shifted towards low-electricity price

periods. In countries that apply predominantly air conditioning systems, such as North-America, South-America and Asia, ice storage was and is the most used thermal energy storage system. In European countries, where hydronic systems prevail [129], the heat and cold emission system itself could be used as a short-term thermal buffer. Instead of using air coils for cooling and high-temperature radiators for heating, both having low thermal inertia, one could shift towards floor heating, with higher thermal inertia, or even towards concrete core activation, where the entire concrete slab is being thermally activated. These heat emission systems not only make it possible to lower the peak heating and cooling load due to their thermal energy storage capacity, they also enable decreasing the water supply temperature for heating and to increase the water supply temperature for cooling. The reason for this is the large surface area available for heat exchange. Technologies such as cogeneration of heat and power (or trigeneration) and heat pumps are ideally suited to deliver this low exergy heat and cold in the most efficient way.

For buildings requiring both heating and cooling, ground-coupled heat pumps (GCHP) have a high primary energy savings potential. In winter, the ground temperature is higher than the ambient air temperature, such that the heat pump operates at a higher coefficient of performance (COP). In summer, the opposite is true. If the ground temperature is low enough, it is possible to directly cool the building through passive heat exchange (passive cooling). In this case no active cooling is required and the only electricity consumption is related to the circulation pumps. GCHP are ideally suited for buildings with a balanced heating and cooling load, as the heat injection during passive cooling in summer regenerates the ground. At the start of the heating season, the ground is 'fully charged'. At building level, the energy savings potential is due to the low-exergy heating and cooling demand and the thermal storage capacity (small time scale) of the CCA. At installation level, the savings potential is due to the coupling with the ground, enabling high heat pump performance for heating and passive cooling for cooling. How good the opportunities for synergies of the entire system may be, it is difficult to fully exploit this potential in practice. Problems arise during both the design phase and the operation phase.

At building side, the main question is how to guarantee thermal comfort with a slow reacting system such as CCA, knowing that the disturbances due to internal gains and solar gains, act much faster on the building zone temperature [58, 65, 169, 183]. With current control strategies the thermal comfort requirements are often not met with CCA is the only heat and cold emission system. In case there is a fast reacting heat emission system (such as fan coils), current controllers are able to satisfy the thermal comfort requirements but often at a high energy cost [163]. The fast reacting heat emission system

tends to overrule the operation of the CCA. The question arises whether it is possible to guarantee thermal comfort in the CCA-building by means of an optimal control strategy. In that case, the investment cost in a fast reacting heat emission system can be avoided.

At installation level, the main question is how to size the ground coupled heat pump system and the backup system to guarantee that the heating and cooling demand can always be met, without oversizing the system. Oversizing the GCHP system should by all means be avoided as the cost related to the drilling of the borefield constitutes the main part of the investment cost. To improve the economical feasibility of GCHP systems, design guidelines suggest to size the borefield to cover only the smallest of both loads. This results in smaller and thus cheaper borefields. Current control strategies however, assume that the borefield is large and can be continuously operated. If the borefield temperatures exceeds the lower or upper temperature bounds, the backup system is used. While this is a sound operation in case of large borefields, for compact borefields this may not be the case. Such a strategy could result in borefield thermal depletion or thermal build-up. The operation should guarantee a long term sustainable operation with the annual building heating and cooling demand being delivered at the lowest cost [35, 177]. This requires an optimal use of the limited resources, i.e. of the amount of heat and cold stored in the borefield. The decision on when to switch between the ground coupled system and the backup system should thus depend on the available amount of heat and cold in the borefield, the future heating and cooling load, the efficiency of the heat and cold production devices and the electricity price profiles.

The discussion above reveals the need for the development of a control strategy for buildings with a CCA-GCHP in general, and CCA-HyGCHP systems in particular, which enables to guarantee thermal comfort at the lowest cost. To this end, the thermal energy storage capacity of the CCA at building side and the seasonal energy storage capacity of the borefield at source side, should be optimally exploited. Current control strategies are not suited for this purpose. They are based on static building models. The time delay of the system response is accounted for by heuristic rules, requiring a lot of trial-and-error to tune the control parameters. Model predictive control (MPC), however, has the potential to deal with the numerous control requirements. With MPC, the control variables are optimized online. Each control time step the control variables are selected which minimize a given cost function, taking into account the system dynamics and constraints. In this case, the cost function could be a weighted sum of energy cost and thermal discomfort. The controller model could include both the dynamics of the building and the dynamics of the borefield.

MPC is already well-established in the chemical industry, where it has originally been developed. The first report on MPC is found in the '70s and is applied

to the control of a distillation column. The main advantage of MPC in this application is its ability to actively incorporate constraints, both on the input variables and on the state variables. Meanwhile, MPC has been proven successful in the areas of aerospace, automotive, power systems... [144]. The basis of MPC is the solution of an optimal control problem at each time step, using updated system information obtained by monitoring. Whereas MPC popped up in the '70s, optimal control theory was already developed and implemented in the '50s for use in the space industry. In these early years, the optimal solution was found analytically, requiring substantial simplifications of the system description and boundary conditions. With the introduction of computers, numerical optimization solvers have been developed. Most of them are gradient-based methods: the minimum is found iteratively, by moving into a descent direction. The most well-known methods are the steepest-gradient and the Newton-based methods, which are very successful for solving convex optimization problems [125]. For problems where the gradients are difficult to derive, direct optimization methods are used as well [98]. Some examples of direct optimization problems are particle swarm optimization [93], Nelder-Mead-Simplex [123] and genetic algorithms [63] ... which are available in commercial software.

The development of MPC for CCA-GCHP systems faces a large number of challenges. First, a dynamic system model must be developed, both for the building and for the borefield. A lot of simulation environments exist to model the building and/or the borefield in detail, based on first principles [e.g. 30, 155]. Those are, however, far too complex to be incorporated in the optimal control problem (OCP) formulation. One needs to develop simple dynamic models for control. The challenge in system identification of a building lies in the large amount of unmeasured disturbances acting on the system (solar gains, internal gains, ventilation losses), the small number of sensors and limited space for applying good excitation signals when the building is occupied. The challenge in system identification of a borefield lies in the very broad dynamic range, with time constants ranging from hours to multiple years. The broad range in time constants in the system constitutes also a challenge for the optimal control part. It is computationally impossible to guarantee thermal comfort with a hourly time scale while optimizing the use of a seasonal energy storage with a time scale of several years. How to formulate the optimal control problem in order to take both the short term and the long term control objectives into account, constitutes a second challenge. Third, due to the dependency of the heat pump COP on the temperatures of the heat source and the heat sink, the optimization problem becomes nonlinear. This temperature dependency of the COP is often neglected to make the optimization problem convex. The performance loss resulting from this simplification has not yet been assessed.

1.2 Research objectives

This work aims at developing MPC for GCHP systems with seasonal energy storage, with the focus on office buildings with CCA in the West-European climate. The motivation for this application is fivefold. First, the savings potential of GCHP, both in terms of primary energy consumption and in terms of monetary costs, is the largest for buildings with both heating and cooling demand. This is because the borefield can be sized smaller thanks to the thermal regeneration of the ground in summer by passive cooling. Contrary to residential buildings in the West-European climate, office buildings have substantial cooling loads due to high internal and solar gains. Second, from a control point of view the potential of MPC, both in terms of energy savings and in terms of thermal comfort, may be largest for slowly reacting systems such as CCA. Conventional controllers are based on the assumption of steady-state system operation, which is far from reality for CCA. On top of that, MPC can account for future disturbances by incorporating weather predictions and occupancy profile predictions in the optimization. The latter brings us to the third reason why we focus on office buildings. Compared to residential buildings, the occupancy profiles of office buildings are more predictable. Fourth, thermal comfort requirements are usually more stringent in working environments than at home. Finally, the investment cost of an MPC is more likely to be justified for large buildings than for small buildings, as the absolute savings are higher for larger buildings.

Specifically, the following questions are addressed:

- At building level: How to describe the building dynamics in the optimal control problem formulation (OCP), and how to identify this model?
- At installation level: How to deal with the nonlinearity introduced by the heat pump performance?
- At borefield level: How to describe the borefield dynamics?
- At system level: How to deal with the combination of short and long term time scales?
- How does the resulting MPC compare to current rule-based control (RBC) strategies?
- How can MPC contribute to improving the economical feasibility of CCA-HyGCHP systems?

1.3 Overview of the dissertation

The dissertation consists of 9 chapters which are briefly discussed below.

Chapter 2 introduces the methodologies being central in this work, being optimal control, model predictive control and system identification.

Chapter 3 gives a concise overview of the literature on optimal control of HVAC systems in buildings, with the focus moving from the building level, towards the installation level, to conclude with examples of integrated system approaches.

Chapter 4 describes the reference system, implemented in the TRNSYS simulation environment, which consists of a two-zone office with CCA connected to a HyGCHP system. Additionally, this chapter describes the reference control strategy and the installation sizing.

The next three chapters define the controller model requirements for the three subsystems.

Chapter 5 focuses on the controller building model. The impact of the model structure and the identification data set used for parameter estimation is assessed. The evaluation is performed in an MPC framework, with the detailed 2-zone office model, described in Chapter 4, as simulator.

Chapter 6 incorporates the heat pump characteristics in the optimal control problem formulation and evaluates the impact of a detailed heat pump model, yielding a nonlinear optimization problem, versus a simplified model, yielding a convex optimization problem. The analysis is performed for an air-to-water heat pump system connected to a floor heating system. The choice for an air-source heat pump allows one to focus on the time horizon of one day. Nevertheless, the results provide useful insights for the control of ground coupled heat pumps.

Chapter 7 focuses on the controller borefield model. Different techniques to obtain a low-order borefield model are described in detail. The impact of the borefield model is illustrated for the optimization of the operation of a HyGCHP system which guarantees long term thermal balance. In this step, the building loads are assumed known.

Chapter 8 integrates the insights obtained at component level to develop an MPC strategy for the integrated CCA-HyGCHP system. The potential of MPC to contribute to the design and operation of cost-efficient CCA-HyGCHP systems is evaluated.

Chapter 9 summarizes the main conclusions and suggestions for future research.

Chapter 2

Concepts

This chapter introduces the concepts central in this work: optimal control, optimization, MPC and system identification.

2.1 Optimal control

2.1.1 General description

Optimal control deals with problems in which a time variable control profile $u(t)$ is sought for a dynamic system such that a certain optimality criterion is met [96]. To this end, an optimization problem is solved over a chosen time horizon t_{end} , which comprises (i) the definition of the objective function J , (ii) the system dynamics \dot{x} , (iii) the state and control path constraints c_{path} and (iv) the boundary conditions $c_{boundary}$. A general optimal control problem (OCP) formulation has the format represented by Equations (2.1)-(2.4).

$$\min_{u(t)} J = \int_0^{t_{end}} L(u(t), x(t), t) dt + M(u(t_{end}), x(t_{end}), t_{end}) \quad (2.1)$$

$$\dot{x} = f(x, u, t) \quad (2.2)$$

$$c_{path}(x(t), u(t)) \leq 0 \quad (2.3)$$

$$c_{boundary}(x(t_0), x(t_{end})) = 0 \quad (2.4)$$

2.1.2 Classification

Finding an optimal control input trajectory boils down to finding the solution to a constrained optimization problem. Optimization problems can be categorized into two broad categories, being the convex and the non-convex problems. The latter category can be further divided into nonlinear and mixed-integer problems. The optimization problem is convex if (i) the cost function J is convex and (ii) if the feasible set is convex. The latter requires all inequality constraints (≤ 0) to be convex and all equality constraints to be linear. For convex optimization problems fast and efficient algorithms to find a global optimal solution exist [23]. However, if one of the above mentioned conditions for convexity is not satisfied, the OCP can be expected to be non-convex. Non-convexity may arise from nonlinearity in the objective function or the constraints, or from a non-convex search domain, such as a discrete variable. The former category is often denoted as nonlinear optimization problem, while the latter is denoted as a mixed integer problem. Both types of optimization problems are harder to solve than convex problems and convergence to global optimality is not guaranteed due to the existence of multiple local minima. An overview of the different optimization problem classes is presented by e.g., Nocedal and Wright [125].

2.1.3 Solution methods

In the former paragraph three types of optimization problems were distinguished. For convex problems, fast and efficient convex solvers exist [23]. Most of them are direct methods, based on a gradient-search or Newton-search methods [125], categorized under the family of quadratic programming (QP) problems. A special class consists of the linear-quadratic regulator problems, for which a closed-loop formulation for the control input u^* can be derived from the Riccati-equations.

For nonlinear problems, it is less evident to find a suitable solution method. Three basic families are distinguished [39]:

- the Hamilton-Jacobi-Bellman equation / Dynamic Programming
- the indirect methods / calculus of variations/ Pontryagin
- the direct methods (control discretization)

The first two methods are based on the Hamiltonian-Bellman principle of optimality, namely 'any subarc of an optimal trajectory is also optimal'. The indirect method, yields an analytical solution for the $u^*(t)$ as a function of the

current state x_0 and the adjoint variable k [154]. The advantage is that insight is gained in the parameters and variables determining the $u^*(t)$ -profile. The disadvantage is that it requires solving a boundary value problem which is only tractable, i.e. computationally feasible, if the number of state variables n_x , input variables n_u and constraints n_{eq} and n_{ineq} is limited. Dynamic Programming (DP) [15, 19] also suffers from this so-called 'curse of dimensionality' [142], but it is conceptually easier to implement. It results in a look-up table which can be determined off-line, avoiding an online optimization problem solving.

Contrary to the first two families of methods, the direct methods are suitable for large-scale nonlinear optimal control problems. The control input profile $u^*(t)$ is discretized with a control time step Δt_c , dividing the control horizon $t = [0H_c]$ into N_c control intervals k in which $u^*(k)$ is assumed to be constant. The smaller Δt_c , the more the discrete-time solution approaches the optimal continuous time signal, but the larger the number of optimization variables. To determine the corresponding state trajectories $x^*(t)$, advanced nonlinear solvers such as MUSCOD and ACADO [80] adopt a variable discretization time step, such that the discretization error remains below a user-defined tolerance level. Different implementations of direct methods are the single shooting and direct multiple shooting [40], the latter being more computationally robust in case of highly nonlinear dynamics.

For mixed-integer problems, one can rely on very powerful commercial solvers, such as CPLEX [29]. Löfberg [111] gives an overview of currently available numerical solvers for the different types of optimization problems.

2.2 Model predictive control

The repeated solution of an optimal control problem in an online framework forms the basis of model predictive control (MPC). MPC combines the benefits of feedforward and feedback control. At each control time step, the control profile for the next H_c control time steps is optimized using knowledge of the current state (= feedback), the building dynamics and future disturbance predictions (= feedforward). Only the first control time step is applied, and after this time step the optimization process is repeated, using updated system information and disturbance predictions. A schematic view of the MPC framework is given in Figure 2.1.

The combination of feedforward and feedback results in a good control performance even in the presence of model mismatch and prediction errors [116]. This is an important asset for practical implementation, as it allows the use of

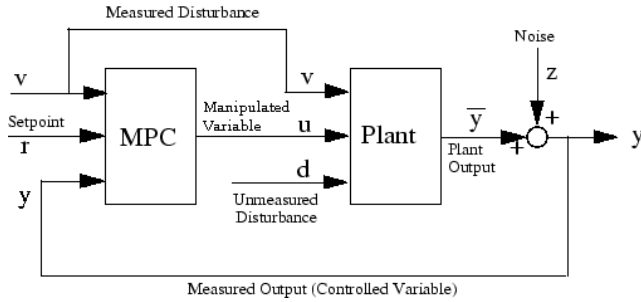


Figure 2.1: Block Diagram of the information flows for a general model predictive control scheme [118].

simple controller models and simple disturbance prediction methods. Robust MPC is a specific type of MPC which explicitly accounts for the impact of non-idealities (noise in the feedback signal, model mismatch and prediction errors) on the optimality of the solution [see e.g. 21, 119]. Stochastic MPC focuses on applications which are characterized by stochastic disturbances, such as solar radiation [see e.g. 127]. The formulation incorporates the future MPC action in the predictions to obtain a less conservative control. Nonlinear MPC deals with applications where the performance loss due to a convex approximation is not tolerated [see e.g. 4, 38, 50].

2.3 System identification

System identification (SI) in the framework of MPC aims at identifying a model which captures the control relevant system dynamics. Ideally, this model is as simple as possible. SI comprises following steps:

1. Defining the model requirements
2. Defining the model type
3. Defining an appropriate set of model structures
4. Obtaining a persistent identification data set
5. Parameter estimation
6. Model validation
7. Model selection

The presentation below is written from a users' perspective. For a comprehensive study on system identification, the reader is referred to the work of Ljung [110] and the work of Pintelon and Schoukens [140] .

2.3.1 Step 1: Model requirements

The first step in the system identification procedure is to define the model requirements:

- Which input/output-relationship(s) do we want to describe?
- Which time scales are we interested in?

For the application of control, the model needs to describe the response of the controlled variables (CV) to the manipulated variables (MV) and to uncontrolled variables or disturbances. The time scale of interest depends on the control objectives and on the time constants of the system.

We will illustrate this with two straightforward examples. First, consider the case where we want to control the compressor power of a heat pump to guarantee thermal comfort in a building with floor heating. The compressor power is the MV, the zone temperature the CV and the ambient air temperature, internal gains and solar gains are the disturbances. The response of the zone temperature to the compressor power is dominated by the dynamics of the floor heating which has a dominant time constant of the order of hours. The control relevant time scale then ranges from, let's say, one hour to one day. The time constant related to the response of the zone temperature to the ambient air temperature, lies within this range. Therefore, the controller building model should also incorporate a dynamic description of the heat transfer through the building envelope. The dominant time constant of the heat pump, by contrast, is of the order of minutes. Since this is far smaller than the control relevant dynamics, the heat pump dynamics can in this case be neglected: a static representation of the heat pump characteristics is sufficient.

If the same building is heated by a heat pump connected to an air-conditioning system, the controller model requirements differ. Since air-conditioning systems react much faster to a change in the compressor power than a floor heating system does, the control relevant dynamics are shifted towards the subhourly time scale. In this case, it might be that the heat pump dynamics can not be neglected by the controller (requiring a dynamic instead of a static heat pump description), while the dynamics related to the building envelope thermal mass may be neglected (and thus replaced by a static model), since the outer wall is quasi-static within the time frame of one hour.

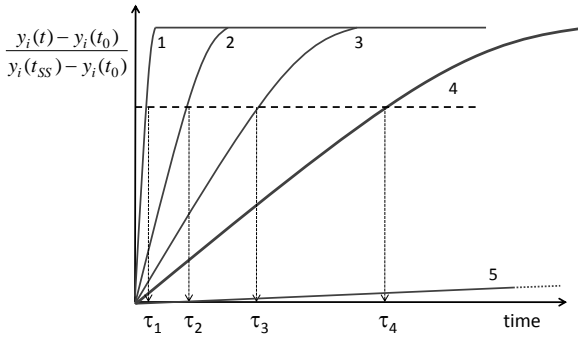


Figure 2.2: Illustration of how to distinguish between the processes which can be represented by a static model on the one hand, and the ones which require a dynamic description, on the other hand, based on the response of the system variables to a step excitation of the manipulated variables (MV). For the depicted example, the normalized response of 5 system variables (y_1, y_2, y_3, y_4, y_5) is shown. If y_4 is the controlled variable, with a dominant time constant τ_4 with respect to the MV, y_1 can be described by a static model in the optimization and y_5 by a constant value. y_2 , y_3 and y_4 require a dynamic representation.

To summarize: a dynamic model is required for the processes with time constants of the same order of magnitude as the control relevant ones, i.e. the ones characterizing the relation between the controlled variable(s) and the manipulated variable(s). Processes with significantly smaller or with significantly larger time constants, can be represented by a static model. This is illustrated in Figure 2.2. The response of the controlled variable, y_4 , to a step excitation of the manipulated variable is dominated by a time constant τ_4 . The response of the variables y_1 , y_2 , y_3 and y_5 which influence y_4 , is characterized by respectively τ_1 , τ_2 , τ_3 and τ_5 . For this example, one could judge that the dynamics related to y_1 ($\tau_1 \ll \tau_4$) and to y_5 ($\tau_5 \gg \tau_4$) can be neglected: y_1 can be represented as an algebraic instead of a differential state, while y_5 can simply be considered constant (within the time horizon of the optimization).

The dynamic range of interest can be expressed in terms of time constants i.e. τ_{min} (s) and τ_{max} (s) - or in terms of frequencies, i.e. f_{min} (Hz) and f_{max} (Hz):

$$\text{Control relevant dynamics} = \begin{cases} f_{min} \leq f \leq f_{max} \\ \text{or} \\ \tau_{min} \leq \tau \leq \tau_{max} \end{cases} \quad (2.5)$$

2.3.2 Step 2: Model type

The entire system identification procedure is determined by the amount, the nature and the quality of the system information available. Information can be available in the format of physical insight and/or measurement data. The choice of the model type depends on the answer to a first question: Do we have enough system knowledge to describe it by first-principles equations? If so, do we know the corresponding model parameters?

- If the answer to both the first and the second question is positive, a first-principles model or 'white-box' model can be developed.
- If the first principle equations can be written down, but the numerical values of the corresponding model parameters are unknown, experimental data are required to estimate these parameters. The combination of a first-principles-based model structure with 'parameter estimation', is denoted by the term 'grey-box modeling'.
- If the system is too complex to be described by first-principle equations, we have to rely on black-box modeling. The black-box modeling approach aims at describing the input/output-relation by fitting the model parameters (which in this case do not necessarily have a physical meaning) to the measured input/output data. Different black-box model structures exist. The most well-known black-box model structures are the ARX, ARMAX, Box-Jenskin and OE-models [see e.g., 110, 171], which differ mainly in the way they deal with unmeasured inputs (system noise) and with measurement errors (measurement noise).

The different steps of the white-box, grey-box and black-box modeling approaches are visualized in Figure 2.3. White-box models generally require a significant amount of physical insight and information. They also tend to be more complex and are therefore less suitable for incorporation in an optimization framework. The black-box modeling approach, by contrast, allows to minimize the amount of prior system knowledge. The drawback of a black-box model is that the model quality is only guaranteed for the frequency range covered by the identification data set (see Step 3). The grey-box modeling approach combines the strengths of both approaches: compared to the white-box modeling approach, the required amount of prior knowledge and the model structure complexity are reduced. Compared to the black-box modeling approach, the model structure and the corresponding model parameters have a physical meaning. This alleviates the task of determining the appropriate number of model parameters.

White-box	Grey-box	Black-box
Prior knowledge required	Less prior knowledge required	No prior knowledge required
Formulation system equations	Simplified system equations	Selection blackbox model structures
Parameters physical meaning	Parameters physical meaning	Parameters no physical meaning
Physical insight in process	More physical insight in process	Only input-output relation

Figure 2.3: Comparison of the white-box modeling approach (left) with the black-box modeling approach (right).

2.3.3 Step 3: Model structures

The term 'model structure' is traditionally used to distinguish between transfer models on the one hand, and state space models on the other hand. In this work, the term refers to the imposed information flow path between the input(s) and the output(s). For white-box and grey-box models, the model structure defines the level of detail with which the processes are described. For black-box models it defines the variable (e.g. transfer function in Laplace variable s versus transfer function in Warburg variable \sqrt{s}) and the way noise is dealt with. The higher the complexity level, in general, the larger the number of parameters. This in turn increases the required amount of system knowledge and/or information contained in the identification data set. The procedure of selecting an appropriate model structure, illustrated by the identification of a controller building model, is well described by Bacher and Madsen [9].

Step 4 and Step 5 focus on respectively the conditions to be fulfilled by the identification data set and on the parameter estimation procedure. These two steps only apply to the grey-box and the black-box modeling approach.

2.3.4 Step 4: Identification data

The quality of the experimental data, also referred to as the 'persistency' of the identification data set, roughly depends on four factors: the frequency content of the excitation signal, the signal-to-noise ratio, the measurement length and the measurement time step. These four factors are not entirely independent, as discussed below.

Frequency content of the excitation signal The frequency range covered by the data set should match the frequency range of interest (defined by f_{min} and f_{max}), or, in other words, the excitation signal should excite the control relevant dynamics identified in Step 1. The frequency content of the excitation signal, found by the Fourier transform of the time domain signal, can be visualized in a Bode-diagram which shows the amplitude and the phase of each frequency contained in the signal. For instance, if we are interested in the control relevant dynamics of a floor heating system (with a dominant time constant of a couple of hours), a heating/cooling signal with an switching time of 5 minutes, will not provide any useful information. Applying a step heat input of a couple of hours, by contrast, will. Typical excitation signals are for instance: step functions, block functions, pseudo-random binary functions (PRBF), multisine functions and white noise. These signals are interesting as they cover a wide frequency spectrum (step function, block functions, PRBF, white noise) or as they excite a limited number of well-chosen frequencies (multisine function). The latter is interesting in the presence of unmodelled disturbances and measurement noise since the frequencies in the output signal which are not contained in the excitation signal, and which thus correspond to system noise and measurement noise, can be filtered out. This brings us to the next factor determining the richness of the data set, namely the signal-to-noise ratio.

Signal-to-noise-ratio The signal-to-noise-ratio is proportional to the amplitude of the response of the output to the excited input, and inversely proportional to the amplitude of the response of the output to unmodelled disturbances and to measurement noise. Therefore, there are three ways to increase the signal-to-noise-ratio: increase the amplitude of the excited input (e.g. apply a higher heating power or by increasing the crest-factor of the signal), minimize the presence of disturbances (e.g. avoid unmodelled internal gains due to stochastic occupancy behavior) and use well-calibrated sensors. The signal-to-noise-ratio can also be decreased by repeating the same experiment a number of times and use the averaged values to filter out (the white fraction of) measurement noise. This brings us to the third factor, being the impact of the measurement length. Note that most processes are to less or more extent nonlinear. Therefore, the magnitude of the signals should correspond to typical values during operation.

Measurement length In the ideal case, i.e., (1) an excitation signal covering the entire frequency range of interest and (2) the absence of system and measurement noise, the required measurement length t_m (s) equals the largest time constant τ_{max} . In practice, longer time intervals are needed to compensate for the lack of information contained in the input signal and to compensate for

the presence of noise:

$$t_m \geq \tau_{max} \quad (2.6)$$

Sampling frequency The measurement frequency f_s or the sampling time interval Δt_s is defined by the Nyquist criterion:

$$f_s \geq 2f_{max} \text{ or } \Delta t_s \leq \frac{\tau_{min}}{2} \quad (2.7)$$

In practice, again to compensate for measurement errors, an even smaller sampling time ($\Delta t_s \leq \frac{\tau_{min}}{5}$) is advised. The combination of the above mentioned 4 factors (the frequency content of the excitation signal, the signal-to-noise-ratio, the measurement length and the sampling time) defines the richness of the data set. As discussed in Step 6, the fitness of the data set to estimate the parameters of a certain model structure, can be assessed after the parameter estimation procedure, based on the magnitude of the uncertainty interval for the parameter values found. If the uncertainty interval is too large, the system identification procedure can be repeated for a richer data set based on Design of Experiments (DOE). A very interesting paper describing the different steps in DOE, illustrated with an example on the identification of a biochemical process, is the paper of Balsa-Canto et al. [12].

2.3.5 Step 5: Parameter estimation

Parameter estimation (PE) boils down to solving an optimization problem, namely finding the parameter set θ which minimizes a scalar function l of the model error evaluated over the entire identification data set. For a given estimate of the parameter set $\hat{\theta}$, the prediction error $\epsilon(t, \hat{\theta})$ can be presented as follows [110]:

$$\epsilon(t, \hat{\theta}) = y(t) - y(t|\hat{\theta}) \quad (2.8)$$

with $y(t)$ representing the measured output at time step t and $y(t|\hat{\theta})$ the model output at that time step with the given parameter estimate $\hat{\theta}$.

The cost function to be minimized is then represented by:

$$\theta^* = \operatorname{argmin} V_N(\theta, Z^N) \quad (2.9)$$

where

$$V_N(\theta, Z^N) = \frac{1}{N} \sum_{t=1}^N l(\epsilon(t, \theta)) \quad (2.10)$$

with N denoting the number of measurement time steps and Z the input signal applied during the measurements.

The family of methods which correspond to Eq.(2.13) is referred to as *Prediction Error Methods* (PEM). Different PEM methods exist, which differ (among others) in the way $\epsilon(t, \hat{\theta})$ and $V_N(\theta, Z^N)$ are defined [171].

With the so-called 1-step-ahead prediction, $\epsilon(t, \hat{\theta})$ is calculated using the measured output at the previous time step $y(t-1)$, see Eq.(2.11). In the general PEM case $\epsilon(t, \hat{\theta})$ only uses the measured output at time t_0 , see Eq.(2.12).

$$\epsilon(t, \hat{\theta}) = y(t) - y(t|t-1, \hat{\theta}) \quad (2.11)$$

$$\epsilon(t, \hat{\theta}) = y(t) - y(t|t_0, \hat{\theta}) \quad (2.12)$$

The most common choice for the scalar function l is the sum of squared errors. With substitution of Eq.(2.8), Eq.(2.10) becomes:

$$V_N(\theta, Z^N) = \frac{1}{2N} \sum_{k=1}^N l(y(k) - y(\hat{\theta}, k))^2 \quad (2.13)$$

For a linear model, the combination of the one-step-ahead prediction (Eq.(2.11)) with Eq.(2.13) results in a simple linear regression (LR) problem, which has a unique solution. In the other cases, PEM requires solving a nonlinear optimization problem since the cost function $V_N(\theta)$ is nonlinear in the parameters. As a consequence, these methods need a good initial guess to guarantee convergence to the global minimum. The impact of the PE method on the quality of the obtained models, is very well illustrated in the work of Bianchi [20]. He compared different PEM for both the offline and online identification of a controller building model. As an example, the LR technique fails in all cases where solar radiation is present, while the PEM with Eq.(2.12) yields good results. In this study, the latter approach is used (see Chapter 5 and Chapter 7). The resulting nonlinear problem is solved with the Levenberg-Marquard method [125] (Chapter 7) or with the exact Newton method implemented in ACADO [80].

The uncertainty on the parameter values can be estimated from the Fisher Information matrix (under some hypothesis on the estimator properties), which in turn is determined from the Hessian (i.e. the matrix with the second order derivatives) of the cost function in the optimum. To put it simply: the flatter the cost function in the optimum, the larger the uncertainty on the parameter values found, the steeper the cost function, the smaller the uncertainty. The shape of the cost function depends on both the model structure and the identification data set. An appropriate combination of model structure and data set will yield a well-conditioned optimization problem. Problems arise when the dynamics related to a certain parameter are not excited. In that case, the identification data set does not contain the information required to define the value of this parameter - or - from the view of the optimization: the cost function is not

sensitive to the value of this parameter. This problem arises in case (a) the model structure is too complex (and thus contains redundant parameters) and/or (b) the identification data set is not sufficiently rich. In both cases, the system identification procedure has to be repeated (see Step 2 and Step 3). This explains why, in general, system identification requires an iterative procedure. A systematic approach to iteratively improve the excitation signal for a given model structure, and given the existing constraints (e.g. limited measurement time, limited number of measurements, limited power, limited energy use) is design of experiments [51].

Note that besides the Fisher Information matrix there are other PE performance indicators, such as the Akaike Information Criterion (AIC), expressed in Eq.(2.14), and the Rissanen's Minimum Description Length Criterion (MDL). Low AIC values and MDL values indicate good model accuracy (i.e. low $V_N(\theta, Z^N)$) and acceptable number of parameters (i.e. low $\dim(\theta)$).

$$\text{AIC} = V_N(\theta, Z^N) + \frac{\dim(\theta)}{N} \quad (2.14)$$

Both AIC and MDL assist the selection of an appropriate model structure, which is neither too simple nor too complex. The smaller the data set (small N), the more $\dim(\theta)$ is penalized. This is important to avoid overfitting, especially for small data sets (small N). Over-fitting means that an amount of (redundant) model parameters are fitted to describe the noise content of the identification data set - rather than the system dynamics. This is reflected in bad cross-validation results (see Step 6).

2.3.6 Step 6: Model validation

Broadly speaking, there are five ways to validate a given model [176]:

1. checking if the parameter values are physically meaningful (in the case of a grey-box model) (see Step 4),
2. quantifying the uncertainty on the parameter values (see Step 4),
3. validation in the time domain,
4. validation in the frequency domain,
5. residual analysis.

The latter three techniques compare the model output to the measured output for a validation data set, i.e. a data set which differs from the identification

data set and which is -by preference- representative for the conditions to which the system is submitted in reality. The validation data are obtained from measurements on the actual system ('experimental validation') or from simulations with a detailed model ('intermodel comparison').

The model error is often quantified in terms of the root mean square error (*RMSE*) of the model output, which in the time domain is defined as:

$$\text{RMSE} = \sqrt{\frac{\sum_{k=1}^N (y(\theta, k) - y_m(k))^2}{N}} \quad (2.15)$$

With the residual analysis, the frequency spectrum of the prediction error $\epsilon(t, \hat{\theta})$ is analyzed. In the case of a perfect model, the frequency spectrum of the residuals equals the one of the measurement noise, which, in general, is considered to be white noise. If, by contrast, the model structure neglects important dynamics, the error will be correlated with the input (or with unmodeled input). This will result in a 'colored noise' spectrum.

2.3.7 Step 7: Model selection

For the purpose of control, the model fitness should finally be evaluated within the optimal control framework. If the model is found to yield unsatisfactory control performance, the system identification procedure has to restart from Step 1.

Chapter 3

Literature review

Optimization-based control strategies such as model predictive control (MPC), have shown to outperform traditional control strategies for a variety of heating and cooling systems, building types and climates. Those systems are characterized by the presence of thermal mass which acts as active or passive energy storage, limited installed capacity and/or time dependent efficiencies or costs. Thermal mass can be included at the building level (e.g. heavy-weight building envelope, floor heating and concrete core activation) or at the installation level (e.g. buffer tank, ice storage tank and ground thermal energy storage). Time dependency of the efficiency holds for devices such as chillers, heat pumps, cooling towers and dry coolers, where the heat or cold production efficiency depend on the operation conditions. Time dependent energy costs (on the short term) are restricted to electricity driven devices. This chapter gives a non-exhaustive overview of research on optimal control of building heating and cooling. The overview is clustered in five sections. Section 3.1, Section 3.2 and Section 3.3 each focus on one of the sublevels, respectively the building, the installation and the borefield. Section 3.4 deals with optimal control from an integrated systems' perspective. Finally, Section 3.5 deals with the interaction between control and design. Each section ends with the related research question addressed in this work.

3.1 Optimal control at building level

Research on optimal control of heating systems has in particular focused on the building level, see e.g. [27, 64, 66, 68, 90, 103, 161, 195–197]. For fossil

fuel driven devices such as gas boilers, the optimization potential primarily lies in accurately predicting the heating load. This way the right amount of heat is produced at the right time to satisfy the thermal comfort requirements with minimal primary energy consumption. As confirmed by earlier studies [27, 150, 186] and by practice [161], the potential benefits for optimal control compared to conventional PI-control strategies are the highest for heavy-weight buildings in mild climates with large daily temperature swings, i.e. situations in which prediction and anticipation can make a difference.

Whereas the concept of MPC for energy and comfort management has proven to have clear advantages over other control strategies, it also has drawbacks which currently hamper its widespread implementation. Dounis and Caraiscos [41] identified different problems, among which (1) the need for an adequate controller model structure, (2) the need for online estimation of the corresponding parameters which is robust in the presence of noise, (3) the fact that the adopted thermal comfort models do not reflect the complex, nonlinear features which characterize thermal comfort and (4) the lack of user friendliness, user interaction and learning methods. The identification of the system dynamics is indeed perceived as a major challenge for a successful implementation of MPC. This explains the large research effort in the field of system identification of controller building models, weather predictions and occupancy prediction. Two distinct approaches are observed here. The first one is to incorporate highly detailed models for the building (see, e.g.[28, 170]) and the installation [58]. This approach allows reusing simulation models used in the design phase. However, the complexity of the resulting optimal control problem (OCP) becomes prohibitively large. The alternative is to use simplified building control models. Those can be achieved by model reduction of a detailed physical model [see e.g., 131]), parameter estimation of an RC-model based on the electrical analogy [see e.g., 9, 11, 53, 101]) or by system identification using black box models [see e.g., 49]). This approach requires the selection of a model structure which is as simple as possible but still catches the control relevant processes. Thanks to their simple structure, those models can be identified or fine-tuned online, as stressed by Kummert [102] and Bianchi [20]. Moreover, the computational power to run the optimization can be significantly reduced. The standard MPC framework, with a receding horizon procedure, incorporates a feedback mechanism which allows - to a great extent - compensating for model and prediction errors [116]. Additionally, low-level local proportional-integral controllers can compensate for small modeling and prediction errors to ensure stable and robust zone temperature control [197]. It is indisputable that for implementation in low-level devices with limited computational power, simplified optimal control formulations are highly desirable. On the other hand, the benefits from a simplified formulation have to be outweighed against the performance loss caused by the approximations made.

On the building model level, the use of simplified models for the optimal control of floor heating systems is found to be acceptable. The building model should enable predicting both the thermal comfort and the heating load. Thermal comfort is a function of the operative temperature T_{op} , which in turn is a weighted sum of the room air temperature and the radiative temperature [47]. An accurate prediction of T_{op} requires a detailed building model which distinguishes between convective and radiation heat transfer processes into and inside the building zones. However, in the case of floor heating, the fast fluctuations of the operative temperature T_{op} caused by solar radiation or internal gains can not be compensated by the heat production system due to the high thermal inertia of floor heating. This explains why low order building models, which only capture the slow dynamics needed to predict the building load, are found to be adequate for optimal control of floor heating systems. The studies of Wimmer [186] and Bianchi [20] indicate that a third-order or even a second-order lumped capacitance model is able to capture the control relevant dynamics imposed by the floor heating time constant in a well-insulated heavy-weight residential building. The capacity of the zone air, inner walls and outer walls are all lumped to one capacity at an average zone temperature T_z . The impact of the solar gains on the heating load are taken into account by adding a positive ΔT to the ambient air temperature T_{amb} . The study of Karlsson and Hagentoft [90], dealing with the application of MPC for controlling a floor heating system in a well-insulated light-weight building, also shows that a second-order lumped-capacitance model is a good approximation for a detailed numerical step-response model derived from a Simulink model of the reference room. Similarly, the study of Peeters et al. [137] shows that an accurate prediction of the solar gains has only a minor impact on the total daily heat demand of a floor heating system.

Kummert [102] investigated the impact of simplifications on the level of thermal discomfort evaluation. The optimization was performed with a quadratic approximation of the discomfort based solely on the operative temperature. The actual thermal discomfort level was evaluated with a detailed simulation model, using the simulated mean radiative and air temperature, as well as the humidity. The results indicate that the use of more detailed thermal discomfort models does not alter the relative control performance of the investigated optimal control formulations.

Contrary to residential buildings, office buildings are characterized by the presence of large solar gains and internal gains. The controller model should be able to predict the heating and cooling loads in the presence of these high gains. First, the question arises which model structure is required for buildings with high solar and internal gains and second, which measurement data are needed to perform the system identification? Should the solar gains and internal

gains be in the identification data set? Third, how should this model be used in an MPC framework? Is prediction of the solar and internal gains required or not? It is indisputable that for low-cost implementation of MPC, minimizing the effort and amount of data required for system identification is highly desirable. On the other hand, the practical and economical benefits of a simplified building model have to be outweighed against the performance loss caused by the approximations made.

Objective 1 *A first objective in this work is to investigate the impact of the controller building model and the identification data used for parameter estimation, on the performance of an MPC controller for office buildings with CCA in the presence of large solar and internal gains. This objective is addressed in Chapter 5.*

3.2 Optimal control at installation level

For electricity-driven devices such as heat pumps and chillers there is additional opportunity for optimization due to the structure of the electricity cost, namely the time-of-day price dependency and the additional charge on peak power demand. This explains the extensive research effort in the field of optimal control of cooling dominated, air-conditioned buildings, e.g. [3, 88, 95, 114, 115, 170]. For this type of buildings, the optimization potential primarily lies at the installation level, namely in optimizing the charging and discharging of active thermal energy storage devices (e.g., ice storage) as well as in optimizing the switching between active cooling, free cooling and night ventilation. Also for heat pump systems in heating dominated buildings, the first investigations of optimal control focused on the installation level. Heat pump operation and electrical backup heating were optimized for charging a buffer tank for a day-night electricity price profile [149, 198].

On the heat pump model level, the influence of simplifications has not yet been investigated. Several representations are found in the literature. Gayeski et al. [58] represent the heat pump thermal power \dot{Q}_{hp} and the compressor power P_{hp} as quadratic polynomials in the compressor frequency f , the ambient temperature T_{amb} and the supply water temperature T_{ws} . Because of the model complexity, a simple form of direct search, called a pattern search, was selected as optimization method (see e.g., [174]). Rink et al. [149] and Zaheeruddin et al. [198] did not incorporate the part load efficiency in their studies. The heat pump was characterized by the COP, which was represented by a linear function of the mean storage tank temperature. The resulting nonlinear problem was first

solved analytically, using the Maximum Principle [96]. This solution method yields a global optimal solution but is restricted to theoretical studies as it limits the number of dynamic states, constraints and boundary conditions. Next, the nonlinear problem was solved numerically, inducing problems of convergence and local minima. Wimmer [186] and Bianchi [20], on the contrary, used a predefined COP profile based on the forecast of T_{amb} and a constant value for T_{ws} . Thanks to this simplification, i.e. neglecting the T_{ws} dependency of the COP in the OCP formulation, a convex optimization problem was obtained which could be solved with a standard quadratic programming solver [125].

Objective 2 *A second objective is to assess the impact of the controller heat pump model in OCP formulation. The aim is to quantify how much can be gained by explicitly integrating the temperature dependency of the COP into the optimization (yielding a nonlinear problem), versus solving an approximated, but convex formulation.* This objective is addressed in Chapter 6.

3.3 Optimal control at borefield level

When the GCHP system is designed to cover the entire heating and cooling demand, the control at borefield level is straightforward. The borefield size is then determined such that the temperature limits are only met at the end of the design life time, normally chosen 20 to 25 years. In this case, the borefield can be used permanently.

Such large borefield design is however suboptimal from a life cycle cost point of view. The economical feasibility of GCHP systems largely depends on the required ground heat exchanger (GHE) length. This explains why research in the domain of GCHP systems, contrary to research in the domain of CCA, has mainly focused on the design level. Compared to the other components of the heating and cooling installation, the sizing of the GHE is critical. Oversizing compromises the economical feasibility of the GCHP system, while undersizing may result in operation failure [31, 194]. The GHE length depends on roughly four factors: (1) the thermal properties of the ground, the borehole and the circulating fluid, (2) the borefield heat injection and extraction loads, (3) the borefield heat injection and extraction power rates, (4) the heat injection and extraction imbalance. The first factor explains the importance of conducting an in-situ Thermal Response Test (TRT) for determining the ground thermal conductivity and the borehole thermal resistance [see e.g., 60, 152, 158, 187]. The sensitivity on the next two factors explains the need for a dynamic building load

calculation [126, 168]. Such a dynamic simulation however requires incorporation of a control strategy. As such, system operation influences the installation sizing and thus the required GHE length. The impact of the control strategy on the building load calculation, and thus on the borefield size, is especially true for GCHP systems connected to slowly reacting heat emission systems such as CCA, as will be discussed in Section 3.4. Finally, the larger the imbalance between heat injection and extraction, the larger the required GHE length.

Various studies have shown that - from a life cycle cost point of view - a hybrid ground-coupled heat pump (HyGCHP) configuration is optimal [31, 69, 71, 108, 146, 191]. The borefield is then sized to entirely cover the smallest of the two loads, and only a fraction of the dominant load. This fraction is determined such that the amount of injected and extracted heat are more or less in balance. The remaining part of the dominant load is then covered by a supplementary heater or cooler. For HyGCHP two additional control tasks arise. First, the operation should fulfill the design condition for borefield long term thermal balance. Second, switching between the different devices, i.e. the GCHP system on the one hand, and the supplementary heater/cooler on the other hand, should be such that the total annual running costs are minimized. As clearly explained by De Ridder et al. [35], this is the only way to realize the potential of HyGCHP to decrease the total life cycle cost in practice.

Yavuzturk and Spitler [191] and Xiaowei [189] compared different rule-based control (RBC) algorithms for HyGCHP in cooling dominated climates with focus on the control settings for switching between the GCHP and the supplementary cooling tower. Optimizing these settings has shown to be a complex task due to the large number of decision variables. Moreover, none of these control algorithms balance the loads in the ground [69]. In practice, these parameters are defined heuristically, leaving a large potential for operation improvement [126]. In a nutshell: the actual system efficiency of HyGCHP systems with today's control strategies may not fulfill the expectations formulated in the HyGCHP design phase.

A long term sustainable and energy efficient operation of a HyGCHP system requires to take the temperature dependency of the heat and cold production efficiencies into account, as well as the long term borefield thermal balance condition. These control objectives could be formulated as an optimal control task, allowing to additionally take into account the installed capacities of the heating and cooling devices, and the electricity price time dependency. The application of optimal control theory to HyGCHP is still a research area to be explored [165]. According to the authors' knowledge, only two publications on optimal control of borefield thermal energy storage on a seasonal time scale are available, namely by Franke [54] and De Ridder et al. [35]. The former deals with borefields for solar energy storage, while the latter focuses on HyGCHP

systems. De Ridder et al. [35] clearly explain why an optimal control approach is required to realize the cost savings potential of HyGCHP. The entire concept of HyGCHP is based on sizing the borefield as compact as possible. To maximize the use of the borefield, the operation will hit both the upper and lower bounds set on the borefield and/or brine fluid temperature. The fact that optimal control allows operating the system near its boundaries, was identified as a crucial asset compared to rule-based controllers.

De Ridder et al. [35] proposed an optimization based control strategy which explicitly incorporates the condition for long term borefield thermal balance. At each time step, the optimal power rates of the different HyGCHP devices are taken from a look-up table, as a function of (a) the building load and (b) the mean borefield temperature. The optimization method used is Dynamic Programming (DP), which allows explicitly accounting for the stochasticity of the weather. The method guarantees that - for a given borefield size - the seasonal energy storage capacity is fully exploited, i.e. the borefield is fully regenerated at the start of the heating season, and fully depleted at the start of the cooling season. The drawback of DP is the practical limitation of the number of state variables. The presented DP approach was formulated as a function of one single state variable, namely the mean borefield temperature. If the number of state variables is restricted to one, this is a good choice as it enables us to impose somehow long term borefield thermal balance. As will be shown in Chapter 7, however, a first-order borefield model is not sufficient to adequately describe the heat exchange between the borefield and the surrounding ground, being an important term in the borefield thermal balance equation. Moreover, for determining the optimal switching between the different devices, the mean borefield temperature is not the right variable. The actual heat pump efficiency and the availability of passive cooling depend on the brine fluid temperature, not on the mean borefield temperature. Finally, the mean borefield temperature can not be directly measured. To summarize, a general framework to optimize HyGCHP operation requires a dynamic borefield model which (1) predicts the response of the brine fluid temperature to a time-varying borefield load - such that the heat pump COP and passive cooling efficiency can be quantified - and (2) accurately captures the long term borefield dynamics - such that long term sustainability can be imposed.

Objectives 3 and 4 *A third objective is to develop a borefield model which can be used to optimize the operation of a HyGCHP system. The model should be able to predict the response of the brine fluid temperature to typical borefield loads in order to assess the heat pump COP and the availability of passive cooling. To impose long term borefield thermal balance, the model should additionally capture the long term borefield dynamics. The aim is to investigate the minimum*

required model order to capture these control relevant dynamics as well as the methodology to derive such a low-order borefield model. A fourth objective is to analyze the optimal HyGCHP operation for a given building heating and cooling load profile, such that the total annual energy cost is minimized while guaranteeing a long term sustainable operation. These objectives are addressed in Chapter 7.

3.4 Optimal control at system level

Optimal control at system level has started only recently with the introduction of low-exergy heating systems combining heat pump systems to floor heating [20, 186] or concrete core activation [57, 58, 78, 107]. The integrated system approach allows to exploit the thermal capacity of the heat emission system to shift the heat and cold production to time periods with higher heat and cold production efficiency or lower electricity prices (load shifting), or to decrease the power peak demand (peak shaving) in case of a peak electricity demand charging scheme. The incorporated controller building models are dynamic, while the incorporated installation models are static. The latter is allowed as the time constants of heat pumps, chillers or cooling towers are in the order of magnitude of minutes, being much smaller than the time constants at building level. This is not the case for GCHP systems. As discussed in the previous paragraph, the COP of the heat pump and the availability of passive cooling depend on the brine fluid temperature, which in turn depends on the borefield temperature distribution. System level optimization of building climate control with a GCHP system therefore adds a new time scale to the optimization, as the borefield time constants range up to tens of years. It is computationally not feasible to solve an optimization problem explicitly integrating both the short and the long term time scales. The formulation of a computationally efficient optimal control problem for the integrated CCA-HyGCHP system is therefore to be investigated.

Objective 5 *A fifth objective is the development of an MPC strategy which optimizes the operation of a CCA-HyGCHP system from an integrated system perspective. To this end, a computationally efficient formulation should be found which enables capturing both the control relevant dynamics at building side and at borefield side. This objective is addressed in Chapter 8.*

3.5 Integration of control and design

The CCA dynamics and borefield dynamics do not only increase the control complexity but also the complexity of sizing of the heating and cooling installation. In practice, design and control are carried out in two consecutive steps. However, as discussed below, both CCA systems and GCHP systems benefit from an integrated approach of control and design. For systems combining CCA and a GCHP system, the interaction between control and design is even more pronounced.

As stated in Section 3.1, the thermal capacity of CCA not only allows load shifting but also load shaving. The latter in turn allows to reduce the installed heating and cooling power and thus to reduce the investment cost. The potential of CCA for peak load reduction has, however, not yet received much attention [148]. The smaller the production capacity, namely, the more challenging it is to satisfy thermal comfort as lower power rates require the controller to better anticipate on the future building loads. Therefore, for buildings with CCA, installation sizing should be based on a dynamic building load calculation incorporating the control strategy that will be implemented. The benefits of an integrated approach for the design and control of CCA and its installation are well illustrated by the study of Tödttli et al. [173] for the case of a heating curve/cooling curve based control strategy. An additional advantage of MPC, regarding this design issue, is that MPC explicitly takes input and state constraints into account. The potential of MPC to minimize energy use thanks to knowledge of the building dynamics, system characteristics and future disturbances, together with the ability to incorporate knowledge about the input constraints, explains why MPC allows to reduce the heating and cooling installation size without compromising thermal comfort.

Recalling the fact that the borefield investment cost is the main bottleneck for the implementation of GCHP systems, as well as the fact that the required GHE length scales almost linearly with the peak borefield load [69], revealed that MPC can really make a difference for CCA-GCHP systems, and not only from energy cost point of view. The potential of MPC to exploit the thermal capacity of CCA for load shifting and peak shaving could entail large investment cost savings, at least if an MPC control strategy is incorporated in the design phase as suggested by Tödttli et al. [173].

Objective 6 *A sixth objective is to integrate the use of MPC in both the design and operation phase of HyGCHP systems and to assess the benefits on the Net Present Value compared to conventional design and control strategies. This objective is also addressed in Chapter 8.*

3.6 Summary

To summarize, MPC for the application of CCA-HyGCHP systems has the potential to:

- solve the controllability problems of CCA related to its thermal inertia - by incorporating a dynamic building model
- minimize the energy costs - by considering the efficiency of the different heat and cold production systems and the time dependency of the electricity price,
- guarantee long term sustainable operation of the borefield - by incorporating the long term thermal balance condition in the optimization,
- decrease the investment cost - by exploiting the thermal capacity of CCA for load shifting and peak shaving to reduce the required installation size.

Chapter 4

System description

4.1 Introduction

This chapter describes the office building with concrete core activation (CCA) and a hybrid ground coupled heat pump (HyGCHP) installation which is used as a reference. The chapter starts with a description of the building emulator model in TRNSYS, the occupancy and weather profiles and the defined thermal comfort requirements. Next, the heating curve/cooling curve-based control strategy used as reference, is presented. The chapter concludes with the sizing of the components of the HyGCHP system.

4.2 Overview

Figure 4.1 gives a schematic presentation of the system, comprising the two zone office building, the heat and cold at distribution and production level and the borefield thermal energy storage. Each level is treated in more detail below.

4.2.1 Two zone office building with concrete core activation

The building considered in this study is an office building with concrete core activation (CCA), controlled ventilation and solar shading. The office is North-South oriented. The North (N) and South (S) zone offices are separated by a

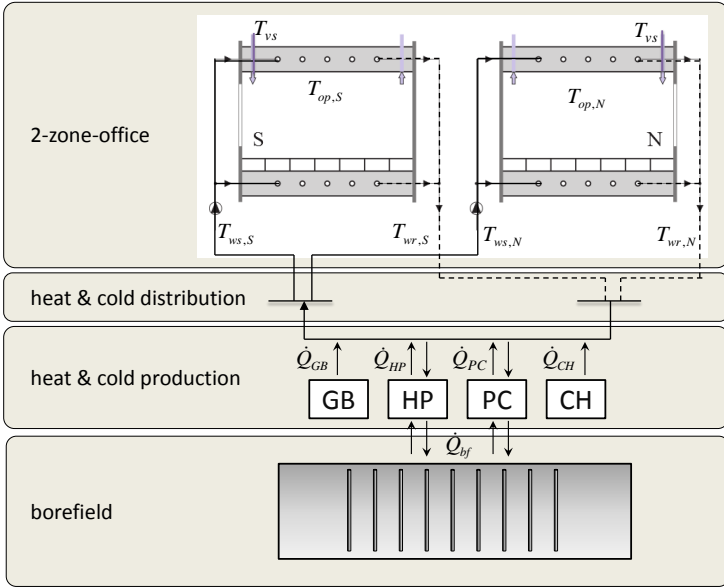


Figure 4.1: Schematic presentation of the system with indication of the two zone office, the heat and cold distribution, the heat and cold production and the borefield. $T_{op,S}$ and $T_{op,N}$ denote the zone operative temperature in respectively the South and North zone, $T_{ws,S}$ and $T_{ws,N}$ the corresponding supply water temperatures and $T_{wr,S}$ and $T_{wr,N}$ the corresponding return water temperatures. The heat and cold production system comprises a gas boiler (GB), a heat pump (HP), a heat exchanger for passive cooling (PC) and a chiller (CH). The heating power is $\dot{Q}_h = \dot{Q}_{HP} + \dot{Q}_{GB}$ and the cooling power $\dot{Q}_c = \dot{Q}_{PC} + \dot{Q}_{CH}$. \dot{Q}_{bf} represents the thermal power extracted from or injected in the borefield by means of the HP and the PC.

central corridor. A cross section is shown in Figure 4.2. Table 4.1 summarizes the properties of a representative unit of the building. The offices have a raised floor and only in the corridor a suspended ceiling is placed. The outer wall has 0.1 m mineral wool insulation and high quality windows. The solar shading has a g-value of 25%. Table 4.2 presents the building characteristic values, with the heating load calculated according to EN12831 [25] and the cooling load to

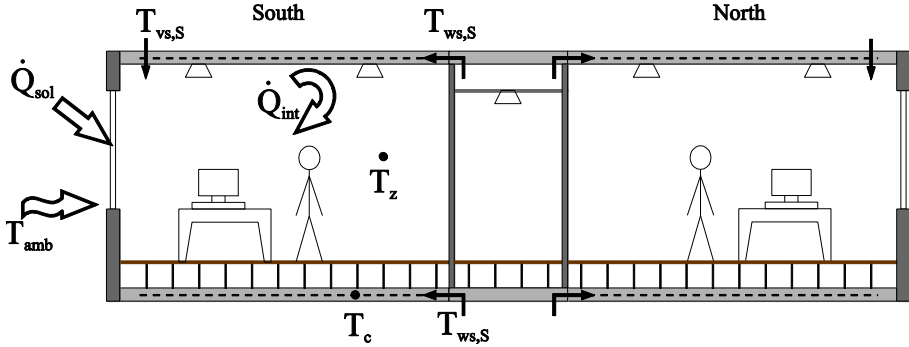


Figure 4.2: Schematic presentation of the two zone (South and North) office building with the disturbances ambient temperature T_{amb} , solar radiation \dot{Q}_{sol} and internal gains \dot{Q}_{int} , the inputs water supply temperature T_{ws} and ventilation temperature T_{vs} and the measured outputs operative temperature T_{op} and concrete core temperature T_c .

Table 4.1: Wall and window properties [164].

Wall	U (W/m ² K)	Remark
Outer wall	0.41	0.1 m mineral wool
Internal wall	0.79	Gypsum board
Floor/Ceiling	1.38	Uncovered ceiling - raised floor
Suspended ceiling	1.11	
Window	U (W/m ² K)	g-value
Window	1.29	0.36
Solar shading		0.25

VDI2078 [178].

Solar shading The South zone of the office building is equipped with an automated solar shading system. It has a controller with hysteresis which lowers the shading device when $\dot{Q}_{sol} > 250 \text{ W/m}^2$, and pulls it up again when $\dot{Q}_{sol} < 150 \text{ W/m}^2$. The North zone has no solar shading.

Ventilation The air handling unit (AHU) provides hygienic supply air at a flow rate of $36 \text{ m}^3/\text{h}$ pers between 7AM and 7PM [164]. The ventilation air

Table 4.2: Building characteristics [164].

two zone office building parameters		
Heated office volume	(m ³)	72
Heated office area	(m ²)	24
Transmission area	(m ²)	8.6
U-value total façade	(W/m ² K)	0.85
Percentage of glazing	(%)	50
Heating power w/o reheat capacity	(W/m ²)	26
Cooling power South zone (peak at 5 PM)	(W/m ²)	31

supply temperature T_{vs} equals the lower value of the thermal comfort band, i.e. $T_{vs} = 20^\circ\text{C}$ in winter and $T_{vs} = 22^\circ\text{C}$ in summer. In this study, the use of the AHU to assist temperature control, is not investigated. The developed MPC only optimizes the production of heat and cold supplied to the TABS.

Occupation profile The office is occupied on weekdays between 8AM - 12PM and 1PM - 6PM. The internal gains are based on a scheduled occupancy model and comprise the sensible heat gains from the people \dot{Q}_{people} , from the electrical appliances \dot{Q}_{appl} , and from the lighting \dot{Q}_{light} . The values are taken from the ASHRAE Fundamentals, Chapter 18 [72]: $\dot{Q}_{people} = 75 \text{ W/person}$ (63% convective, 27% radiative), $\dot{Q}_{light} = 7 \text{ W/m}^2$ (80% convective, 20% radiative) and $\dot{Q}_{appl} = 13.8 \text{ W/m}^2$ (50% convective, 50% radiative). The resulting profiles per zone, calculated for an occupancy density of 1 person per 10 m^2 and a zone floor area of 12 m^2 , are shown in Figure 4.3. Note that also during non-occupied hours and weekends, there is still a small amount of internal gains due to appliances and lighting, respectively of 2 W/m^2 and 3 W/m^2 .

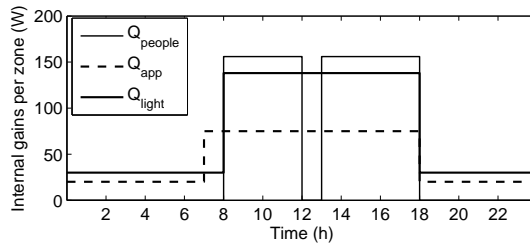


Figure 4.3: Internal gains per zone for a week day.

Implementation in TRNSYS The two zone office building is implemented in TRNSYS [155] by means of the TYPE56 building model. The CCA ceiling and CCA floor are integrated in TYPE56 by means of the EMPA-model [100].

4.2.2 Heat and cold distribution

As shown in Figure 4.1, the implemented heat and cold distribution system is kept very simple entailing some important control limitations. First, as there is only one supply collector, simultaneous space heating and space cooling is not possible. Second, as there are no 3 way mixing valves, the supply water temperature to the North and the South zones, $T_{ws,N}$ and $T_{ws,S}$, are equal to the temperature at collector level. Third, the flow rates through the CCA are constant. By consequence, as both the flow rates and the supply water temperatures to the zones are equal, no zone-level control is implemented in this work for the CCA-HyGCHP system (see Chapter 8). Note that in Chapter 5, where the focus is on the building level, 3-way-valves are incorporated and $T_{ws,N}$ and $T_{ws,S}$ are individually controlled. The impact of zone-level control versus the here described 'lumped-building-level' control on the system performance is assessed for the case of an idealized boiler/chiller in Chapter 8.

4.2.3 Heat and cold production

The heating installation comprises a heat pump (HP) and a gas boiler (GB). The cooling installation comprises a heat exchanger (HE) for passive cooling (PC) and a chiller (CH) for active cooling. The heat exchanger and the chiller are connected in series with the chiller coming first. This configuration results in a smaller temperature difference to be bridged by the chiller, resulting in a better performance of this component. However, it also requires a larger HE as the temperature difference over the latter is also reduced. The HP and the PC heat exchanger are connected to the borefield. The sizing of the devices and of the borefield is based on a dynamic building load calculation, as will be discussed in Section 4.6. The installation is sized for a office building comprising 150 modules of the above described two zone office module, resulting in a total conditioned floor area of 3600 m². To this end, the two zone office model loads are simply scaled. Since the CCA floor and ceiling of the two zone model condition a surface of 48 m² (there is transmission to the upper and lower zones), the scaling factor is 75. Note that this is a theoretical building: abstraction is made of the ground floor (different floor boundary conditions), the upper floor (different ceiling boundary conditions), non-office spaces (e.g. service rooms) and heat and cold distribution losses.

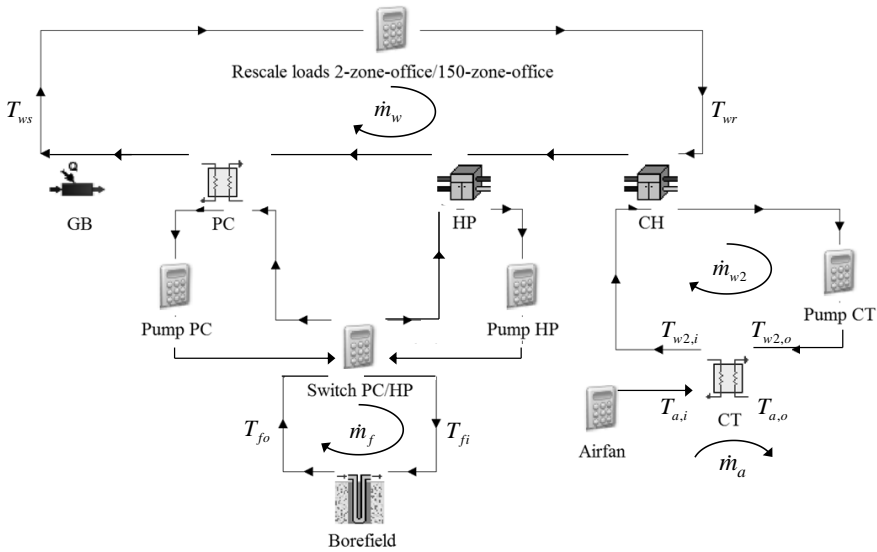


Figure 4.4: View of the installation model in the TRNSYS simulation environment, with annotation of the most important variables.

Implementation in TRNSYS Table 4.3 gives an overview of the TRNSYS components used to model the HyGCHP installation. Each component is characterized by its Type number. The table lists the input and output variables, indicated on the printscreen of the TRNSYS simulation environment in Figure 4.4: the water mass flow rate at building level \dot{m}_w (kg/s) with corresponding supply water temperature T_{ws} ($^{\circ}\text{C}$) and return water temperature T_{wr} ($^{\circ}\text{C}$), the brine mass flow rate through the borefield \dot{m}_f (kg/s) with corresponding borefield fluid inlet temperature $T_{f,i}$ ($^{\circ}\text{C}$) and borefield fluid outlet temperature $T_{f,o}$ ($^{\circ}\text{C}$), the water mass flow rate between the condenser of the chiller and the cooling tower (CT) \dot{m}_{w2} (kg/s) with corresponding chiller inlet and outlet temperatures $T_{w2,i}$ ($^{\circ}\text{C}$) and $T_{w2,o}$ ($^{\circ}\text{C}$) and the air mass flow rate through the cooling tower, \dot{m}_a (kg/s) and the corresponding inlet and outlet air temperatures $T_{a,i}$ ($^{\circ}\text{C}$) and $T_{a,o}$ ($^{\circ}\text{C}$). Note the calculator component at the top, which scales the heating and cooling loads of the two zone office to the loads for the total office building (scaling factor 75).

Table 4.3: TRNSYS implementation of installation components.

	TRNSYS	Description	Control	Input	Output	Parameter
GB	Type6	aux. heater	on/off	$\dot{m}_w, T_{w,i}$	$T_{w,o}$	heating power \dot{Q}_{GB}
HP	Type668	WWHP	on/off	$\dot{m}_w, T_{w,i}$ $\dot{m}_f, T_{f,o}$	$T_{w,o}$ $T_{f,i}$	look-up table \dot{Q}_{HP} look-up table P_{HP}
PC	Type5b	contour flow HE	on/off	$\dot{m}_w, T_{w,i}$ $\dot{m}_f, T_{f,i}$	$T_{w,o}$ $T_{f,o}$	$(UA)_{PC}$
CH	Type668	WWHP	on/off	$\dot{m}_w, T_{w,i}$ $\dot{m}_{w2}, T_{w2,i}$	$T_{w,o}$ $T_{w2,o}$	look-up table \dot{Q}_{CH} look-up table P_{CH}
CT	Type5b	contour flow HE	on/off	$\dot{m}_{w2}, T_{w2,o}$ $\dot{m}_a, T_{a,i}$	$T_{w2,i}$ $T_{a,o}$	$(UA)_{CT}$
Borefield	Type557a	duct storage	on/off	$\dot{m}_f, T_{f,i}$	$T_{f,o}$	see Section 4.8

4.3 Weather data

The Typical Meteorological Year of Uccle (Belgium) is used as input to the building zone, as provided by the Meteororm weather database in TRNSYS. This moderate sea climate is representative for the European Atlantic climate. Figure 4.5(a) shows the ambient temperature profile, Figure 4.5(b) shows the solar radiation $\dot{Q}_{sol,N}$ (kW/m²) on a North oriented facade, Figure 4.5(c) the solar radiation $\dot{Q}_{sol,S}$ (kW/m²) on a South oriented facade and Figure 4.5(d) illustrates the impact of the proposed solar shading control scheme on $\dot{Q}_{sol,S}$ (kW/m²) reaching the window.

4.4 Thermal comfort requirements

The main objective of building climate control is to satisfy thermal comfort at a minimal energy cost. Quantifying thermal comfort is not straightforward, not only because of the large number of variables that influence the thermal comfort sensation, but also because it is to a great extent person dependent.

Fanger [47] defined the concepts of Percentage of People Dissatisfied (PPD) and Predicted Mean Vote (PMV) to quantify thermal comfort while taking its subjective character into account. The PPD is an estimation of the percentage of occupants who would not be satisfied by the thermal environment [101], while the PMV is an estimation of the average vote of a large group of persons submitted to a given thermal environment. The appreciation ranges from -3 (too cold), over 0 (neutral), to +3 (too warm). Based on statistical data, Fanger [47]

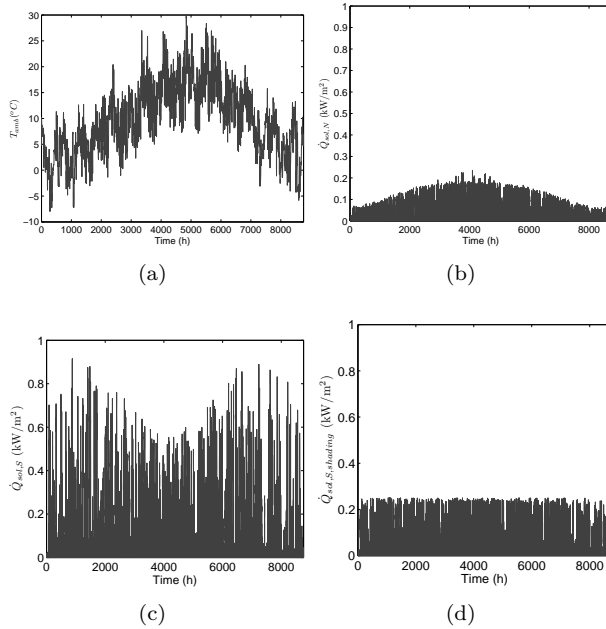


Figure 4.5: (a) Reference year ambient air temperature profile for Uccle (Belgium), Meteornorm data TRNSYS SEL-University of Wisconsin-USA and TRANSSOLAR-Stuttgart [155], (b) Solar radiation on a North-oriented facade, (c) Solar radiation on the South-oriented facade, (d) Solar radiation on the South-oriented facade - effect of solar shading.

expressed the PPD and the PMV as a function of four environmental variables (the indoor air temperature T_a , the mean radiative temperature T_{mr} , the air velocity and the relative humidity) and two individual parameters (clothing factor and metabolic rate). T_{mr} is a weighted sum of the surface temperatures of the zone, i.e. the inner walls, the ceiling, the floor and the windows, and is important in the thermal comfort sensation as it determines the radiative heat transfer between the body and the zone. As PMV and PPD both express thermal comfort as a function of the same variables, there is a one-to-one - although non-linear - relation between both.

The influence of T_a and T_{mr} can be lumped into one value, the operative temperature T_{op} . T_{op} is defined as the average of both temperatures, weighted by their respective heat transfer coefficients h_c and h_r [73]. For typical values of h_r and h_c , the relative weight of T_{mr} and T_a on T_{op} is respectively 0.45 and 0.55. By consequence, T_{op} is often calculated as the mean value of T_a and T_{mr} ,

as expressed in Eq.(4.1) [76].

$$T_{op} = \frac{h_r T_{mr} + h_c T_a}{h_r + h_c} \approx \frac{T_{mr} + T_a}{2} \quad (4.1)$$

Air velocity, clothing factor and metabolic activity affect thermal comfort, however, they are usually non-controlled and even non-simulated aspects. Controllable parameters are air humidity and operative temperature. The ASHRAE standard 55 [6] defines a comfort zone as a function of both variables, represented in the psychrometric chart shown in Figure 4.6(a). The graph shows two regions, respectively for summer (red) and winter (blue) weather conditions, as the clothing factor is assumed to be adapted to the weather. The graph shows that the comfort zone is almost uniquely determined by T_{op} for humidity ratios below 50%. For higher humidity levels, the maximum allowed T_{op} is negatively correlated with the humidity ratio. This graph explains why in hot and humid climates air humidity control is crucial, contrary to relatively colder (and thus less humid) climates such as the European Atlantic climate considered in this work. By consequence the requirement for thermal comfort can, for the climate investigated, be translated to a requirement on the operative temperature T_{op} .

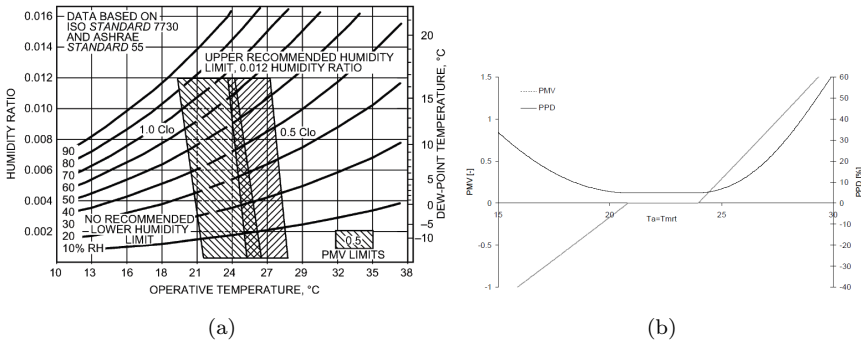


Figure 4.6: (a)ASHRAE thermal comfort zones for winter and summer conditions, indicated by respectively the blue and the red surface [6]. (b) PPD and PMV with weather adapted clothing value [101].

Figure 4.6(b) shows the PPD as a function of T_{op} (as $T_a = T_{mr}$). The graph is made using constant values for the relative humidity, air velocity and metabolic rate, while the clothing factor is varied. This graph is very useful for the purpose of control, as it expresses thermal comfort as a function of the controllable variable, i.e. T_{op} . The graph shows that there is a temperature interval for which the PPD remains low, i.e. about 5%, while outside this interval the PPD

Table 4.4: Categories for global thermal comfort environment from ISO7730, Annex A (PPD: Predicted Percentage Dissatisfied; PMV: Predicted Mean Vote).

Thermal state of the body as a whole		
Comfort class	PPD (%)	PMV (-)
A	≤ 6	$-0.2 \leq \text{PMV} \leq +0.2$
B	≤ 10	$-0.5 \leq \text{PMV} \leq +0.5$
C	≤ 15	$-0.7 \leq \text{PMV} \leq +0.7$

increases almost quadratically. Most thermal discomfort cost representations for implementation in optimal control, are based on this shape of the PPD as a function of T_{op} . The optimal T_{op} depends on the clothing factor. Most standards assume that people gradually adapt their clothing to the weather. To express this adaptation, the concept of a running mean ambient temperature T_{rm} ($^{\circ}\text{C}$) is introduced. The definition for T_{rm} adopted in this study, expressed in Eq.(4.2), follows the EN15251 standard [26]. Subscript d denotes this day, $d - 1$ denotes yesterday and so forth.

$$T_{rm} = \frac{\bar{T}_{amb,d} + 0.8\bar{T}_{amb,d-1} + 0.4\bar{T}_{amb,d-2} + 0.2\bar{T}_{amb,d-3}}{2.4} \quad (4.2)$$

The thermal comfort requirements can be expressed in terms of the PPD and PMV and depend on the building comfort class, characterized by respectively the labels A, B and C, as listed in Table 4.4. Alternatively, the PPD and PMV limits can be translated into an allowable temperature interval for T_{op} as a function of T_{rm} . This relation between the T_{op} -range and T_{rm} , as defined by ISO7730 for buildings of Class B, is shown in Figure 4.7 (a). This band defines the lower and upper band on T_{op} , denoted by respectively $T_{comf,min}$ and $T_{comf,max}$, and is clearly season dependent. For the Uccle weather profile considered in this work, shown in Figure 4.5, the corresponding thermal comfort bound as a function of the time of the year, is shown in Figure 4.7 (b).

The standards allow T_{op} to exceed the comfort bounds if the peaks are limited in time. For a Class B building, ISO7730 restricts the total annual number of *Kelvin exceeding hours* (Kh_{tot}) (Kh/year) to 100 Kh per year. This is equivalent to the temperature being 1°C outside the thermal comfort range during 6% of the occupation time, evaluated over an entire year for a typical office occupation profile. Kh_{tot} is calculated according to Eq.(4.3) with Kh_u and Kh_o expressing the number of temperature exceeding hours respectively below $T_{comf,min}$ (*under*)

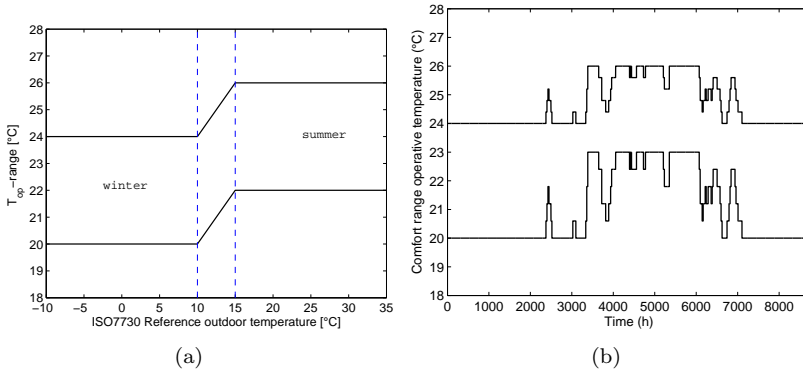


Figure 4.7: (a) Operative temperature range as a function of the running mean ambient air temperature T_{rm} for a Class B building, according to ISO7730 [85], (b) Corresponding operative temperature range for the reference year.

and above $T_{comf,max}$ (*over*) during office hours, evaluated over the entire year.

$$Kh_{tot} = Kh_u + Kh_o \quad (4.3)$$

with

$$Kh_u = \int_0^{1y} Occ(t) \max(0, T_{comf,min}(t) - T_{op}(t)) dt \quad (4.4)$$

$$Kh_o = \int_0^{1y} Occ(t) \max(0, T_{op}(t) - T_{comf,max}(t)) dt \quad (4.5)$$

The variable Occ is 1 during office hours and 0 otherwise. In this work, a control strategy is judged to be satisfactory with respect to thermal comfort if the condition $Kh_{tot} \leq 100$ Kh is fulfilled.

Besides the requirements on the relative humidity and on T_{op} , there are following requirements with respect to the floor surface temperature $T_{floor,s}$ ($^{\circ}C$), the ceiling surface temperature $T_{ceiling,s}$ ($^{\circ}C$) and the temperature gradient \dot{T}_{op} ($^{\circ}C/h$) [77]:

$$19^{\circ}C < T_{floor,s} < 27^{\circ}C \quad (4.6)$$

$$T_{ceiling,s} < T_{op} + 6^{\circ}C \quad (4.7)$$

$$\dot{T}_{op} < 3.3^{\circ}C/h \quad (4.8)$$

The condition on $T_{floor,s}$ is always respected since we have a raised floor which represents an insulation layer between the CCA and the zone air. Sourbron [164] showed that T_{ws} must remain between 7.5°C and 45°C to satisfy the condition on $T_{ceiling,s}$. The lower limit on T_{ws} is to prevent condensation at the ceiling surface. For a HP/PC system with low temperature heating and high temperature cooling these T_{ws} -limits are satisfied. \dot{T}_{op} appears to be close to the upper bound of $3.3^\circ\text{C}/4\text{h}$ in the morning if the internal gains profile is represented by a block function. This means that for a more representative profile, with a smoother distribution of the loads in time, condition Eq.(4.8) is definitely met as well.

4.5 Reference control strategy

4.5.1 Methodology

The reference control strategy is a rule-based controller using a heating curve (HC) and cooling curve (CC) corresponding to today's current practice. The methodology is described below in 4 steps (A, B, C and D). A flow chart with the first three steps is presented in Figure 4.8.

Step A: Temperature limits for the control variable T_{cv} First, the thermal comfort bounds for the operative temperature, $T_{comf,min}$ and $T_{comf,max}$, are determined based on the actual running mean outdoor temperature $T_{rm}(t)$. Next, the temperature limits for the controlled variable T_{cv} ($^\circ\text{C}$), denoted by $T_{cv,min}(t)$ and $T_{cv,max}(t)$ are determined. This requires the definition of the following control parameters, which are also indicated in Figure 4.8:

1. the choice of the controlled variable T_{cv}
2. the start time t_S (h) and the stop or end time t_E (h) for the installation. Together, t_S and t_E determine the period for which the T_{cv} -limits are more stringent. It can be compared to the switching times between day operation (here denoted by the term HVAC_{ON}) and night setback (denoted by the term HVAC_{OFF})
3. the temperature limits for T_{cv} , defined by the control parameters ΔT_{min} and ΔT_{max} for the HVAC_{ON}-period and by $\Delta T_{min,n}$ and $\Delta T_{max,n}$ for the HVAC_{OFF}-period.

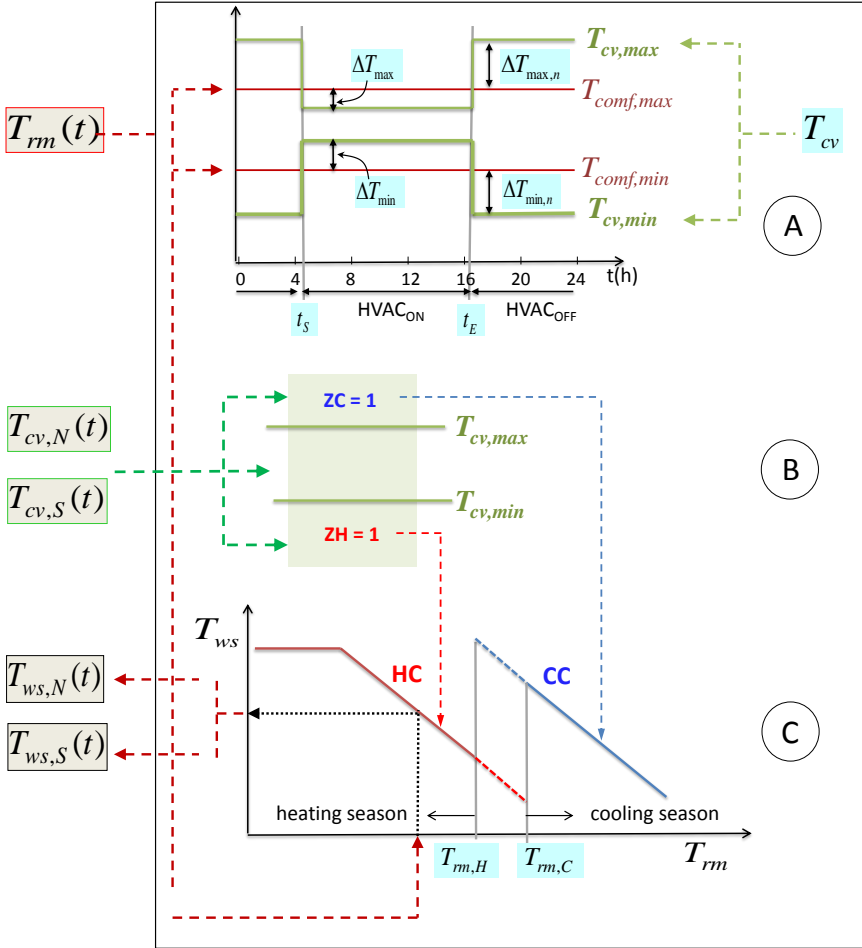


Figure 4.8: Flow chart of the rule-based control strategy used as a reference. In step A the temperature limits on the control variable T_{cv} are defined. Based on this, the heating request from the zone (ZH) or cooling request from the zone (ZC) is determined in step B. In step C the supply water temperature T_{ws} is defined from the heating curve (HC) or from the cooling curve (CC) as a function of the running mean outdoor temperature T_{rm} which also defines the system modus (heating season/mid season/cooling season). The control parameters are indicated in blue.

Step B: Zone heating or cooling request The actual $T_{cv}(t)$ is measured and fed back to the controller. $T_{cv}(t)$ is compared to $T_{cv,min}(t)$ and $T_{cv,max}(t)$. If $T_{cv}(t)$ is higher than $T_{cv,max}(t)$, the signal zone cooling (ZC) request is set to 1. If $T_{cv}(t)$ is lower than $T_{cv,min}(t)$, the signal zone heating request (ZH) is set to 1. If $T_{cv}(t)$ lies between the bounds, both ZH and ZC are set to zero.

Step C: Supply water temperature setpoint $T_{ws,set}(t)$ The HC defines the setpoint in heating mode, denoted by $T_{ws,h}$. The CC defines the setpoint in cooling mode, denoted by $T_{ws,c}$. In both cases, the setpoint is determined from the actual T_{rm} and for this reason, control strategies based on this kind are referred to as 'weather compensated HC/CC-based control strategies'. Additionally, T_{rm} defines three regions (see Figure 4.7(a)):

1. heating season for $T_{rm} \leq T_{rm,H}$
2. cooling season for $T_{rm} \geq T_{rm,C}$
3. mid season for $T_{rm,H} \leq T_{rm} \leq T_{rm,C}$

During the heating season and the mid season $T_{ws,set} = T_{ws,h}$ if a heating request signal is sent from the zone (ZH = 1). During the cooling season and the mid season $T_{ws,set} = T_{ws,c}$ if a cooling request signal is sent from the zone (ZC = 1).

Step D: On/off status of HP, GB, PC and CH Modulating heating and cooling devices allow to closely track $T_{ws,set}(t)$ defined by the HC/CC. For on/off-controlled devices, such as the ones considered here, an extra step is required to translate the setpoint for T_{ws} into an appropriate on/off-signal. This translation is a trade-off between two conflicting objectives: tracking the setpoint as closely as possible to avoid large temperature swings of the operative temperature on the one hand, and avoiding on/off-cycling on the other hand. Because of the latter, systems with only one heating or cooling device, often translate the setpoint on the supply water temperature T_{ws} to a setpoint on the return water temperature T_{wr} since T_{wr} changes far slower to a step heat or cold input than T_{ws} . The on/off-control is then defined based on a hysteresis control on T_{wr} with the dead band ΔT_{wr} (°C) as tuning parameter. Here, a slightly different approach is adopted. First, the heating power $\dot{Q}_{h,dem}$ (W) required to achieve $T_{ws,h}$ or the cooling power $\dot{Q}_{c,dem}$ (W) to achieve $T_{ws,c}$ are

determined:

$$\dot{Q}_{h,dem}(t) = \dot{m}_w (T_{ws,h}(t) - T_{wr}(t)) \quad (4.9)$$

$$\dot{Q}_{c,dem}(t) = \dot{m}_w (T_{wr}(t) - T_{ws,c}(t)) \quad (4.10)$$

The heat pump is switched on when $\dot{Q}_{h,dem}(t)$ is larger than a fraction f_{h1} (-) of the heat pump thermal power $\dot{Q}_{HP}(t)$ at the operation conditions. If $\dot{Q}_{h,dem}(t)$ exceeds a fraction f_{h2} of $\dot{Q}_{HP}(t)$, the gas boiler is additionally switched on. The same approach is adopted for defining the status of passive cooling and the chiller. The circulation pumps for passive cooling are switched on when $\dot{Q}_{c,dem}(t)$ exceeds a fraction f_{c1} (-) of the actual passive cooling capacity $\dot{Q}_{PC}(t)$ and the chiller is switched on if the cooling demand exceeds a fraction f_{c2} of $\dot{Q}_{PC}(t)$:

$$\text{HP} = \text{ON} \text{ if } \dot{Q}_{h,dem}(t) \geq f_{h1} \dot{Q}_{HP}(t) \quad \text{else HP} = \text{OFF} \quad (4.11)$$

$$\text{GB} = \text{ON} \text{ if } \dot{Q}_{h,dem}(t) \geq f_{h2} \dot{Q}_{HP}(t) \quad \text{else GB} = \text{OFF} \quad (4.12)$$

$$\text{PC} = \text{ON} \text{ if } \dot{Q}_{c,dem}(t) \geq f_{c1} \dot{Q}_{PC}(t) \quad \text{else PC} = \text{OFF} \quad (4.13)$$

$$\text{CH} = \text{ON} \text{ if } \dot{Q}_{c,dem}(t) \geq f_{c2} \dot{Q}_{PC}(t) \quad \text{else CH} = \text{OFF} \quad (4.14)$$

Note that Eqs.(4.11)-(4.14) imply priority for HP operation in heating mode and priority for PC operation in cooling mode. The operation is very sensitive to the value of f_{h1} , f_{h2} , f_{c1} and f_{c2} . They influence the thermal comfort, the total delivered heating and cooling energy as well as the relative share of the HP and the GB for heating and of the PC and the CH for cooling.

4.5.2 Settings

Overview Table 4.5 lists the control parameters for the 2 reference control strategies, from now on referred to as the 'HC/CC-control strategies'. The parameters have been manually tuned for two choices for the control variable T_{cv} . The first HC/CC-control strategy is based on feedback of the zone operation temperature T_{op} . While the common choice is to feed back the zone air temperature T_a , since this variable is easily measured, T_{op} is chosen since it is the variable we really want to control. The second implementation of the HC/CC-control strategy uses the CCA surface temperature $T_{c,s}$ as feedback signal. This choice is motivated by the findings of Sourbron and Helsen [162]. Based on an extensive search over the entire parameter space, the choice of

Table 4.5: Control parameter settings for the 2 considered reference HC/CC-based control strategies.

T_{cv}	t_S (h)	t_E (h)	ΔT_{min} (°C)	ΔT_{max} (°C)	$\Delta T_{min,n}$ (°C)	$\Delta T_{max,n}$ (°C)	f_{h1} (-)	f_{h2} (-)	f_{c1} (-)	f_{c2} (-)
T_{op}	4AM	5PM	-1.0	+0.5	+5	+5	0.5	2	0.5	1
$T_{c,s}$	4AM	5PM	0.0	+2.0	+5	+5	0.5	2	0.5	1

$T_{c,s}$ as controlled variable was found to be able to yield both better thermal comfort and lower energy cost than the feedback of T_{op} . In this work it is chosen to keep both HC/CC-implementations in order to distinguish between a standard HC/CC-controller and a more advanced one. They are referred to as respectively the HC/CC- T_{op} and HC/CC- $T_{c,s}$ to distinguish between both.

To avoid cycling, the status of the devices is updated only once an hour. An exception to this rule is the use of the GB: if switched on, it maximally operates during 12 minutes. This was done to avoid excessive use of the GB at the start of the day.

Supply water temperature setpoint The slope and the offset of the heating curve (HC) and the cooling curve (CC) are based on a static description of the building. The idea behind this approach is to compensate for the building heat losses (or gains) in steady state conditions.

$$\dot{Q}_{supply,ss} = \dot{Q}_{loss,ss} \quad (4.15)$$

The steady state building losses $\dot{Q}_{loss,ss}$ (W), depend on the heat transfer coefficient of the overall building envelope $(UA)_b$ (W/K) and on the difference between the operative temperature T_{op} and the ambient temperature T_{amb} :

$$\dot{Q}_{loss,ss} = (UA)_b (T_{op} - T_{amb}). \quad (4.16)$$

The heating or cooling power supplied to the zone through the CCA, $\dot{Q}_{supply,ss}$ (W), can be approximated as follows:

$$\dot{Q}_{supply,ss} = (UA)_{CCA} (T_{ws} - T_{op}) \quad (4.17)$$

with $(UA)_{CCA}$ (W/K) the heat transfer coefficient between the supply water and the zone. Substituting Eqs.(4.16) and (4.17) in Eq.(4.15) yields:

$$(UA)_{CCA} (T_{ws} - T_{op}) = (UA)_b (T_{op} - T_{amb}). \quad (4.18)$$

and after rearranging the terms:

$$T_{ws} = T_{op} + \frac{(UA)_b}{(UA)_{CCA}} (T_{op} - T_{amb}). \quad (4.19)$$

The steady state assumption thus yields an explicit expression for the setpoint for T_{ws} which depends on the operative temperature T_{op} , the temperature difference with the surroundings, $T_{op} - T_{amb}$ and on the ratio between the heat transfer coefficient from the zone to the surroundings, $(UA)_b$, and the heat transfer coefficient from the supply water to the zone, $(UA)_{CCA}$. Following this reasoning, the slope of the heating curve, optimally determined as the ratio between $(UA)_b$ and $(UA)_{CCA}$, is the only tuning parameter in a heating curve. However, due to ventilation losses \dot{Q}_{vent} , to solar gains \dot{Q}_{sol} and to internal gains \dot{Q}_{int} , the net heat demand will differ from the transmission losses calculated in Eq.(4.16). The expression for the setpoint for T_{ws} then becomes:

$$T_{ws} = T_{op} + \frac{1}{(UA)_{CCA}} ((UA)_b(T_{op} - T_{amb}) + \dot{Q}_{vent} - \dot{Q}_{sol} - \dot{Q}_{int}), \quad (4.20)$$

which can be rewritten as:

$$T_{ws} = T_{op} + \frac{(UA)_b}{(UA)_{CCA}} (T_{op} - T_{amb}) + \Delta T. \quad (4.21)$$

The offset of the heating curve, determined by ΔT , is then a second tuning parameter. For the geometrical data and material properties of the zone considered, the calculated values for $(UA)_b$ and $(UA)_{CCA}$ amount to respectively 29 W/K and 126 W/K, resulting in a slope of $-0.227^\circ\text{C}/^\circ\text{C}$. The transmission losses at design operation temperatures (DOT), i.e. $T_{amb} = -8^\circ\text{C}$ and $T_{op} = 20^\circ\text{C}$, amount to approximately 800 W per office zone. The tuning parameter ΔT , which accounts for the presence of internal gains, solar gains and ventilation losses, is based on the TRNSYS simulation results. The resulting expressions for the HC and the CC are given by Eq.(4.22) and Eq.(4.23).

$$T_{ws,h} = -0.2 T_{rm} + 26.7 \quad (4.22)$$

$$T_{ws,c} = -0.15 T_{rm} + 22.2 \quad (4.23)$$

Note that, in practice, the slope and the offset of the heating curve are most often determined by trial-and-error.

4.6 Reference design

The installation is sized according to current design guidelines, presented in a flowchart in Figure 4.9. It consists of roughly three steps. The first step is the building load calculation, from which the heating and cooling demand profile and the corresponding load duration curves (LDC) are determined. This serves as input for the second step, where the capacity of the heat and cold production devices, in this case the HP, the GB, the PC heat exchanger and the CH, are determined. The third step is the borefield sizing, based on the borefield loads. In the case of a stand-alone GCHP system (i.e., no supplementary heater or cooler), the latter are equal to the building heating and cooling loads. In the case of HyGCHP systems, by contrast, the building loads are first 'processed', before passing them to the borefield design software. The three steps are discussed in more detail below.

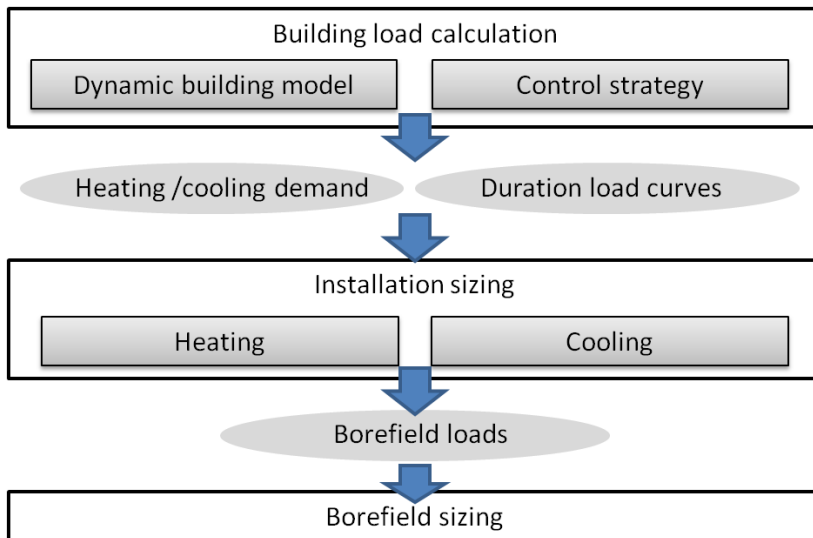


Figure 4.9: Overview of steps in ground-coupled heat pump design procedure

4.6.1 Building load calculation

For the design of conventional heating and cooling installations (e.g. GB and CH), where the installed capacity does not dominate the investment cost, the heating loads are often based on a static building load calculation,

e.g., the EN12831 standard [25]. Calculation of the cooling loads is less straightforward due to the time-dependent character of the solar and internal gains and by consequence the impact of the building thermal mass on the operative temperature response. The insights gained from dynamic cooling load calculations have been translated to 'cooling load factors' incorporated in the cooling load calculation guidelines of e.g., the VDI2078 standard [178] and Spitler et al. [167].

For the design of a (Hy)GCHP installation, however, where the installed capacity dominates the investment cost, a dynamic load calculation is recommended [70, 139]. Building simulation environments such as TRNSYS and EnergyPlus, are well suited for this purpose, since they provide a library with, among others, detailed building components and weather data files. Since the actual heating and cooling installation is not yet defined at this stage, the installation is at this stage often idealized. This idealized heater/cooler is often a perfectly modulating device which allows to track the supply water temperature setpoint defined by the controller. Therefore, as indicated on top of Figure 4.9, a dynamic load calculation requires to define a control strategy which actually 'operates' the system.

The building load calculation is performed with the TRNSYS two zone office model, presented in Figure 4.2. The weather profile corresponds to the Uccle (Belgium) reference year (Meteonorm data, TRNSYS). The corresponding T_{amb} , $\dot{Q}_{sol,N}$ and $\dot{Q}_{sol,S,schad}$ -profiles are depicted in respectively Figure 4.5(a), Figure 4.5(b) and Figure 4.5(d). Note that the load calculation is performed with inclusion of the automated solar shading for the South office. Also the internal gains, depicted in Figure 4.3, are incorporated. The heating and cooling installation are represented by an ideal heater (TRNSYS Type 6) and cooler (TRNSYS Type 92). The control input to these components is the setpoint of the supply water temperature. The power of the ideal heater and cooler is twice the static design heating and cooling load, calculated according to respectively the standards EN12831 [25] and VDI2078 [178] [164]. The factor two was chosen to ensure that the supply water temperature setpoint set by the controller, discussed next, can be achieved most of the times. Contrary to the hydraulic network of the HyGCHP system, shown in Figure 4.1, there are three-way-valves at zone level, which allow individual control of the North and the South zone. This way, the loads for the North and South zone can be quantified independently.

The control settings are listed in Table 4.6. Both HC/CC-control strategies have individually been tuned to obtain good control performance (both in terms of thermal comfort and in terms of energy). The control parameters listed in Table 4.6 have slightly different values compared to the ones for the HyGCHP

Table 4.6: Control parameter settings of the HC/CC-control strategies used for building load calculation (see Figure 4.8).

	t_S (h)	t_E (h)	ΔT_{min} (°C)	ΔT_{max} (°C)	$\Delta T_{min,n}$ (°C)	$\Delta T_{max,n}$ (°C)
HC/CC - T_{op}	4AM	5PM	+1	+1	+5	+5
HC/CC - $T_{c,s}$	4AM	5PM	+3	+3	+5	+5

Table 4.7: Results building load calculation with the HC/CC-control strategy.

	Thermal comfort		Specific loads			
	$Kh_{tot,N}$ (Kh)	$Kh_{tot,S}$ (Kh)	$Q_{h,tot}$ ($\frac{kWh}{m^2a}$)	$Q_{c,tot}$ ($\frac{kWh}{m^2a}$)	$Q_{h,max}$ ($\frac{W}{m^2}$)	$Q_{c,max}$ ($\frac{W}{m^2}$)
HC/CC - T_{op}	31	30	17	-29	54	-51
HC/CC - $T_{c,s}$	35	27	13	-27	54	-51

installation, listed in Table 4.5. The former are tuned for the boiler/chiller with modulating power, the latter for the HyGCHP system with on/off-switching devices. The results of the building load calculation for both HC/CC-control strategies are presented in Figure 4.10. Figure 4.10(a) and Figure 4.10(b) show the profiles for $T_{op,N}$ and $T_{op,S}$, with indication of the $T_{comf,min}$ and $T_{comf,max}$. Figure 4.10(c) and (d) show the heating and cooling power profiles $\dot{Q}_h(t)$ (W/m^2) and $\dot{Q}_c(t)$ (W/m^2) and Figure 4.10(e) and (f) show the corresponding load duration curves (LDC). The results are summarized in Table 4.7. For both HC/CC-control strategies, the total number of temperature exceeding hours remains below the maximum of 100 Kh. The peak power demands, $\dot{Q}_{h,max}$ (W/m^2) and $\dot{Q}_{c,max}$ (W/m^2), correspond to the maximal power of the boiler and the chiller. However, the annual specific heat demand $Q_{h,tot}$ (kWh/m^2) and cold demand $Q_{c,tot}$ (kWh/m^2) obtained with HC/CC- T_{op} is respectively 30% and 7% higher than with HC/CC- $T_{c,s}$. This confirms the observation of Sourbron and Helsen [162] that the control performance obtained with simple HC/CC-based control strategies can drastically be improved by an appropriate choice for the controlled variable $T_{c,v}$. The installation sizing, discussed in the next paragraph, is illustrated for the building loads obtained with HC/CC- $T_{c,s}$.

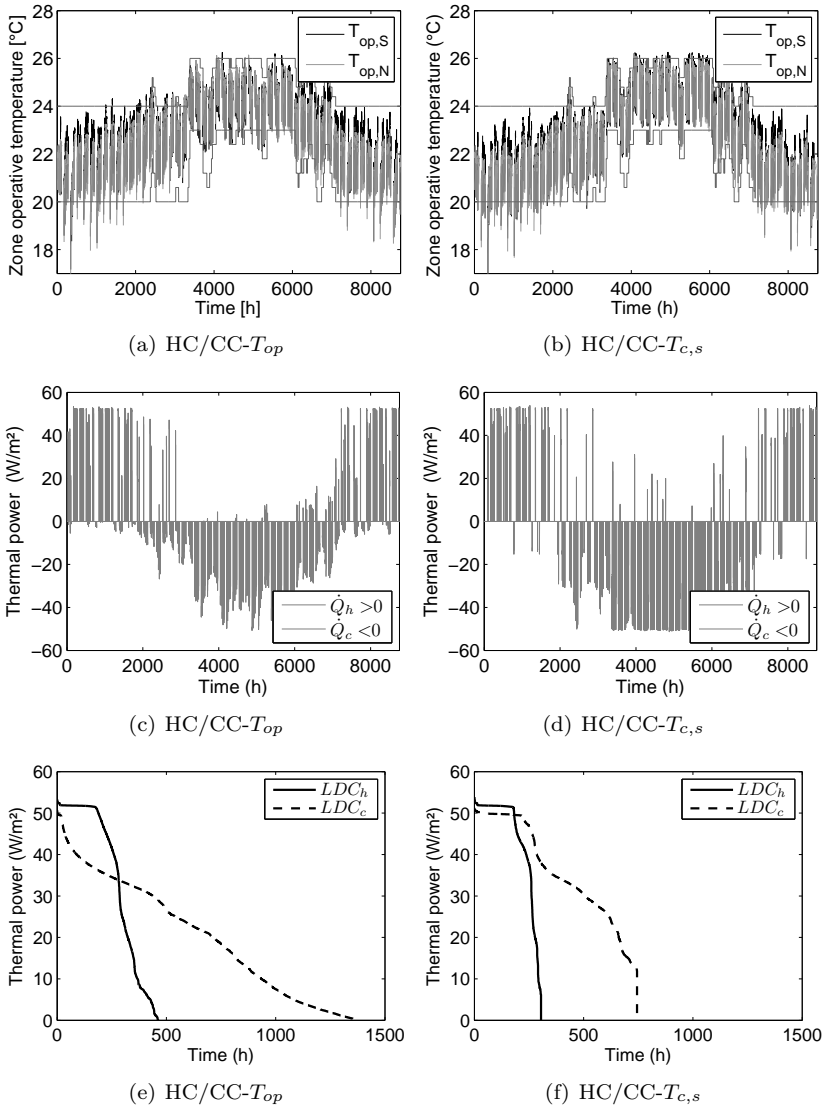


Figure 4.10: TRNSYS-simulation results for the two zone office building with a boiler/chiller installation, controlled with a standard HC/CC-control strategy 'HC/CC- T_{op} ' (left) and an advanced HC/CC-control strategy 'HC/CC- $T_{c,s}$ ' (right). (Top) Zone operative temperature in the North and South office zone, (middle) heating loads and cooling loads and (bottom) corresponding heating and cooling load duration curves.

4.6.2 Installation sizing

The building load calculation obtained with the control strategy HC/CC- $T_{c,s}$ serves as input for the installation sizing. First, the capacity of the HP, GB, CH, and PC heat exchanger is calculated. Next, the borefield loads are determined. According to current HyGCHP design guidelines, the borefield is sized to cover the smallest of the two loads entirely [31, 70, 71]. Since the building is clearly cooling dominated, the borefield is sized to cover the heating load. The fraction of the cooling demand which can not be covered by passive cooling, is met by the chiller. This fraction is determined from balancing the heating and cooling loads at borefield level, which means that the total annual amount of heat injected and extracted to the borefield are imposed to be equal. This condition, imposed at design level, avoids borefield thermal build-up or thermal depletion which would in turn require a larger GHE length. Note that during operation, however, this condition is currently not considered.

The loads for the two zone office building module are scaled to obtain the values for the total office building (3600 m²), see Figure 4.11(a). The corresponding heating and cooling load duration curves, which indicate the number of hours the load trespasses a certain power, are shown in Figure 4.11(b). The total annual heat demand amounts to 47 MWh and the total annual cooling demand to 97 MWh, which indicates that the building is strongly cooling dominated. The meaning of the horizontal line on the left and right figure, is explained further in the text.

Heating power The heat pump nominal thermal power $\dot{Q}_{HP,nom}$ (W) is chosen such that an a priori defined fraction GEO_h (-) of the total heating demand is covered by the heat pump:

$$\int_0^{1 \text{ y}} \min(\dot{Q}_h, \dot{Q}_{HP,nom}) dt = GEO_h \int_0^{1 \text{ y}} \dot{Q}_h dt \quad (4.24)$$

Since the building is cooling dominated, the heat pump is sized to cover the heat demand. In this study, GEO_h is taken 0.98 of the design heating load. For the considered design loads, this means that the HP delivers 47 MWh of heating.

The gas boiler nominal power, denoted by $\dot{Q}_{GB,nom}$ (W), is such that - in combination with the heat pump - the peak heating demand is covered:

$$\dot{Q}_{GB,nom} = \dot{Q}_{h,max} - \dot{Q}_{HP,nom} \quad (4.25)$$

Cooling power The heat extracted from the building by passive cooling, $\dot{Q}_{PC}(W)$, is directly injected to the borefield by means of the PC heat exchanger. The total heat injection rate to the borefield, $\dot{Q}_{bf,in}(W)$, calculated according to Eq.(4.26), additionally includes the electricity consumption of the primary circulation pumps $\dot{P}_{prim}(W)$ since the latter is eventually converted to heat through friction. COP_{PC} is defined as the ratio between the passive cooling power \dot{Q}_{PC} and P_{prim} .

$$\dot{Q}_{bf,in} = \dot{Q}_{PC} + P_{prim} = \left(1 + \frac{1}{COP_{PC}}\right)\dot{Q}_{PC} \quad (4.26)$$

The heat exchange rate per unit borehole length $\dot{q}_b(W/m)$ is physically constrained by the borehole and ground thermal properties. The required GHE length therefore scales almost linearly with the maximal heat exchange rate $\dot{Q}_{bf,max}$. To maximize the passive cooling power without increasing the required GHE length, the maximal heat injection rate $\dot{Q}_{bf,in,max}$ is constrained by $\dot{Q}_{bf,ex,max}(W)$:

$$\dot{Q}_{bf,in,max} \leq \dot{Q}_{bf,ex,max} \text{ with } \dot{Q}_{bf,ex,max} \approx \frac{COP_{HP} - 1}{COP_{HP}}\dot{Q}_{HP,nom} \quad (4.27)$$

The UA-value of the PC heat exchanger $(UA)_{PC}(W/K)$ is sized for this heat transfer rate:

$$(UA)_{PC} = \frac{\dot{Q}_{bf,in,max}}{\Delta T_{lm}} \quad (4.28)$$

with $\Delta T_{lm}(^{\circ}C)$ the logarithmic mean temperature difference over the PC heat exchanger. To avoid that the amount of PC is constrained by the size of the PC heat exchanger (instead of by the size of the borefield), the PC heat exchanger is sized large enough: ΔT_{lm} is set to $1.5^{\circ}C$.

The chiller is sized such that - in combination with PC - the peak cooling demand $\dot{Q}_{c,max}(W)$ can be covered:

$$\dot{Q}_{CH,nom} \geq \dot{Q}_{c,max} - \dot{Q}_{PC,nom} \quad (4.29)$$

4.6.3 Borefield sizing

The parameter which determines the borefield investment cost is the GHE length (roughly 50 €/m GHE). A first quick estimate of the GHE length is found by dividing the peak load to be covered, by the maximal heat transfer rate per unit GLE length $\dot{q}'_b(W/m)$, which varies between 30 to 50 W/m for typical borefield and ground properties. The sizing equation proposed by Kavanaugh and Rafferty [92], translated to user-friendly calculation spread sheets [17, 139], yields a more accurate first estimate.

A precise GHE length calculation, however, requires a dynamic building load calculation together with the use of borefield design tools, such as EED [42] and GLHEPRO [166]. These design tools determine the GHE length which covers the user defined borefield loads. The GHE length is iterated until the upper limit (in the case of excess heat injection) or the lower limit (in the case of excess heat extraction) on the fluid brine temperature T_f is reached at the end of the simulation time. Usually, the number of simulation years is set to 20, which is long enough to observe the impact of borefield thermal build up (in the case of excess heat injection) or thermal depletion (in the case of excess heat extraction). To this end, EED [42] and GLHEPRO [166] require following inputs:

1. the ground, borehole and brine thermal properties,
2. the minimum and maximum brine fluid temperature,
3. the borefield configuration,
4. the monthly HP heating energy and PC cooling energy (kWh/month),
5. the monthly HP and PC peak power (kW),
6. the monthly HP and PC peak power duration (h),
7. the number of simulation years (year).

Based on these inputs, the response of T_f is determined by means of dimensionless step response functions or *g-functions* (see Chapter 7 on p. 145).

The focus in this study is on the following inputs (4) defining the monthly HP and PC energy, (5) peak powers and peak power durations which serve as input to the borefield design tool. The ground, borehole and brine thermal properties and the borefield configuration, are taken as given values and listed in Table 4.8. The simulation time is 20 years.

Heat pump loads Since the HP covers almost the entire heating demand ($GEO_h=0.98$), the monthly heating loads covered by the heat pump, Q_{HP} (kWh/month), peak powers $\dot{Q}_{HP,peak}$ (kW) and peak power durations $\Delta t_{HP,peak}$ (h) can directly be determined from the building heating loads. The values, scaled for the entire office building (3600 m²), are listed in Table 4.9. These values are directly translated into borefield heat extraction loads $Q_{bf,ex}$

Table 4.8: Inputs to the borefield design software

Ground thermal conductivity	k_g	(W/mK)	2.4
Ground thermal capacity	c_g	(J/kg K)	2343
Grout thermal conductivity	k_{gr}	(W/mK)	0.7
BHE radius	r_b	(m)	0.075
Tube radius	r_0	(m)	0.02
BHE spacing	B	(m)	5
Brine freezing point	$T_{f,fr}$	(°C)	-2.0
Maximum brine temp.	$T_{f,max}$	(°C)	20
Number of simulation years	t_{sim}	(year)	20

and heat extraction powers $\dot{Q}_{bf,ex}$, according to Eq.(4.30). For the design calculation, COP_{HP} is assumed to be constant.

$$\dot{Q}_{bf,ex}(t) = \frac{COP_{HP} - 1}{COP_{HP}} \dot{Q}_{HP}(t) \quad (4.30)$$

Here, we assumed COP_{HP} equal to 6. To deliver 47 MWh of heat at building level, 39 MWh of heat must then be extracted from the borefield.

Passive cooling loads The fraction of the cooling load covered by passive cooling, GEO_c (-), is constrained by the condition for a long term sustainable system operation. To avoid thermal build-up, the annual rise of the mean borefield temperature, ΔT_{bf} , should be limited. The temperature change of a borefield with a total thermal capacity C_{bf} (J/K) can be found by Eq.(4.31).

$$C_{bf} \Delta T_{bf} = \int_0^{1y} (\dot{Q}_{bf,in}(t) - \dot{Q}_{bf,ex}(t) - \dot{Q}_{bf,\infty}(t)) dt \quad (4.31)$$

The second term on the right hand side, $\dot{Q}_{bf,in}$, defined by Eq.(4.26) represents the heat injected to the borefield by the use of passive cooling. The second term, $\dot{Q}_{bf,ex}$, represents the heat extracted from the borefield by the heat pump as defined by Eq.(4.30). The term $\dot{Q}_{bf,\infty}$ represents the heat loss to the surroundings, comprising the heat exchange with the ambient at the surface and the heat exchange with the ground far field (the latter having by far the major contribution [44]). $\dot{Q}_{bf,\infty}$ can be a heat loss term or a heat gain term, depending on the temperature difference between the borefield and the ambient air temperature on the one hand, and the borefield and the undisturbed ground temperature on the other hand. As the borefield temperature is time varying, $\dot{Q}_{bf,\infty}$ also varies in time.

Excess heat injection, which causes T_{bf} to rise, will at a certain T_{bf} -level be balanced by the increased thermal losses to the surroundings, i.e., $\dot{Q}_{bf,\infty}$ will

be negative in sign. At this T_{bf} -level, the annual mean T_{bf} -variation ΔT_{bf} will equal zero. As long as this equilibrium temperature does not jeopardize the use of passive cooling, there is no problem. The more compact the borefield and the lower the ground thermal conductivity, however, the smaller the tolerated amount of excess heat injection will be. To determine the annually amount of passive cooling which balances the borefield, following conservative assumption is made:

$$\dot{Q}_{bf,\infty} = 0 \quad (4.32)$$

Substituting Eq.(4.32) in Eq.(4.31), the annual amount of heat which can be injected by passive cooling, is calculated based on the following equation:

$$\Delta T_{bf} = \frac{1}{C_{bf}} \int_0^{1y} \left(\left(\frac{COP_{PC} + 1}{COP_{PC}} \right) \dot{Q}_{PC} - \frac{COP_{HP} - 1}{COP_{HP}} \right) \dot{Q}_{HP} dt = 0 \quad (4.33)$$

Since the values for COP_{PC} are high, typically between 10 and 20, the annual amount of heat injection allowed is almost equal to the 39 MWh extracted by the heat pump. For the given office building, which - with the HC/CC-control strategy - has an annual cooling demand of 97 MWh, this means that 40% of the design cooling load is realized through passive cooling.

Note, first, that Eq.(4.33) is too conservative - and thus suboptimal - for borefields with large BHE spacing B and highly conducting soils, since in those cases, the approximation made by Eq.(4.32) definitely does not hold. For compact borefields, however, Eq.(4.33) provides a good (still conservative) guess for the allowed annual amount of heat rejection. Second, Eq.(4.33), imposed at the design phase, is not fulfilled with current HyGCHP control algorithms.

While the total amount of passive cooling may be more or less prescribed by Eq.(4.31), the distribution over the year is not. In the design phase, passive cooling is usually assumed to operate in base load. This base load power, $P_{PC,base}$, presented by the horizontal line in Figure 4.11, is then determined such that the surface below the LDC for cooling equals the total annual 'passive cooling budget'. The fraction of the cooling load above $P_{PC,base}$, is then to be covered by the chiller.

Based on this base-load-cooling assumption, the monthly cooling loads covered by passive cooling Q_{PC} (kWh/month), monthly peak power $\dot{Q}_{PC,peak}$ (kW) and corresponding peak power duration $\Delta t_{PC,peak}$ (h) are determined. The results are graphically presented in Figure 4.12. The graphs clearly shows that, while almost the entire building heating demand (Q_h) is covered by the heat pump (Q_{HP}), only half of the cooling demand (Q_c) is covered by passive cooling

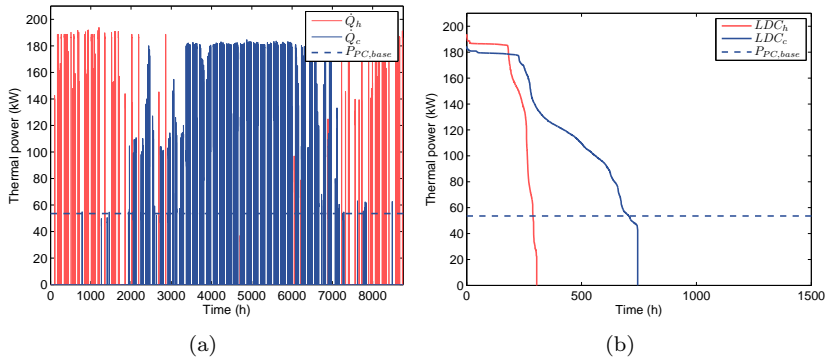


Figure 4.11: Annual office heating and cooling load profile (left) and corresponding load duration curves (LDC) (right). The horizontal line at the thermal power $P_{PC,base}$ (kW) defines the fraction of the cooling load covered by PC on the one hand (surface of the LDC below $P_{PC,base}$) and the fraction covered by the CH on the other hand (surface of the LDC above $P_{PC,base}$).

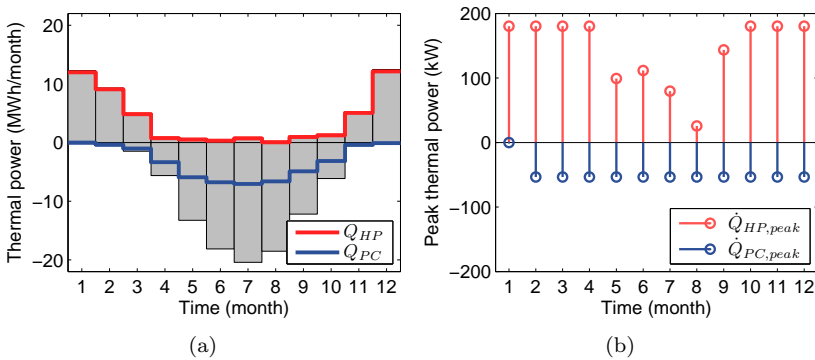


Figure 4.12: Borefield design values (a) Monthly HP heating energy Q_{HP} (>0) and PC cooling energy Q_{PC} (<0), compared to the total monthly heating and cooling demand of the office (grey bars). (b) Monthly peak HP and PC peak power.

(Q_{PC}). The numerical values, given as input to the borefield design software GLHEPRO [166], are tabulated in Table 4.9.

Table 4.9: Borefield design values

Month	Q_{HP} (kWh)	Q_{PC} (kWh)	$\dot{Q}_{HP,peak}$ (kW)	$\dot{Q}_{PC,peak}$ (kW)	$\Delta t_{HP,peak}$ (h)	$\Delta t_{PC,peak}$ (h)
Jan	14175	115	192	19	7.6	0.2
Feb	10916	415	192	20	5.8	0.2
Mrt	6200	1262	190	39	4.4	0.2
Apr	1793	5084	170	96	0.2	7.4
Mei	1	13118	1	160	0.2	10.6
Jun	74	17937	16	179	0.2	12
Jul	68	21558	11	182	0.2	12
Aug	261	19455	29	181	0.2	12
Sep	1403	13377	59	157	0.2	7.6
Okt	2417	6777	189	94	3.8	7
Nov	6901	799	191	26	4.8	0.2
Dec	13379	210	192	21	5.6	0.2

Table 4.10: Reference design heating and cooling installation

$\dot{Q}_{HP,nom}$ (kW)	$\dot{Q}_{GB,nom}$ (kW)	$\dot{Q}_{PC,nom}$ (kW)	$\dot{Q}_{CH,nom}$ (kW)	GEO_h (%)	GEO_c (%)	n_b (-)
179	8	124	51	98	47	26

4.6.4 Result

Table 4.10 summarizes the results for the installation sizing: the thermal power capacity of the HP, GB, PC and CH, denoted by respectively $\dot{Q}_{HP,nom}$, $\dot{Q}_{GB,nom}$, $\dot{Q}_{PC,nom}$ and $\dot{Q}_{CH,nom}$. For the borefield characteristics listed in Table 4.8 and the load values listed in Table 4.9, the required GHE length determined with GLHPRO amounts to almost 3600 m, equivalent to 26 BHEs with a depth of 125 m. Assuming a specific investment cost of 50 €/m GHE (a rough first estimate which includes the costs of piping and engineering [62]), the borefield investment cost amounts to 180 000 €. This is a major term in the total heating and cooling installation cost (see Chapter 8).

4.7 Chapter highlights

This chapter presented the system used as a reference, with description of:

- the two zone office building with concrete core activation (CCA),

- the lay-out of the HyGCHP installation with HP, GB, PC and CH,
- the occupancy profiles and weather profiles,
- the thermal comfort requirements,
- the reference HC/CC-control strategies which serve as comparison for MPC
- the installation and borefield sizing
 - based on a dynamic building load calculation with a HC/CC-control strategy
 - using current HyGCHP design guidelines

Chapter 5

Building level control

5.1 Introduction

The question addressed in this chapter is: *What is the impact of the controller building model and the identification data set used for parameter estimation, on the performance of MPC for office buildings with CCA in the presence of solar and internal gains?*

While the theoretical savings of MPC for building climate control compared to conventional control strategies are promising, the practical savings largely depend on the level of model mismatch and the quality of the disturbance predictions. Obtaining a suitable controller building model constitutes a major bottleneck and is currently an active research domain. Questions to be answered are: Which model structure is adequate? Which variables should be measured to identify the corresponding model parameters? Which information should be contained in the identification data set? The more detailed the model, the larger the number of parameters to be identified and thus the more information needed. While detailed models theoretically allow better control performance, simpler models may be better suited for practical implementation. Evaluation of the suitability of the building model for incorporation within an MPC framework therefore requires consideration of the complexity of the system identification task, as well as the actual control performance within the MPC framework. With respect to prediction errors, especially for buildings with high solar gains, the stochastic character of solar radiation may jeopardize the MPC performance.

In this chapter, the performance of an MPC for the 2-zone office building described in Chapter 4 is evaluated for different controller building models

and prediction errors. As stated in Section 3.1, optimal control at building level has already received significant research attention. Section 5.2 covers the lessons learned from the literature which serve as input for the OCP formulation presented in Section 5.3.3. Based on the insights gained, a grey-box modeling approach is put forward. To answer the questions what the grey box model structure should look like and which identification data are required to estimate the corresponding parameters, different controller building models are identified in Section 5.4. In Section 5.5 these models are evaluated within the MPC framework. The simulations are performed for the reference design year using the TRNSYS building model as simulator. The first part evaluates the impact of the controller building model in the case of perfect disturbance predictions. The second part evaluates the MPC performance in case of imperfect disturbance predictions: the predictions are simply based on the past weather and occupancy data, denoted by the term 'persistence prediction'. In both the first and the second part, the supply water temperature of the North and South zone are optimized individually. The third part evaluates the impact of optimizing only one setpoint temperature - equal for both zones. This way, the performance loss of lumped building level control versus zone level control is quantified. In each part, MPC is compared to a reference rule based control (RBC) strategy.

5.2 Literature study

5.2.1 Choice of cost function

The main objective of building climate control is to satisfy thermal comfort at a minimal energy cost. The OCP formulation should be such that the solution of the optimization problem also optimizes the *actual* control performance. This section starts with the lessons learned from the literature with respect to the formulation of the cost function.

Thermal discomfort representation

As explained in Section 4.4, the requirement for thermal comfort for climates such as the European Atlantic climate, can be translated in a requirement for the operative temperature T_{op} . Karlsson and Hagentoft [90], Kummert [101] and Gayeski [59] incorporated a representation which closely matches the PPD function as depicted in Figure 4.6, shown in Chapter 4, Section 4.4. The temperature interval for which the PPD is close to 5%, is considered as the tolerated thermal comfort band. When T_{op} lies inside this temperature interval,

the thermal discomfort cost is zero. Below the lower temperature bound $T_{comf,min}$ and above the upper temperature bound $T_{comf,max}$, the thermal discomfort cost increases quadratically. Mathematically this is translated into so-called soft constraints on T_{op} , represented by the set of Eq.(5.1). Soft constraints require introduction of slack variables, here denoted ϵ_c (K) and ϵ_h (K), which are penalized quadratically in the cost function term J_d (K^2h). H_c (h) is the time horizon over which the thermal discomfort cost is evaluated. In this chapter, this thermal discomfort representation is adopted.

$$J_d = \int_0^{H_c} (\epsilon_h^2 + \epsilon_c^2) dt \quad \text{with} \quad \begin{cases} \epsilon_h & \geq T_z - T_{comf,max} \\ \epsilon_c & \geq T_{comf,min} - T_z \end{cases} \quad (5.1)$$

Based on a detailed PPD evaluation using a detailed building simulator model, Kummert and André [103] showed that the control profile minimizing this approximated PPD representation (based on T_{op} evaluation only) indeed minimizes the actual PPD (including relative humidity). This observation is important as it allows one to restrict the controller building model in the OCP formulation to a *thermal* model. Evidently, building climate control in hot and humid climates requires incorporation of a hygrothermal model [55, 56].

Based on the quadratic shape of the PPD-curve, a simplified approach is to represent the thermal discomfort cost by a quadratic penalization of the deviation of T_{op} from the zone temperature setpoint [see e.g., 20, 186]:

$$J_d = \int_0^{H_c} (T_{op} - T_{op,ref})^2 dt \quad (5.2)$$

This discomfort representation is adopted in Chapter 6, where the focus is more on the installation level than on the building level, or, expressed in terms of objectives, more on the energy cost than on the thermal discomfort cost.

Energy cost representation

If abstraction is made of the heat and cold production efficiency, a linear energy cost representation J_e (Wh) is a straightforward choice to minimize the total heating and cooling energy demand [67, 101]:

$$J_e = \int_0^{H_c} (\dot{Q}_h + |\dot{Q}_c|) dt \quad \text{with} \quad \begin{cases} \dot{Q}_h & \geq 0 \\ \dot{Q}_c & \leq 0 \end{cases} \quad (5.3)$$

where \dot{Q}_h (W) denotes the heating power and \dot{Q}_c (W) the cooling power. However, also quadratic expressions, penalizing the time integral of the square of the predicted power demand, i.e. J_e (W²h), are found [see e.g. 143]:

$$J_e = \int_0^{H_c} (\dot{Q}_h^2 + \dot{Q}_c^2) dt \quad (5.4)$$

The benefit of a quadratic cost compared to a linear one, is that the resulting optimization problem is better conditioned and thus in practice easier to implement. Moreover, in Chapter 6 it is shown that the quadratic J_e -representation, which gives rise to a smooth and continuous heating and cooling power profile, is beneficial for the control performance of modulating heat pump systems. In this chapter, which deals with a modulating heating and cooling device, we will therefore adopt the quadratic energy cost representation. In Chapter 8, by contrast, dealing with on/off-controlled devices, the linear J_e -representation will be adopted. Note that if the efficiency of the heat and cold production is taken into account, as well as the specific energy cost (€/Wh), J_e is expressed in terms of (€) or (€²) for respectively the linear and quadratic J_e -representation.

Single-objective versus multi-objective optimization

Thermal comfort can be maximized irrespective of the corresponding energy cost [see e.g., 90]. Alternatively, cost functions containing only the energy cost, with the thermal comfort requirement translated into hard constraints, are found [see e.g., 128]. These approaches are often too conservative and might entail more than proportional energy costs compared to a less stringent formulation. A smarter way to deal with these conflicting objectives is to include both thermal discomfort and energy cost in the cost function:

$$J = \alpha_e J_e + \alpha_d J_d \quad (5.5)$$

This multi-objective representation suggests that thermal discomfort, just like energy, has a monetary value. This is indeed the case. Seppanen et al. [156], for instance, set up correlations expressing the effect of temperature on the task performance in office environments. Fisk and Seppanen [52] translated the impact of temperature and air quality to the costs related to health care, absence rate and task performance.

Such a multi-objective approach is adopted by most researchers [see e.g., 20, 101, 103, 179, 186] and is also adopted in this work. The ratio between the weighting

factors α_e and α_d (the units of which depend on the definition of J_e , respectively J_d) allows to determine the relative weight between both objectives. The trade-off between thermal comfort and energy cost can be left to the occupant. To assist this choice, a trade-off curve which visualizes J_d as a function of J_e would thus be helpful. The performance for the different MPC formulations in this work is therefore - in most cases - analyzed by means of the trade-off curves which are obtained by varying the ratio between α_e and α_d .

5.2.2 Choice of controller building model

Various model structures, ranging from black-box models to detailed first-principle models, in what follows referred to as 'white-box models', are discussed in the literature. The quality of a black-box model largely depends on the quality of the identification data set. As a consequence, this modeling approach is very sensitive to measurement errors and unmodelled or unmeasured inputs. For the application in buildings this is an important drawback due to the significant presence of these non-idealities, as recognized by Rabl [145]. Complex statistical tools to suppress all kinds of noise are required to obtain a satisfactory model quality [49]. White-box models, by contrast, are solely based on prior physical knowledge. While this may be an optimal choice in theory, it is not practical for the application in buildings. Incorporating a detailed building model such as TRNSYS Type56, in the optimization, yields an optimization problem which is computationally expensive to solve [28]. Instead, a simplified building model structure, such as a lumped resistance-capacitance (RC)-network representing the most important thermal processes, is preferred. Not only they allow to solve the optimal control problem much faster (and with more efficient solvers), they also require significantly less data for determining the model parameters and require significantly less input data to predict the model output. The parameters of such a lumped model can be determined from physical insight, as investigated by among others Fraisse et al. [53], Kummert [101], Ngendakumana [124] and Masy [117]. This approach requires a considerable amount of physical insight in the control relevant dynamics to concentrate all available information on the building structure and material properties into a few number of model parameters. For large-scale application of MPC, this step of concentrating the control relevant dynamics into a few number of model parameters should be automatized to reduce the required amount of physical knowledge and insight. This results in the so-called grey-box modeling approach: the model structure is based on physical insight, while the corresponding model parameters are determined from measurement data. Compared to the black-box approach, the grey-box approach is less sensitive to measurement noise and unmodelled disturbances as the relation between the different states is a priori defined.

Compared to the white-box approach, the required amount of data and physical insight is reduced. Grey-box modeling for building climate control purpose has been studied by Bacher and Madsen [9] and applied in an MPC framework by Bianchi [20] and Gayeski [59].

5.3 System description

5.3.1 System

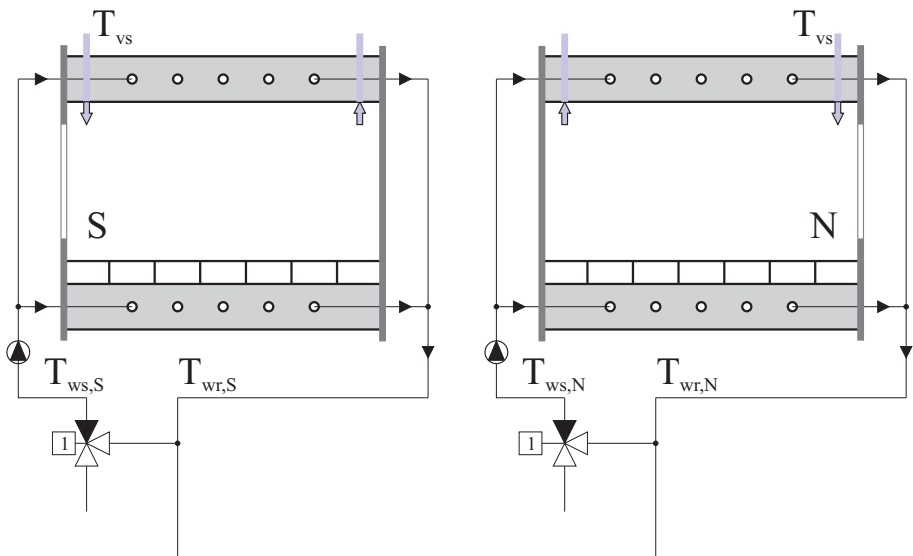


Figure 5.1: two zone office model with hydraulic network layout and indication of the control variables $T_{ws,N}$, $T_{ws,S}$ and T_{vs} .

This chapter focuses on the control at building level. The layout of the hydraulic network is shown in Figure 5.1. Contrary to the reference case described in Chapter 4, the 3-way-valves at zone level allow individual control of the supply water temperature to the North and to the South zone, denoted by respectively $T_{ws,S}$ and $T_{ws,N}$. The heat and cold production system is represented by the combination of an ideal boiler/chiller. The supply water temperature setpoint for the ideal boiler/chiller is calculated in a post-processing step according to

Eq.(5.6). $T_{ws,set}$ equals the maximum of $T_{ws,N}$ and $T_{ws,S}$ in heating mode, respectively the minimum of both in cooling mode.

$$T_{ws,set} = \begin{cases} \max(T_{ws,N}, T_{ws,S}) & \text{if heating} \\ \min(T_{ws,N}, T_{ws,S}) & \text{if cooling} \end{cases} \quad (5.6)$$

These are ideal devices in the sense that the setpoint for $T_{ws,set}$ is perfectly tracked, at least if the required power does not trespass the maximum installed heating power $\dot{Q}_{h,max}$ (W) or cooling power $\dot{Q}_{c,max}$ (W):

$$T_{ws,prod} = \begin{cases} \min(T_{ws,set}, T_{wr} + \frac{\dot{Q}_{h,max}}{\dot{m}_{prod}c_{p,w}}) & \text{if heating} \\ \max(T_{ws,set}, T_{wr} - \frac{|\dot{Q}_{c,max}|}{\dot{m}_{prod}c_{p,w}}) & \text{if cooling} \end{cases} \quad (5.7)$$

with \dot{m}_{prod} the water mass flow rate returning to the heat and cold production system and $c_{p,w}$ (J/kgK) the specific thermal capacity of water. $\dot{Q}_{h,max}$ and $\dot{Q}_{c,max}$ are equal to twice the static design load (see Chapter 4). The ventilation air supply temperature T_{vs} is equal for both zones and determined by the rules described in Chapter 4. Besides these controlled inputs, there are the following uncontrolled inputs or 'disturbances': T_{amb} , \dot{Q}_{int} and \dot{Q}_{sol} . The controller should define the setpoints for $T_{ws,N}$ and $T_{ws,S}$ such that the operative temperatures, $T_{op,N}$ and $T_{op,S}$, lie within the defined thermal comfort interval.

The interaction between the TRNSYS simulation model used as emulator and the controller implemented in Matlab, is shown in Figure 5.2. At each TRNSYS simulation time step (0.2 h), Matlab is called (through the TRNSYS Type 155) to provide the values for $T_{ws,N}$ and $T_{ws,S}$. With the reference control strategy, presented in Section 5.3.2, $T_{ws,N}$ and $T_{ws,S}$ are determined by a heating curve/cooling curve (HC/CC). The operation mode (heating, neutral or cooling), in turn, is based on feedback of the controlled variable T_{cv} , for which two choices are evaluated. With the MPC strategy presented in Section 5.3.3, an optimal profile for $T_{ws,N}(t)$ and $T_{ws,S}(t)$ is determined based on predictions of $T_{amb}(t)$, $\dot{Q}_{int}(t)$ and $\dot{Q}_{sol}(t)$ and on a dynamic controller building model which relates the $T_{op,N}(t)$ and $T_{op,S}(t)$ to all input variables. The dynamic controller building model development is discussed in Section 5.4.

5.3.2 Reference control strategy

The control strategies used as reference are the two HC/CC-based control strategies used for the building load calculation, presented in Section 4.6.1 on

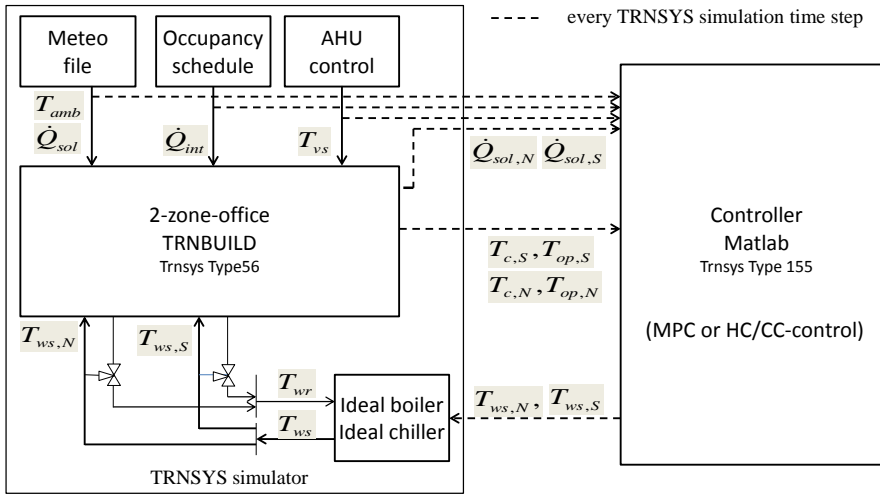


Figure 5.2: Block diagram representing the information flows between the simulator model implemented in TRNSYS and the controller implemented in Matlab (HC/CC-control or MPC).

p.51. The first one, denoted by HC/CC- T_{op} , uses feedback of the operative temperatures $T_{op,N}$ and $T_{op,S}$. The second one, denoted by HC/CC- T_{c} , uses feedback of the concrete core surface temperatures $T_{c,s,N}$ and $T_{c,s,S}$. For HC/CC- T_{op} , 2 different sets of control parameter values are evaluated. The first one yields better thermal comfort, the second one, denoted by HC/CC- $T_{op}(2)$, yields a lower annual electricity consumption.

5.3.3 MPC formulation

Figure 5.3 presents a flow chart of the MPC framework. The procedure contains the following steps:

1. feedback of the TRNSYS-simulation results for T_c and T_{op} to the MPC,
2. prediction of the controlled input T_{vs} and the disturbances T_{amb} , \dot{Q}_{int} and \dot{Q}_{sol} for the entire control horizon H_c ,
3. determination of the controller model initial state X_0 by the observer,
4. solving the OCP,

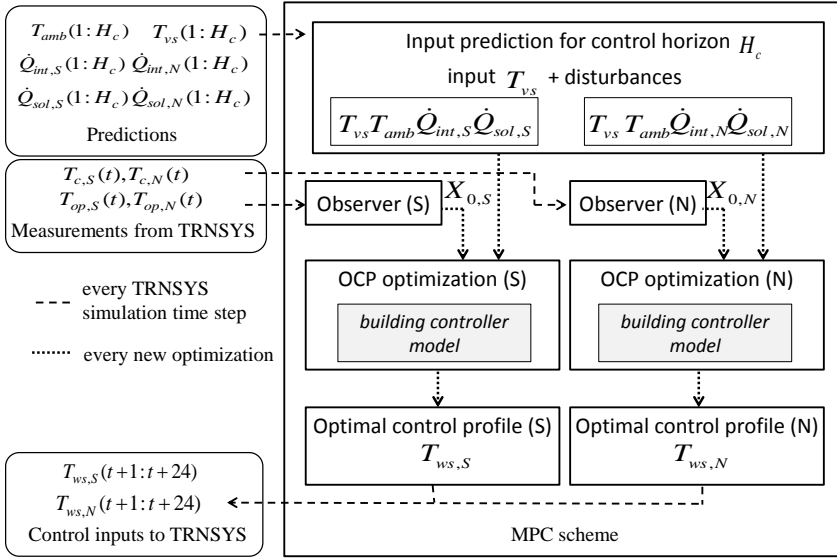


Figure 5.3: Overview of the MPC framework

5. returning the calculated control input variables T_{ws} to TRNSYS.

$T_{ws,N}$ and $T_{ws,S}$ are separately optimized. This is allowed since there is little thermal interaction between the zones: first, they are separated by the corridor and, second, they are kept at the same temperature. The above described procedure is thus simply repeated for both zones, as indicated in Figure 5.3. In what follows, the supply water temperature is represented by T_{ws} (which can be either $T_{ws,N}$ or $T_{ws,S}$).

The OCP formulation, comprising the definition of the cost function, the building dynamics, state initialization and state and input constraints, is presented below, followed by the receding horizon strategy.

Cost function Based on the literature study, discussed in Section 5.2.1, the cost function J (€) is defined as a weighted sum of the predicted energy cost J_e and thermal discomfort cost J_d , both evaluated over the control horizon H_c (h), see Eq.(5.8). J_e (kW²h), see Eq.(5.9), penalizes the sum of squared electric powers, a cost representation which is found to yield good performance for low-exergy emission systems combined with heat pumps as will be shown in Section 6. J_d (K²h), see Eq.(5.10), penalizes temperatures above and below the comfort band presented in Figure 4.7 on p.44, through soft constraints on

the operative temperature T_{op} . The ratio between the weighting factors α_e ($\text{€}/\text{kW}^2\text{h}$) and α_d ($\text{€}/\text{K}^2\text{h}$) allows to move along the trade-off curve of energy cost versus thermal discomfort. The optimal profile is discretized with a control time step Δt_c of 1 h and the control horizon H_c is 48 h. The relatively long control horizon of 48 h is required due to the large dominant time constant of the CCA (about 10 h), especially to optimize the transition between week days and weekend days [13].

$$\min_{T_{ws}} (\alpha_e J_e + \alpha_d J_d) \quad (5.8)$$

$$J_e = \sum_{k=0}^{H_c} \left[\left(\frac{\dot{Q}_h}{COP_h} \right)^2 + \left(\frac{\dot{Q}_c}{COP_c} \right)^2 \right] \Delta t_c \quad (5.9)$$

$$J_d = \sum_{k=0}^{H_c} (\epsilon_h^2 + \epsilon_c^2) \Delta t_c \quad \text{with} \quad \begin{cases} \epsilon_h & \geq T_z - T_{comf,max} \\ \epsilon_c & \geq T_{comf,min} - T_z \end{cases} \quad (5.10)$$

Controller building model To solve the above defined OCP problem with a convex solver, a linear discrete-time representation of the building dynamics is required. This way, the building dynamics are translated into a set of n_x H_c linear equality constraints. The state space matrix representation is expressed by Eq.(5.11). \mathbf{X} (n_x by 1) denotes the state vector, \mathbf{A} (n_x by n_x) the system matrix related to the states and \mathbf{B} (n_x by n_u) the system matrix related to the inputs \mathbf{U} .

$$\mathbf{X}(k+1) = \mathbf{A}\mathbf{X}(k) + \mathbf{B}\mathbf{U}(k) \quad (5.11)$$

$$\text{with } \mathbf{U}(k) = [T_{ws}(k) T_{vs}(k) T_{amb}(k) \dot{Q}_{int}(k) \dot{Q}_{sol}(k)]^T$$

Section 5.4 will discuss the controller building model in more detail.

State initialization The state vector is initialized with \mathbf{X}_0 . If all states are measured, \mathbf{X}_0 is directly obtained from the measurement data fed back to the MPC at the start of the optimization. If not, an observer is used to estimate the unmeasured states. In this study, a Kalman filter [182] is used for this purpose.

$$\mathbf{X}(0) = \mathbf{X}_0 \quad (5.12)$$

Input constraints The minimum and maximum supply water temperature $T_{ws,min}$ and $T_{ws,max}$ are set to respectively 17°C and 40°C.

$$T_{ws,min} \leq T_{ws} \leq T_{ws,max} \quad (5.13)$$

Receding horizon strategy The solution of the OCP, defined by Eqs.(5.8)-(5.13), yields a 48 h profile for the control input variables $T_{ws,N}$ and $T_{ws,S}$, and the corresponding prediction of the operative temperatures $T_{op,N}$ and $T_{op,S}$. The actual T_{op} -profile obtained in TRNSYS will differ from the predicted one due to model mismatch between the simplified building model and the detailed TRNSYS model and due to errors on the disturbance predictions T_{amb} , \dot{Q}_{int} and \dot{Q}_{sol} . Therefore, the optimization process should be repeated at regular time intervals, using updated measurement feedback and disturbance predictions. In this study, the optimization is performed only once a day, at 0AM: the first 24 h-values of the calculated $T_{ws,N}$ and $T_{ws,S}$ -profiles are directly applied to TRNSYS. 0AM is a good point in time to perform the optimization, as at that moment there are the least amount of disturbances acting on the building, the fast transients related to the occupancy have died out, and the transients related to the start up of the heating or cooling in the morning have not yet started. The measurements are then the least prone to process and measurement noise.

5.3.4 Control performance criteria

The control performance is evaluated in terms of:

- the total number of temperature exceeding hours Kh_{tot} (Kh) (see definition Section 4.4)
- the annual specific electricity demand for cooling and heating P_{tot} (kWh/m²/year).

Both performance indicators constitute the trade-off curves, used for analysis.

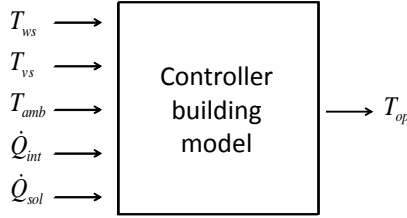


Figure 5.4: Input-output description of the controller building model.

5.4 Controller building model

5.4.1 Model structure

The controller building model should describe the response of T_{op} of a single zone (see Figure 5.3) to the controllable inputs (T_{ws} and T_{vs}) and to the disturbances (T_{amb} , \dot{Q}_{int} and \dot{Q}_{sol}), schematically represented in Figure 5.4. Note that one could define the heat power to the CCA \dot{Q}_{ws} as control input instead of T_{ws} without fundamentally altering the model structure. The choice for T_{ws} as control variable is motivated by the knowledge that current heat pump controllers require a setpoint for T_{ws} . Additionally, T_{ws} is easier to measure than \dot{Q}_{ws} and thus more practical for system identification purpose as well.

Based on physical insight in the main heat transfer processes of a building zone, two model structures are proposed. The first model structure, depicted in Figure 5.5(a), describes the heat transfer between the supply water and the CCA, between the CCA and the zone and between the zone and the ambient air. There are only two states, respectively the mean CCA temperature, denoted by T_c ($^{\circ}\text{C}$), and the mean zone temperature, denoted by T_z ($^{\circ}\text{C}$), with corresponding thermal capacity C_c (J/K) and C_z (J/K). The thermal resistances between the states and the model inputs T_{ws} , T_{vs} and T_{amb} are represented by the R -components (K/W). The internal heat gains \dot{Q}_{int} (W) and solar gains \dot{Q}_{sol} (W) are assumed to directly apply to the T_z -node. Only the fraction of \dot{Q}_{sol} that actually reaches the zone, i.e. $g_{wd}\dot{Q}_{sol}$ with g_{wd} (-) denoting the g-factor of the windows, is applied to T_z . The heat transfer arising from ventilation is represented by a thermal resistance between the ventilation air supply temperature T_{vs} and the zone temperature T_z .

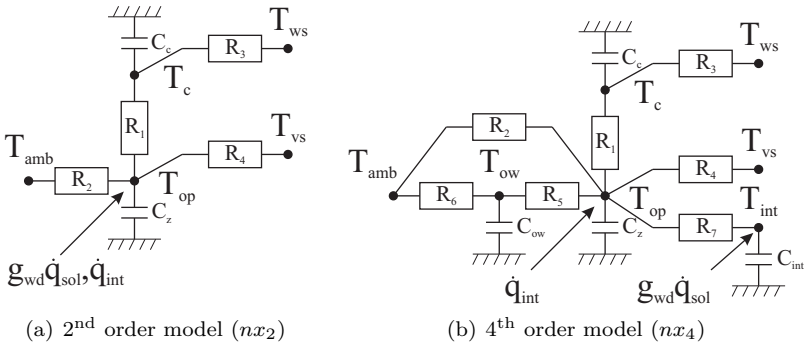


Figure 5.5: Simplified building representation by means of (a) a 2nd order model and (b) a 4th order model

The second model structure, depicted in Figure 5.5(b), allows to describe the heat transfer processes in more detail. First, the heat transfer from the building zone to the ambient air is split into the transmission losses through the outer wall on the one hand, and through the windows on the other hand. To this end, T_{wo} ($^{\circ}\text{C}$), representing the outer wall temperature, is added as an extra state. A second additional state, T_{int} , represents the thermal mass of the inner walls and furniture. This state is added to distinguish between the radiative and the convective heat transfer processes in the zone: while the convective gains directly influence the zone air temperature, the radiative gains are first absorbed by the surfaces. Assuming that the internal gains are mainly convective, and the solar gains mainly radiative, the inputs \dot{Q}_{int} and \dot{Q}_{sol} are applied to respectively the node T_z and the node T_{int} .

In both the 2nd and 4th order model, T_z is assumed to be a representative measure for T_{op} .

5.4.2 Model equations

Writing down the energy balance equations for the 2nd order model represented in Figure 5.5(a) gives rise to the following set of differential equations:

$$\begin{aligned}\dot{T}_c &= (R_1 C_c)^{-1} (T_z - T_c) + (R_3 C_c)^{-1} (T_{ws} - T_c) \\ \dot{T}_z &= (R_1 C_z)^{-1} (T_c - T_z) + (R_4 C_z)^{-1} (T_{vs} - T_z) \\ &\quad + (R_2 C_z)^{-1} (T_{amb} - T_z) + C_z^{-1} \dot{Q}_{int} + C_z^{-1} g_{wd} \dot{Q}_{sol}\end{aligned}\quad (5.14)$$

with \dot{T} (Kh) denoting the time derivative of T . The 7 physical parameters C_c , C_z , R_1 , R_2 , R_3 , R_4 and g_{wd} are now lumped into 7 model parameters p_1 to p_7 :

$$\begin{aligned}\dot{T}_c &= p_1 (T_z - T_c) + p_2 (T_{ws} - T_c) \\ \dot{T}_z &= p_3 (T_c - T_z) + p_4 (T_{vs} - T_z) + p_5 (T_{amb} - T_z) + p_6 \dot{Q}_{int} + p_7 \dot{Q}_{sol}\end{aligned}\quad (5.15)$$

The corresponding state space formulation is:

$$\begin{bmatrix} \dot{T}_c \\ \dot{T}_z \end{bmatrix} = \begin{bmatrix} -(p_1 + p_2) & p_1 \\ p_3 & -(p_3 + p_4 + p_5) \end{bmatrix} \begin{bmatrix} T_c \\ T_z \end{bmatrix} + \begin{bmatrix} p_2 & 0 & 0 & 0 & 0 \\ 0 & p_4 & p_5 & p_6 & p_7 \end{bmatrix} \begin{bmatrix} T_{ws} \\ T_{vs} \\ T_{amb} \\ \dot{Q}_{int} \\ \dot{Q}_{sol} \end{bmatrix}\quad (5.16)$$

For the 4th order model represented in Figure 5.5(b), the energy balance gives rise to the following set of differential equations:

$$\begin{aligned}\dot{T}_c &= (R_1 C_c)^{-1} (T_z - T_c) + (R_3 C_c)^{-1} (T_{ws} - T_c) \\ \dot{T}_z &= (R_1 C_z)^{-1} (T_c - T_z) + (R_7 C_z)^{-1} (T_{int} - T_z) + (R_5 C_z)^{-1} (T_{ow} - T_z) \\ &\quad + R_4 C_z^{-1} (T_{vs} - T_z) + (R_2 C_z)^{-1} (T_{amb} - T_z) + C_z^{-1} \dot{Q}_{int} \\ \dot{T}_{int} &= (R_7 C_{int})^{-1} (T_z - T_{int}) + C_{int}^{-1} g_{wd} \dot{Q}_{sol} \\ \dot{T}_{ow} &= (R_5 C_{ow})^{-1} (T_z - T_{ow}) + R_6 C_{ow}^{-1} (T_{amb} - T_{ow})\end{aligned}\quad (5.17)$$

The 12 physical parameters C_c , C_z , C_{int} , C_{ow} , R_1 to R_7 and g_{wd} are now lumped into 12 model parameters p'_1 to p'_{12} :

$$\dot{T}_c = p'_1 (T_z - T_c) + p'_2 (T_{ws} - T_c) \quad (5.18)$$

$$\dot{T}_z = p'_3 (T_c - T_z) + p'_4 (T_{int} - T_z) + p'_5 (T_{ow} - T_z) \quad (5.19)$$

$$+ p'_6 (T_{vs} - T_z) + p'_7 (T_{amb} - T_z) + p'_8 \dot{Q}_{int} \quad (5.20)$$

$$\dot{T}_{int} = p'_9 (T_z - T_{int}) + p'_{10} \dot{Q}_{sol} \quad (5.21)$$

$$\dot{T}_{ow} = p'_{11} (T_z - T_{ow}) + p'_{12} (T_{amb} - T_{ow}) \quad (5.22)$$

with corresponding state space formulation:

$$\begin{bmatrix} \dot{T}_c \\ \dot{T}_z \\ \dot{T}_{int} \\ \dot{T}_{ow} \end{bmatrix} = \begin{bmatrix} -(p'_1 + p'_2) & p'_1 & 0 & 0 \\ p'_3 & -(p'_3 + p'_4 + p'_5 + p'_6 + p'_7) & p'_4 & p'_5 \\ 0 & p'_9 & -p'_9 & 0 \\ 0 & p'_{11} & 0 & -(p'_{11} + p'_{12}) \end{bmatrix} \begin{bmatrix} T_c \\ T_z \\ T_{int} \\ T_{wo} \end{bmatrix} \\ + \begin{bmatrix} p'_2 & 0 & 0 & 0 & 0 \\ 0 & p'_6 & p'_7 & p'_8 & 0 \\ 0 & 0 & 0 & 0 & p'_{10} \\ 0 & 0 & p'_{12} & 0 & 0 \end{bmatrix} \begin{bmatrix} T_{ws} \\ T_{vs} \\ T_{amb} \\ \dot{Q}_{int} \\ \dot{Q}_{sol} \end{bmatrix} \quad (5.23)$$

The model parameters p_i and p'_i are determined by parameter estimation (PE) in Section 5.4.3.

5.4.3 Parameter estimation

Search region

Initial model ini As stated in Section 2.3, PE requires a good initial guess as the optimization problem of finding the set of parameters minimizing the sum of squared errors between the model output and the measurements, is non-linear. Since the model parameters have a physical meaning, the initial values can be determined from the material properties and geometry of the surfaces surrounding the office zone. The resulting starting values for the 2nd and 4th-order model are listed in Table 5.1. Following rules have been used to define the initial values of the *RC*-network [164]:

- material properties are typical values, in this case taken from the Belgian building standard NBN62-002:2008,
- the CCA is modelled using the star network approach developed by EMPA [100] with a fictitious concrete core node as central point,
- the surface convective heat transfer for floor and ceiling is modelled using the correlation from Awbi and Hatton [8],
- the surface convective heat transfer for vertical walls is modelled as a constant: $h_{\text{inside}} = 7.7 \text{ W/m}^2\text{K}$ and $h_{\text{outside}} = 25 \text{ W/m}^2\text{K}$,
- the internal capacity C_{int} is the thermal capacity of the lightweight separation wall of the office zone, while the thermal resistance R_7 includes convection and conduction to the center of this wall,
- the outer wall is modelled by an optimized RCR-network, following the methodology proposed by Masy [117]: from outside to inside it is composed as $0.96R - 0.79C - 0.04R$ with $R =$ the total thermal resistance and C the total capacity of the wall,
- the g-factor of the window, g_{wd} , is assumed to be independent of the solar incident angle, and taken equal to 0.36.

Table 5.1: Initial parameter values for the 2nd and the 4th-order model (*ini*).

nx_2			nx_4					
p_1	1.12e-1	[1/h]	p'_1	1.12e-1	[1/h]	p'_7	1.04e-3	[1/h]
p_2	6.02e-2	[1/h]	p'_2	2.03e+0	[1/h]	p'_8	4.53e-3	[K/kJ]
p_3	2.03e+0	[1/h]	p'_3	2.80e+0	[1/h]	p'_9	6.43e-1	[1/h]
p_4	2.40e-1	[1/h]	p'_4	3.21e-1	[1/h]	p'_{10}	1.04e-3	[K/kJ]
p_5	1.00e-1	[1/h]	p'_5	2.40e-1	[1/h]	p'_{11}	7.49e-2	[1/h]
p_6	4.53e-3	[K/kJ]	p'_6	1.00e-1	[1/h]	p'_{12}	7.48e-3	[1/h]
p_7	1.60e-3	[K/kJ]						

Search region The search region, defined by the set of constraints given in Eqs.(5.24-5.25), is chosen relatively large to minimize the impact of the initial model (and thus of the amount of prior system knowledge required). The lower bound for p_i or p'_i is set to 10% of the initial value listed in Table 5.1, while the upper bound is 10 times larger:

$$0.1 p_{i,\text{ini}} \leq p_i \leq 10 p_{i,\text{ini}} \quad (5.24)$$

$$0.1 p'_{i,\text{ini}} \leq p'_i \leq 10 p'_{i,\text{ini}} \quad (5.25)$$

Identification data sets

Measurement time step and measurement length Due to its simplified model structure and thus limited number of parameters, the controller building model can not capture all dynamics of the office zone. The aim is to select the ID set such that the obtained model captures the dynamics relevant for control purpose. While T_{op} responds very rapidly to changes in \dot{Q}_{sol} , for instance, it changes much slower to changes in the controlled input variable T_{ws} . This means that, even if an accurate thermal comfort assessment would require inclusion of the T_{op} response to the fast changes in \dot{Q}_{sol} , the CCA thermal inertia limits the control relevant dynamics to the hourly time scale. The slowest dynamics, on the other hand, are determined by the building inertia. Based on the eigenvalues of the initial physical model, the dominant time constant of the building is estimated to be about 100 h. Therefore an identification data length of 100 h with a measurement time step of 1 h is chosen, yielding a total of 100 data points. With the ACADO solver used, this is, for the given model structures with respectively 7 and 12 parameters, approximately the upper limit.

Measured variables In this study measurements are replaced by detailed TRNSYS simulations. It is assumed that all inputs are perfectly measured, as well as the operative temperature T_{op} and the mean concrete core temperature T_c . T_{op} and T_c are both an output of the TRNSYS building type Type56. In practice, T_{op} can be measured through a radiative/convective temperature sensor, while measuring T_c requires monitoring of the concrete core temperature at different locations.

Excitation signals Starting from a detailed building simulation model, virtually all combinations of excitation signals for the inputs T_{ws} , T_{vs} , T_{amb} , \dot{Q}_{int} and \dot{Q}_{sol} are possible. In practice, these inputs are only to a limited extent controllable. The changes in T_{ws} and T_{vs} are limited by the installed heating and cooling power, while the profiles for T_{amb} , \dot{Q}_{int} and \dot{Q}_{sol} largely depend on the choice of the measurement period (i.e., summer/winter, week/weekend). In this study, 5 different identification data sets (DS) are proposed, each with a different building excitation signal. The 5 data sets are summarized in Table 5.2. At time step

Table 5.2: Data sets for parameter estimation (DS1 - DS3: theoretical input profiles; set DS4 - DS5: more realistic input profiles)

Data set	HVAC		Weather		Occupancy
	T_{ws}	T_{vs}	T_{amb}	\dot{Q}_{sol}	\dot{Q}_{int}
DS1	Step	Step	Step	0	0
DS2	Step	Step	Step	0	Step
DS3	Step	Step	Step	Step	Step
DS4	Block	Block	Summer	Summer	Block
DS5	Block	Block	Winter	Winter	Block

$t = 0$, the building is at a steady state temperature with the ambient air of 20°C .

The first three data sets, DS1 to DS4, comprise step excitations of an increasing number of inputs. DS1 to DS3 comprise the response of T_{op} and T_c to a step input of T_{ws} and T_{amb} . In DS1 there is additionally a step excitation of T_{vs} , in DS2 of \dot{Q}_{int} and finally in DS3 all 5 inputs are excited by a step signal. The last two data sets, DS4 and DS5, represent the office zone under realistic conditions, respectively a typical working week in summer and a typical working week in winter: the profiles for T_{amb} and \dot{Q}_{sol} are extracted from the Uccle Meteo data, the profiles for T_{ws} and T_{vs} are block functions, representing the on-off behavior of the heating and ventilation system during a typical working week, and \dot{Q}_{int} is also represented by a block function, approximating the internal gains during office hours. The main difference between DS4 and DS5 is the amplitude of \dot{Q}_{sol} , which in DS4 amounts to 850 W/m^2 and in DS5 26 W/m^2). The first 3 data sets are interesting in order to learn how to excite the zone for the purpose of PE when a detailed building simulation model is available. This is often the case for larger buildings for which there is a tendency towards simulation assisted design. The results of DS4 and DS5 are useful to assess the model quality obtained from measurement data of a building under operation. As an illustration the input and output profiles for DS3 (step input of all 5 inputs) and DS4 (typical working week in summer) are plotted in Fig. 5.6. The left graphs depict the profiles for the temperature inputs (T_{ws} , T_{vs} , T_{amb}), the graphs in the middle the heat inputs (\dot{Q}_{sol} and \dot{Q}_{int}) and the graphs at the right the corresponding outputs (T_c and T_z).

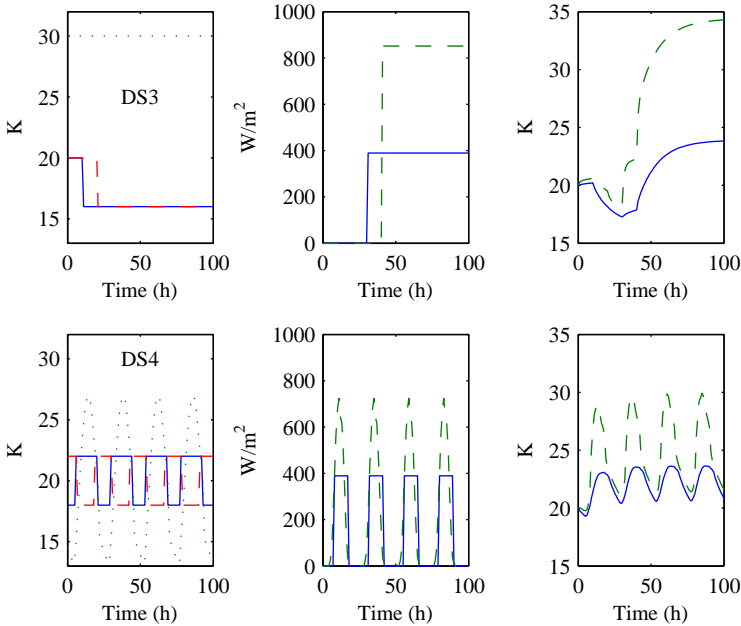


Figure 5.6: Inputs T_{ws} , T_{vs} , T_{amb} (left), inputs \dot{Q}_{sol} and \dot{Q}_{int} (middle), and measured outputs T_c and T_z (right) for the identification sets DS3 (above) and DS4 (below)

Parameter estimation

The PE results for the 2nd order models are summarized in Table 5.3. The last 5 columns list the ratio of the parameter found with the respective data set, to the parameter of the initial model (`nx2-ini`). For DS1 to DS3, the parameter values found lie within the search region defined by Eq.(5.25). For DS4 and DS5, by contrast, the search region had to be enlarged as the constraint on p was found to be active for, among others, p_3 , p_4 , p_5 and p_6 . Note that DS1, which contains neither \dot{Q}_{int} nor \dot{Q}_{sol} in the excitation signal (see Table 5.2), does not allow to estimate the corresponding model parameters p_6 and p_7 (see Eq.5.15). DS1, containing \dot{Q}_{int} in the excitation signal but not \dot{Q}_{sol} , allows to estimate p_6 but not p_7 . As p_6 and p_7 theoretically only differ by one factor, namely the g-factor of the window g_{wd} , p_7 for DS1 is taken equal to p_6 times the g-factor of 0.36, as was done to set up the initial models `nx2-ini` and `nx4-ini`.

The time constants τ of the resulting 2nd and 4th order building models,

Table 5.3: Parameter estimation result for the 2nd order model.

	Initial model		(ini)	Ratio $p_i/p_{i,ini}$				
	nx2-ini			DS1	DS2	DS3	DS4	DS5
p_1	1.12e-1	[1/h]	(1)	0.7	0.7	0.7	0.6	1.1
p_2	6.02e-2	[1/h]	(1)	1.5	1.6	1.6	1.3	0.8
p_3	2.03e+0	[1/h]	(1)	0.7	0.7	1.6	15.6	14.4
p_4	2.40e-1	[1/h]	(1)	0.9	0.8	1.6	0.1	9.1
p_5	1.00e-1	[1/h]	(1)	1.1	1.2	1.6	0.1	15.6
p_6	4.53e-3	[K/kJ]	(1)	x	0.7	0.7	12.1	11.7
p_7	1.60e-3	[K/kJ]	(1)	x	$g_{wd}p_6$	0.7	2.8	10.7

represented by respectively the 'x' and the 'o' markers in Figure 5.7, allow a physical interpretation of the PE results. The relatively large difference in time constants of the different models, indicate a significant impact of the identification data set on the building dynamics captured by the model. For the 2nd order model, the smallest time constant, referred to as τ_1 and related to the zone dynamics (T_{op}), is about 0.4 h for DS1 and DS2. The largest one, referred to as τ_2 and related to the dynamics of the CCA (T_c) amounts to 9 h. With DS4 and DS5, by contrast, τ_1 is one order of magnitude smaller, i.e. 0.02 h. τ_2 is only a little higher, namely 11 h. The time constants obtained with DS3 lie somewhere in between.

The impact of the identification data set for the 4th order building models is relatively smaller than for the 2nd order models. Except for DS4, which constitutes a clear exception, the following results are obtained. The smallest time constant τ_1 , which can be attributed to the dynamics of the zone (T_{op}), is for all data sets (except from DS4) about 0.15 h. For τ_2 , which can be attributed to the dynamics of the internal mass (T_{int}), the variation is larger: τ_2 ranges from 1.5 h to 3 h. For τ_3 , which can be attributed to the dynamics of the CCA (T_c) and τ_4 , related to the dynamics of the outer wall (T_{wo}), there is again considerable correspondence between the results. τ_3 amounts to 9 to 10 h and τ_4 amounts to 80 h. In comparison with these results, the time constants of the model obtained with DS4 (typical summer) are all shifted towards smaller values, indicating that all the degrees of freedom have been used to match the fast changes observed for T_{op} in response to \dot{Q}_{sol} . As a consequence, the large dynamics related to the building envelope are not captured by the model. The largest time constant for nx4-DS4 amounts to 12 h, which is even less than the dominant time constant of a typical T_{amb} -profile.

Comparison of the two model structures shows that both the 2nd and 4th order models capture the dynamics of the CCA, which has a dominant time constant of approximately 10 h. For the initial model (ini) and the data sets without solar

gains (DS1 and DS2), the time constant related to T_{op} in the 2nd order model lies in between the time constants of T_{op} and T_{int} of the 4th order model. This well illustrates the lumping effect caused by model order reduction. With DS4 and DS5, by contrast, the time constant related to T_{op} for the 2nd order model is smaller than for the 4th order model. This should not be the case, as the spread in the τ -values should decrease with decreasing model order. From this we conclude that DS4 and DS5 are not well suited for estimating the parameters of the 2nd order model.

The results are obtained with a measurement sampling time step of 1 h. As a consequence, the uncertainty on the time constants below 2 h is very large (cfr. the Nyquist criterion). To investigate the reliability of these values, the sampling time should be reduced down to 0.1 h or even less.

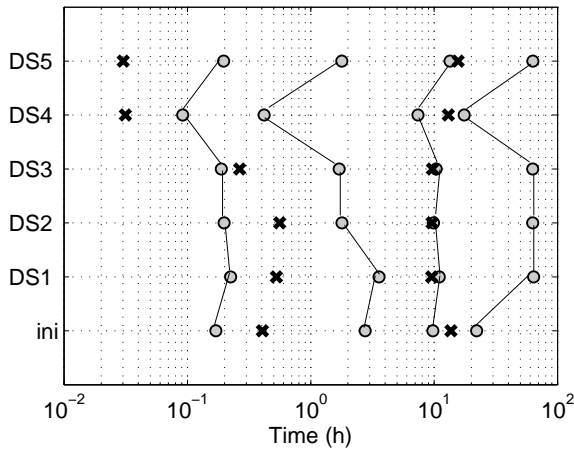


Figure 5.7: Time constants of the 2nd order building model (indicated by the markers 'x') and 4th order building model (indicated by the markers 'o' and connected by lines for inter-model comparison) obtained with PE for the 5 different identification data sets (DS1 - DS5). The initial models are shown on the first row (ini).

5.4.4 Validation results

Table 5.4 and Table 5.5 list the RMSE ($^{\circ}\text{C}$) for T_{op} for respectively the 2nd and 4th order models. The rows represent the models (identified by using the 5 data sets), while the columns contain the corresponding validation results

for each of the 5 data sets. The RMSE is calculated according to Eq.(5.26), with T_z being the zone temperature predicted by the model and T_{op} the actual measured operative temperature.

$$\text{RMSE} = \sqrt{\frac{\sum_{k=1}^N (T_z(k) - T_{op}(k))^2}{N}} \quad (5.26)$$

The sum of squared errors between both temperatures is evaluated for the entire validation set, comprising of $N=100$ data points. Note that the values of the RMSE are here mainly used for comparing the *relative accuracy of the different models*. The absolute value of the RMSE scales with the input signal as can be seen from Eq.(5.26). The absolute value of the RMSE is therefore only relevant for the validation results of DS4 and DS5 which correspond to realistic input profiles.

The terminology used in this section is:

- val-DS1 refers to data set DS1 used for validation
- nx2-DS1 refers the 2nd order model with parameters estimated with data set DS1
- nx4-DS1 refers the 4th order model with parameters estimated with data set DS1
- nx-DS1 refers to both 2nd and 4th order model with parameters estimated with data set DS1

Table 5.4: RMSE (°C) on zone operative temperature T_{op} (2nd order)

	val-DS1	val-DS2	val-DS3	val-DS4	val-DS5
nx2-ini	0.4	0.7	6.5	3.1	0.8
nx2-DS1	0.4	2.8	12.0	5.1	2.6
nx2-DS2	0.5	0.2	2.1	2.3	0.9
nx2-DS3	1.3	0.7	0.8	1.8	0.9
nx2-DS4	4.3	0.9	3.1	1.3	2.1
nx2-DS5	0.6	0.2	3.8	2.9	0.6

The validation results show that the initial 2nd order model **nx2-ini** accurately predicts the response of T_{op} to a step change in T_{ws} , T_{vs} and T_{amb} (see first two columns). The response to \dot{Q}_{int} and \dot{Q}_{sol} , contained in DS3 and DS4, is not

Table 5.5: RMSE ($^{\circ}\text{C}$) on zone operative T_{op} (4th order)

	val-DS1	val-DS2	val-DS3	val-DS4	val-DS5
nx4-ini	0.9	0.7	5.1	2.2	0.6
nx4-DS1	0.1	2.6	11.8	5.2	2.5
nx4-DS2	1.1	0.1	8.5	3.3	0.9
nx4-DS3	1.0	1.5	0.3	1.1	1.1
nx4-DS4	2.5	0.8	1.7	1.0	1.3
nx4-DS5	0.9	1.7	20.5	8.5	0.6

well described and results in unacceptably high RMSE values. Compared to **nx2-ini**, **nx4-ini** performs less well for DS1 to DS2 and slightly better for DS3 and DS4. However, the RMSE for the latter two validation data sets remains unacceptably high. These results indicate that, first, the typical rules of thumb for determining the RC-values of a simplified building model are not suitable for describing the response of T_{op} to \dot{Q}_{int} and \dot{Q}_{sol} . Second, increasing the complexity of the model structure does not guarantee improvement of the model quality.

The models **nx2-DS1** and **nx4-DS1** do not include the response of the building to the inputs \dot{Q}_{int} or \dot{Q}_{sol} (see e.g. Table 5.3: p_6 and p_7 are zero). The RMSE for DS3 and DS4 (which both contain a significant amount of \dot{Q}_{sol}), however, are decreased from resp. 31°C and 13°C to 12°C and 5°C for the 2nd order model, and from resp. 25°C and 10°C to 12°C and 5°C for the 4th order model, compared to the initial models. This indicates that it is better to not describe the response to \dot{Q}_{int} or \dot{Q}_{sol} at all, than to describe it erroneously. However, the RMSE remains unacceptably high. Moreover, the validation results for the other data sets, i.e. DS1, DS2 and DS5, are not improved and in some cases even deteriorated compared to the initial models. Therefore no general conclusion can be drawn regarding the model quality improvement obtained through PE with a step excitation of the temperature inputs T_{ws} , T_{vs} and T_{amb} compared to a well chosen initial model.

Compared to DS1, DS2 has additionally a step excitation of \dot{Q}_{int} . The validation results for the models obtained with DS2 are now significantly improved compared to the initial models, and this for all data sets. Contrary to **nx2-DS1** and **nx4-DS1**, **nx2-DS2** and **nx4-DS2** do include the response of the building to \dot{Q}_{int} and \dot{Q}_{sol} . For **nx2-DS2**, the RMSE for DS3 and DS4 amounts to respectively 2 and 1.5, compared to 12 and 5 for **nx2-DS1**. Since \dot{Q}_{sol} is not contained in the identification data set, this improvement is explained by the fact that parameter p_7 of **nx2-DS2** has been set equal to $g_{wd}p_6$ (see Table 5.3. This trick could not be applied for **nx4-DS1** (in the 4th-order model \dot{Q}_{int} and \dot{Q}_{sol} apply to different

nodes), which explains why the validation results for **nx4-DS2** are inferior to the ones for **nx2-DS2**. Analogously to the initial models, the increased model complexity of the 4th order model therefore does not yield an improved model quality.

DS3 has a step excitation of the five inputs, including \dot{Q}_{sol} . The latter input is treated as a pure radiative term in TRNSYS, and is there absorbed by the inner wall surfaces. As a consequence, this data set should enable to further improve the quality of the 4th order model compared to the previous data sets. The validation results indicate that the prediction error for the data sets including solar gains, **DS3** to **DS5**, is indeed further reduced compared to the models obtained with **DS2**. This improvement is at the expense of a slight deterioration of the response prediction for **DS1** and **DS1**.

DS4 is similar to **DS3** as it excites all five inputs. The difference between both data sets is the frequency contained in the excitation signal. Step functions and block-functions contain a broad frequency range, contrary to a sinusoidal function which has only one frequency. In **DS3**, the building is excited by a step input of T_{amb} , while in **DS4** it is excited by a sinusoidal input representing a realistic profile of T_{amb} . **DS4** therefore contains less information than **DS3**. This is confirmed by the validation results, showing an increased RMSE with **DS4** compared to **DS3** for all data sets. The relatively high RMSE for the first data set (val **DS1**) compared to the other models indicates that the deteriorated model performance of **nx-DS4** can indeed be attributed to a less good description of the T_{amb} response.

DS5, finally, differs from **DS4** only in the inputs T_{amb} and \dot{Q}_{sol} . Representing a typical winter condition, the amplitude of \dot{Q}_{sol} is far smaller than in **DS5**. The obtained model fails to predict T_{op} for the data sets **DS3** and **DS4** containing large \dot{Q}_{sol} -values. For the validation sets without \dot{Q}_{sol} (**DS1** and **DS2**), on the contrary, the model performs better than **DS4**. Compared to **nx-DS1** and **nx-DS2**, on the other hand, **nx-DS5** performs worse.

From the validation results discussed above, following major trends are observed. First, there is a clear distinction between the models identified with data containing strong excitation of \dot{Q}_{sol} (**DS3** and **DS4**) and those without (**DS1**, **DS2** and **DS5**). The latter are unable to predict the response of T_{op} to \dot{Q}_{sol} , impeding the use of these models for typical summer weather conditions (**DS4**). The good validation results for **nx2-DS2** are explained by the fact that the model parameter p_6 , identified in the presence of input \dot{Q}_{int} , has been used to estimate p_7 , the model parameter defining the response of T_{op} to \dot{Q}_{sol} . That this trick can be applied, can be regarded as an advantage of the grey-box modeling approach over black-box system identification.

Second, data sets with step input signals (DS1 to DS3) yield better models than data sets representing a building under typical operation conditions (DS4 to DS5). It may thus be worth to first identify an initial model off-line, based on a detailed building simulation model, which can then be further fine tuned on-line. Especially the lack of frequency content of a typical T_{amb} -profile may corrupt the model quality.

Third, a 4th order model performs better than a 2nd order one only if the identification data contain \dot{Q}_{sol} as excitation signal (DS3 and DS4). The other data sets apparently do not contain enough information to estimate the parameters of the 4th order model well. The satisfactory model accuracy for nx2-DS2 even suggests that a 2nd order model is sufficient to describe the response of T_{op} to all inputs, including \dot{Q}_{int} and \dot{Q}_{sol} and that, at least for the investigated data sets, the additional parameters of the 4th order model are redundant.

In the next chapter we will investigate how these models perform in an MPC framework. How sensitive is the control performance to the controller building model used? And do we need a model which is able to predict the response of T_{op} to \dot{Q}_{sol} or not? The latter is important since, as we have seen, this requires a richer identification data set with inclusion of the solar gains. For practical implementation, measuring \dot{Q}_{sol} entails significant additional measurement effort, so it would be interesting if this requirement for measuring \dot{Q}_{sol} could be relaxed.

5.4.5 Incorporation of the model in the MPC framework

To solve the OCP (defined in Section 5.3.3) with a convex solver, a discrete-time representation of the identified building models is required. The discretization time equals the control time step Δt_c , namely 1 h. This way, the building dynamics are translated into a set of $n_x H_c$ linear equality constraints. The model equations for the 2nd and 4th order model are shown in respectively Eqs.(5.27) and (5.28). \mathbf{A} ($n_x \times n_x$) denotes the system matrix related to the states, \mathbf{B}_T ($n_x \times 3$) the system matrix related to the temperature inputs T_{ws} , T_{vs} and T_{amb} , \mathbf{B}_Q ($n_x \times 2$) the system matrix related to the thermal power inputs \dot{Q}_{int} and \dot{Q}_{sol} and ΔT_z an on-line updated term to compensate for model mismatch. The distinction between \mathbf{B}_T and \mathbf{B}_Q is made to emphasize the difference between the models which take the thermal power inputs into account (ini, DS2, DS3, DS4 and DS5) and those which do not (DS1). In the latter case \mathbf{B}_Q is equal to zero.

Discrete-time representation of 2nd order model:

$$\begin{bmatrix} T_c(k+1) \\ T_z(k+1) \end{bmatrix} = \mathbf{A} \begin{bmatrix} T_c(k) \\ T_z(k) \end{bmatrix} + \mathbf{B}_T \begin{bmatrix} T_{ws}(k) \\ T_{vs}(k) \\ T_{amb}(k) \end{bmatrix} + \mathbf{B}_Q \begin{bmatrix} \dot{Q}_{int}(k) \\ \dot{Q}_{sol}(k) \end{bmatrix} + \begin{bmatrix} 0 \\ \Delta T_z(k) \end{bmatrix} \quad (5.27)$$

Discrete-time representation of 4th order model:

$$\begin{bmatrix} T_c(k+1) \\ T_z(k+1) \\ T_{int}(k+1) \\ T_{ow}(k+1) \end{bmatrix} = \mathbf{A} \begin{bmatrix} T_c(k) \\ T_z(k) \\ T_{int}(k) \\ T_{wo}(k) \end{bmatrix} + \mathbf{B}_T \begin{bmatrix} T_{ws}(k) \\ T_{vs}(k) \\ T_{amb}(k) \end{bmatrix} + \mathbf{B}_Q \begin{bmatrix} \dot{Q}_{int}(k) \\ \dot{Q}_{sol}(k) \end{bmatrix} + \begin{bmatrix} 0 \\ \Delta T_z(k) \\ 0 \\ 0 \end{bmatrix} \quad (5.28)$$

For the models obtained with data set **DS1**, the omission of the response of T_{op} to the inputs \dot{Q}_{int} and \dot{Q}_{sol} is the main source of model mismatch. The predicted T_z will be lower than the actual T_{op} , especially during occupancy hours and periods with high solar gains. To compensate for this model mismatch, the MPC will track the actual T_{op} , fed back from the TRNSYS simulator, and compare this to the one predicted by the optimization. Based on this comparison, two simple error compensation strategies are presented and evaluated. The first method, referred to as c_1 and expressed by Eq.(5.29), is to update ΔT_z each 24 h: ΔT_z for the next day d , denoted by $\Delta T_{z,d}$, updates the correction factor of the previous day, $\Delta T_{z,d-1}$, with the mean value of the prediction error over the past 24 h. $T_{op,MPC(d-1)}(k)$ in Eq.(5.29) represents the prediction for T_{op} made within the MPC framework for the past 24 h, while $T_{op}(t)$ represents the actual measured values. To prevent unstable control behavior, ΔT_z may not react too quickly to the last observed prediction errors. Here, the learning factor β is chosen equal to 5%.

$$c_1 : \Delta T_{z,d} = \Delta T_{z,d-1} + \beta \overline{(T_{op}(t-24:t) - T_{op,MPC(d-1)}(1:24))} \quad (5.29)$$

The recorded prediction error profile, however, contains more information than what is deployed by method c_1 . Given the origin of the model mismatch, we know that the prediction error on T_{op} will be correlated with the inputs \dot{Q}_{int} and \dot{Q}_{sol} . The second method, referred to as c_2 , uses this information: the correction term ΔT_z is updated for each time of the day individually, resulting in a 24h-profile $\Delta T_z(k)$, see Eq.(5.30). The difference between week days (*wd*) and weekend days (*wknd*) is acknowledged by storing two distinct ΔT_z -profiles,

as expressed in Eq.(5.31).

$$c_2 : \begin{cases} \Delta T_z(k) & = \Delta T_z(k)_{wd} \quad \text{or} \quad \Delta T_z(k)_{wknd} \quad \text{for } k = 1 : 24 \\ \Delta T_z(k) & = \Delta T_z(k)_{wd} \quad \text{or} \quad \Delta T_z(k)_{wknd} \quad \text{for } k = 25 : H_c \end{cases} \quad (5.30)$$

with the vectors being updated as follows:

$$\Delta T_z(k)_{wd} = \Delta T_z(k)_{wd} + \beta (T_{op}(t - 24 + k) - T_{op,MPC(d-1)}(k)) \quad (5.31)$$

if $d - 1 = \text{week day}$

$$\Delta T_z(k)_{wknd} = \Delta T_z(k)_{wknd} + \beta (T_{op}(t - 24 + k) - T_{op,MPC(d-1)}(k))$$

if $d - 1 = \text{weekend day}$

The models obtained with DS2 to DS5 are able to capture the influence of \dot{Q}_{int} and \dot{Q}_{sol} on T_{op} , at least to a certain extent (see validation results Section 5.4.4). It will be investigated whether these models can also benefit from the prediction correction methods c_1 and c_2 . The results are compared to the case without model correction, referred to as c_0 .

5.5 Control performance evaluation

This chapter evaluates the sensitivity of the MPC performance on the controller building model for the following three scenario's: (1) perfect disturbance predictions, (2) imperfect disturbance predictions, (3) lumped building level instead of zone level control. MPC is each time compared to the reference HC/CC controller described in Chapter 4.

5.5.1 Scenario 1: Perfect disturbance predictions

The assumption of perfect disturbance predictions allows us to isolate the impact of model mismatch on the MPC performance. To include the effect of the solar shading (for the South zone), the data vector with the $\dot{Q}_{sol, South}$ prediction is preprocessed for H_c before it is applied to the MPC: the prediction of $\dot{Q}_{sol, South}$ is corrected with $g_{solshade}$ at times when the solar shading is down, according to the device's controller settings (see Chapter 4 on p.36).

Figure 5.8(a) and Figure 5.8(b) show the T_{op} profile for the South zone obtained with MPC using respectively the `nx4-ini` and `nx4-DS4` models with T_{ws} , T_{vs} , T_{amb} , \dot{Q}_{int} and \dot{Q}_{sol} as inputs. The profiles for the `nx4-ini` model illustrate how an incorrect description of the response of T_{op} to \dot{Q}_{int} and \dot{Q}_{sol} may result in an intolerably bad MPC performance. While MPC with the `nx4-DS4` model succeeds to keep T_{op} within the comfort band, `nx4-ini` results in too low temperatures. This result is explained by comparing the predicted operative temperature $T_{op, pred}$ with the actual T_{op} , depicted in Figure 5.8(c) and Figure 5.8(d). While `nx4-DS4` predicts T_{op} relatively accurately, `nx4-ini` significantly overestimates T_{op} . The MPC therefore asks to start cooling at full capacity for the next hours. As a consequence the actual T_{op} drops significantly. The next time the MPC is called, the optimization determines to first reheat the building, before starting cooling again. As expected from the validation results listed in Table 5.4 and Table 5.5, also the models which do *not* include \dot{Q}_{int} and \dot{Q}_{sol} as inputs (`nx2-DS1` and `nx4-DS1`), yield unsatisfactory control performance. With these models, T_{op} is underestimated. As a consequence, the MPC proposes to start heating when not required - or does not start cooling when required - which results in a high thermal discomfort cost. In summary, models which do not well describe the response of T_{op} to \dot{Q}_{int} and \dot{Q}_{sol} , are not suited for implementation in MPC, *at least not in this way*. In what follows, the impact of adding an adaptive correction term ΔT_z to the model equations, as indicated by respectively Eq. (5.29) and Eq. (5.30), is investigated.

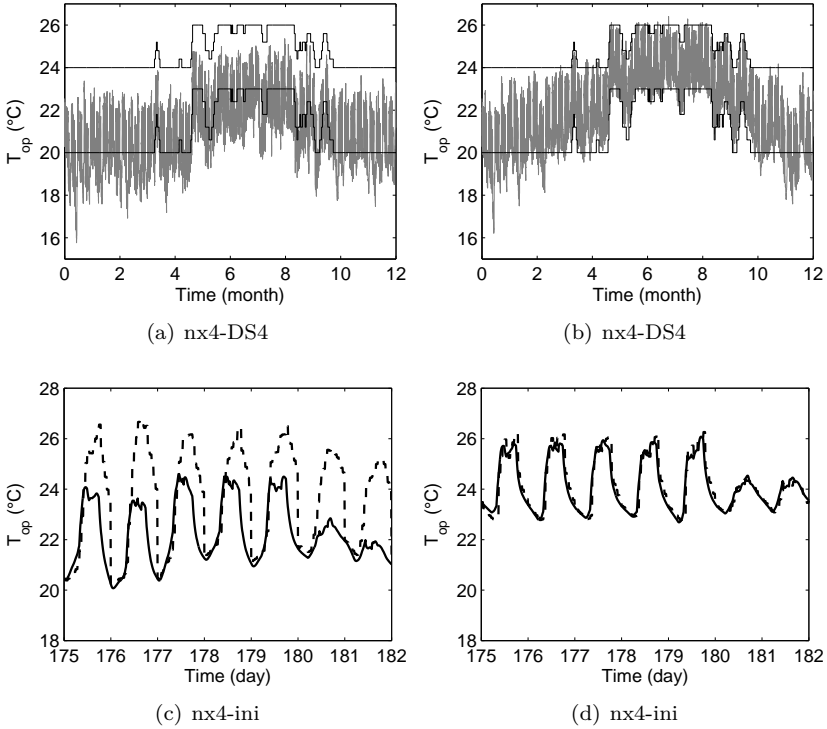


Figure 5.8: (a),(b) Annual T_{op} -profile obtained with MPC incorporating respectively model `nx4-DS4` and model `nx4-DS4`. (c),(d) Comparison of the actual T_{op} (full line) and the predicted one (dashed line) for a typical summer week.

Figures 5.9(b),(c) and (d) allow a first qualitative comparison of the control performance obtained with the different implementations of ΔT_z (see Eqs.(5.30)-(5.31)). The specific annual electricity consumption P_{tot} (kWh/m²/year) for space heating and cooling, is displayed on the x -axis. The total amount of temperature exceeding (both positive and negative) hours (Kh) is displayed on the y -axis. Distinction between the model structures is made by the markers, distinction between the identification data sets is made by the colors. The maximal thermal discomfort level is indicated by the horizontal line at 200 Kh, which corresponds to a fraction of 10% of the office hours for the South and North zone together (see Section 4.4). The performance obtained with the HC/CC control is added as a reference.

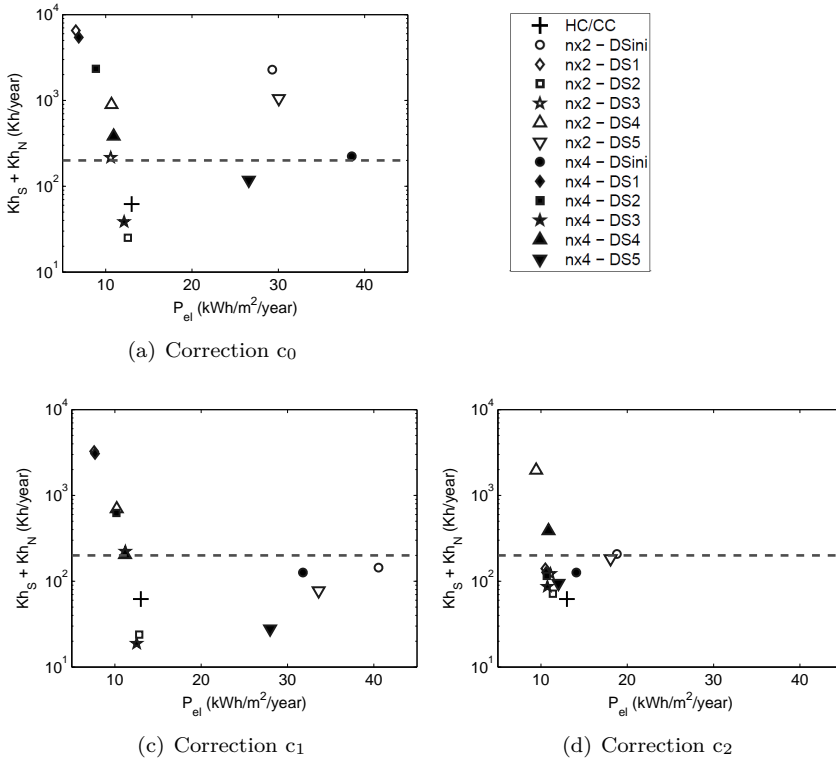


Figure 5.9: Comparison of the MPC control performance obtained with the different model structures (nx_2 (white) versus nx_4 (colored)) and identification data sets (DS1 - DS5) and this for the different choices for ΔT_z . The performance of the HC/CC- $T_{c,s}$ control strategy is indicated by the marker '+'. The thermal discomfort limit of 200 Kh for both zones together, is indicated by the dashed horizontal line.

Figure 5.9(a) shows the results if no correction term is added, i.e. $\Delta T_z = 0$. In this case, the **nx2-DS2** and **nx4-DS3** models are found to be the only ones yielding a satisfactory thermal comfort level at an acceptable cost. When no correction term is added, omitting \dot{Q}_{int} and \dot{Q}_{sol} in the **ini** and **DS1** models inevitably results in a systematic underestimation of T_{op} . This results in an overestimation of the heating loads and an underestimation of the cooling loads. As illustrated by Figure 5.10(a), T_{op} remains in winter between the thermal comfort bounds, but its mean value is about 1°C higher than required. In summer, T_{op} systematically exceeds the upper limit by more than 2°C , which results in an unacceptably high number of temperature exceeding hours.

Figure 5.9 (c) shows the MPC performance in case ΔT_z is constant over the entire prediction horizon, namely equal to the running mean temperature prediction error (see Eq.5.29). The actual and predicted T_{op} for a typical summer week are plotted in Figure 5.10(c) for the **nx2-DS1** model. Compared to the profile in Figure 5.9(a) the predicted T_{op} comes closer to the actual T_{op} , which shows less exceeding hours in this summer week. Comparison of Figure 5.9(c) with Figure 5.9(a) shows that the correction term significantly improves the control performance. In winter, thermal comfort is achieved with reduced heat demand while in summer the number of temperature exceeding hours is reduced. However, the latter still amounts to 2000 Kh, being far above the tolerated limit of 200 Kh for the North and South zone together.

For the models **nx-ini** and **nx-DS1** the prediction error is strongly correlated with \dot{Q}_{int} and \dot{Q}_{sol} ; the models **nx-ini** since they do not *adequately* describe the response of T_{op} to those inputs, and the models **nx-DS1** since they simply do not incorporate these inputs. This correlation is illustrated for the model **nx4-ini** in Figure 5.10(a) which depicts both the actual and predicted T_{op} for a typical summer week. This prediction error profile as a function of time contains valuable information which should be deployed to improve the predictions of T_{op} and thus the MPC performance. A simple and straightforward way to capture this information is to use the prediction error profile of the last 24 hours to update the vector ΔT_z (see Eqs.(5.30)-(5.31)). To avoid instability resulting from a too fast changing correction action, a low value for the learning factor β is chosen, namely 0.05 and the ΔT_z -profile is each time smoothed to remove peaks caused by random disturbances. Distinction is made between week days and weekend days. Figure 5.10(e) reveals that with this approach the **nx2-DS1** model achieves a good prediction of T_{op} . Figures 5.10(b), 5.10(d) and 5.10(e) show that the **nx4-DS4**-model, which was already good at the start, benefits slightly from method c_1 , while no further improvement is realized with method c_2 .

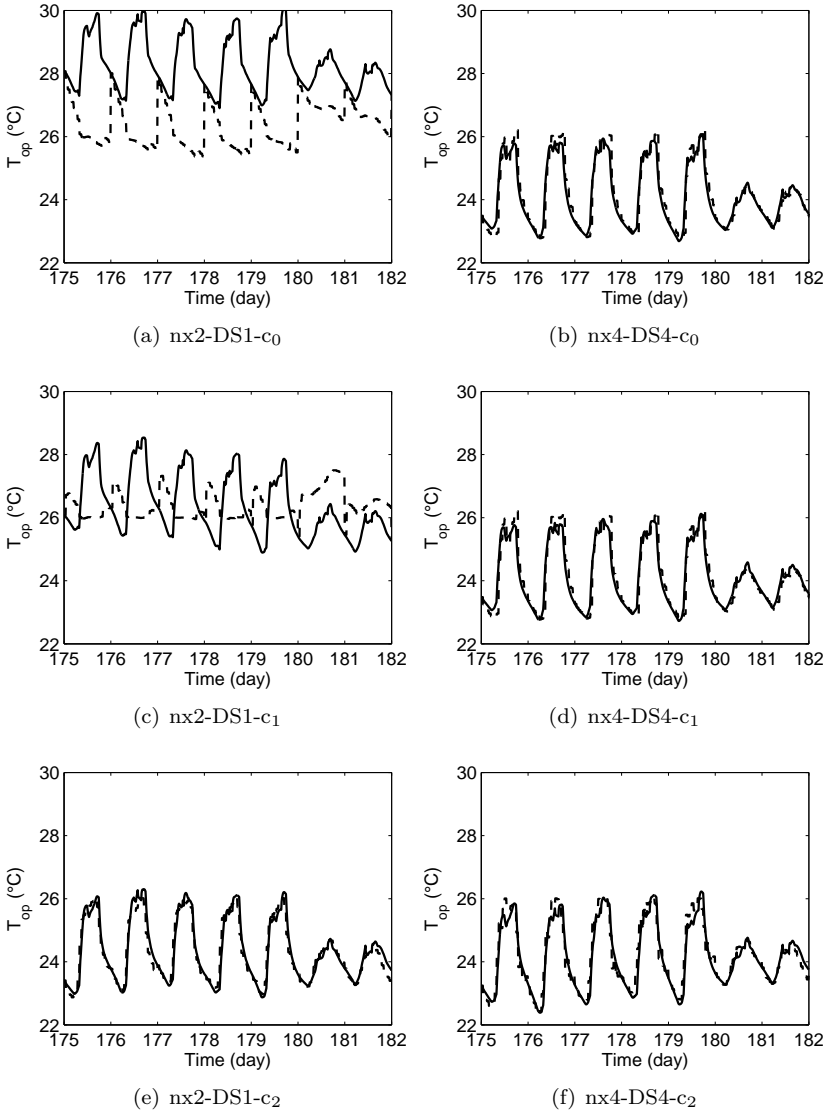


Figure 5.10: Comparison of actual T_{op} (full line) and predicted T_{op} (dashed line) for models $nx2-DS1$ (left) and $nx4-DS4$ (right) with correction c_0 (top), c_1 (middle) and c_2 (bottom).

Table 5.6: RMSE ($^{\circ}\text{C}$) on the prediction of the operative temperature of the South zone $T_{op,S}$ as a function of the model order (nx2 and nx4), the identification data set (DS1-DS5) and the error correction method (c_0 , c_1 , c_2). De initial models (ini) are added as a reference.

	RMSE ($^{\circ}\text{C}$)						
	c_0	c_1	c_2	c_0	c_1	c_2	
nx2- <i>ini</i>	2.8	1.8	1.1	nx4- <i>ini</i>	1.9	1.5	0.6
nx2-DS1	2.2	1.6	0.4	nx4-DS1	2.0	1.6	0.4
nx2-DS2	1.1	1.1	0.4	nx4-DS2	1.3	1.1	0.4
nx2-DS3	1.2	1.2	0.5	nx4-DS3	1.1	1.1	0.4
nx2-DS4	1.7	1.5	1.3	nx4-DS4	1.5	1.2	0.7
nx2-DS5	2.2	1.7	0.9	nx4-DS5	1.5	1.3	0.5

Table 5.7: Control performance (expressed as Kh_{tot} and P_{tot}) as a function of the model order (nx2 and nx4), identification data set (DS1-DS5) and error correction method (c_0 , c_1 , c_2). De initial models (*ini*) and the HC/CC-control strategies are added as a reference.

	Kh_{tot}	Kh_{tot}	Kh_{tot}	P_{tot}	P_{tot}	P_{tot}
	c_0 (Kh)	c_1 (Kh)	c_2 (Kh)	c_0 [$\frac{\text{kWh}}{\text{m}^2\text{y}}$]	c_1 [$\frac{\text{kWh}}{\text{m}^2\text{y}}$]	c_2 [$\frac{\text{kWh}}{\text{m}^2\text{y}}$]
HC/CC - $T_{c,s}$	62	62	62	13	13	13
HC/CC - T_{op}	62	62	62	14	14	14
HC/CC - $T_{op}(2)$	200	200	200	12	12	12
MPC nx2- <i>ini</i>	2281	144	208	29	41	19
MPC nx2-DS1	6679	3497	165	6	7	11
MPC nx2-DS2	25	24	88	13	13	11
MPC nx2-DS3	216	222	122	11	11	11
MPC nx2-DS4	895	697	1969	11	10	9
MPC nx2-DS5	1052	77	183	30	34	18
MPC nx4- <i>ini</i>	224	126	127	39	32	14
MPC nx4-DS1	5728	3199	139	7	8	11
MPC nx4-DS2	2339	624	115	9	10	11
MPC nx4-DS3	39	19	87	12	13	11
MPC nx4-DS4	383	204	388	11	11	11
MPC nx4-DS5	118	28	95	27	28	12

Figure 5.9 (d) indicates that, in general, introduction of the time-dependent profile for ΔT_z significantly improves the MPC performance. For the DS4-models, on the contrary, the thermal comfort level significantly deteriorates. Analysis of the ΔT_z -profile shows that this is caused by instability of the prediction correction profile, despite the low β -factor. This can be explained by the fact that for these models, which explicitly take the effect of \dot{Q}_{int} and \dot{Q}_{sol} into account, ΔT_z is less correlated to \dot{Q}_{int} and \dot{Q}_{sol} and therefore more

sensitive to other sources of model mismatch with the TRNSYS-model. This indicates that, if the model is already fairly good by itself, the simple approach adopted here to capture the information contained in the prediction error profile, is inadequate. In that case, the use of more sophisticated disturbance prediction models should be investigated. However, for the majority of the models investigated, the improvement obtained with this simple correction approach is significant.

The impact of the model structure (nx2 versus nx4), the identification data set (DS1-DS5) and the prediction correction method (c_0 , c_1 and c_2) on the prediction error of T_{op} is summarized in Table 5.6. The RMSE ($^{\circ}\text{C}$) is calculated using the model within the MPC framework over an entire year, with the MPC being called each 24h. The impact on the resulting MPC performance is summarized in Table 5.7. Comparison of the two tables shows a strong correlation between the prediction quality and the model performance.

From both Table 5.6 and Table 5.7 it is clear that the correction method c_2 drastically improves the results for most models. Correction method c_1 improves the performance less and, moreover, only for the models **nx-ini** and **nx-DS1** which not or badly describe the response of T_{op} to \dot{Q}_{sol} .

The comparison reveals that the control performances achievable with the DS1-models, which do not have \dot{Q}_{int} and \dot{Q}_{sol} as input, are comparable to the control performances of the DS2, DS3, DS4 and DS5-models which make use of perfect \dot{Q}_{int} and \dot{Q}_{sol} -predictions. This result is of huge practical relevance as it indicates that one can avoid \dot{Q}_{int} and \dot{Q}_{sol} -predictions which in practice are difficult to measure and hard to obtain. Instead, their effect can be taken into account by simply compensating for the recorded model prediction error. An additional benefit is that the MPC performance with the DS1- models using correction method c_2 does not seem to be very sensitive to the model structure. With the DS2, DS3, DS4 and DS5-models incorporating \dot{Q}_{int} and \dot{Q}_{sol} -predictions, on the contrary, the MPC performance seems to be more sensitive to both the model structure and identification data set used. In this case, a 4th order model is required and data set DS3, containing consecutive step-excitations of the five inputs, yields by far the best performance. This was already indicated by the analysis of the parameter estimation data, see Section 5.4.4. The results obtained with DS4 and DS5, which are idealized representations of four typical office days in respectively summer and winter, suggest that the winter period - characterized by smaller solar gains - is better suited for performing system identification.

Finally, comparison with the well-tuned HC/CC reference controller shows that MPC has the potential to reduce the electricity consumption by over 15% for

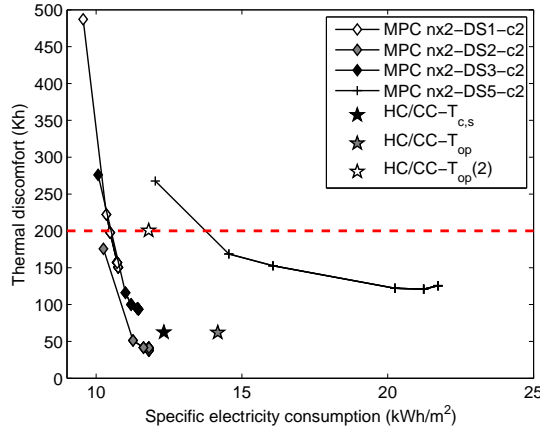


Figure 5.11: Evaluation of thermal discomfort versus electricity demand obtained with MPC (Scenario 1: perfect disturbance prediction) with controller building models nx2-DS1 , nx2-DS2 , nx2-DS3 and nx2-DS5 , all evaluated with the correction term c_2 . The results for nx2-DS4 , having unsatisfactory control performance, are not displayed. The control performance obtained for three HC/CC-control strategies are shown as a reference. The thermal discomfort limit of 200 Kh for both zones together, is indicated by the dashed horizontal line.

the same or even a fewer number of temperature exceeding hours Kh_{tot} . One of the reasons is that MPC makes use of the entire comfort temperature range while the HC/CC control is more conservative. The fact that the optimal MPC operation for the proposed cost function lies at the temperature boundaries, i.e. at the lower limit in winter and at the upper limit in summer, explains why the MPC performance is so sensitive to prediction errors on T_{op} .

The prediction correction method c_2 with the time-dependent profile for $\Delta T_z(k)$ allows to a large extent to compensate for the model mismatch introduced by the neglect of the inputs \dot{Q}_{int} and \dot{Q}_{sol} in the controller models obtained with DS1. The question arises to which extent this correction method allows to avoid the need for an accurate prediction of \dot{Q}_{int} and \dot{Q}_{sol} . The answer can be derived from Figure 5.12. Figure 5.12(a) shows the trade-off curve between Kh_{tot} and P_{tot} obtained with respectively the nx2-DS2 model (with all inputs perfectly predicted) and the nx2-DS1 model (which only accounts for the inputs T_{ws} , T_{vs} and T_{amb}). For a thermal discomfort level corresponding to approximately 150 Kh (for the two zones together), the difference in total annual electricity consumption is only 3%. Considering the difference in complexity, this is only

a small energy cost increase. The problem with the nx2-DS1 model, however, is that this 150 Kh is quasi the lowest thermal discomfort level that can be achieved. Increasing the weight of the thermal discomfort cost J_d in the cost function, does not result in a lower number of temperature exceeding hours. The trade-off curves displayed in Figure 5.12(b) and Figure 5.12(c) suggest that the problem lies in an underestimation of the cooling loads. This holds for all models that are not able to incorporate the predictions of \dot{Q}_{int} and \dot{Q}_{sol} . However, the question arises whether this problem originates from the neglect of \dot{Q}_{int} and \dot{Q}_{sol} as inputs, or whether it rather originates from the fact that the correction term ΔT_z is based on *past data* instead of *exact future predictions*.

The results of this first case, with perfect disturbance predictions, show that the MPC performance is extremely sensitive to the controller building model. If the model mismatch is too large, the MPC performs worse than a standard HC/CC control (see Figure 5.9). Without model mismatch correction term (ΔT_z correction c_0), MPC fails in 75% of the cases. Fortunately, model mismatch compensation can significantly improve the MPC performance. Updating the zone temperature prediction of the next 48 h with the recorded prediction error of the last week day or weekend day (ΔT_z correction c_2) is shown to work extremely well. MPC then outperforms the standard HC/CC control strategy in 75% of the cases. For a comparable thermal comfort level, the energy cost savings amount to almost 20%. With ΔT_z correction c_2 , the difference between a 2nd and a 4th order model is almost negligible. This is an important observation as one would expect the 4th order model to be more accurate, especially under the investigated assumption of perfect disturbance prediction. Contrary to the model structure, the identification data set used for PE, however, remains an important factor. An inadequate identification data set, such as DS4, results in a bad control performance even in case of prediction error correction. To conclude, using very simple 2nd order building models in an MPC framework, with a correction term compensating for model mismatch, allows savings up to 20% compared to conventional HC/CC control. In the next paragraph, the energy savings potential is investigated in case the assumption of perfect disturbance prediction is relaxed.

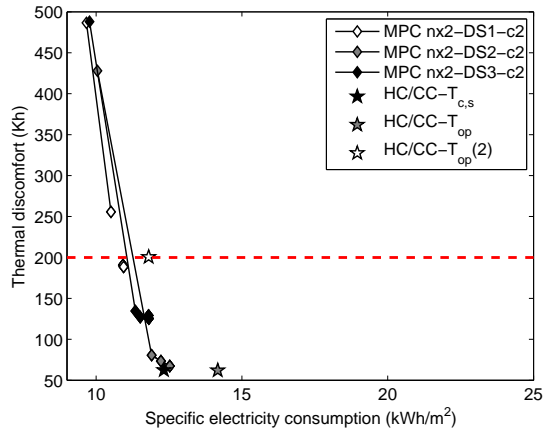


Figure 5.12: Evaluation of thermal discomfort versus electricity demand obtained with MPC (Scenario 2: persistent disturbance prediction) with controller building models $nx2-DS1$, $nx2-DS2$ and $nx2-DS3$, all evaluated with the correction term c_2 . The results for $nx2-DS4$ and $nx2-DS5$, having unsatisfactory control performance, are not displayed. The control performance obtained for three HC/CC-control strategies are shown as a reference. The thermal discomfort limit of 200 K/h for both zones together, is indicated by the dashed horizontal line.

5.5.2 Scenario 2: Imperfect disturbance predictions

Various studies suggest that a simple weather forecast, based on the past day, yields satisfactory control performance [see e.g., 101, 186]. In this section, we evaluate how this so-called '*persistent prediction*' compares to the case with perfect disturbance prediction. This allows to quantify the impact of the disturbance prediction quality on the MPC performance. The results also allow to analyze whether the conclusions with respect to the controller building model, formulated under the assumption of perfect disturbance prediction, still hold in this more realistic scenario. A more detailed model may be more sensitive to prediction errors than a simple model.

Figure 5.13 compares the control performance obtained by the persistent disturbance prediction ('Scenario 2') with the perfect prediction case ('Scenario 1'). The trade-off curves are evaluated with the controller building model $nx2-DS2$ and prediction correction method c_2 . For this model, which is among the best performing for Scenario 1, the annual specific electricity consumption P_{el} increases with $0.8 \text{ kWh/m}^2 \text{ year}$, which is a relative increase of 7%. The

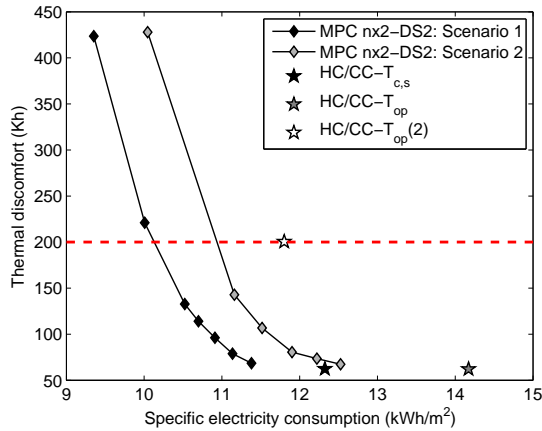


Figure 5.13: Comparison of the control performance in the J_e - J_d -plane in the case of perfect disturbance prediction ('Scenario 1') and in case of persistent prediction ('Scenario 2') with controller building model nx2-DS2 and correction method c_2 . The control performance obtained for three HC/CC-control strategies are shown as a reference. The thermal discomfort limit of 200 Kh for both zones together, is indicated by the dashed horizontal line.

electricity consumption reduction which as achieved by MPC compared to a standard HC/CC-strategy ('HC/CC T_{op} ' and 'HC/CC $T_{op}(2)$ ') is thereby decreased from respectively 25% and 16% to 13% and 7%. Moreover, the annual specific electricity consumption obtained with the best HC/CC-strategy ('HC/CC $T_{c,s}$ '), based on feedback of the concrete core surface temperature $T_{c,s}$, is 1.6% less than with MPC Scenario 2 for the same thermal comfort level. It should thus be concluded that *good predictions are crucial to obtain high MPC performance*.

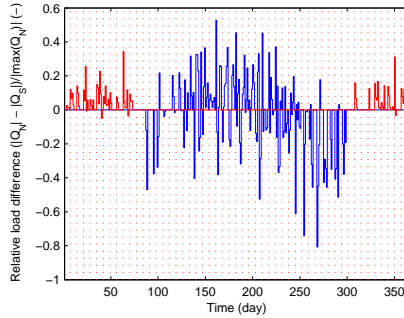


Figure 5.14: Relative difference in heating demand (red) and cooling demand (blue) between the North zone and South zone in case of zone-level MPC. The results are obtained with the controller building model `nx2-DS2` with correction term c_2 . The South zone has automated solar shading.

5.5.3 Scenario 3: Zone-level versus lumped-building-level control

In the above described cases, $T_{ws,S}$ and $T_{ws,N}$ have been optimized individually. Such a zone-level control strategy requires measurement feedback from both zones, as well as three-way mixing valves to enable a different supply water temperature setpoint to each zone. If one of these conditions is not satisfied, the above implemented zone-level control strategy is not realizable and only one setpoint temperature - equal for both zones - can be defined:

$$T_{ws} = T_{ws,N} = T_{ws,S} \quad (5.32)$$

For this so-called lumped-building-level control scenario, the following questions are addressed:

- Which temperatures should be monitored (and fed back to the MPC) such that satisfactory thermal comfort is achieved in both zones?
- What is the performance loss of a lumped-building-level control compared to a zone-level control?

To satisfy thermal comfort in both zones using only one zone as reference, it is logical to select the most demanding zone as reference, i.e., for heating the zone with the largest heating loads, for cooling the zone with the largest cooling

loads. The relative difference between the heating, respectively cooling demand for the North and South zone is plotted in Figure 5.14. In general, the difference in heating load is less than 10% and the difference in cooling load less than 30%. The heating load is larger for the North zone than for the South zone. With respect to the cooling load, three periods are distinguished. In early spring and autumn the South zone requires more cooling than the North zone, while in summer the South zone requires less cooling. The latter is thanks to the solar shading being activated once \dot{Q}_{sol} exceeds 250 W/m^2 and until it drops below 150 W/m^2 (see description solar shading control Section 4.2.1). As a result, the North zone is in general more demanding, both for heating and cooling. Three implementations of the lumped-building-level MPC are evaluated:

- MPC_N: optimization based on $T_{op,N}$ and $T_{c,N}$
- MPC_S: optimization based on $T_{op,S}$ and $T_{c,s}$
- MPC_{SN}: optimization based on $\frac{T_{c,N}+T_{c,s}}{2}$ and $\frac{T_{op,N}+T_{op,S}}{2}$.

Table 5.8: Control performance with zone-level MPC (MPC_{ref}) versus lumped-building-level MPC (MPC_N, MPC_S and MPC_{SN}). Thermal discomfort is expressed in terms of annual number of temperature exceeding hours Kh for the South and North zone separately. Energy cost is expressed in terms of specific annual electricity consumption, P_{el} , evaluated for both zones together.

	South zone			North zone			Total	P_{el} (kWh/m ²)
	Kh_u (Kh)	Kh_o (Kh)	Kh_{tot} (Kh)	Kh_u (Kh)	Kh_o (Kh)	Kh_{tot} (Kh)		
MPC _{ref}	19	13	32	21	7	28	11.0	
MPC _N	12	54	66	22	2	24	11.5	
MPC _S	39	9	48	101	12	113	11.7	
MPC _{SN}	11	507	518	30	413	443	9.3	

The results of MPC_N, MPC_S and MPC_{SN} are tabulated in Table 5.8. The zone-level MPC, MPC_{ref}, is added as reference. All values are obtained with the controller building model **nx2-DS2**, the correction method c_2 and the same values for the weighting factors α_d and α_e for the thermal discomfort cost and the energy cost in the cost function. Thermal discomfort is evaluated for the North and South zone separately, with distinction being made between the number of temperature exceeding hours under $T_{comf,min}$ (Kh_u) and temperature exceeding hours above $T_{comf,max}$ (Kh_o). The total number of temperature exceeding hours (Kh_{tot}) should remain below the imposed limit of 100 Kh/y per zone. The

corresponding specific electricity consumption P_{el} (kWh/m²), evaluated for both zones together, is shown in the last column. The results show that, as expected from the discussion above, MPC_N yields satisfactory thermal comfort for both zones. With MPC_S the upper bound of 100 Kh/y is exceeded in the North zone by 13 Kh/y. The problem arises from an underestimation of the heating loads, resulting in a large number of Kh below $T_{comf,min}$, namely $Kh_{N,tot}=101$. As this is a relatively small violation of the thermal comfort requirement, this problem might be solved by increasing the weighting of the thermal discomfort cost, as will be investigated below. The thermal discomfort cost with MPC_{SN}, respectively 518 Kh/y and 443 Kh/y for the South and the North zone, however, is significantly higher than the limit of 100 Kh/y per zone. This indicates that the zone averaged temperatures are not suited for determining the required heating and cooling demand, at least not with the given cost function which pushes the predicted T_{op} towards the upper limit $T_{comf,max}$ in summer, and towards the lower limit $T_{comf,min}$ in winter.

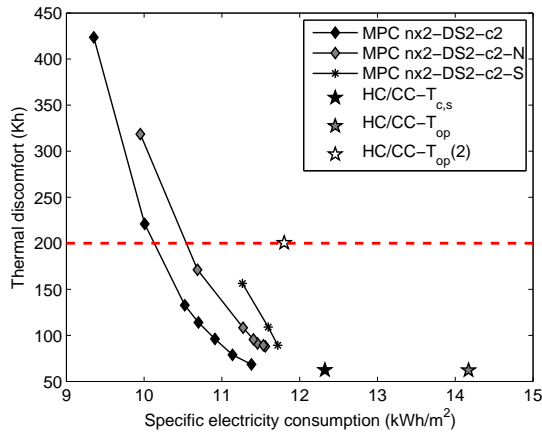


Figure 5.15: Evaluation of thermal discomfort versus annual specific electricity demand obtained with respectively zone-level MPC, lumped-building-level MPC with the North zone as reference (N) and lumped-building-level MPC with the South zone as reference (S). The depicted results are obtained with controller building model $nx2-DS2$ and the prediction correction method c_2 . The control performance of three HC/CC-control strategies are shown as a reference. The thermal discomfort limit of 200 Kh for both zones together, is indicated by the dashed horizontal line.

Figure 5.15 compares the trade-off curves for MPC_N and MPC_S with the one obtained with MPC_{ref}. The results for MPC_{SN} are not shown as the resulting

thermal discomfort levels are unacceptably high for the entire range of weighting factors. Compared to the zone-level MPC, the electricity consumption increase is less than 5% with MPC_N and about 10% with MPC_S.

5.6 Summary and conclusions

The question addressed in this chapter is: *What is the impact of the controller building model and the identification data set used for parameter estimation, on the performance of an MPC controller for office buildings with CCA in the presence of large solar and internal gains?*

For the application of MPC in residential floor heating systems, it was shown that a second order building model was able to capture the control relevant dynamics [20, 90], with the two model states representing the lumped capacity of the floor heating and the lumped capacity of the zone. The main difference between the office building considered here and the residential buildings considered by Bianchi [20] and Karlsson and Hagetoft [90], is the **presence of large internal and solar gains** and - by consequence - the need for cooling. To minimize the energy cost related to space cooling, accurate prediction of the cooling loads is needed. The model of Bianchi [20] did not include internal gains or solar gains explicitly as a model input. The impact of the solar gains was translated into an on-line identified positive term, ΔT , which was added to the ambient air temperature input. This approximation was shown to be admissible for determining the heating loads (the solar gains may not be so high during the heating season). The search for an appropriate controller building model in this chapter was motivated by the expectation that this approximation would not be allowed in the case of cooling dominated buildings.

Two **model structures** have been proposed with following 5 inputs: the supply water temperature T_{ws} , the ventilation air temperature T_{vs} , the ambient air temperature T_{amb} , the internal gains \dot{Q}_{int} and the solar gains \dot{Q}_{sol} . The first model structure is a 2nd order model with the same structure as the one proposed by Bianchi [20]. The other one is a 4th order model, with the temperature of the internal thermal mass and the temperature of the outer wall as additional states. The motivation for these extra states was to distinguish between the inertia of the zone air, which is relatively small, and the inertia of the internal thermal mass and the building envelope, which are relatively large. This way, the 4th order model is able to capture the fast fluctuations of the operative temperature as a response to the internal and solar gains.

While the 2nd order model identified by Bianchi [20] describes the response of the zone temperature to 2 inputs, namely the heat pump thermal power and the ambient air temperature, the 2nd order model here, is intended to describe the response to the 5 inputs mentioned above, and this with the same number of parameters. The 4th order model has more degrees of freedom to describe the response of the operative temperature to these 5 inputs. On the other hand: determining a larger number of parameters also requires a richer

identification data set. A pertinent question for both the 2nd and the 4th order model is therefore to define the **identification data set** which enables to adequately determine the model parameter values. 5 identification data sets were evaluated, each with a measurement time step of 1 h and a measurement length of 100 h (measurements were mimicked by simulation data). The first 3 data sets comprise step excitations of the different inputs: data set 1 only contains step excitations of the temperatures, while data set 2 and 3 also contain step excitations of the internal and/or solar gains. Data sets 4 and 5 represent a typical working week in respectively the summer and the winter season. For each identification data set, the model parameters of the 2nd and 4th order model were estimated, yielding a total of 10 building models.

A first **evaluation** of the model accuracy was performed **off-line**. For all 10 models, the T_{op} -prediction error for the 5 data sets was quantified. The results reveal a *significant impact of the identification data*: first, only the models identified with a data set including internal and/or solar gains in the excitation signal (i.e. DS2, DS3, DS4 and DS5) are able to reasonably well predict the operative temperature for a typical office working week (i.e. with an RMSE below 2°C). Second, the operative temperature T_{op} prediction accuracy varies strongly between those data sets: the models obtained with DS3, with a step excitation signal on the 5 inputs, clearly outperform the models obtained with DS4 and DS5. This indicates that the model quality obtained with on-line identification, i.e. based on measurement data of a typical working week, may be unsatisfactory, at least with the proposed system identification strategy. The validation results also revealed that the *impact of the model structure* is strongly dependent on the identification data set used: for the data set with no solar gains or internal gains (i.e., DS1), there was hardly any difference between the 2nd and the 4th order model. With DS5, corresponding to a typical working week in winter, the quality of the 4th order model even deteriorated compared to the 2nd order one. Only with the information-rich data sets (DS3 and DS4), the prediction quality is improved with increased model order. These results indicate that for on-line identification, where the quality of the identification data set may not be as high as in the considered cases, it is recommended to start with a very simple model. The model complexity may gradually be increased if more data, i.e. from longer measurement periods, are available. The question is, however, whether a more complex model is überhaupt needed, especially if the model is incorporated in an MPC framework.

The second **evaluation** of the models was performed within the **MPC framework**. The impact of the building model on the control performance, i.e. the obtained thermal comfort level and the associated energy cost, was assessed. The evaluation was performed by a one-year simulation in TRNSYS with the detailed office building model as emulator. The identified building models

were used by the MPC to calculate the optimal supply water temperature to both zones. The MPC was called only once a day, with a prediction horizon of 48 h and a control time step of 1 h. Three cases were evaluated. In the first case the MPC had perfect knowledge of the future disturbances. Despite this assumption, however, the MPC outperformed the reference heating curve/cooling curve control strategy for only 2 out of the 12 models (including the initial models), respectively *nx2-DS2* and *nx4-DS3*. This unsatisfactory result can be explained by the combination of 2 factors: first, the fact that most models do not accurately predict the operative temperature in the presence of internal gains and solar gains and, second, the fact that the control performance is very sensitive to prediction errors. The latter is due to choice of the thermal discomfort cost representation in the MPC formulation. Thermal discomfort is represented by soft constraints on the operative temperature: thermal discomfort is considered zero within the thermal comfort band defined by the ISO7730 standard [85] and increases quadratically when the temperature exceeds these bounds. The optimization will thus push the operative temperature towards the upper temperature limit to minimize the cooling demand, and towards the lower temperature limit to minimize the heating demand. A small prediction error can then cause the actual temperature to lie outside the thermal comfort band, resulting in the observed large annual thermal discomfort cost. One could therefore opt to redefine the thermal discomfort cost, e.g. by penalizing the deviation from a reference operative temperature lying in the middle of the thermal comfort range. This conservative approach would however be suboptimal as it would require higher heating and cooling demand compared to operating at the temperature limits. The only way to achieve a superior control performance with MPC compared to a well-tuned reference control strategy, is thus to have an accurate prediction of the operative temperature. At first instance only 2 out of the 12 identified models, as indicated above, seem to be able to meet this requirement. By means of a relatively simple correction method, however, the prediction quality - and by consequence the MPC performance - of most models was shown to be significantly improved. The method consists of *exploiting the information contained in the prediction error profile to improve the future predictions*. This was accomplished by adding an error-compensation term ΔT_z to the building model equations. As known a priori from physical insight and as confirmed by the results, the prediction error is namely correlated with the internal and solar gains. A time dependent error correction term, based on the prediction error-profile of the past week day/weekend day (and thus capturing the time-dependency of the internal and solar gains) was found to significantly improve the control performance: the MPC performance was superior to well-tuned heating curve/cooling curve-based strategies for 9 out of the 12 models. An important observation was that also the models *without the internal gains and solar gains as inputs*, were able to yield satisfactory

control performance thanks to this on-line error correction method. In other words, the impact of the internal and solar gains can be indirectly captured by considering their impact on the operative temperature. For the implementation of MPC in practice, this is an interesting result since tracking the prediction error on the operative temperature is far easier than predicting the internal and solar gains to each zone. However, 3 out of the 12 models do not perform well despite this error-compensation method, namely $nx2$ -DS4, $nx2$ -DS5 and $nx4$ -DS4. These are the models which explicitly include the internal and solar gains as inputs, but not accurately. For these models the MPC performance is unsatisfactory - with or without prediction error compensation. By contrast, the models which (a) *accurately* describe the response of the operative temperature to the internal and solar gains, or (b) do *not* include the internal and solar gains as inputs at all, clearly benefit from this online prediction correction. This is an important result for practice: Since obtaining a model with (a) an accurate response to the internal and solar gains is more difficult than (b) obtaining a model which only captures the response to the inputs T_{ws} , T_{vs} and T_{amb} , option (b) seems the most robust choice. An additional advantage of this option, as mentioned before, is that predictions of the internal gains and solar gains are avoided. The results therefore indicate that following findings formulated by Bianchi [20] for the residential buildings with floor heating, also hold for cooling dominated buildings with CCA: first, a 2nd order model is able to capture the control relevant dynamics and (2) solar gains (and in this case also the internal gains) do not need to be explicitly included as input. Contrary to the approach suggested by Bianchi [20], however, the impact of the gains should be translated into a time-dependent correction term on the operative temperature, not as a constant term for the entire prediction horizon. A promising subject for further research, considering the large benefits gained by the relatively simple model correction methods applied, may be the identification of dynamic models for the prediction error. Future research is also needed to define the optimal excitation profiles for the controllable inputs T_{ws} and T_{vs} for a building in operation, for instance by means of Design of Experiments [5].

The model impact on the MPC performance was also investigated for the case without perfect disturbance prediction. Instead, a **persistent disturbance prediction** was applied, based on the disturbances of the last 24 hours (for T_{amb} and \dot{Q}_{sol}) and of the last week day/weekend day (for \dot{Q}_{int}). As expected, the MPC performance of the models without the internal gains and solar gains as inputs, are less affected than the other models.

A last question addressed in this chapter, was the performance of zone level control versus **lumped-building level control**. Zone level control with MPC has not yet received much attention, with most studies focusing on single zone level control [e.g. 67] or lumped-building level control [e.g. 20, 101]. For

buildings with an outspoken difference in internal and/or solar gains, treating the building as a single zone may be, however, suboptimal, resulting in too high thermal discomfort levels, or, with a conservative control strategy based on the 'worst-case-zone', high energy costs. The impact of lumped-building level control versus zone level control for the studied office building was found to be an increase in energy cost of about 5%. For buildings without automated solar shading, this figure would of course be higher due to a more outspoken difference in the heating and cooling loads. It should be noted that the gap between the performance of a zone level MPC versus a lumped-building level MPC can be decreased by adding low-level rule-based controllers, as investigated by Bax and Krishnasing [13], which is here left for further research.

5.7 Chapter highlights

- Very simple, 2nd order models are found to yield satisfactory control performance when incorporated in an MPC framework for the control of office buildings with CCA in the presence of large solar and internal gains. More detailed 4th order models do not necessarily yield better control performance.
- The identification data (ID) set used for parameter estimation (PE) has a crucial impact on the model accuracy. The best models are obtained with step excitations of the 5 model inputs (T_{ws} , T_{vs} , T_{amb} , \dot{Q}_{int} and \dot{Q}_{sol}).
- Within an MPC framework the impact of model mismatch (and thus of the ID set used for PE) is significantly reduced through feedback of the actual measured $T_{op}(t)$ to the MPC.
- In the case of perfect disturbance prediction, MPC realizes a primary energy consumption reduction of 15% to 25% (compared to respectively an advanced HC/CC-control strategy based on feedback of the concrete core surface temperature $T_{c,s}$) and a conventional HC/CC-control strategy based on feedback of T_{op}) while at the same time thermal comfort is improved.
- In the case of persistent-disturbance prediction, the realized primary energy consumption reduction ranges from 7% to 13%, revealing the important impact of accurate disturbance predictions.
- The performance loss of a lumped-building-level optimization versus a zone-level-optimization amounts to 5% (in the case of solar shading on the south facing windows).

Chapter 6

Heat pump level control

6.1 Introduction

The aim of the study presented in this chapter is to assess the impact of the controller heat pump model in optimal control problem (OCP) formulation. More specifically, the aim is to quantify how much can be gained by explicitly integrating the temperature dependency of the coefficient of performance (COP) into the optimization (yielding a nonlinear problem), versus solving an approximated, but convex formulation.

The heat pump is a central component in a ground coupled heat pump (GCHP) system. As the heat pump dynamics are much faster than the control relevant dynamics at building level, a static representation of the heat pump characteristics can be used within the OCP formulation [58]. The COP, which determines the efficiency of the heat production, depends on both the heat source and the heat supply temperature. The smaller the temperature gap to be bridged by the heat pump, the larger the COP. The question arises whether it is important to take this temperature dependency into account when optimizing the system operation with respect to energy cost. One would assume the answer to be positive, as a control strategy yielding very high supply temperatures, for instance, is arguably an energy efficient one. However, explicitly accounting for the temperature dependency of the COP requires to solve a nonlinear optimization problem. Following the guideline 'keep the formulation as simple as possible', one should investigate whether a nonlinear formulation is necessary. Despite the existence of efficient nonlinear solvers, a convex formulation is still preferred as convergence to the global optimum is guaranteed. Also for

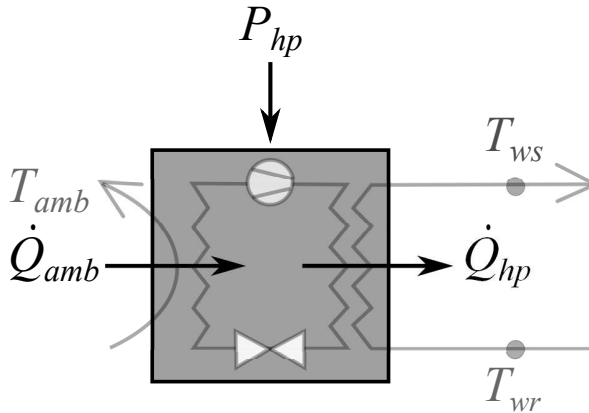


Figure 6.1: Schematic representation of an air-to-water heat pump.

practical implementation on low-level controllers with limited computational power, simplified OCP formulations are highly desirable. Therefore we need to assess how much can be gained by solving the nonlinear optimization problem, which explicitly takes the temperature dependency of the COP into account, compared to solving a convex approximation.

In this chapter the impact of the heat pump model on the resulting control performance is quantified. To exclude the impact of the long term dynamics of the ground, a modulating air-to-water heat pump is considered. The study is performed for a residential building with floor heating. The most detailed model incorporates the dependence of the heat pump performance on the source temperature, the supply temperature and the compressor frequency, while the most simple one assumes a constant COP. The performance at the heat pump level is assessed using performance maps from the heat pump manufacturer. The control performance obtained with the different controller heat pump models is compared through performance maps. These maps show the trade-off curves obtained by varying the weighting factor between the energy cost term and the thermal comfort term in the cost function. Finally, the insights obtained from this study are translated to guidelines for the OCP formulation of a GCHP.

6.2 Physical background

Figure 6.1 gives a simplified representation of the operation of an air-to-water heat pump. The compressor drives a thermodynamic cycle which extracts heat

\dot{Q}_{amb} from the ambient air at evaporator side and supplies the heat \dot{Q}_{hp} to the building at condenser side. The first law of thermodynamics yields following relation between the thermal power delivered to the building \dot{Q}_{hp} , the thermal power extracted at evaporator \dot{Q}_{amb} and the compressor power P_{hp} :

$$\dot{Q}_{hp} = \dot{Q}_{amb} + P_{hp} \quad (6.1)$$

The heat pump coefficient of performance (COP) is defined as the ratio between the delivered thermal power \dot{Q}_{hp} and the required compressor power P_{hp} :

$$COP = \frac{\dot{Q}_{hp}}{P_{hp}} \quad (6.2)$$

The second law of thermodynamics sets an upper bound for the COP, which is referred to as the COP_{Carnot} . This upper bound solely depends on the heat source temperature T_{source} (here T_{amb}) and the heat supply temperature T_{supply} (here T_{ws}), both expressed in Kelvin.

$$COP_{Carnot} = \frac{T_{supply}}{T_{supply} - T_{source}} \quad (6.3)$$

The COP of a real heat pump is lower due to the irreversibilities in the compressor, the heat exchangers and the expansion valve. The actual COP can be estimated by means of a detailed first-principles heat pump model [see e.g., 10, 87]. These models are however highly nonlinear, require a large number of state variables and are thus too complex for incorporation in an optimal control formulation. An alternative is to represent the heat pump characteristics by polynomial fits based on experimental data [see e.g., 59, 157]. This approach has been adopted here.

6.3 Optimal control problem formulation

In this paragraph the different parts of the OCP formulation proposed for optimizing the operation of a modulating air-to-water heat pump connected to a floor heating system in a residential building are presented, i.e. (i) the cost function, (ii) the building model, (iii) the building temperature constraints, (iv) the controller heat pump model and (v) the control variable or input constraints.

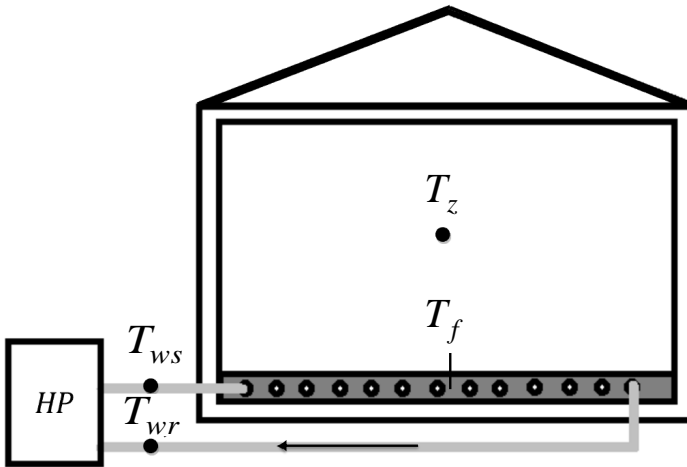


Figure 6.2: Sketch of the building with indication of the model states: the supply water temperature T_{ws} , the return water temperature T_{wr} , the floor temperature T_f and the zone temperature T_z .

6.3.1 Cost function

The aim is to optimize the heat pump operation with respect to both thermal comfort and energy cost. As those are conflicting objectives, a multi-objective approach is put forward. The cost function, represented by Eq.(6.4) is a weight sum of the energy cost J_e and the thermal discomfort cost J_d , evaluated over a time horizon $[0, t_{end}]$, which is taken as 1 day in the current study.

$$J_{tot} = (1 - K) \int_0^{t_{end}} J_e(t)dt + K \int_0^{t_{end}} J_d(t)dt \quad (6.4)$$

The relative weight of these objectives is determined by the value of the weighting factor K (-). For $K = 1$, the optimal control profile minimizes the thermal discomfort cost, regardless of the corresponding energy cost. For $K = 0$, the heat pump operation minimizes the energy cost under the given constraints. In this study, J_d (K^2), represented by Eq.(6.5), is defined as the squared difference

between the zone temperature T_z ($^{\circ}\text{C}$) and the reference zone temperature, represented by $T_{z,ref}$ ($^{\circ}\text{C}$). $T_{z,ref}$ is taken constant over the 24 hours.

$$J_d(t) = (T_z(t) - T_{z,ref})^2 \quad (6.5)$$

The energy cost J_e , represented by Eq.(6.6), is proportional to the electricity price c_{el} (e/kWh) and the heat pump compressor power P_{hp} (kW):

$$J_e(t) = c_{el}(t)P_{hp}(t) \quad (6.6)$$

This expression for J_e was also adopted by Rink et al. [149] and Gayeski [59]. However, also other expressions for J_e are found in the literature. Wimmer [186] and Bianchi [20], for instance, minimize the square of the predicted electricity cost while Ferkl et al. [48] propose a hybrid formulation with a linear term for representing the energy cost and an additional penalization of changes in the controlled variable to smoothen the control action. Contrary to the former 2 studies [59, 149] which explicitly take the T_{ws} -dependency of the COP into account, the latter 3 studies [20, 48, 186] use a predefined COP-profile in the OCP formulation. The impact of a quadratic penalization of the predicted energy cost, as expressed by Eq.(6.7), will be investigated in Section 6.4.3.

$$J_e^*(t) = (c_{el}(t)P_{hp}(t))^2 \quad (6.7)$$

6.3.2 Controller building model

The building dynamics are defined by a set of ordinary differential equations, Eqs. (6.8a)-(6.8d). They correspond to a single-zone model with four differential states as indicated in Figure 6.2: the supply temperature of the water circuit T_{ws} , the return temperature of the water circuit T_{wr} , the floor temperature T_f and the zone temperature T_z . The inputs to the model are the thermal power delivered by the heat pump, \dot{Q}_{hp} (W) and the ambient air temperature T_{amb} ($^{\circ}\text{C}$). This model is based on the controller model for MPC of a heat pump system in a residential building with floor heating, identified by Wimmer [186]. \dot{m}_w ($\frac{\text{kg}}{\text{s}}$) is the mass flow rate of the water circuit and c_w ($\frac{\text{J}}{\text{kgK}}$) the specific heat capacity of water. C_{ws} , C_{wr} , C_f and C_b ($\frac{\text{J}}{\text{K}}$) represent the thermal capacity of respectively the water at temperature T_{ws} , the water at temperature T_{wr} , the floor at temperature T_f and the building at temperature T_z . κ_{wf} , κ_{fz} and κ_b ($\frac{\text{W}}{\text{K}}$) represent the overall heat exchange coefficient between respectively T_{wr} and T_f , T_f and T_z and T_z and T_{amb} . The values for the building model

Table 6.1: Building model parameters

C_{ws}	$(\frac{J}{K})$	1.19×10^5	\dot{m}_w	$(\frac{kg}{s})$	0.266
C_{wr}	$(\frac{J}{K})$	5.36×10^6	$\kappa_{w,f}$	$(\frac{W}{K})$	1160
C_f	$(\frac{J}{K})$	4.55×10^7	$\kappa_{f,z}$	$(\frac{W}{K})$	6155
C_b	$(\frac{J}{K})$	2.25×10^8	κ_b	$(\frac{W}{K})$	260

parameters are listed in Table 6.1.

$$C_{ws}\dot{T}_{ws} = \dot{m}_w c_w (T_{wr} - T_{ws}) + \dot{Q}_{hp} \quad (6.8a)$$

$$C_{wr}\dot{T}_{wr} = \dot{m}_w c_w (T_{ws} - T_{wr}) + \kappa_{wf} (T_f - T_{wr}) \quad (6.8b)$$

$$C_f\dot{T}_f = \kappa_{wf} (T_{wr} - T_f) + \kappa_{fz} (T_z - T_f) \quad (6.8c)$$

$$C_b\dot{T}_z = \kappa_{wf} (T_f - T_z) + \kappa_b (T_{amb} - T_z) \quad (6.8d)$$

6.3.3 Initial condition and temperature constraints

Inspired by the daily cycle of the ambient air temperature, free periodic boundary conditions are imposed on the model states $\bar{T} = [T_{ws}, T_{wr}, T_f, T_z]^T$, see Eq.(6.9). t_0 (h) and t_{end} (h) are respectively 0 AM and 12 PM. The combination of these periodic boundary conditions with an ambient air temperature profile with a period of one day (24h), depicted in Figure 6.5, eliminates boundary effects which would otherwise dominate the solution.

$$\bar{T}(t_0) = \bar{T}(t_{end}) \quad (6.9)$$

Eq.(6.10) sets lower and upper bounds on the building temperatures. The lower bound \bar{T}_{min} and the upper bound \bar{T}_{max} are chosen as $[10, 10, 15, 18]^T$ °C and $[65, 50, 30, 22]^T$ °C respectively.

$$\bar{T}_{min} \leq \bar{T}(t) \leq \bar{T}_{max} \quad (6.10)$$

6.3.4 Controller heat pump model

To evaluate the energy cost, the OCP formulation requires a heat pump model which relates the thermal power \dot{Q}_{hp} to the corresponding compressor power P_{hp} , as shown in Figure 6.3. Here, we propose four different empirical approximations

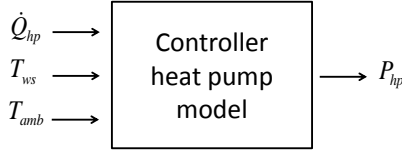


Figure 6.3: Input-output description of the controller heat pump model.

of the physical laws that govern heat pump operation, based on the heat pump manufacturer data [32]. The models are discussed with increasing level of simplification. The resulting OCP formulations are denoted as respectively OCP A, OCP B, OCP C and OCP D, with OCP A including the most detailed model and OCP D the most simplified one.

OCP A

In this first formulation the control variable is the compressor frequency f . Modulation of f in the frequency inverter alters the compressor speed and thus the compressor power P_{hp} . P_{hp} and thermal power \dot{Q}_{hp} are determined from a quadratic fit in the compressor frequency f (Hz), the ambient air temperature T_{amb} ($^{\circ}\text{C}$) and the supply water temperature T_{ws} ($^{\circ}\text{C}$), represented by respectively Eqs. (6.11a) and (6.11b).

$$P_{hp} = a_0 + a_1 T_{amb} + a_2 T_{ws} + a_3 f + a_4 T_{amb}^2 + a_5 T_{ws}^2 + a_6 f^2 + a_7 T_{amb} T_{ws} + a_8 T_{amb} f + a_9 T_{ws} f \quad (6.11a)$$

$$\dot{Q}_{hp} = b_0 + b_1 T_{amb} + b_2 T_{ws} + b_3 f + b_4 T_{amb}^2 + b_5 T_{ws}^2 + b_6 f^2 + b_7 T_{amb} T_{ws} + b_8 T_{amb} f + b_9 T_{ws} f \quad (6.11b)$$

The fits are derived from manufacturer data which include the data at part load conditions. The numerical values of the coefficients a_i and b_i are listed in Table 6.2.

OCP B

Formulation B neglects the influence of part load efficiency. Therefore, the optimized variable is the thermal power \dot{Q}_{hp} instead of the compressor frequency f . As given by Eq.(6.12), the compressor power P_{hp} is calculated as the ratio between the thermal power \dot{Q}_{hp} and the COP. The dependency of the COP on both the ambient air temperature T_{amb} and the supply water temperature T_{ws} is taken into account by a quadratic fit in these two variables, as represented by Eq.(6.13).

$$P_{hp} = \frac{\dot{Q}_{hp}}{\text{COP}(T_{amb}, T_{ws})} \quad (6.12)$$

$$\text{COP} = c_0 + c_1 T_{amb} + c_2 T_{ws} + c_3 T_{amb}^2 + c_4 T_{ws}^2 + c_5 T_{amb} T_{ws} \quad (6.13)$$

The coefficients c_i , listed in Table 6.2, are based on the catalogue data at full load [32], i.e., at the maximal frequency f_{max} . The deviation of the fit from these catalogue data, both depicted in Figure 6.4, is maximally 3%.

OCP C

Formulation C further simplifies the heat pump model. Not only the impact of the compressor frequency f on the heat pump efficiency is neglected, but also the influence of the supply water temperature T_{ws} . Only the dependency on the ambient air temperature T_{amb} is taken into account. The control variable is the thermal power \dot{Q}_{hp} . The compressor power P_{hp} is calculated according to Eq.(6.14).

$$P_{hp} = \frac{\dot{Q}_{hp}}{\text{COP}(T_{amb})} \quad (6.14)$$

The COP is found by evaluating the quadratic fit for the COP in Eq.(6.13) with a constant value for T_{ws} , namely the steady state temperature for the daily mean value of the ambient air temperature T_{amb} and the zone temperature setpoint $T_{z,set}$. This way, the COP can be defined prior to the optimization. As a consequence, J_e becomes linear and the resulting OCP convex.

OCP D

Compared to OCP C, Formulation D also neglects the dependency of the COP on the ambient air temperature T_{amb} . The COP is assumed constant for the entire horizon. As indicated by Eq.(6.15), this results in a constant ratio between

Table 6.2: Coefficients of the fits for the compressor power P_{hp} (a_i), the heat pump thermal power \dot{Q}_{hp} (b_i) representing the heat pump in OCP A, the COP (c_i) and the maximal heat pump thermal power $\dot{Q}_{hp,max}$ (d_i).

a_0	2.01	b_0	$-1.88 \cdot 10^{-1}$	c_0	8.24
a_1	$5.75 \cdot 10^{-2}$	b_1	$-4.92 \cdot 10^{-2}$	c_1	$1.58 \cdot 10^{-1}$
a_2	$-1.22 \cdot 10^{-1}$	b_2	$-1.16 \cdot 10^{-2}$	c_2	$-1.95 \cdot 10^{-1}$
a_3	$9.90 \cdot 10^{-2}$	b_3	$1.80 \cdot 10^{-2}$	c_3	$1.01 \cdot 10^{-3}$
a_4	$3.00 \cdot 10^{-3}$	b_4	$3.16 \cdot 10^{-5}$	c_4	$1.48 \cdot 10^{-3}$
a_5	$1.54 \cdot 10^{-3}$	b_5	$3.75 \cdot 10^{-4}$	c_5	$-2.33 \cdot 10^{-3}$
a_6	$-3.42 \cdot 10^{-8}$	b_6	$-2.99 \cdot 10^{-6}$	d_0	9.35
a_7	$-1.66 \cdot 10^{-3}$	b_7	$4.50 \cdot 10^{-5}$	d_1	$3.19 \cdot 10^{-1}$
a_8	$2.44 \cdot 10^{-3}$	b_8	$5.07 \cdot 10^{-4}$	d_2	$-6.13 \cdot 10^{-2}$
a_9	$-6.28 \cdot 10^{-4}$	b_9	$2.60 \cdot 10^{-4}$	d_3	$4.44 \cdot 10^{-3}$
				d_4	$2.45 \cdot 10^{-3}$

the control variable \dot{Q}_{hp} and the compressor power P_{hp} .

$$P_{hp} = \frac{\dot{Q}_{hp}}{\text{COP}_{cte}} \quad (6.15)$$

The COP is found by evaluating the expression for the COP in Eq.(6.13) with the daily mean ambient air temperature for T_{amb} and the corresponding steady state value for T_{ws} .

6.3.5 Input constraints

In OCP A, the control variable f is allowed to take any value between 0 and the maximal compressor frequency f_{max} which is equal to 100 Hz. The input constraints are represented by Eq.(6.16).

$$0 \leq f \leq f_{max} \quad (6.16)$$

In practice, however, the heat pump is switched off below a certain frequency f_{min} , as the compressor losses become too large. This discontinuity is taken into account in the simulator model, as indicated in the last row (symbol 'S') in Table 6.3 on p.122.

In OCP B, OCP C and OCP D, the control variable is the heat pump thermal power \dot{Q}_{hp} . The original constraint on the compressor frequency f is replaced by a constraint on the thermal power \dot{Q}_{hp} , given by Eq.(6.17). $\dot{Q}_{hp,max}$ is represented by an empirical fit with the catalogue data [32], see Eq.(6.18). The coefficients d_i are listed in Table 6.2. The fit is taken linear in the supply water

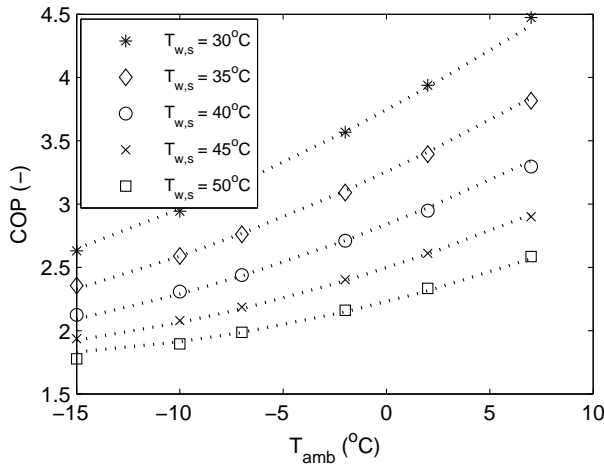


Figure 6.4: Catalogue data for the COP of a modulating air-to-water heat pump as a function of the source temperature T_{amb} and the supply temperature T_{ws} at maximum compressor frequency, indicated by the markers [32]. The quadratic fit (see Eq.(6.13)) is presented as dotted lines.

temperature T_{ws} to ensure that all constraints are linear in the optimization variables.

$$0 \leq \dot{Q}_{hp} \leq \dot{Q}_{hp,max}(T_{amb}, T_{ws}) \quad (6.17)$$

$$\dot{Q}_{hp,max} = d_0 + d_1 T_{amb} + d_2 T_{ws} + d_3 T_{amb}^2 + d_5 T_{amb} T_{ws} \quad (6.18)$$

Influence of heat pump model on OCP complexity

Simplifying the heat pump model may result in a suboptimal heat pump operation, as will be discussed in Section 6.4. On the other hand, if the approximations give rise to a convex OCP, the computational effort to solve the OCP is significantly reduced. An overview of the discussed controller heat pump models is given in Table 6.3.

- OCP A incorporates a detailed heat pump model. \dot{Q}_{hp} and P_{hp} are described by a quadratic fit in the ambient air temperature T_{amb} , the supply water temperature T_{ws} and the compressor frequency f (see Eqs. 6.11a -6.11b). T_{ws} and f are both optimization variables, respectively a state variable and a control variable. As the multiplication

of optimization variables is a nonlinear operation, OCP A is nonlinear.

- OCP B does not include the effect of the compressor frequency f on the efficiency. The COP is however still a function of the state variable T_{ws} . As a consequence, the calculation of the compressor power P_{hp} (see Eq. 6.12) requires the division of two optimization variables, namely the control variable \dot{Q}_{hp} and the state dependent COP. As this is a nonlinear operation, the resulting OCP remains nonlinear. The advantage of OCP B with respect to OCP A lies in the availability of heat pump data. OCP A requires access to part load data, which are in practice hard to obtain. OCP B, by contrast, only requires catalogue data to set up the heat pump model.
- OCP C neglects the influence of the supply water temperature T_{ws} on the COP. This way, the COP can be predicted prior to the optimization, based on the predictions of the ambient temperature only. Now, the compressor power P_{hp} in Eq.(6.14) is linear in the optimization variable \dot{Q}_{hp} . As all other constraints are linear, i.e. the equations describing the building dynamics (Eq.(6.8a) - (6.8d)), the state constraints (Eq.(6.10)) and input constraints (Eq.(6.16) or Eq.(6.17)), OCP C is convex.
- OCP D assumes a constant COP and is thus, for the same reason as mentioned for OCP C, convex.

The evaluation of the optimal profiles in the simulator, denoted by 'S' in Table 6.3, is performed based on the manufacturer performance data (look-up table).

Table 6.3: Overview of the controller heat pump models (A, B, C and D) and the heat pump simulator (S).

	Model Equation(s)	Control input constraint	Model variables			Required data	Resulting OCP
			f	T_{ws}	T_{amb}		
A	$P_{hp}(f, T_{ws}, T_{amb})$ $\dot{Q}_{hp}(f, T_{ws}, T_{amb})$	$0 \leq f \leq 100$	×	×	×	part load	nonlinear
B			-	×	×	catalogue	nonlinear
C	$P_{hp} = \frac{\dot{Q}_{hp}}{COP}$	$0 \leq \dot{Q}_{hp} \leq \dot{Q}_{hp,max}$	-	-	×	catalogue	convex
D			-	-	-	catalogue	convex
S	Lookup-table	$f \in \{0, 30 - 100\}$	×	×	×	part load	-

6.3.6 Solving the optimal control problem

The continuous optimal control problem has to be discretized for a direct numerical solver. The control variable is discretized using a piece-wise constant function, i.e. f or \dot{Q}_{hp} is constant during one discretization time step. The smaller the discretization time step, the smaller the difference between the continuous and the discretized optimal control profiles. Small discretization time steps, however, involve more control variables to be optimized over the given time horizon, which significantly increases the computation time. The formulations discussed in this paper adopt a discretization time step of 30 minutes, which is found to be sufficiently small to approximate the continuous optimal control profile. Given the time horizon of 24 hours, this yields 48 control variables to be optimized. The Automatic Control And Dynamic Optimization toolkit ACADO [80], used for this study, discretizes the OCP with the *multiple shooting* method developed by Bock and Plitt [22]. While the control variables are discretized with a fixed discretization time step, i.e., 30 minutes, the state variables are discretized with a variable time step such that the discretization error remains below a user-defined value. For this purpose, a standard *Runge-Kutta 45* integrator is used. The resulting discrete-time optimization problem is solved with a Sequential Quadratic Programming approach using an *exact Hessian* approximation [125].

6.3.7 Boundary conditions

The analysis and comparison of the different OCP formulations is made for two scenarios: first, for a constant electricity price profile (the term c_{el} is omitted in the energy cost term) and second, for the day-night electricity price tariff depicted in Figure 6.5(a). The electricity price amounts to 0.15 €/kWh during on-peak (from 7 AM to 10 PM) and to 0.09 €/kWh during off-peak. The predicted ambient air temperature profile is shown in Figure 6.5(b), which is a periodic signal representing a winter day with a mean temperature of 0 °C.

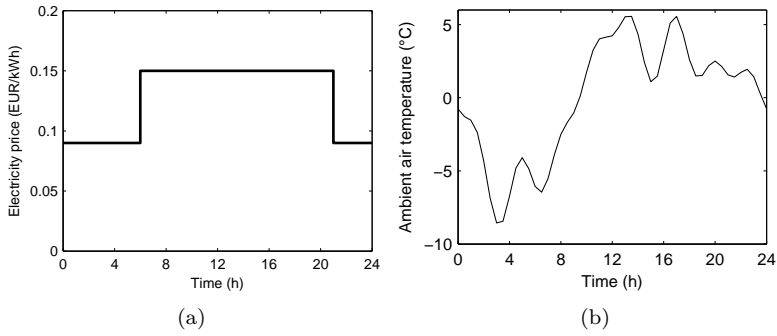


Figure 6.5: (a) Electricity price profile for the variable electricity price scenario, (b) The predicted ambient air temperature for both scenarios.

6.4 Control performance evaluation

First the optimization-based control strategies and the HC control strategy are compared for the constant electricity price scenario. Next, the comparison is performed for the day-night electricity price scenario. For both scenarios, the results reveal that the convex approximations, i.e. OCP C and OCP D, result in higher electricity consumption than OCP A, OCP B and the HC control strategy due to high fluctuations in the proposed trajectories for the heat pump thermal power. In a third part, the impact of penalizing power peaks in the cost function of OCP C and OCP D, is investigated. The results reveal that with this modified cost function, the control performance of all optimization-based control strategies are almost identical. In a fourth and last part, a sensitivity analysis of the ambient air temperature and the building model parameters is performed to check the generality of the results.

6.4.1 Case 1: Constant electricity price scenario

The performance obtained with the different OCP formulations and the HC control strategy is visualized by the trade-off curves, presented in Figure 6.6(a). The points at the left end of the curves represent the results for the OCP minimizing the energy cost term J_e , i.e., the weighting factor K in the cost function (see Eq.(6.4)) equals 0. The resulting thermal discomfort level amounts to approximately 100 K²h which corresponds, for the adopted definition of J_e and the time horizon of 24 hours, to a root mean square temperature deviation ΔT_z of about 2°C from the zone temperature setpoint of 20°C. This is close to the maximal tolerated thermal discomfort level as the lower limit on the zone temperature is set to 18°C by Eq.(6.10). The points at the right end of the curves represent the results for the OCP minimizing the thermal discomfort cost J_d , i.e., the weighting factor K is equal to 1. In this case, the setpoint zone temperature $T_{z,ref}$ is tracked as closely as possible, irrespective of the required energy cost. The graph reveals that the control performance is greatly affected by the heat pump model. As expected, OCP A yields the best performance for the entire range of thermal discomfort. OCP B performs almost as good. The difference in electricity consumption is only 1%. Surprisingly, the same performance is achieved with the HC control strategy. OCP C and OCP D, on the contrary, perform significantly worse. The electricity consumption is 1 to 7% higher for OCP D and up to 14% higher for OCP C.

To explain these results, we analyze the profiles for the compressor frequency f , the supply temperature $T_{w,s}$ and the zone temperature T_z obtained when

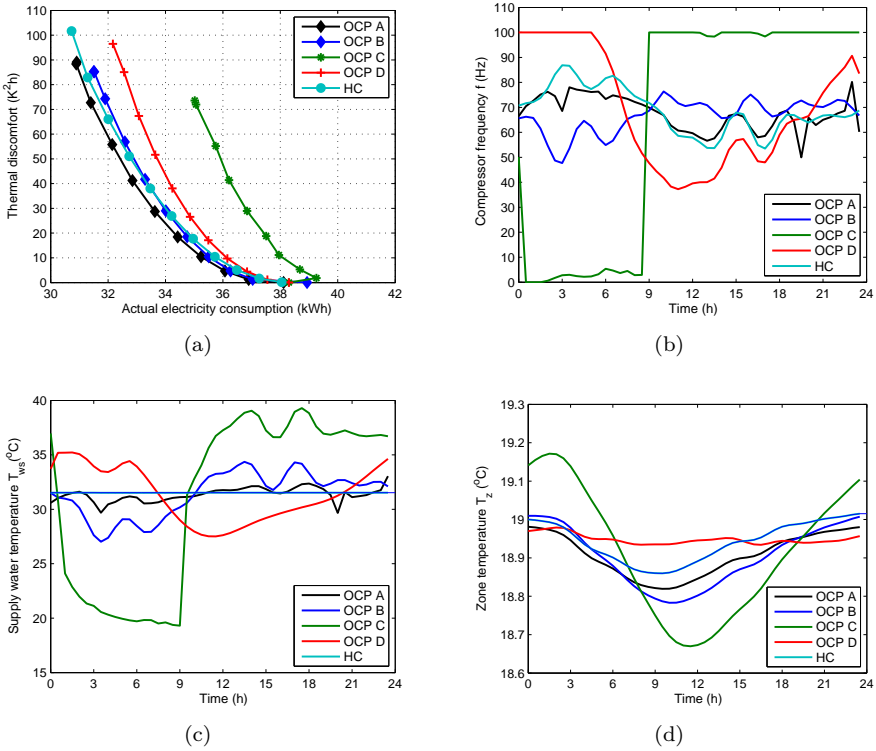


Figure 6.6: Comparison of the solutions obtained for the different optimal control problems ('OCP A', 'OCP B', 'OCP C', 'OCP D') and the heating curve control strategy ('HC') for the constant electricity price scenario: (a) Trade-off curves obtained by varying the weighting factor K in the cost function (Eq. (6.4) for OCP) or by varying the setpoint temperature for the zone (HC), (b) f -trajectories yielding a daily mean zone temperature of approximately 19 °C, (c) corresponding $T_{w,s}$ -trajectories, (d) corresponding T_z -trajectories.

applying the calculated trajectories for f (OCP A), \dot{Q}_{hp} (OCP B, OCP C and OCP D) or $T_{w,s}$ (HC) to the simulator. The depicted profiles yield a daily mean zone temperature of approximately 19 °C, as shown in Figure 6.6(d). Figure 6.6(b) depicts the compressor frequency f . It is observed that OCP A results in an almost constant trajectory for f . The variation of f in time is slightly negatively correlated to the variation of the ambient air temperature, depicted in Figure 6.5.

This means that the compressor frequency is slightly higher at low ambient air temperatures and slightly lower at high ambient air temperatures. The resulting profile for $T_{w,s}$, depicted in Figure 6.6(c), is also relatively flat and, because of the positive dependency of \dot{Q}_{hp} on T_{amb} , the variation in time is slightly positively correlated with T_{amb} .

Compared to OCP A, OCP B tends to shift the heat pump operation more towards the afternoon. This way, OCP B tries to take advantage of the higher ambient air temperature. As shown in Figure 6.6(b), this results in an f -trajectory which is positively correlated to T_{amb} . By consequence, the positive correlation of $T_{w,s}$ to T_{amb} is even more pronounced than for OCP A, as shown in Figure 6.6(c). However, this results in a higher electricity consumption than predicted by OCP B. This is explained by the fact that part load efficiency, neglected by OCP B, is a function of T_{amb} . Figure 6.7 shows that at low T_{amb} , the COP is positively correlated with the compressor frequency f . At high T_{amb} , the COP is negatively correlated with f . This reflects that the compressor is designed to operate at full capacity at colder outdoor conditions and at part load at warmer outdoor conditions. OCP B does not incorporate this knowledge. With OCP B, the calculated optimal profile for the heat pump thermal power \dot{Q}_{hp} requires a higher compressor frequency at high T_{amb} and vice versa. This explains the slightly higher actual electricity consumption with OCP B.

The use of a predicted COP-profile in OCP C results in an on-off operation, concentrating the heat production in the period with high predicted COP. This results in high values for $T_{w,s}$ during operation. The fact that high $T_{w,s}$ -values deteriorate the COP is not taken into account in OCP C. As a consequence, the actual electricity consumption is much higher than predicted. Moreover, this operation strategy yields large fluctuations in the zone temperature T_z , as can be seen in Figure 6.6(d). In the predictions made by OCP C, this higher thermal discomfort level is compensated by a lower energy cost. In reality this is not the case.

OCP D, which assumes a constant COP, has no incentive to shift the heat pump operation to the afternoon. Minimization of the multi-objective cost function results in a constant zone temperature, requiring the heat pump to operate more at night to compensate for the higher building losses. Therefore, contrary to the results obtained with OCP A, OCP B and OCP C, the $T_{w,s}$ -trajectory is negatively correlated to T_{amb} . This solution corresponds to the optimal trajectory for $T_{w,s}$ obtained for the case of a floor heating system connected to a boiler studied by Zaheer-Uddin et al. [197].

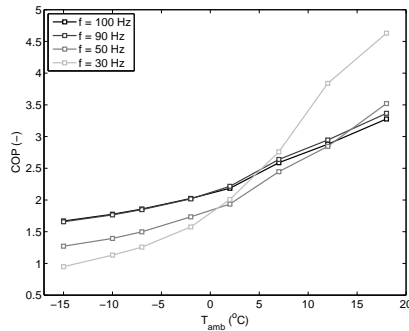


Figure 6.7: Manufacturer data for the COP as a function of the ambient air temperature T_{amb} and the compressor frequency f for a constant supply water temperature $T_{w,s}$ of 40°C [32].

The HC control strategy, finally, also requires the heat pump to operate at higher frequency during the night than during the day to track the constant setpoint for the supply water temperature, $T_{w,s}^*$. Night setback, i.e., decreasing the setpoint temperature for T_z at night, could therefore push the operation more towards the one proposed by OCP A.

Discussion The results illustrate that continuous heat pump operation at part load, as proposed by OCP A, OCP B and the HC control, yields the best control performance for the investigated case. There are two reasons why part load is beneficial for the COP. First, spreading the required heat supply over the entire day, enables low setpoints for the supply water temperature $T_{w,s}$ which is beneficial for the COP (see e.g. the catalogue data at maximal compressor frequency f_{max} , depicted in Figure 6.4). Second, at part load the temperature differences across the condenser and across the evaporator are smaller than at full load, which again positively affects the COP. Comparison of the graphs reveals that the cost function is very flat near the optimum. The f -profiles resulting from the OCP A, OCP B and the HC control differ, but the resulting energy cost is nearly the same. Large fluctuations in the heat pump power, on the contrary, as obtained with OCP C and - to less extent- with OCP D, is clearly suboptimal. This operation strategy causes high fluctuations in the supply water temperature $T_{w,s}$ which significantly affects the actual COP, as also indicated by Karlsson and Fahlén [89].

6.4.2 Case 2: Variable electricity price scenario

Figure 6.8(a) compares the trade-off curves obtained with the OCP formulations and the HC control for the variable electricity price scenario. Similar to the constant electricity price scenario, OCP A yields the best performance, closely followed by OCP B. The difference in energy cost is about 1%. The difference with the HC control strategy increases to 5%. The energy cost for both OCP C and OCP D is now approximately 16% higher.

The trajectories for the compressor frequency f , the supply water temperature $T_{w,s}$ and the zone temperature T_z , are shown in respectively Figure 6.8(b), Figure 6.8(c) and Figure 6.8(d). The depicted cases again correspond to the choice of a weighting factor K yielding a mean zone temperature of 19 °C. The different OCP formulations yield the same solution for the off-peak electricity price period. For the given ambient air temperature profile, corresponding to a cold day, the heat pump then operates at maximum frequency. During on-peak, the profiles are similar to those obtained for the constant electricity price scenario. OCP A and OCP B result in a continuous operation at part load, characterized by a smooth f -profile which is slightly negatively correlated to T_{amb} for OCP A and positively correlated to T_{amb} for OCP B. This results in a respectively constant $T_{w,s}$ -profile during on-peak for OCP A and a smooth but positively correlated profile for $T_{w,s}$ for OCP B. OCP C and OCP D again result in an on/off-operation with high $T_{w,s}$ values compared to the other OCP formulations. The HC control strategy remains the same as for the constant electricity price scenario. To make beneficial use of the off-peak electricity price, the setpoint for $T_{w,s}$ should be shifted upwards during off-peak and shifted downwards during on-peak. The insights gained from the solution obtained with OCP A, could thus be easily incorporated in the HC formulation.

Discussion For the investigated case with a day-night electricity price tariff, the energy cost with OCP A and OCP B is approximately 5% lower than with the HC control strategy. The heat pump operates at full capacity during the off-peak electricity price period. During the on-peak electricity price period the heat pump operates at part load, with an almost constant compressor frequency. Compared to the constant electricity price scenario, the supply water temperature trajectory is shifted upwards during off-peak and shifted downwards during on-peak. OCP C and OCP D result in higher electricity cost than the HC control strategy, despite the fact that they do take advantage of the off-peak electricity price. This is caused by a deterioration of the COP due to on-off heat pump operation during the on-peak price period.

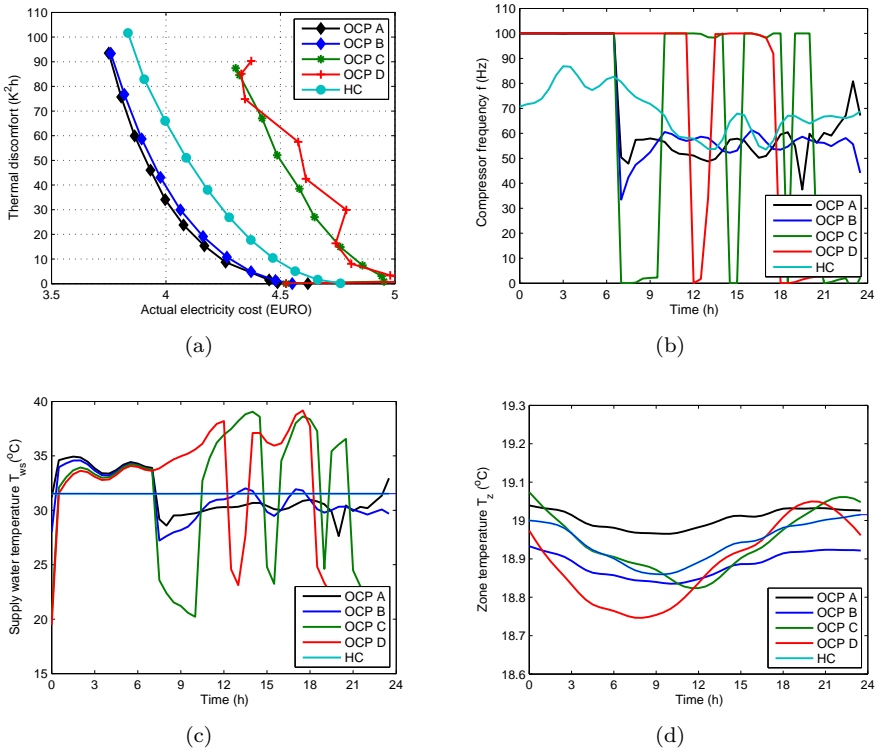


Figure 6.8: Comparison of the solutions obtained for the different optimal control problems ('OCP A', 'OCP B', 'OCP C', 'OCP D') and the heating curve control strategy ('HC') for the variable electricity price scenario: (a) Trade-off curves obtained by varying the weighting factor K in the cost function (Eq. 6.4 for OCP) or by varying the setpoint temperature for the zone (HC), (b) f -trajectories yielding a daily mean zone temperature of approximately 19 $^{\circ}C$, (c) corresponding $T_{w,s}$ -trajectories, (d) corresponding T_z -trajectories.

6.4.3 Modified cost function

The problem with OCP C and OCP D, which both neglect the dependency of the COP on the supply water temperature $T_{w,s}$, is that they tend to concentrate the heat pump operation in certain time periods. This results in high values for $T_{w,s}$ which negatively affects the actual COP. The question rises whether the control performance obtained with the OCP using these simplified heat pump models, would be improved if the square of the predicted electricity cost J_e is

minimized, as suggested by Wimmer [186] and Bianchi [20]. The cost function is then given by Eq.(6.19). The weighting factor K is again varied to obtain the trade-off curves between both objectives.

$$J_{tot} = (1 - K) \int_0^{t_{end}} J_e(t)^2 dt + K \int_0^{t_{end}} J_d(t) dt \quad (6.19)$$

The resulting control performances are depicted in Figure 6.9(a) and Figure 6.9(b) for respectively the constant and the variable electricity price scenario. For both cases, the performance improvement of OCP C and OCP D achieved by the modified cost function, denoted as respectively OCP C* and OCP D*, is significant. Now, the trade-off curves almost coincide with the ones obtained with OCP A and OCP B. Figure 6.9(c) and Figure 6.9(d) compare the f -profiles for a given K -value and Figure 6.9(e) and Figure 6.9(f) compare the corresponding $T_{w,s}$ -profiles. The graphs show that the improved control performance is indeed obtained by smoothing the operation profile. Through penalization of power peaks, OCP C*, which accounts for the T_{amb} -dependency of the COP, converges towards the solution obtained with OCP B which accounts for both the T_{amb} and $T_{w,s}$ -dependency. OCP D*, which assumes a constant COP, converges towards the HC control strategy. As previously noted, the fact that the trade-off curves coincide despite the different profiles for the compressor frequency f and supply water temperature $T_{w,s}$, indicates that the cost function is very flat near the optimum. On-off operation of the modulating heat pump should however be avoided.

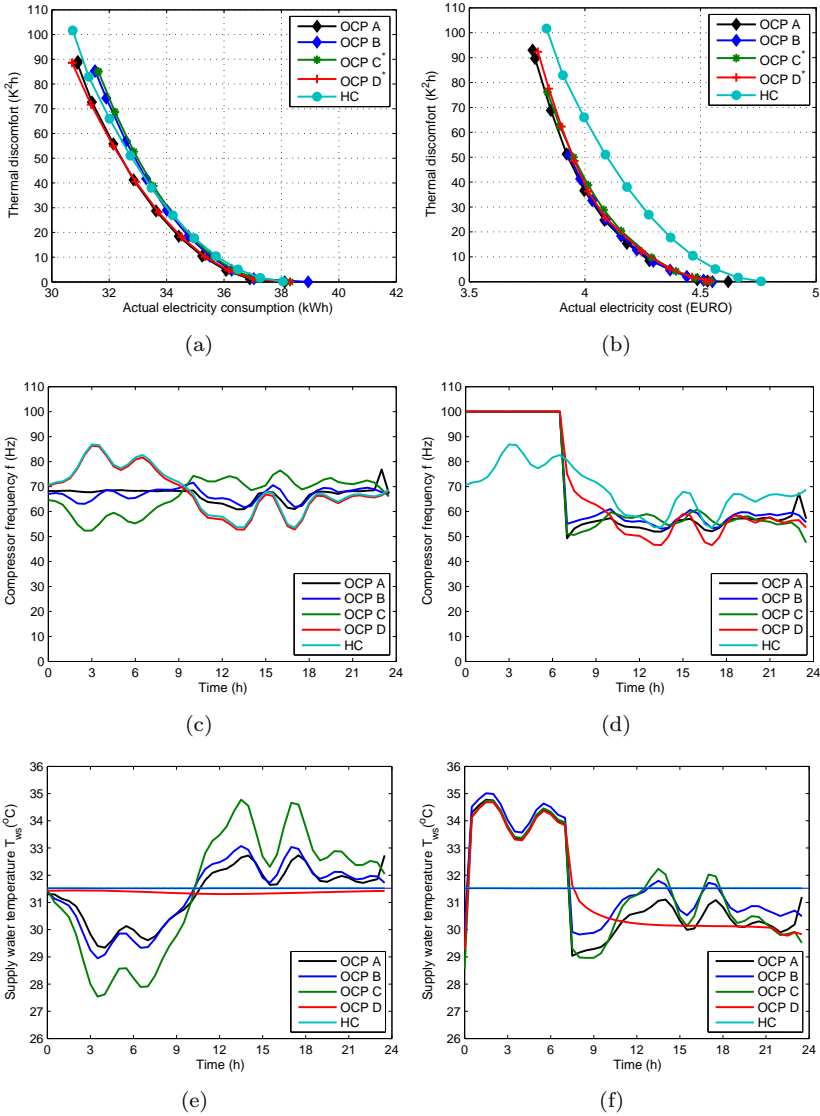


Figure 6.9: Comparison of the solutions obtained for the different optimal control problems ('OCP A', 'OCP B', 'OCP C*', 'OCP D*') and the heating curve control strategy ('HC') for the constant electricity price scenario (left) and the variable electricity price scenario (right). Superscript * refers to the OCPs with quadratic energy cost in the cost function (Eq. 6.4 for OCP A and OCP B, Eq.6.19 for OCP C* and OCP D*) or by varying the setpoint temperature for the zone (HC), (c, d) f - trajectories yielding a daily mean zone temperature of approximately 19 $^{\circ}C$, (e, f) corresponding $T_{w,s}$ - trajectories.

6.4.4 Influence of boundary conditions and building model parameters

A sensitivity analysis is performed to check the generality of the conclusions drawn. First, the mean value of the ambient air temperature profile is varied between -5°C and $+10^{\circ}\text{C}$ and its amplitude is varied between 0°C and 15°C . Second, the values for the building model parameters are varied based on a broad range for following physical parameters [20]:

- Time constant for heating the volume of water at temperature $T_{w,s}$, τ_{hp} : [180-3600] s,
- Water volume at return water temperature, $V_{w,r}$: [0.5-10.5] m^3 ,
- Overall thermal capacity of the heat emission system, C_f : [55-655] J/K,
- Overall heat transfer coefficient between heat emission system and zone, $\kappa_{f,z}$: [500-6500] W/K,
- Overall building heat loss coefficient, κ_b : [50-1600] W/K,
- Time constant of the building, τ_b : [50-650] h.

The sensitivity study shows that the results presented in this study hold for the different ambient air temperature profiles, as well as for the majority of investigated combinations of building parameter values. Only for the cases combining a high building heat loss coefficient with a low heat emission thermal capacity, corresponding to badly insulated buildings with a fast-reacting heat emission system, the conclusion does not hold. For these cases, the solutions found with the convex approximations minimizing the modified cost function (OCP C* and OCP D*), differ substantially from the solution obtained with the nonlinear OCP formulations which incorporate the more detailed heat pump models (OCP A and OCP B). However, these cases are not appropriate for installing a heat pump. Much more energy can be saved by insulating the building.

6.5 Summary and conclusions

For the investigated *modulating AWHP system*, a first comparison suggests a significant impact of the controller heat pump model on the control performance. The nonlinear OCP formulations with the T_{ws} and f -dependent models result in

continuous HP operation at part load while the convex approximations give rise to large power fluctuations. The latter result in an energy cost increase of 7% to 16%. However, by penalizing power peaks in the cost function, the control performance obtained with the convex approximations is almost identical to the one obtained with the nonlinear models. Analysis of the different control trajectories and the resulting control performance reveals that the cost function is very flat near the optimum.

In the case of a GCHP, high power rates not only result in increased supply temperatures but also in decreased source temperatures. For a *GCHP* the benefit of part load operation will therefore be even more pronounced than for an AWHP. In practice, most GCHP systems are still of the single speed type, allowing only on/off-operation. The size of the heat pump is then extremely important. Oversizing should by all means be avoided such that the heat pump has more running hours (less on/off-cycling), and a lower power (better COP).

6.6 Chapter highlights

- In the case of a constant electricity price, optimal operation of a modulating AWHP system for a residential floor heating system is characterized by a smooth and continuous heat pump operation at part load.
- In the case of a day-night electricity price tariff, the AWHP operates at full load during (a fraction of) the off-peak electricity price period, and at part load during the on-peak electricity price period.
- This result is found as the solution of a nonlinear OCP which explicitly takes the dependency of the heat pump COP on (1) the source temperature (T_{amb}), (2) the supply water temperature (T_{ws}) and (3) the compressor frequency f , into account.
- This result is also obtained with a constant COP approximation if the cost function penalizes power peaks.
- A heating curve (HC) control strategy is close to optimal for the constant electricity price scenario, while for the day-night electricity price scenario the energy cost is 5% higher.

Chapter 7

Borefield level control

7.1 Introduction

A first objective addressed in this chapter, is the development of a borefield model which can be used to optimize the operation of a HyGCHP system. The model should predict the fluid temperature response to typical borefield loads in order to assess the heat pump COP and the availability for passive cooling. To impose long term borefield thermal balance, the model should also capture the long term borefield dynamics. The aim is to investigate the minimum required model order to capture these control relevant dynamics. A second objective is to analyze the optimal HyGCHP operation for a given building heating and cooling load profile, such that the total annual energy cost is minimized while guaranteeing long term sustainable borefield operation.

Section 7.2 presents the optimal control problem (OCP) formulation which defines the borefield model requirements. Section 7.3 starts with the physical background on the heat transfer processes occurring inside and around the BHE. An overview of the existing borefield models highlights the need for a simplified borefield model which can be used in an optimization framework. Section 7.4 describes the investigated approaches to derive a low-order model for a single borehole heat exchanger (BHE). These models are validated by the Duct Storage Model (DST) implemented in TRNSYS [75, 172]. Section 7.5 illustrates their use within the proposed OCP formulation. Analysis of the optimal HyGCHP operation shows that the term 'seasonal storage' is not suited to describe the role of the borefield in the HyGCHP system. The borefield serves as a dissipater of heat and cold rather than as a storage medium.

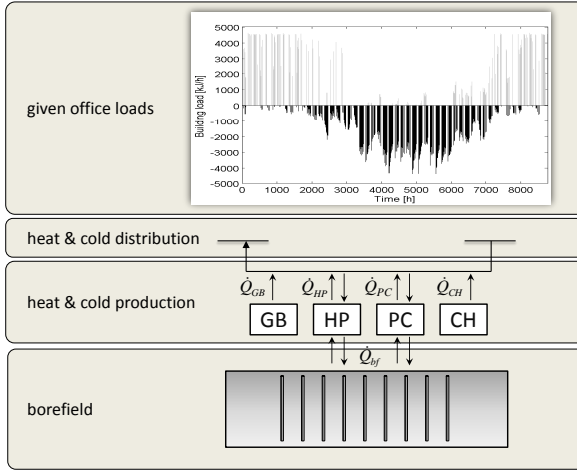


Figure 7.1: Schematic presentation of the controlled HyGCHP system comprising a ground-coupled heat pump (HP), a passive cooling (PC) heat exchanger, a gas boiler (GB) and a chiller (CH). The HP and the PC are connected to the borefield. The heat delivered to the building, i.e. $\dot{Q}_{HP} + \dot{Q}_{GB}$, must equal the given office heating load \dot{Q}_h (>0). The cold delivered, i.e. $\dot{Q}_{PC} + \dot{Q}_{CH}$, must equal the given office cooling load \dot{Q}_c (<0).

7.2 Optimal control problem formulation

This section presents an optimal control problem (OCP) formulation to optimize the use of the borefield for a given building heating demand \dot{Q}_h (W) and building cooling demand \dot{Q}_c (W). A simplified representation of the system is depicted in Figure 7.1. Heat is provided by the heat pump (HP) or by the gas boiler (GB). Cold is provided by passive cooling through the passive cooling (PC) heat exchanger or by active cooling with the chiller (CH).

Meeting the building heating and cooling demand At each time step, the building heating and cooling demand must be met, as expressed by Eqs.(7.1a)-(7.1b).

$$\dot{Q}_h = \dot{Q}_{HP} + \dot{Q}_{GB} \quad (7.1a)$$

$$\dot{Q}_c = \dot{Q}_{PC} + \dot{Q}_{CH} \quad (7.1b)$$

Minimizing corresponding annual operation cost The objective is to minimize the total annual energy cost by defining at each control time step the optimal distribution of the heating and cooling load over the GCHP system on the one hand and the backup heating and cooling system on the other hand. This requires to account for the heat and cold production efficiency of each device as expressed by Eqs.(7.2a-7.2d).

$$COP_{HP} = \frac{\dot{Q}_{HP}}{P_{HP}} \quad (7.2a)$$

$$\eta_{GB} = \frac{\dot{Q}_{GB}}{\dot{Q}_{gas}} \quad (7.2b)$$

$$COP_{PC} = \frac{\dot{Q}_{PC}}{P_{PC}} \quad (7.2c)$$

$$COP_{CH} = \frac{\dot{Q}_{CH}}{P_{CH}} \quad (7.2d)$$

P_{HP} (W) represents the electricity consumption of the HP compressor and of the circulation pumps at borefield side. \dot{Q}_{gas} (W) represents the primary gas power. P_{PC} (W) represents the electricity consumption of the circulation pumps. P_{CH} (W) represents the electricity consumption of the CH compressor and of the circulation pumps to cooling tower.

As indicated by Eqs.(7.3a)-(7.3c) COP_{HP} , COP_{PC} and COP_{CH} depend on the temperatures at source and supply side. T_{fo} ($^{\circ}\text{C}$) denotes the brine fluid outlet temperature, T_{amb} ($^{\circ}\text{C}$) the ambient temperature and T_{ws} ($^{\circ}\text{C}$) the supply water temperature.

$$COP_{HP} = f(T_{fo}, T_{ws}) \quad (7.3a)$$

$$COP_{PC} = f(T_{fo}, T_{ws}) \quad (7.3b)$$

$$COP_{CH} = f(T_{amb}, T_{ws}) \quad (7.3c)$$

Taking into account the electricity price, denoted by c_{el} ($\text{€}/\text{kWh}$), and the gas price, denoted by c_{gas} ($\text{€}/\text{kWh}$), the cost function can be expressed by Eq.(7.4).

$$\min \int_0^{1 \text{ year}} (c_{el}(P_{HP} + P_{PC} + P_{CH}) + c_{gas}\dot{Q}_{gas})dt \quad (7.4)$$

Substituting Eqs.(7.2a)-(7.2d) into Eq.(7.4), yields Eq.(7.5).

$$\min \int_0^{1 \text{ year}} \left(c_{el} \left(\frac{\dot{Q}_{HP}}{COP_{HP}} + \frac{\dot{Q}_{PC}}{COP_{PC}} + \frac{\dot{Q}_{CH}}{COP_{CH}} \right) + c_{gas} \frac{\dot{Q}_{GB}}{\eta_{GB}} \right) dt \quad (7.5)$$

Input constraints To obtain a feasible solution, the optimization must account for the limited heating or cooling capacity of each device:

$$\dot{Q}_{HP} \leq COP_{HP} P_{HP,max} \quad (7.6a)$$

$$\dot{Q}_{GB} \leq \eta_{GB} Q_{GB,max} \quad (7.6b)$$

$$\dot{Q}_{PC} \leq UA_{PC}(T_{ws} - T_{fo}) \quad (7.6c)$$

$$\dot{Q}_{CH} \leq COP_{CH} P_{CH,max} \quad (7.6d)$$

Through the dependency of COP_{HP} and COP_{CH} on the operation conditions, the maximal \dot{Q}_{HP} and \dot{Q}_{CH} are variables. The maximal \dot{Q}_{PC} is even more sensitive to the operation conditions. As indicated by Eq.(7.6c), there is no passive cooling capacity if T_{fo} approaches T_{ws} .

State constraints The critical point for freezing is at the heat pump evaporator outlet. T_{fi} should not drop below a minimum value $T_{f,min}$, as expressed by Eq.(7.7a). If an anti-freeze solution is used, the risk for frost formation moves towards the ground around the BHE, giving rise to Eq.(7.7b) as additional constraint.

$$T_{fi} \geq T_{f,min} \quad (7.7a)$$

$$T_{g,i} \geq T_{g,min} \quad (7.7b)$$

Long-term sustainable operation Finally, thermal build-up or thermal depletion of the borefield should be prevented. This implies that for the design reference year, thermal balance should be ensured. In other words, the temperature distribution around the BHE should be the same at the beginning and at the end of the year. The optimal operation profile calculated for the reference year, can then serve as reference for the entire life length of the borefield, while year-by-year variations in the heating and cooling load may allow small deviations from this reference profile. Mathematically, this condition requires the optimal solution for the reference year to be periodic. This periodicity can be directly imposed by representing the optimal control profiles as weighted sums of a set linearly independent periodic functions, with a period being an integer fraction of 8760 h or 1 year. The optimization then determines the contribution to the optimal control profile of each of these functions, i.e. the amplitude and the phase. If the temperature distribution around the boreholes can be extracted from the controller model, periodicity can also be imposed by periodic boundary conditions on all N ground temperatures $T_{g,i}$ in the

controller model, see Eq.(7.8). The ground temperature distribution in the borefield at the beginning of the year ($t = 0$) and at the end of the year ($t = 1$ year) should be identical. The latter approach is adopted in this study.

$$T_{g,i}(0) = T_{g,i}(1 \text{ year}) \quad \forall i = 1 : N \quad (7.8)$$

Controller borefield model requirements Solving the above formulated OCP therefore requires a model which predicts the variation of T_{fo} as a function of the optimization variables \dot{Q}_{HP} and \dot{Q}_{PC} . This variation depends on the net heat injected from the borefield \dot{Q}_{bf} , found by Eq.(7.9). The first term represents the heat extracted by the heat pump, the second term the heat rejected by passive cooling. The electricity consumption of the circulation pumps in PC mode, P_{prim} (W) enters the energy equation since the pumping power is eventually - through the friction losses of the circulating fluid inside the GHE - dissipated as heat. In HP operation mode, this heat is extracted by the HP and thus included in the term \dot{Q}_{HP} . In PC mode, by contrast, this heat source is superposed on \dot{Q}_{PC} . Substituting Eq.(7.3b) into Eq.(7.9) yields Eq.(7.10).

$$\dot{Q}_{bf} = (\dot{Q}_{HP} - P_{HP}) + (|\dot{Q}_{PC}| + P_{PC}) \quad (7.9)$$

$$\dot{Q}_{bf} = -\frac{COP_{HP} - 1}{COP_{HP}} \dot{Q}_{HP} + \frac{COP_{PC} + 1}{COP_{PC}} |\dot{Q}_{PC}| \quad (7.10)$$

The T_{fo} -prediction should be accurate in both the short and the long term. The former depends on the control time step, which for building climate control is usually 1 h. The latter depends on the control horizon. Guaranteeing borefield thermal balance on an annual basis corresponds to a horizon of 1 year. However, a longer time scale is required to assess the ground and brine temperature evolution in the case of borefield thermal imbalance.

7.3 Heat transfer processes in borefields

7.3.1 Introduction

A borefield consists of a number of vertical ground loop heat exchangers or *borehole heat exchangers* (BHE), connected in series and/or in parallel. A typical borefield configuration with a Tichelmann-layout is shown in Figure 7.2. Figure 7.3 zooms in on a single BHE with a single U-tube heat exchanger, embedded in a conductive filling material or grout, surrounded by ground. To describe the borefield thermal dynamics, one has to start with the description of the thermal processes occurring inside and around a single BHE, in the literature denoted by respectively the *inner problem* and the *outer problem*, both indicated in Figure 7.3. Once the response of a single BHE to a heat injection or extraction profile can be described, the thermal interference between different BHEs inside a borefield can be taken into account, as well as the heat exchange between the borefield and the so-called far field, i.e. the ground at undisturbed ground temperature $T_{g,\infty}$ ($^{\circ}\text{C}$).

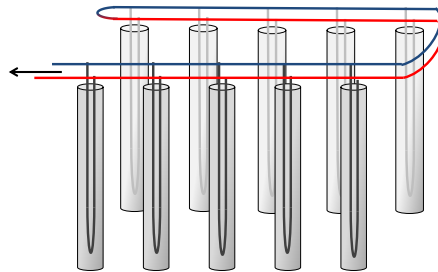


Figure 7.2: Scheme of a borefield with BHEs connected in parallel (Tichelmann-layout).

The development of models describing the thermal dynamics of borefields has started in the '70s and was motivated by the need for borefield design tools. Since the borefield represents the largest share of the GCHP system investment cost, tools were needed to determine the minimal required BHE length. Static design guidelines based on the peak heating or cooling demand enable a first rough estimation of the BHE length. However, to prevent thermal ground

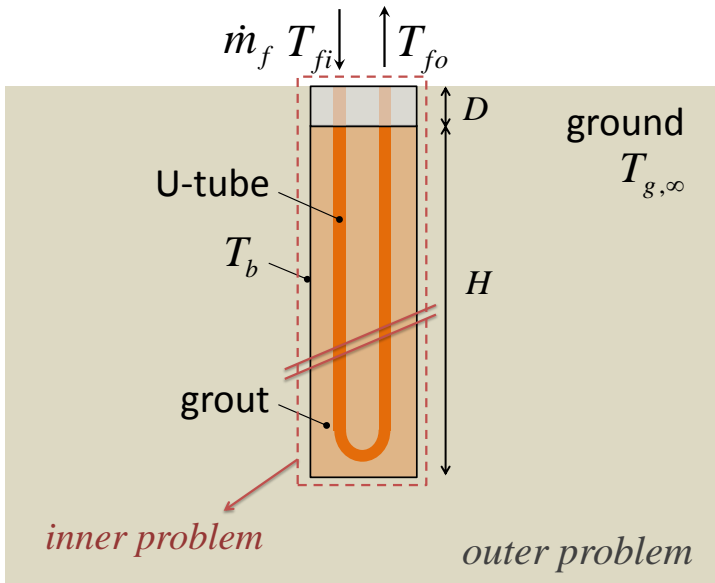


Figure 7.3: Scheme of a BHE with a single U-tube heat exchanger with indication of the length of the insulated upper part D (m), the active borehole depth H (m), the brine fluid mass flow rate \dot{m}_f (kg/s), the fluid inlet temperature $T_{f,i}$ ($^{\circ}\text{C}$), the fluid outlet temperature $T_{f,o}$ ($^{\circ}\text{C}$), the mean borehole wall temperature T_b ($^{\circ}\text{C}$) and the undisturbed ground temperature $T_{g,\text{inf}}$ ($^{\circ}\text{C}$). Two regions are distinguished: the so-called 'inner problem', comprising the heat transfer processes within the BHE, and the 'outer problem', comprising the heat transfer processes in the surrounding ground.

depletion or thermal build-up due to undersizing, or too large investment costs due to oversizing, design tools were developed which not only took the maximum heat injection or extraction rate into account, but the annual loads as well [see e.g., 17, 42, 92, 139, 166]. These loads are based on a static or dynamic building load calculation and an estimation of the heat pump COP and the COP for passive cooling. The design question is then: 'What is the required BHE length for the given load profile, the given ground thermal properties and the given brine and BHE properties?'. From an economical point of view, the answer is the length for which the borefield outlet temperature hits its maximal or minimal value at the end of the borefield life, typically taken 20 years. One therefore needs to simulate the borefield outlet temperature response to a multi-year load profile and this as a function of the ground thermal properties and the

different design parameters. The borefield model therefore needed (1) to be a first-principles model, i.e. explicitly a function of the physical parameters, and (2) to take the long term characteristics of the borefield into account, and (3) to be computationally fast as to be integrated in an iterative design process. The annual load profile was, and is still, often lumped into the monthly energy values and monthly power peak values. The hourly and sub-hourly time scale, corresponding to respectively the dynamics of the BHE grout and of the circulating fluid, the so-called *inner problem* (see indication in Figure 7.3), could in this view be neglected. Instead, the focus was on the *outer problem*, i.e. the description of the heat diffusion process around the BHE, the thermal interaction between the BHEs and the interaction of the borefield as a whole with the far field. Due to the fact that the heat diffusion process is linear - at least if we assume the ground thermal properties to be time and temperature invariant - the temperature response to a time varying heat input profile can be found by convolution of the step responses. A second benefit of the linearity of the heat diffusion process, is that the temperature field of a borefield can be described by spatial superposition of the temperature fields caused by the individual BHEs. A computationally elegant description of the borefield dynamics exploits this knowledge. The modeling then boils down to three parts: (1) modeling the step response of a single BHE, (2) applying spatial superposition to obtain the borefield temperature field, (3) applying temporal superposition to determine the response to a time-varying input signal. While computational power has drastically increased during the last 40 years, the above mentioned approach is still - in one or an other way - adopted to speed up computation time.

The first three sections aim at providing a better understanding of how to describe the heat transfer processes in borefields in general and in a single BHE in specific, based on a literature overview: Section 7.3.2 presents the governing first principle equations, Section 7.3.3 presents different approaches to model the heat transfer inside the BHE (inner problem) and Section 7.3.4 presents different approaches to model the heat transfer processes around the BHE (outer problem). The overview discusses only a few models, which are schematic presented in Figure 7.4 with the horizontal position reflecting the time scales incorporated in the model and the vertical position the model and/or system complexity. Good reviews on the existing models are published by, among others, Murugappan [120], Yavuzturk and Spitler [192], Lamarche and Beauchamp [105], Yang et al. [190] and Javed and Claesson [86]. For a comprehensive study of the fundamentals of the heat transfer processes inside and around a BHE, we refer to the work of Eskilson [43]. All encountered models are first principle (white-box) models, requiring knowledge of the ground and borefield thermal properties. Section 7.3.5 deals with characterization of the physical parameters. Section 7.3.6 deals with the validation of the models. Section 7.3.7 discusses the fitness of the models encountered in the literature,

for incorporation in an optimization framework such as the optimal control problem presented in Section 7.2.

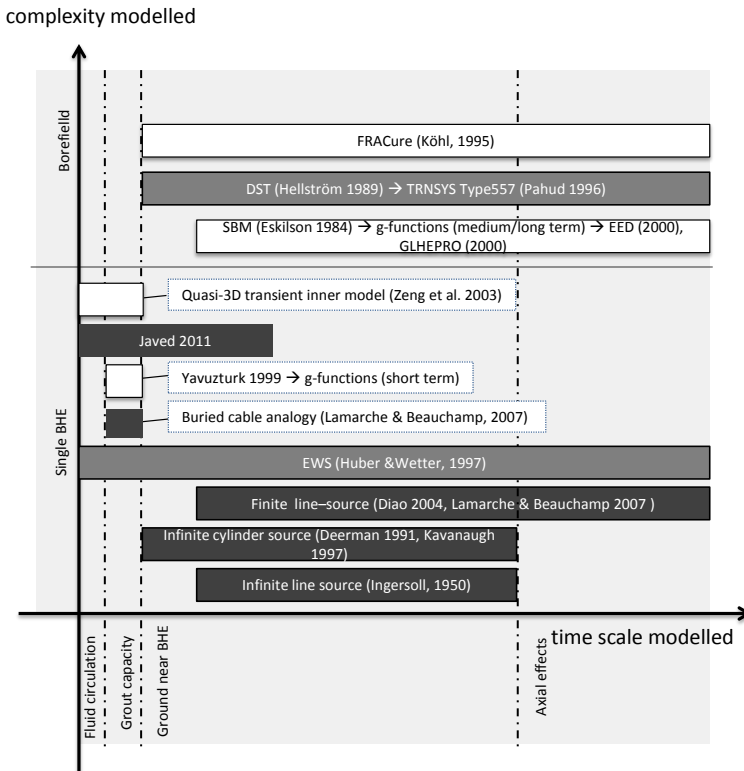


Figure 7.4: Overview of the discussed BHE and borefield models, with the horizontal position reflecting the time scales incorporated in the model (left: fast dynamics related to the inner problem, right: slow dynamics related to the heat exchange with the far field) and with the vertical position reflecting the model complexity (below: simplified representations, above: detailed representations).

7.3.2 First principle equations

Fourier's law Except from the convective heat transfer due to the circulation of the brine fluid inside the tubes, the heat transfer inside the BHE (inner problem) and around the BHE (outer problem) is mainly conductive and can thus be described by Fourier's law ([175]):

$$q'' = -k \nabla T \quad (7.11)$$

with q'' (W/m²) denoting the heat flux per unit surface and k (W/mK) the thermal conductivity of the medium (e.g. the grout or the ground). Substituting Eq.(7.39) in the energy balance equation for a unit volume with density ρ (kg/m³) and specific thermal capacity c (J/kgK):

$$\rho c \frac{\partial T}{\partial t} = k \nabla^2 T \quad (7.12)$$

yields:

$$\begin{aligned} \frac{\partial T}{\partial t} &= \frac{k}{\rho c} \nabla^2 T \\ &= \alpha \nabla^2 T \end{aligned} \quad (7.13)$$

with α (m²/s) the thermal diffusivity of the conductive medium. In polar coordinates, the transient conduction equation Eq.(7.13) can be expressed as:

$$\frac{1}{\alpha} \frac{\partial T}{\partial t} = \frac{\partial^2 T}{\partial z^2} + \frac{\partial^2 T}{\partial r^2} + \frac{1}{r} \frac{\partial T}{\partial r} + \frac{1}{r^2} \frac{\partial^2 T}{\partial \theta^2} \quad (7.14)$$

with z (m) the axial position (e.g. the distance to the ground surface), r (m) the radial position (i.e. the distance to the centre of the BHE) and θ (rad) the angular position. Solution of this partial differential equation (PDE) requires an initial condition and 2 boundary conditions for each spatial dimension. Depending on the initial and boundary conditions, Eq. 7.14, can be solved analytically and/or numerically. It should be noted that most borefield models, whether they are based on an analytical or a numerical solution method (or both), exploit the fact that heat diffusion is a linear process and thus allows temporal and spatial superposition of temperature fields.

Temporal superposition Temporal superposition or convolution allows to describe the temperature response of the ground at a certain position, $T_g(r, z, t)$, to a time-varying heat input signal $q'_b(t)$ as the convolution of the *impulse* response function $G'(r, z, t)$:

$$T_g(r, z, t) = T_g(r, z, t = 0) + \int_{-\infty}^{t+\infty} q'_b(t - \tau) G'(r, z, \tau) dt \quad (7.15)$$

If the continuous $q'_b(t)$ -profile is discretized into n piece-wise constant parts $q'_b(i)$, the temperature response can be found as the sum of the *step* responses to the consecutive heat pulses $q'_b(i) - q'_b(i - 1)$:

$$T_g(r, z, t) = T_g(r, z, t = 0) + \sum_{i=1}^n (q'_b(i) - q'_b(i - 1))G(r, z, t - t_i) \quad (7.16)$$

with i the index denoting the end of a time step.

The step response functions $G(r, z, t)$ can also be written as a function of *dimensionless* space and time variables, \tilde{r} (-) and \tilde{t} (-). These so-called *g-functions* can be used to describe both the outer problem and the inner problem, and can be determined analytically and/or numerically (see Figure 7.4 and discussion below). The use of *g-functions* is common in the field of borefield modeling. Since the number of superposition calculations is proportional to the square of the number of discretization time steps, an 8760 h simulation creates a significant computational burden [192]. To address this problem, aggregation algorithms have been developed [192] to lump the response to heat inputs further away in the past, into larger blocks (i.e. larger discretization time step) and this way reduce the number of superposition calculations. A theoretical analysis of the impact of consecutive pulses and their pulse length on the temperature at a certain time step t , has been performed by Eskilson [45].

Spatial superposition In a borefield, the ground surrounding a BHE can not simply be considered as an infinite medium due to the thermal interaction between the different BHEs. The borefield temperature field is calculated by spatial superposition of the contribution of each BHE to the temperature field, see Eq.(7.17), with n_b denoting the number of BHEs:

$$T(r, z, t) = \sum_{i=1}^{n_b} T_i(r_i, z_i, t) \quad (7.17)$$

The combination of temporal and spatial superposition can also be deployed to increase the computation speed of models which cover the broad range of time constants, i.e. ranging from the small time constants inside and/or near the BHE up to the large time constants near the far field. The global temperature field is then found as the sum of a finite number of temperature fields which each focus on a different time scale and which are updated at appropriate time intervals.

7.3.3 Modeling the inner problem

The inner problem describes the processes within the BHE (see Figure 7.3), i.e. the heat exchange between the circulating fluid and the BHE wall. Two parts are distinguished: convective heat transport due to the brine fluid circulation inside the tubes on the one hand, and conductive heat transport from the tubes - through the grout - to the BHE wall, on the other hand. Most borefield models treat the inner problem statically, i.e. the so-called *steady flux assumption*. Only for subhourly simulations, for which the transient processes inside the BHE can not be neglected, dynamic models of the inner problem are required. Also for describing the brine fluid temperature evolution along the tube, different approaches exist.

Steady flux assumption

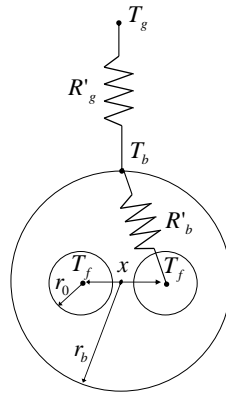


Figure 7.5: Horizontal cross cut of a single U-tube BHE, with indication of the tube radius r_0 , the BHE radius r_b , the tube inter distance x , the mean fluid temperature T_f , the mean BHE wall temperature T_b and the surrounding ground temperature T_g . R'_b (K/(W/m)) represents the borehole thermal resistance per unit length and R'_g (K/(W/m)) the thermal resistance for heat transfer in the ground. R'_b (see Eq.(7.23)) suffices to model the inner problem statically.

A *steady-flux assumption* of the heat transfer inside a BHE is often tolerated as the dynamics related to the inner problem are much faster than the ones

needed for design purposes. The most simple static model expresses the heat transfer as a function of the difference between the mean fluid temperature (T_f) and the mean borehole wall temperature (T_b), both indicated in Figure 7.5, see Eq.(7.18):

$$T_b(t) - T_f(t) = q'_b(t)R'_b \quad (7.18)$$

R'_b (K/(W/m)) is the unit length resistance of the BHE which takes into account convection between the fluid and the wall, conduction in the tube wall and conduction in the grout. q'_b (W/m) represents the heat extraction rate per unit length. Given the mean fluid temperature T_f and BHE depth H , the borefield inlet temperature T_{fi} (°C) and outlet temperature T_{fo} (°C) are found using the following assumptions:

$$T_f(t) = \frac{T_{fi}(t) + T_{fo}(t)}{2} \quad (7.19)$$

$$\dot{m}c_p(T_{fo}(t) - T_{fi}(t)) = Hq'_b(t) \quad (7.20)$$

$$T_{fo}(t) = T_f(t) + \frac{q'_b(t)H}{2\dot{m}c_p} \quad (7.21)$$

or, by substituting Eq.(7.18) in Eq.(7.21):

$$T_{fo}(t) = (T_b(t) - q'_b(t)R'_b) + \frac{q'_b(t)H}{2\dot{m}c_p} \quad (7.22)$$

The problem of finding T_{fo} as a function of q'_b then boils down to two subproblems, being, first, finding an expression for the borehole resistance R'_b and, second, finding an expression for T_b as a function of q'_b .

According to Yavuzturk and Spitler [192], the borehole resistance R'_b can be expressed as the sum of the thermal resistance of the convective heat transfer from the fluid to the pipe, $R'_{convection}$ (K/(W/m)), the thermal resistance for the conductive heat transfer through the shell of the U-tubes, R'_{pipe} (K/(W/m)) and the thermal resistance for the conductive heat transfer through the grout, R'_{grout} (K/(W/m)):

$$R'_b = R'_{convection} + R'_{pipe} + R'_{grout} \quad (7.23)$$

with:

$$R'_{convection} = \frac{1}{4\pi r_{in} h_{in}} \quad (7.24)$$

$$R'_{pipe} = \frac{\ln(r_{out}/r_{in})}{4\pi k_{pipe}} \quad (7.25)$$

and

$$R'_{grout} = \frac{1}{k_{gr}\beta_0(r_b/r_{out})^{\beta_1}} \quad (7.26)$$

with r_{in} (m) and r_{out} (m) respectively the pipe inner and outer radius, k_{pipe} (W/mK) the pipe thermal conductivity and h_{in} (W/m²K) the convection coefficient and β_0 (-) and β_1 (-) resistance shape factor coefficients which depend on the borehole and pipe geometry. The convection coefficient h_{in} can be determined by the Dittus-Boelter correlation, which is a function of the Reynolds number Re (-), the Prandtl number Pr (-), the thermal conductivity of the brine fluid k_f (W/mK) and the inner pipe radius r_i :

$$h_{in} = \frac{0.023Re^{0.8}Pr^n k_f}{2r_{in}} \quad (7.27)$$

with $n = 0.4$ for heating and $n = 0.3$ for cooling. β_0 (-) and β_1 (-) are based on experimental and/or finite element analysis [136]. For typical borehole and pipe geometries, β_0 and β_1 amount to approximately +20 and -1. The effective borehole thermal resistance R_b (K/W) is expressed by Eq.(7.28), with H (m) the active BHE depth (see Figure 7.3).

$$R_b = \frac{R'_b}{H} \quad (7.28)$$

Eqs.(7.23) - (7.28) provide a first estimate of R_b which can be used in the initial borefield design phase. For the final design phase, however, it is recommended to define R_b experimentally through a thermal response test (TRT), see Section 7.3.5.

The second subproblem, i.e. finding an expression for T_b as a function of q'_b (see Eq.(7.22)), is the subject of Section 7.3.4 which deals with the description of the outer problem.

Transient models

For subhourly simulations the steady-flux assumption (see Eq.(7.18)) does not hold. The steady-flux assumption is only valid for time scales larger than the borehole time t_{bh} (s), defined by Eskilson [43] as:

$$t_{bh} = \frac{\pi r_b^2 \rho_{gr} c_{gr} \Delta T}{\Delta T / R'_b} = \frac{r_b^2 \rho_{gr} c_{gr}}{\alpha_g \rho_g c_g} \pi k_g R'_b \quad (7.29)$$

t_{bh} represents the time needed to increase the borehole temperature (with borehole radius r_b , grout thermal capacity c_{gr} (J/m³K) and grout density ρ_{gr} (kg/m³)) with ΔT (°C) by means of a temperature change ΔT of the brine fluid temperature (with the latter corresponding to a maximum heat transfer rate from the fluid to the borehole q'_b of $\Delta T/R'_b$). For a characteristic value of 0.1 K/(W/m) for R'_b , 3.3 W/mK for k_g and a ratio of 2 for $\frac{\rho_{gr}c_{gr}}{\rho_g c_g}$, following simplified expression for t_{bh} is obtained [43]:

$$t_{bh} = \frac{5r_b^2}{\alpha_g} \quad (7.30)$$

with α_g (m²/s) representing the ground thermal diffusivity. For r_b equal to 0.075 m and α_g 8.0×10^{-7} m²/s t_{bh} amounts to 10 h. Note that the ratio of 2 for $\frac{\rho_{gr}c_{gr}}{\rho_g c_g}$ is based on the assumption that the borehole is filled with water (as applied in Sweden). For typical grout materials, such as bentonite, this ratio is close to 1. The estimate of t_{bh} , used to determine the time scale below which the transient effects inside the borehole can not be neglected, is therefore on the safe side.

Being minor in magnitude, the axial component is often neglected when modeling the transient conduction inside the grout [190]. Eq. 7.14 then boils down to:

$$\frac{1}{\alpha} \frac{\partial T}{\partial t} = \frac{\partial^2 T}{\partial r^2} + \frac{1}{r} \frac{\partial T}{\partial r} + \frac{1}{r^2} \frac{\partial^2 T}{\partial \theta^2} \quad (7.31)$$

Yavuzturk et al. [193] solved this PDE for various GHE geometries, using a fully implicit finite volume approach [133, 134]. They developed an algorithm to automatically generate polar grids for a variety of borehole radii r_b , pipe radii r_0 and tube inter distance x . To facilitate the integration into commercial borefield *design* software, this numerical model was used to generate step responses which were in turn translated into the g-function format proposed by Eskilson [45] (see Section 7.3.4).

Recently, the transient description of the inner problem has also been solved analytically. Lamarche and Beauchamp [104] proposed an analytical solution of Eq.(7.31), based on the buried cable analogy [24]. This promises to be more flexible and computationally less expensive than numerical methods, but has not been integrated into commercial building simulation software yet. Javed and Claesson [86] presented a combination of analytical and numerical methods to describe the short-term response for the BHE.

Brine fluid circulation

The axial variation of the brine fluid temperature, neglected in the two aforementioned inner-problem representations, is taken into account in the models proposed by, among others, Zeng et al. [200] and Lee and Lam [106]. They solve the governing equations respectively analytically and numerically. Both studies use the steady-flux approximation however, i.e. the transient effects related to the thermal capacity of the grout, are neglected. The EWS-model [83] (discussed further), by contrast, takes both the brine fluid circulation and the grout dynamics (though by a single node only), into account. The inner problem is solved numerically, with a schematic presentation of the modeling approach depicted in Figure 7.6.

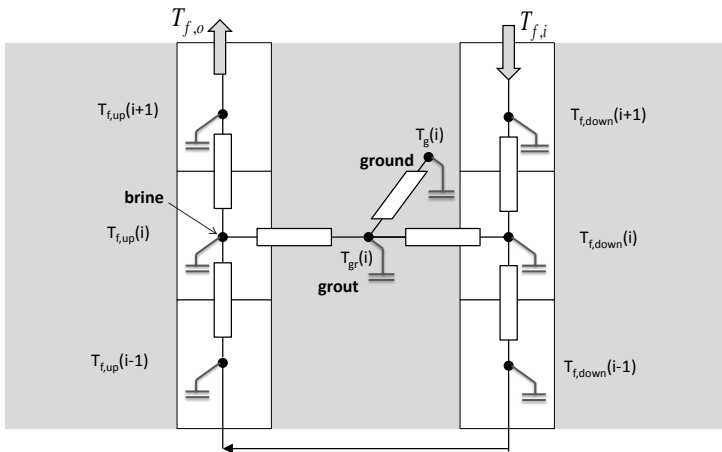


Figure 7.6: Axial cross cut of the resistance-capacity network analogy used by the EWS model to represent the thermal processes inside and around a BHE. As indicated by the allocation of the capacities, the EWS model incorporates the dynamics of the fluid (brine), of the filling material (grout) and of the surrounding ground [82].

7.3.4 Modeling the outer problem

The thermal processes occurring in a borefield are per definition 3-dimensional. If focusing on the thermal response of a single BHE, however, the axial symmetry

allows the use of 2D-cylindrical coordinates with only the radial dimension r and the axial dimension z . Eq. (7.14) then boils down to:

$$\frac{1}{\alpha_g} \frac{\partial T}{\partial t} = \frac{\partial^2 T}{\partial z^2} + \frac{\partial^2 T}{\partial r^2} + \frac{1}{r} \frac{\partial T}{\partial r} \quad (7.32)$$

Solution of this PDE requires an initial condition, i.e. $T(t = 0)$, and 2 boundary conditions for each spatial dimension. For certain combinations of initial and boundary conditions, an analytical solution exists. Section 7.3.4 discusses the infinite line source solution, the cylindrical source solution and the finite line source solution, which allow an approximative but mathematically elegant description of the outer process for a single BHE. For more complex geometries and/or boundary conditions, Eq. (7.32) has to be solved numerically, an example of which is given in Section 7.3.4. Section 7.3.4 presents two examples of 'hybrid' models which combine analytical and numerical methods to describe the complex borefield thermal processes in a computationally efficient way. First, the conclusions of the study of Eskilson [43], on the parameters which may be neglected when modeling the outer problem, are presented.

Negligible parameters and effects

Based on both analytical studies and numerical results, Eskilson [43] has shown that the following parameters and effects are negligible for the thermal performance of BHEs:

- **Ground stratification** The ground can most often be considered as a homogeneous medium: deviations from the average thermal conductivity are negligible.
- **Ground surface** The impact of temperature variations, snow etc. is negligible.
- **Geothermal gradient** Temperature deviations from the effective undisturbed ground temperature $T_{g,\infty}$ due to the geothermal gradient ($\approx 3^\circ\text{C}/100\text{m}$) are negligible.
- **Groundwater infiltration** Except for situations with strong ground water flow, the effect of groundwater infiltration is negligible.
- **Inner problem** Transient thermal effects inside the BHE (grout, tubes and the heat carrier fluid) are insignificant on a time scale above t_{bh} (see Eq.(7.30)).

Analytical solutions

Infinite line-source approximation The most simple way to model the outer process is to treat the BHE as an infinite line source. With this approximation, the radial distance to the source r (m) is the only spatial variable and Eq.(7.32) boils down to:

$$\frac{1}{\alpha_g} \frac{\partial T}{\partial t} = \frac{\partial^2 T}{\partial r^2} + \frac{1}{r} \frac{\partial T}{\partial r} \quad (7.33)$$

with α_g (m^2/s) denoting the ground thermal diffusivity. This PDE is solved with following initial condition, which defines a homogeneous ground temperature distribution at time $t = 0$:

$$T(r, t = 0) = T_0 \quad \forall \quad r \geq 0 \quad (7.34)$$

and with following boundary conditions:

$$-k \frac{\partial T}{\partial r} \Big|_{r=0} = q'_b \quad \forall \quad t > 0 \quad (7.35)$$

$$T(r, t) = T_0 \quad r \rightarrow \infty \quad (7.36)$$

With the first boundary condition, the BHE is represented as a heat source with constant specific heat rate q'_b (switched on at time $t = 0$). Note that the radial dimension of the BHE is neglected (i.e. $r = 0$). With the second boundary condition, the ground is represented as a semi-infinite medium. The temperature response at time t and at a radial distance r from the line source is then described by following equation:

$$\begin{aligned} T(r, t) - T_0 &= \frac{\dot{Q}}{4\pi k_g} \int_x^\infty \frac{e^{-\beta^2}}{\beta} d\beta \\ &= \frac{\dot{Q}}{2\pi k_g} E(\beta) \end{aligned} \quad (7.37)$$

with E representing the exponential function and β (-) the dimensionless integration variable:

$$\beta = \frac{r}{\sqrt{4\alpha_g t}} \quad (7.38)$$

Evaluation of $T(r, t)$ at $r = 0$ yields an estimate of the borehole wall temperature T_b . From this, T_f , T_{fi} and/or T_{fo} can be calculated using Eq.(7.18). This model also enables to determine the diffusivity depth of the energy, denoted by δ . For radial heat transfer, the diffusivity depth equals $1.118\sqrt{\alpha_g t}$.

The diffusivity model can be applied if the considered volume can be considered as semi-infinite. This condition holds if the dimensionless number Fourier Fo (-), expressed by Eq.(7.39) is smaller than 0.1.

$$Fo = \frac{\alpha t}{L^2} \approx \left(\frac{\delta}{L}\right)^2 \quad (7.39)$$

L stands for the characteristic length and δ stands for the distance over which the energy is transported during time t . If δ is small compared to L , the approximation of infinity is justified. This condition holds in the case of a single BHE. The characteristic length for radial heat transport is in that case infinite. For multiple BHEs, L is approximately half of the distance B between the BHEs. The diffusivity model is then only valid for small time steps. Short-term variations can therefore be modeled analytically. Ingersoll et al. [84] were the first to apply the line source model to the modeling and design of BHE. Most models are extensions of this line-source approximation.

A BHE is, however, neither a line source, nor infinite. Due to the *line source assumption*, the infinite line source model is not suitable for time steps smaller than $5\frac{\alpha t}{r_b^2}$, i.e. when the short term dynamics related to the BHE itself and to the ground near the BHE can not be neglected. Due to the *infinite length assumption* it is not suitable for time periods larger than $\frac{H^2}{9\alpha}$, i.e. when axial effects start playing a role. Therefore, the infinite line source solution is only valid within the following time range, with t_{bh} (s) being the borehole time (see Eq.(7.30), [43]) and t_s (s) being referred to as the borehole time constant.

$$5\frac{\alpha t}{r_b^2} \leq t \leq \frac{t_s}{20} \quad \text{with } t_s = \frac{H^2}{9\alpha} \quad (7.40)$$

Finite line-source approximation For time scales longer than $t_s/20$ the *axial effects*, neglected in the infinite line-source approximation, become important. Diao et al. [37] therefore proposed to use the analytical solution based on the *finite* line source model. This finite line source solution considers every segment of the line as a point source. The temperature response to the entire line source is found by integrating over all segments. The mean BHE wall temperature T_b is considered constant and equal to the BHE wall temperature at $z = H/2$. The thermal response of T_b to a step input is presented by Eq.(7.41), as a function of the dimensionless time $\frac{t}{t_s}$ (-) and the dimensionless space variable $\frac{r}{H}$ (-):

$$T_b - T_0 = \frac{q'_b}{4\pi k} g\left(\frac{t}{t_s}, \frac{r}{H}\right) \quad (7.41)$$

with $g(-)$ the g-function, which is represented in Figure 7.7 for 1 BHE and 2 BHEs [105].

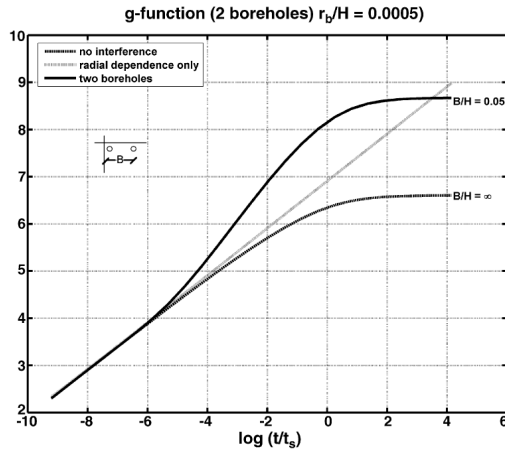


Figure 7.7: g-Function for one BHE ($B/H = \infty$) and two BHEs ($B/H = 0.05$) obtained with the numerical model SBM [45](see Section 7.3.4), compared to the infinite line source model (grey line). The g-function for one BHE (medium and long time-scale) can also be found analytically using the finite line source approximation. The difference between the g-function of the infinite line source approximation (grey) and the finite line source approximation ($B/H = \infty$) indicates the time scale from which axial effects start playing a role. The difference between the g-functions for one BHE ($B/H = \infty$) and for two BHEs ($B/H = 0.05$) indicates the time scale from which BHE thermal interference start playing a role (for the given ratio of the BHE spacing B and the BHE depth H). Source: Lamarche and Beauchamp [105]

Figure 7.7 shows the difference between the dimensionless response functions obtained with the infinite line-source approximation (straight line) and the finite line-source approximation for a single BHE ($B/H \rightarrow \infty$). It is observed that the two methods yield similar results for $\log(\frac{t}{t_s}) \leq -3 \Rightarrow t \leq \frac{t_s}{20}$. For longer time frames the axial effects (as a response to a step heat input) start playing a role. The infinite line source approach is then no longer adequate. For sandy-gravel soil axial effects become important after about 3.7 years, for rocky soil already after about 1.2 years [105].

The approach of Diao et al. [37] however, yields some small discrepancies compared to the infinite line source theory for $t \rightarrow 0$ and a maximum in the step response function is observed. According to Lamarche and Beauchamp [105] these errors are caused by the choice of the reference temperature T_b .

Lamarche and Beauchamp [105] determined T_b by integrating along the BHE length, which yields a correct result. They also rewrote this integral in a computationally more efficient form.

Infinite cylindrical-source approximation Deerman and Kavanaugh [36] applied the cylindric source model, of which the line source model is a simplified variation, to improve the description of the step response for the time scales smaller than $5\frac{\alpha t}{r_b^2}$ (see Eq.(7.40)). The cylindric source model approximates the BHE as a cylinder with infinite length and with a constant heat flux q'_b at $r = r_b$. The initial and boundary conditions for the PDE expressed in Eq.(7.33) are respectively:

$$T(r, t = 0) = T_0 \quad \forall \quad r \leq r_b \quad (7.42)$$

and:

$$-k \frac{\partial T}{\partial r} \Big|_{r=r_b} = q'_b \quad \forall \quad t > 0 \quad (7.43)$$

$$T(r, t) = T_0 \quad r \rightarrow \infty \quad (7.44)$$

The solution to this problem at $r = r_b$ equals:

$$T_b - T_0 = \frac{q'_b}{k} \cdot G(z, p) \quad \begin{cases} z = \frac{\alpha t}{r_b^2} \\ p = \frac{r}{r_b} \end{cases} \quad (7.45)$$

where $G(z, p)$ is the cylindrical source function as described by *Ingersoll et al. (1954)*:

$$G(z, p) = \frac{1}{\pi^2} \int_0^\infty f(\beta) d\beta \quad (7.46)$$

$$f(\beta) = (e^{-\beta^2 z} - 1) \cdot \frac{[J_0(p\beta)Y_1(\beta) - Y_0(p\beta)J_1(\beta)]}{\beta^2 [J_1(\beta)^2 + Y_1(\beta)^2]} \quad (7.47)$$

where J_0 , J_1 , Y_0 , Y_1 are the Bessel functions of the first and second kind. Carslaw and Jaeger [24] developed analytical solutions with varying boundary conditions for regions bounded by cylinder geometry. Deerman and Kavanaugh [36] and Kavanaugh and Rafferty [92] described the use of the cylinder source model in designing ground loop heat exchangers.

Numerical models

Eskilson [45] developed the Superposition Borehole Model (SBM), aimed at describing the response of a borefield for different configurations of the BHEs. Inspired by the computational advantages of a step response model, he created a library with step responses of more than 112 borefield configurations. These step responses, referred to as *g*-functions, are a function of two dimensionless variables, being the dimensionless time $\frac{t}{t_s}$ and the dimensionless length B/H :

$$T\left(\frac{t}{t_s}, B/H\right) = g\left(\frac{t}{t_s}, B/H\right) \quad (7.48)$$

B (m) denotes the distance between two adjacent BHEs. Figure 7.7 shows the *g*-functions for one BHE ($B/H = \infty$) and two BHEs ($B/H = 0.05$). Comparison between both *g*-functions indicates that, for the case $B/H = 0.05$, thermal interference starts playing a role for $\log\left(\frac{t}{t_s}\right) \geq -5$. For sandy-gravel soil this corresponds to a time span of about half a year, for rocky soil only 2 months [105].

By convolution of these individual step response functions the final solution is calculated. These *g*-functions can be used to analyze the medium and long-term behavior of borefield configurations, which is useful for design purposes. They are integrated in commercial borefield design software such as EED [42] and GLHEPRO [166].

Eskilson [43] computed the *g*-functions based on numerical models. This approach is however time-consuming and not flexible with respect to the borefield configuration. Zeng et al. [199] therefore proposed an analytical method for generating these *g*-functions, which has been worked out by Diao et al. [37] and further improved by Lamarche and Beauchamp [105]. Note also that the inner problem in the SBM is described using the steady flux assumption, which formerly limited the use of the *g*-functions to the medium and long time scale. Yavuzturk and Spitler [192] have extended the *g*-functions towards the smaller time steps.

Hybrid models

While the first borefield models were intended for design purpose, the use of integrated building simulation software environments, such as TRNSYS and EnergyPlus, required BHE models with a shorter time step accuracy and high computation speed. The most well-known model in this category is the Duct Storage Model (DST) [74], aimed at describing the response of cylindrically shaped borefields within a building simulation environment. The need for a

computationally fast model resulted in a hierarchical model structure. The borefield temperature field is calculated as the superposition of three solutions which each account for a different time scale. The smallest time scale, related to the heat transfer processes near the BHE as a result of hourly loads, is captured by a 1D-radial finite-difference (FD)-model. The largest time scale, related to the heat exchange processes inside the borefield and to the far field, is captured by a 2D-axial-radial FD-model. The coupling between both time scales, i.e. the medium time scale, is realized by an analytical model. The latter redistributes the heat sources, originating from the short term solution, correctly over the borefield. This redistribution is required as the 1D-radial FD-model is solved only once, namely for a temperature distribution around the BHE based on the mean borefield temperature. As the borefield temperature is not homogeneous, the heat exchange between the BHE and its surrounding ground will depend on the location of the BHE in the borefield. In other words, the nominal solution for the heat transfer rate found with the 1D-radial model, will thus be an overestimation or an underestimation of the actual heat exchange. The redistribution of the heat sources, based on the position of the BHE in the borefield, is thus realized by this analytical model. The inner problem is treated statically, i.e. according to Eq.(7.18). The model has been translated into TRNSYS Type557 [130, 172] and is especially useful for whole-building simulation. The DST model is generally regarded as a reference model [105]. It was recently experimentally validated by Pertzborn et al. [138].

The DST-model uses the steady-state assumption to model the inner problem. For subhourly time scales, as mentioned earlier, this assumption does not hold. For integration in building simulation software, a compromise is required between the computational advantage of the steady-flux assumption on the one hand, and the very detailed, but computationally expensive, numerical models of the inner problem [e.g. 193] on the other hand. The EWS model [82, 185] is an example of a model which forms such a compromise. The model is well documented by Huber and Schuler [82]. The grout thermal capacity, the convective heat transport inside the tubes and the thermal interference between the tubes are represented by a lumped RC-network, depicted in Figure 7.6. The heat transfer in the ground itself, near the BHE, is solved using the Cranck-Nicholson discretization scheme, while the heat transfer to the far-field is modeled analytically. The short-term behavior of the EWS-model has been validated experimentally [82]. The long term behavior has been validated numerically against the very detailed numerical model FRACure [97], the DST-model [75] and WPcalc [121] by respectively Signorelli et al. [159] and Huber and Schuler [82].

7.3.5 Determining the physical parameters

The above mentioned models are all first-principle models, requiring knowledge of the physical properties of the ground and of the BHE. The BHE length is most sensitive to the effective borehole thermal resistance R_b and to the ground thermal conductivity k_g [60, 147]. An on-site determination of these parameters by means of a Thermal Response Test (TRT), is strongly recommended.

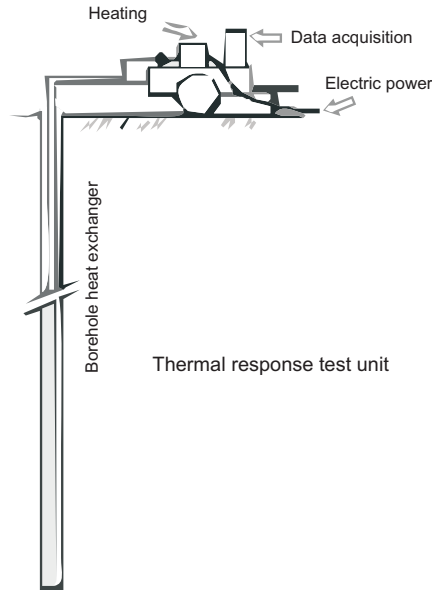


Figure 7.8: Thermal response test set-up

During a TRT heat is injected (or extracted) at a constant power. A schematic representation of such a 'TRT device' is given in figure 7.8. The evolution of water inlet and outlet temperature is registered. From this the step response of the mean fluid temperature T_f is calculated. As there are two parameters to be determined, we need two equations. The first equation describes the inner problem at steady-flux state, yielding an expression for R_b . The second equation describes the temperature distribution in the surrounding ground, yielding an expression for k_g . Gehlin [60] describes five methods for the latter: two analytical approaches, based on respectively the line source theory and the cylinder source theory, and three numerical approaches: a 1-D numerical model [158], a 2-D finite difference model [16] and a transient 2-D finite volume model

in polar co-ordinates [7, 193]. While the analytical TRT evaluation techniques require a constant heat injection or extraction rate, numerical models can also account for time-varying heat transfer rates. On top of that they can handle detailed representations of the BHE geometry and thermal properties of the fluid, the tubes, the grout and the ground. Recently, however, also analytical models have been developed for treating the short term dynamics related to the inner problem [see e.g., 86, 105].

The impact of these parameters (and especially k_g [91, 153]) on the BHE length, explains the importance of a TRT and the large research effort in this domain [see e.g., 60, 152, 158, 160, 181, 187]. The challenge here lies in the development of methodologies (i.e., measurement techniques and models for data analysis) which enable to increase the estimation accuracy and/or decrease the duration time (and thus the cost) of performing a TRT. In this context one can situate the development of models which are accurate on the very short term.

7.3.6 Model validation

Validation of borefield models is not straightforward. Validation of the long term behavior is experimentally almost infeasible, as this would require measurement periods of multiple tens of years. For the long term validation one therefore has to rely on comparison with analytical models [18] and very detailed numerical models [see e.g., 82]. Validation of the short term dynamics is not straightforward either; since the temperature difference between inlet and outlet fluid is relatively small (2 to 6°C), heat power measurements are very prone to measurement errors. Most models are therefore validated by comparison with other models. Until recently, the experimental validation of some models was mentioned, but not well documented. Recently, however, Beier et al. [14] gathered detailed measurement data to enable a correct validation of the short term behavior of BHE models, especially interesting for assisting the data analysis of TRT, as discussed above.

7.3.7 Models for optimal control purpose

For the purpose of optimal control it is computationally advantageous to represent the system by a linear state-space model [116]. The influence of the number of states on the computation time depends on the optimization problem itself, as well as on the optimization method used. Especially for dynamic programming and explicit MPC it is computationally advantageous to keep the number of states, i.e. the model order N , as small as possible [e.g. 81, 142]. With respect to the representation of the building dynamics, several

examples of simplified models for use within the framework of building climate optimal control are presented in the literature [e.g., 20, 101, 109, 186]. With respect to the borefield dynamics, however, such low-order models have not been encountered. Most existing models are intended for the purpose of (1) design, (2) simulation or (3) TRT analysis, as described above, and their format is either a step response model, a high-order numerical model or a combination of both.

Only a few studies report the use of a simplified borefield model for optimization purposes. Vanhoudt et al. [177] and De Ridder et al. [35] implemented dynamic programming [15] to optimize HyGCHP operation with the mean borefield storage temperature as optimization variable. However, the mean borefield temperature alone is insufficient. The brine temperature should be predicted as well since this is the variable defining the heat pump COP and the ability for passive cooling. Franke [54] developed an object-oriented, equation-based model of a solar heating system with borefield thermal storage to optimize the design parameters with respect to both investment costs and running costs. The local thermal process around the boreholes, i.e. the heat transfer between the fluid and the storage medium, is described by a first-order dynamic model. The global process, i.e. the heat transfer within the ground, is represented by an 11th order model extracted from the 300th-order system matrix of the DST-model implemented in TRNSYS [74, 172]. This model reduction was accomplished by means of the singular perturbation approximation technique which yields a model with good long-term prediction properties. Kim et al. [94] also proposed the state model reduction (MR) technique to decrease the computation time for predicting the short and long term dynamics of a BHE. The advantage of the MR approach is that the resulting model captures the dominant dynamics with a minimum number of states. One downside of the reported examples on the use of MR, is the requirement to have access to the system matrix of a detailed, high-order numerical model. This may constitute a practical barrier. A second drawback, which is inherent to the methodology of MR, is that the initial (higher order) numerical model remains an idealized representation of the real system. Bianchi [20] therefore recommends to estimate the parameters of a controller model for MPC from real measurement data. Contrary to the building dynamics, however, the thermal time constant of a BHE (see definition t_s) is very large due to the slow thermal diffusion process in the semi-infinite ground. Time constants range up to the order of magnitude of tens of years. Consequently it is not possible to cover the entire dynamic range by measurement data. To address this problem, parameter estimation (PE) can be started from an initial model which is based on the physics of radial heat diffusion. The values for the physical parameters in this first principle model can be obtained from a thermal response test. Both the MR and the PE approach are evaluated in Section 7.4, with in addition black-box system identification.

7.4 Controller borefield model

Different techniques to obtain a low-order BHE-model are evaluated and compared. The methodology followed is presented Section 7.4.1. Section 7.4.2 describes each modeling technique in detail. Section 7.4.3 evaluates the developed models. Section 7.4.4 investigates the impact of non-idealities encountered in practice. The main results are summarized in Section 7.4.5.

7.4.1 Methodology

As presented in Chapter 2, we start with the definition of the model requirements, followed by the selection of the model types, identification data sets, parameter estimation methods and validation methods. Here, we additionally describe the DST-model used as emulator for validation and identification purposes.

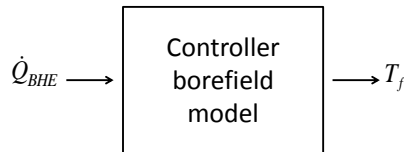


Figure 7.9: Input-output description of the controller borefield model.

Model requirements The OCP defined in Section 8.3 requires a model which relates the borefield fluid outlet temperature $T_{f,o}$ to the hourly borefield load profile \dot{Q}_{BHE} . With a steady state description of the inner problem this is equivalent to finding an expression for the mean fluid temperature T_f (see Eq.(7.18) and Eqs.(7.19-7.22) on p.148). This is represented in Figure 7.9. The controller borefield model we are looking for, has to predict the mean fluid temperature T_f as a response to hourly borefield load profiles \dot{Q}_{BHE} , and this from the hourly time scale up to the annual time scale. For incorporation in an optimization framework, the lowest-order model (i.e. the model with the lowest number of states) which fits this requirement, is looked for.

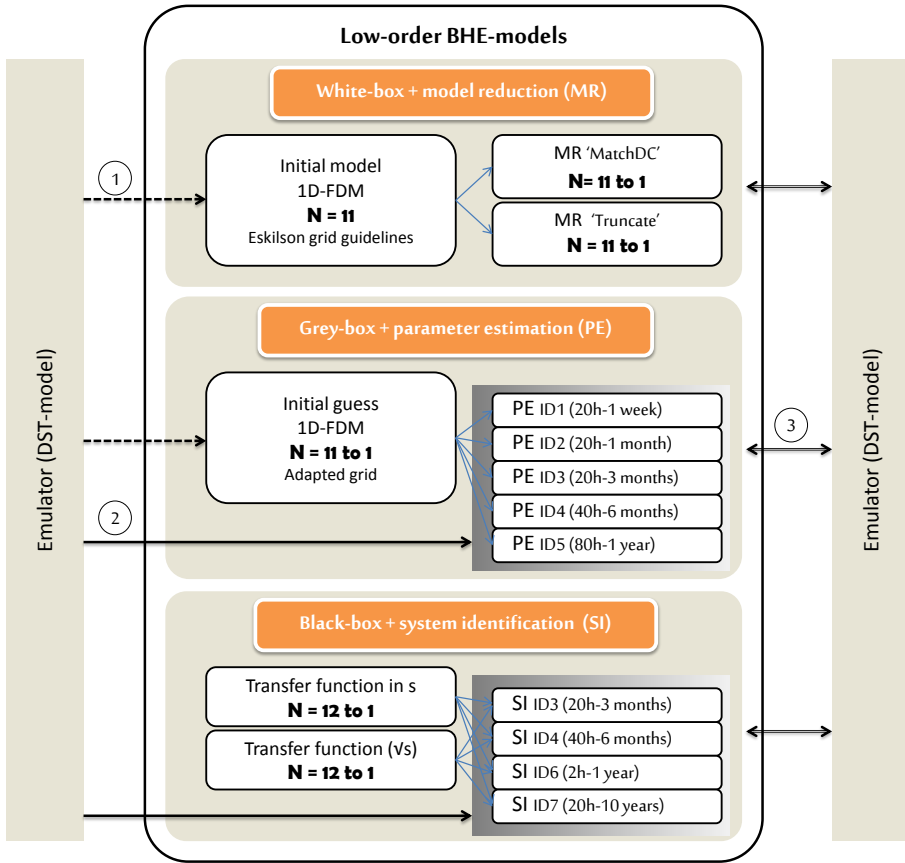


Figure 7.10: Investigated approaches to obtain low-order BHE-models: white-box modeling followed by model reduction (MR) (top), grey-box modeling followed by parameter estimation (PE) (middle) and black-box system identification (SI) (bottom). The white-box model (top) is a 1-D finite difference model (1D-FDM) representing the radial heat diffusion in the ground and is based on Eskilson's grid guidelines, yielding a model order $N = 11$. The physical parameter values are the same as for the BHE emulator (DST-model), see dashed arrow (1). The evaluated MR techniques are 'MatchDC' and 'Truncate'. The initial guess for PE (middle) is a 1D-FDM with the grid adapted to the model order $N = 1 : 11$. PE is performed for 5 identification data (ID) sets (ID1 to ID5), each covering a different time scale, as indicated. The ID data are obtained from the DST-model (with multisine heat profiles as excitation signal), indicated by the full arrow (2). Black-box system identification (bottom) is performed for 2 additional ID sets (ID6 and ID7, covering a large time frame). The models obtained with the 3 approaches are validated with the DST-model for typical load profiles (Val1, Val2) and for a step heat input (Val3), indicated by the double arrow (3).

Model types Three approaches are investigated to obtain a low-order state space description of a borehole heat exchanger (BHE):

- white-box approach,
- grey-box approach,
- black-box approach.

The *white-box approach* starts from a 1-dimensional finite-difference model (1D-FDM) of the radial heat transfer process around the BHE, based on the grid guidelines formulated by Eskilson [43]. Model reduction (MR) is applied to this initial model to reduce the number of states. Two model reduction methods, `MatchDC` and `Truncate`, both implemented in the Matlab function `balread`, are evaluated. Here, the question is to which order the *initial model*, based on the grid guidelines, can be reduced.

The *grey-box approach* also starts from a finite-difference description of the radial heat transfer. Instead of applying the grid guidelines, however, the number of capacitances is varied. This results in a set of *RC*-models with varying model order. The parameters of these *RC*-models are defined by parameter estimation (PE). The identification data are simulation data obtained with the TRNSYS DST-model, described in Section 7.4.1. Also here, the model with the lowest number of states is defined. Additionally, the impact of the identification data set used, is assessed.

The *black-box approach*, requiring no prior knowledge of the ground and borefield thermal properties, is applied for two sets of model structures. The first set comprises rational functions in the Laplace variable s , being the standard and general format for linear models. The second set comprises rational functions in the Warburg variable \sqrt{s} , a format which has been put forward to incorporate the prior knowledge that the process being identified is a diffusion process, which, in the Laplace domain, is a function of \sqrt{s} [141]. In this sense, this second model structure in the variable \sqrt{s} is not a purely black-box model. The coefficients of the rational models in s and \sqrt{s} are defined in the frequency domain with the Matlab FDIDENT-toolbox [99]. The difference between the two model structures is assessed, as well as the influence of the frequency content of the excitation signal.

The three approaches are visualized in Figure 7.10. The resulting models are compared to the DST-model implemented in TRNSYS [74, 172].

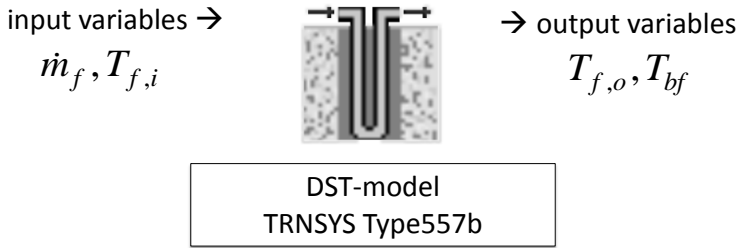


Figure 7.11: Input and output variables of the DST-model implemented in TRNSYS Type557b used as emulator for obtaining identification and validation data.

Borehole emulator The data used for identification and validation are simulation data obtained with the DST-model implemented in TRNSYS Type557b [74, 172], see Figure 7.11. The DST-model (see also Section 7.3.4) is a simulation model for cylindrical duct thermal energy storage systems. The heat transfer between the circulating fluid and the borehole wall is represented by the specific borehole thermal resistance R'_b (mK/W). The dynamics of the circulating fluid are neglected, preventing the use of this model to accurately describe the temperature transients when switching on and off the circulation pump. The ground temperatures are found by superposition of a local solution, a steady-flux part and a global solution. The local solution accounts for the contribution of a single BHE to the temperature variation inside a borefield, related to the short-term effects of the heat injection or extraction, while the steady-flux part and the global solution account for the slow heat redistribution inside and outside the borefield. The global and local problems are solved numerically by using the explicit finite difference method, whereas the steady-flux part is given by an analytical solution. The superposition method is a computationally efficient strategy to deal with the large range of time constants. Due to its high level of detail, the TRNSYS DST-model is often used as a reference, e.g. for validating simplified BHE models [18, 94, 132], for evaluating design strategies [see, e.g. 158] or for analyzing thermal response test evaluation tools [see, e.g. 187].

The BHE implemented in the TRNSYS DST-model has a length H of 121 m, header depth of 1 m, borehole radius r_b of 0.075 m and a specific borehole thermal resistance of 0.1 mK/W. The specific heat of the calorimetric fluid is 4 kJ/kgK and its density is 1000 kg/m³. The ground has a thermal conductivity k_g of 1.9 W/mK and a volumetric heat capacity ρc_g of 2400 kJ/m³K. The

cell size of the numerical grid depends on the simulation time step and the simulation length defined by the user. For this study, these model parameters are set to respectively 0.2 h and 100 years.

The measurable variables are the mass flow rate \dot{m}_f , the fluid inlet temperature T_{fi} and the fluid outlet temperature T_{fo} . From these, the heat input rate \dot{Q}_{BHE} and the mean fluid temperature T_f can be calculated, see Eq.(7.18)-(7.20). Note that T_{bf} , the mean borefield temperature is also an output of the DST-model, but can not be directly measured in practice.

Identification data for grey-box PE and black-box SI The excitation signal used for identification should excite the frequency range of interest. The dynamic time range of a borehole is however very large, ranging from the hourly scale to tens of years. Capturing this entire range in one identification data set (ID set) requires both a small sampling time Δt_s and a long simulation time t_{sim} . This results in a huge amount of data, which is computationally difficult to handle in the time domain. As stated in Chapter 2, parameter estimation boils down to solving a nonlinear optimization problem. For identification in time domain with the prediction error method (PEM), most nonlinear solvers, such as the Levenberg-Marquardt algorithm adopted here, require the inversion of the Hessian matrix (or of a computationally interesting approximation of it). The size of the Hessian is $n_m \times n_y$ times $n_m \times n_y$, where n_m represents the number of measurement time steps and n_y the number of outputs for which the model error needs to be minimized. With the adopted algorithm implementation and the software and the hardware used, this inversion step is found to limit the matrix size to approximately 5000 by 5000, which in turn limits the frequency content contained in the identification data (ID) set for the grey-box models identified in the time domain. Hence for time-domain identification a trade-off must be made between the sampling frequency and the simulation time, and thus between capturing the fast or slow dynamics.

For the black-box system identification performed with the Matlab FDIDENT toolbox [99], there are no computational limitations on the frequency range covered by the identification data. On the other hand, FDIDENT requires the system response to a multisine excitation signal. Moreover, in the basic version of FDIDENT used here, the steady state system response to the multisine excitation signal is needed, which means that the transients at start up should have died out. The steady state response to a multisine input signal is found by repeating the same input a large number of times, until the difference between the response of the $(n+1)^{th}$ time and the $(n)^{th}$ time the signal is applied, is negligible. While in practice both criteria (multisine input signal and steady state regime) are impossible to satisfy, it is easily performed within the TRNSYS

simulation environment. In this sense, the ID sets used correspond to the better than best-case scenario.

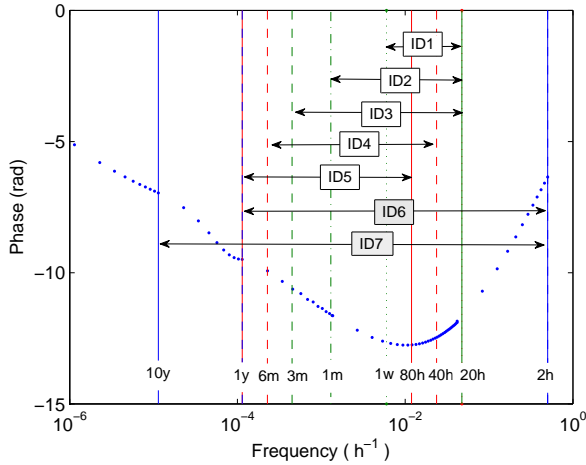


Figure 7.12: Frequency range covered by the different identification data sets. ID1, ID2, ID3, ID4, ID5, are used for PE in the time domain and therefore cover a limited frequency range (trade-off between the short term dynamics (ID 1, ID2, ID3) and the long term dynamics (ID4 and ID5)). ID6 and ID7, used for SI in frequency domain, cover the entire frequency of interest (2h-10y). As a reference, the frequency response of the mean brine fluid temperature T_f to the input \dot{Q}_{BHE} , based on the DST-model simulations, is shown. The discrete markers (blue dots) indicate the frequencies of the multisine excitation signals for which the response of T_f was calculated.

To examine the effect of the frequency content of the identification data on the model performance, 7 identification data (ID) sets are proposed. The excitation signals are multisine profiles for the borehole heat input rate $\dot{Q}_{BHE}(t)$ (kW). Table 7.1 lists the parameter values characterizing the multisines, being the minimal period $T_{p,min}$ (h) and the maximal period $T_{p,max}$ (h) found in the signal, or respectively the maximal frequency f_{max} (h^{-1}) and minimal frequency f_{min} (h^{-1}), and the number of frequencies contained, $N_f(-)$. To capture the

information contained in the signal, the required measurement length t_m (h) and the sampling time Δt_s (h) (or sampling frequency f_s (h^{-1})) are found as:

$$\Delta t_s \leq \frac{T_{p,min}}{2} \text{ or } f_s \geq 2f_{max} \quad (7.49)$$

$$t_{sim} \geq T_{p,max} \quad (7.50)$$

t_{sim} in turn defines the smallest difference Δf (h^{-1}) between two frequencies contained in the signal:

$$\Delta f \geq \frac{1}{t_{sim}} \quad (7.51)$$

The frequencies contained in the multisine f_i are by consequence elements of the following vector of frequencies:

$$f_i \in [f_{min} : \Delta f : f_{max}] \quad (7.52)$$

This way, the number of frequencies N_f (-) in the multisine is limited.

Table 7.1: Parameters of the multisine excitation signals used for identification.

	t_s (h)	$T_{p,min}$ (h)	$T_{p,max}$ (years)	f_{min} (h^{-1})	f_{max} (h^{-1})	df (h^{-1})	N_f (-)
ID1	0.5	21	1/52	6.00×10^{-3}	6.00×10^{-3}	4.75×10^{-2}	79
ID2	0.5	21	1/12	1.30×10^{-3}	1.30×10^{-3}	4.75×10^{-2}	102
ID3	0.5	21	1/4	4.48×10^{-4}	4.48×10^{-4}	4.75×10^{-2}	104
ID4	1.0	42	1/2	4.48×10^{-4}	2.28×10^{-4}	2.37×10^{-2}	104
ID5	2.0	84	1	1.14×10^{-4}	1.14×10^{-4}	1.19×10^{-2}	104
ID6	0.05	2	1	1.14×10^{-4}	1.14×10^{-4}	0.5	160
ID7	0.05	2	10	1.14×10^{-4}	1.14×10^{-5}	0.5	179

The frequency range covered by the 7 ID sets is graphically presented in Figure 7.12. As a reference, the frequency range of interest, represented by the response of the brine fluid temperature T_f to \dot{Q}_{BHE} as a function of f (calculated based on the DST-model simulations), is depicted. The first five data sets (ID1, ID2, ID3, ID4 and ID5) are used for the time-domain identification of the grey-box models. As explained before, the frequency range of these ID sets is limited by the maximal number of time steps (< 5000). ID1 corresponds to a measurement time t_m of 1 week, sampling time Δt_s of 0.5 h, and captures the response of a multisine with a minimal period $T_{p,min}$ of 20 h and a maximal period $T_{p,max}$ of 1 week. ID2 and ID3 extend t_m to respectively 1 month (744 h) and 3 months (2190 h), with a corresponding increase of $T_{p,max}$ as a result. For

ID3, this brings the number of measurement time steps to 4380 ($=t_m/t_s$), which is close to the maximal number allowed. As a consequence, further increase of the measurement time requires a reduction of the sampling frequency. ID4 covers the time scale from 40 h to 6 months (with $\Delta t_s = 1$ h) and ID5 covers the time scale from 80 h to 1 year (with $\Delta t_s = 2$ h). To summarize, ID1 to ID3 focus on the shorter time scale while ID4 and ID5 focus on the medium time scale. This compromise between short or long time scale is not needed for the identification of the black-box models, i.e. the rational function in s and in \sqrt{s} . Two additional ID sets (indicated in grey in Figure 7.12) are proposed: ID6 extends ID5 towards the very short time scales (down to 2 h) and ID7 additionally extends it towards the very long time scale (up to 10 years).

As an illustration, the multisine \dot{Q}_{BHE} -signal for ID3 is depicted in Figure 7.13. Figure 7.13(a) shows the signal in the time domain and Figure 7.13(b) the amplitude in the frequency domain. The highest frequency contained in the \dot{Q}_{BHE} -signal is, as listed in Table 7.1, about 0.05 h^{-1} , while the sampling frequency f_s , shown at the right end of the frequency axis, amounts to 1 h^{-1} . This is about 10 times the Nyquist frequency. This high safety margin contributes to a good signal-to-noise ratio (see Chapter 2). Note also that the contribution of the different frequencies to the \dot{Q}_{BHE} -signal is more or less equal (namely $0.15 - 0.30 \text{ kW}$), while at the same time the $\dot{Q}_{BHE}(t)$ -profile in the time domain nicely covers the entire power range (namely -4 kW to $+4 \text{ kW}$). This behavior, which also improves the signal-to-noise ratio, is achieved by minimizing the peak-to-average ratio or Crest-factor, defined by Eq.(7.53). The Crest factor should be evaluated in the frequency range of interest.

$$Crest = \frac{\max(\dot{Q}_{BHE}(k))}{RMS} \quad \text{with} \quad RMS = \sqrt{\frac{\sum_{k=0}^{t_m} \dot{Q}_{BHE}(k)^2}{n_m}} \quad (7.53)$$

Model validation methods The models are validated in three steps.

In the first step, the model time constants are calculated to check whether they are within a physical range.

In the second step, the models are validated for 3 data sets, depicted in Figure 7.14. The first validation data set (Val1) comprises the T_f -temperature response to an hourly $\dot{Q}_{BHE}(t)$ -profile for one entire year, a profile which is representative for a balanced GCHP system. The second validation data set (Val2) comprises the T_f -response to an unbalanced $\dot{Q}_{BHE}(t)$ -profile and the third validation data set (Val3) comprises the response to a step heat input over a time frame of 10 years. For Val1 and Val2, the model error is quantified

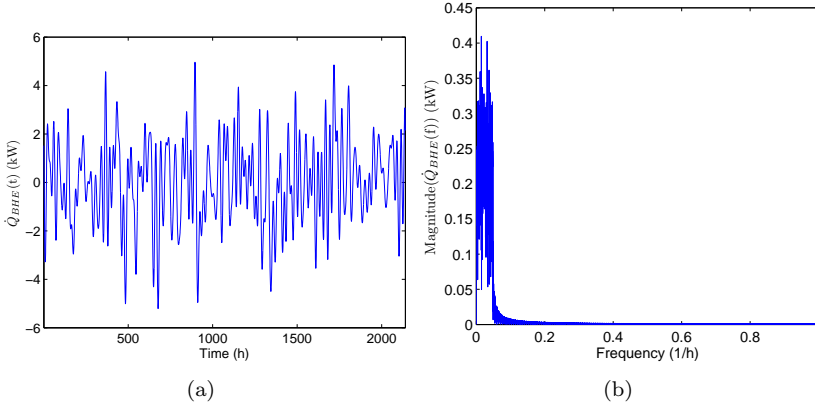


Figure 7.13: Multisine excitation signal with a period of 3 months used for identification (ID set 3). (a) Time domain representation, (b) Frequency domain representation (amplitude only).

in terms of the Root Mean Squared Error (RMSE) ($^{\circ}\text{C}$):

$$\text{RMSE} = \sqrt{\frac{\sum_{k=1}^{n_m} (T_{f,mod}(k) - T_{f,DST}(k))^2}{n_m}} \quad (7.54)$$

where $T_{f,mod}$ ($^{\circ}\text{C}$) represents the model output, $T_{f,DST}$ ($^{\circ}\text{C}$) the DST-model output and $n_m(-)$ the number of data points in the ID set.

For the step response, the model error is quantified in terms of the relative model error (Rel.Error) (%) at time step k :

$$\text{Rel.Error} = 100 \frac{T_{f,mod}(k) - T_{f,DST}(k)}{T_{f,DST}(k) - T_{f,DST}(0)} \quad (7.55)$$

Val1 and Val2 assess the model quality for load variations typically encountered in practice and allow to quantify the model performance for the short and medium time scale (namely from 1 h to 1 year), for both a balanced and an imbalance load profile. The step input is used to evaluate the long term effects of thermal imbalance between the injected and extracted heat loads. This choice of combination of validation sets (Val1, Val2 and Val3) is similar to the combination of sets proposed by Bernier et al. [18]. Note that in what follows, the term 'validation' is not used in its strict sense. In its strict sense, the term 'validation' denotes that the frequency content of the validation data set is covered in the ID set. Here, we will use the term 'validation result' for both

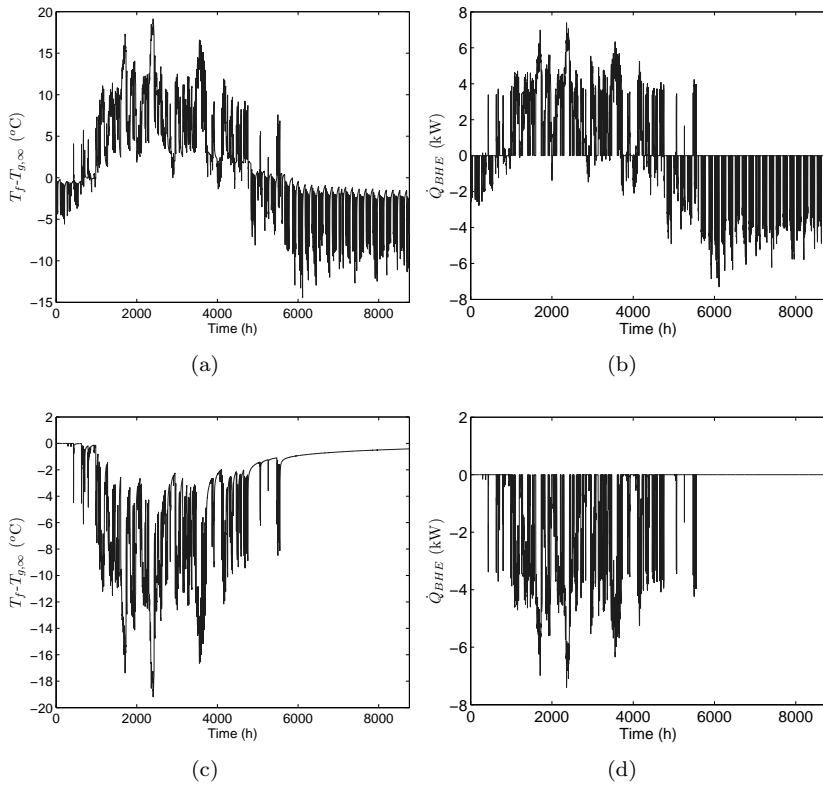


Figure 7.14: Heat injection ($\dot{Q}_{BHE} > 0$) and extraction ($\dot{Q}_{BHE} < 0$) profile used for validation (left) and corresponding fluid temperature profile relative to the undisturbed ground temperature $T_{g,\text{inf}}$ simulated by TRNSYS (right). Validation set 1 (top): balanced annual load profile, Validation set 2 (bottom): imbalanced annual load profile (heating only).

Val1, Val2 and Val3, irrespective of whether the frequency range of the ID set used. This is done to simplify the discussion given the large amount of models and ID sets.

Besides the evaluation of the time constants and the validation in the time domain, the frequency response of the models is compared to the frequency response obtained from the DST-simulation data.

7.4.2 Modeling approaches

White-box modeling with model reduction (MR)

In the case of MR, the initial (white-box) model determines the maximum obtainable degree of accuracy. A very detailed initial model to start from, is for instance the DST-model, as proposed by Franke [54]. In this study the use of a simpler initial model is investigated, namely a one-dimensional finite difference model (1D-FDM). The time frame for which this 1D-representation is accurate, is first discussed. Next, the MR techniques are briefly introduced.

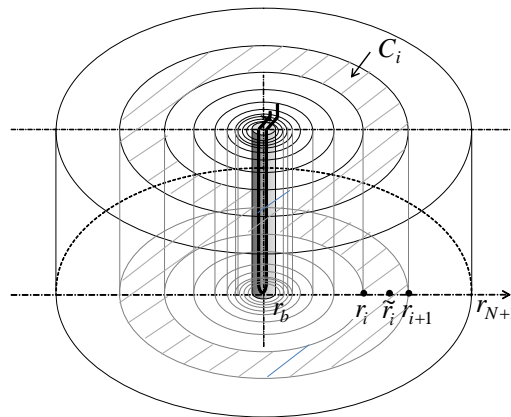


Figure 7.15: Discretization of the ground surrounding a single BHE into a finite number of cylindrically shaped volumes.

Initial model: one-dimensional finite difference model based on Eskilson's guidelines The 1D, radial approximation of the heat diffusion process in the ground can be modeled as a series of concentric volumes, each representing a thermal capacity C_i , separated by thermal resistances R_i . This is schematically shown in Figure 7.15. The inner node (left-hand side in Figure 7.16) represents the mean fluid temperature (T_f) at which the heat is supplied. The outer node represents the undisturbed ground temperature ($T_{g,\infty}$).

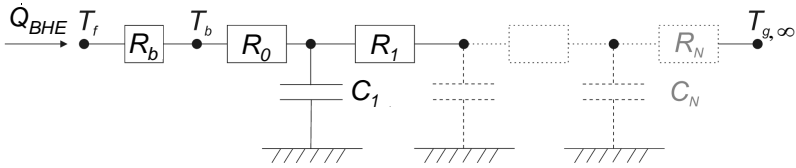


Figure 7.16: RC-network representation of the one-dimensional radial approximation of heat diffusion in the ground.

This representation is based on two assumptions that define the time frame for which this representation is accurate. First, it is assumed that the heat transfer rate from the fluid to the ground is directly proportional to the difference between the mean fluid temperature T_f and the mean borehole wall temperature T_b and inversely proportional to the effective borehole wall resistance R_b (K/W). This assumption holds for time scales larger than the borehole time t_{bh} , which is the time needed to reach a steady state temperature distribution inside the borehole after implying a step heat input, calculated from Eq.7.56, with r_b (m) the borehole radius and α [m^2/s] the thermal diffusivity of the ground. For the parameters r_b and α of the borehole considered,

$$\dot{Q}_{BHE} = \frac{1}{R_b} (T_f - T_b) \quad \text{for } t > t_{bh} \approx \frac{5r_b^2}{\alpha} \quad (7.56)$$

The second assumption is that heat conduction in the ground is considered to occur only radially. In the most general description, the heat transfer from the borehole wall to the surrounding ground is three dimensional with a radial component r , an angular component θ and an axial component z . For axisymmetrical cases, it can be described by a radial and axial component only. Axial conduction, however, starts influencing the temperature distribution around the borehole only for unbalanced heat injection or heat extraction profiles after a couple of years. For time scales shorter than 5% of the steady-state time t_s , calculated according to Eq.(7.57), the axial heat transfer can be neglected [43, 105].

$$T(r, \theta, z, t) \approx T(r, t) \quad \text{for } t < \frac{t_s}{20} \quad \text{with } t_s \approx \frac{H^2}{9\alpha} \quad (7.57)$$

For the borehole considered, t_s amounts to 65 years. For time frames shorter than 3 years or for loads which are balanced on a yearly term, it is therefore allowed to consider only the radial heat transfer component. The RC-model presented in Figure 7.16 is therefore adequate to describe the response of the fluid temperature to a step heat input between those two time scales, 10 h to 3

years ($t_b < t < t_s/20$). Extrapolation of this model to shorter or longer time scales will introduce some errors due to the neglect of the transients related to the inner problem on the other hand, and heat conduction in the axial direction on the other hand.

Eskilson [43] presented the following guidelines for the grid generation :

$$\Delta r_{min} = \min(\sqrt{\alpha \Delta t_{min}}, H/5) \quad (7.58a)$$

$$r_{max} = 3\sqrt{\alpha t_{max}} \quad (7.58b)$$

$$\Delta r = [\Delta r_{min}, \Delta r_{min}, \Delta r_{min}, \beta \Delta r_{min}, \beta^2 \Delta r_{min}, \dots] \quad (7.58c)$$

$$r_1 = r_b \quad (7.58d)$$

$$r_{i+1} = r_i + \Delta r_i \quad (7.58e)$$

$$r_{N+1} \geq r_{max} \quad (7.58f)$$

The grid parameter t_{max} determines the lower bound for the outer radius r_{max} while t_{min} determines the upper bound for the mesh size near the borehole wall Δr_{min} . Δr_{min} is repeated three times, after which the mesh size expands with a factor β until the lower bound of the outer radius r_{max} is reached. The choice of the grid parameters Δt_{min} , t_{max} and β determines the resulting model order N .

The nodes are located in the center of the cylindrical volumes:

$$\tilde{r}_i = \frac{r_i + r_{i+1}}{2} \quad \text{for } i = 1..N \quad (7.59)$$

Subsequently, the values of the thermal resistances R_i and capacities C_i are determined:

$$R_0 = \frac{1}{2\pi k_g H} \ln\left(\frac{\tilde{r}_1}{r_b}\right) \quad (7.60a)$$

$$R_i = \frac{1}{2\pi k_g H} \ln\left(\frac{\tilde{r}_{i+1}}{\tilde{r}_i}\right) \quad \text{for } i = 1..N - 1 \quad (7.60b)$$

$$R_N = \frac{1}{2\pi k_g H} \ln\left(\frac{\tilde{r}_{N+1}}{\tilde{r}_N}\right) \quad (7.60c)$$

$$C_i = \rho c_g \pi (r_{i+1}^2 - r_i^2) H \quad \text{for } i = 1..N \quad (7.60d)$$

Eskilson (1987) has shown that the 1D -FDM based on the above mentioned guidelines predicts the response to a step heat input with a relative error of

Table 7.2: Results for 1-D finite difference models: Model order N and relative model error for the temperature response to a step heat input.

Time frame	Model parameters			Relative model error (%)						
	Δt_{min} [h]	t_{max} [h]	N	1 day	1 week	1 month	6 months	1 year	10 years	t_{max}
1 week	1	189	8	-1.	-1.05	-0.82	-8.44	-13.3	-25.8	-0.79
1 month	1	490	9	-1.7	-1.05	-0.68	-1.03	-2.86	-15.8	-0.54
6 month	1	7.42×10^3	10	-1.7	-1.05	-0.68	-0.48	0.02	-5.8	-0.17
1 year	1	2.94×10^4	11	-1.7	-1.05	-0.68	-0.48	0.06	1.69	1.39
10 year	1	1.17×10^5	12	-1.7	-1.05	-0.68	-0.48	0.06	2.62	>2.62

maximum 1% compared to the analytical solution. Δt_{min} must then be equal or smaller than the simulation time step and t_{max} equal or larger than the simulated time period. The grid expansion term β is 2. These grid guidelines are applied for 5 different time frames, each characterized by a certain value for Δt_{min} and t_{max} , resulting in five models of different order. For each model, the response to a step heat input is compared to the response obtained by the TRNSYS DST-model. The relative model errors are evaluated at different times according to Eq.(7.55).

The results are listed in Table 7.2 and plotted in Figure 7.17. The validity range of the model structure can be clearly observed. First, the fact that the relative model error is larger during the first week agrees with the theory that the steady state approximation of the inner problem is only accurate after the borehole time t_{bh} (see Eq.7.56). Second, the relative model error evaluated at the time value t_{max} for which the numerical grid was sized, given in the last column, remains below 1.5% as predicted by Eskilson (1987). The model set up with t_{max} equal to 10 years forms an exception, as the relative error at t_{max} exceeds 2.5%. This is due to the fact that for time scales longer than 5% of the steady state time t_s (3 years, see Eq.7.57), axial effects start playing a role. As the axial heat losses are not taken into account by the radial model, the response of the fluid temperature to a step heat input is overestimated in the long-term.

The extrapolation characteristics of the models are clear from Figure 7.17 and from the values presented in grey in Table 7.2. The model error drastically increases for time frames larger than t_{max} . It therefore makes sense to choose the grid parameter value t_{max} large, which does not cause a huge increase in the model order N , as is clear from the fourth column of Table 7.2. The majority of nodes are needed to describe the fast dynamics close to the borehole.

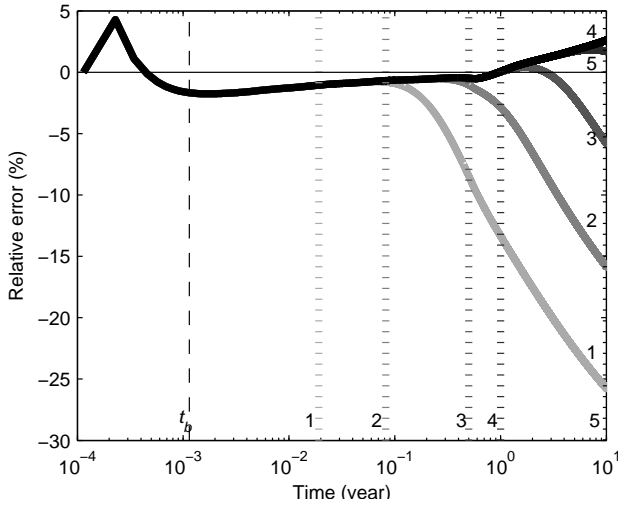


Figure 7.17: Relative model error for the temperature response to a step heat input for the 1D-FDMs set up according to Eskilson's guidelines with the grid parameter Δt_{min} equal to 1 hour and t_{max} equal to respectively (1) one week, (2) one month, (3) 6 months, (4) one year and (5) 10 years, indicated by the dotted vertical lines. The dashed vertical line at the left indicates the borehole time t_{bh} , below which the steady state assumption for the inner process in the borehole is invalid.

Model reduction methods The values in the fourth row of Table 7.2, listed in bold, show that the model order needed to describe the response to a step heat input after 10 years up to 2% accuracy, amounts to 11. In this section it is investigated how the model accuracy is affected when this 11th order model is reduced to lower order models by means of MR. Two methods, namely 'matchDC' and 'Truncate', both implemented in the MATLAB routine `balred` [118], are compared. `balred` first computes a balanced realization of the system matrices. The original states are recombined to new states which are ordered according to their associated Hankel Singular Value (HSV). The latter is a measure for the contribution of that state to the input/output behavior. From this balanced realization a reduced-order approximation is derived, based on the user specified option ('matchDC' or 'Truncate'). The option 'matchDC' guarantees that the steady-state behavior of the initial model is matched. The option 'Truncate' tries to optimize the dynamic behavior over the entire time domain by discarding the states associated with the smallest Hankel singular values. In the latter case a match of DC-gains is not guaranteed [118].

Grey-box modeling with parameter estimation (PE)

Model structure A second approach to obtain low-order models, investigated in this study, is parameter estimation (PE). The model structure, presented in Figure 7.18, is the same as for the white-box model (see Figure 7.16), but the model order N' is varied between 1 and 11. The corresponding model parameters C'_i and R'_i (with i ranging from 1 to N') are determined by PE for different identification data sets which are obtained with the TRNSYS DST-model. The initial values are based on the known geometrical and thermal system properties. This is needed to obtain convergence to physically meaningful parameter values.

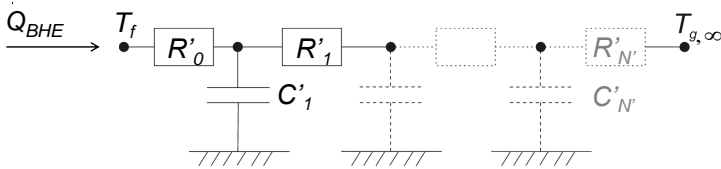


Figure 7.18: Model structure of the grey-box models, based on the one-dimensional radial approximation of heat diffusion in the ground. The model order N' is varied between 1 and 11 and the model parameters R_0 to R'_N (W/K) and C_1 to C'_N (J/K) are determined by parameter estimation (PE), with their initial guess based on physical insights.

Initial parameter values The initial guess for the parameters is obtained from a 1D-FDM. Contrary to the set up of the 1D-FDM used as initial model for MR, where Δr_{min} is found as a function of the parameter Δt_{min} , see Eq.(7.58a), Δr_{min} is calculated as a function of the desired model order N' :

$$\Delta r_{min} = r_{max} \left(2 + \frac{\beta^{N'-2} - 1}{\beta - 1} \right) \quad (7.61)$$

The parameter t_{max} , which defines r_{max} via Eq.(7.58b), is set to 1 year. The grid expansion factor β equal to 2. The R'_i and C'_i -values calculated according to Eqs.(7.58-7.60), are used to determine the initial guess for the parameters. To investigate the impact of the initial guess on the optimization result, the PE procedure has also been performed from initial guesses obtained with other values for t_{max} and β .

Parameter estimation Starting from the initial guess for the model parameters (R'_i and C'_i), the optimal parameters for a given identification data set are found as the solution which minimizes the sum of squared errors between the low-order model output and the TRNSYS DST-model output. The resulting non-linear least squares problem is solved using the Levenberg-Marquardt algorithm. As excitation signals, multisine load profiles of different time lengths are used. Their characteristics are presented in Table 7.1. A careful choice of the initial guess for the parameter values, based on the physical insights (see previous paragraph) is required to obtain convergence to a physically meaningful optimum.

Black-box modeling

Motivation The dynamic time range of a BHE is very large, ranging from the hourly scale to tens of years. Capturing this entire range in one ID set requires both a small sampling time and a long simulation time. This results in a huge amount of data, which is computationally difficult to handle in the time domain. Hence for time-domain identification a trade-off must be made between sampling frequency and simulation time and thus between capturing fast or slow dynamics. For frequency domain identification, on the contrary, there is no computational limitation for the frequency range covered by the identification data. The system identification procedure will be performed for ID3, ID4 and additionally for ID6 (2 h-1 year) and ID7 (2 h-10 years) (see Figure 7.12). In contrast to the grey box-modeling approach, however, the black-box procedure does not incorporate prior knowledge of the borefield and ground thermal properties. Comparison of the model performance obtained with the three modeling procedures will thus allow to:

- quantify the impact of the frequency content of the ID set:
 - (a) white-box (MR): none
 - (a) grey-box (PE): limited frequency range
 - (b) black-box (s) and (\sqrt{s}): entire frequency range of interest
- and quantify the impact of incorporating physical knowledge:
 - (a) white-box (MR): RC-model structure + parameters
 - (b) grey-box (PE): RC-model structure + parameters initial guess
 - (c) black-box (s): none, black-box (\sqrt{s}): diffusion process

Model structure The first set of black-box models are rational transfer functions in the Laplace variable s :

$$\frac{T_f(s)}{\dot{Q}_{BHE}(s)} = \frac{b_z s^z + b_{z-1} s^{z-1} + \dots + b_0}{a_p s^p + a_{p-1} s^{p-1} + \dots + a_0} \quad (7.62)$$

where z denotes the number of zeros, p the number of poles with z always $\leq p$. b_i and a_i are the corresponding coefficients. The rational function in \sqrt{s} is presented by Eq.(7.63):

$$\frac{T_f(s)}{\dot{Q}_{BHE}(s)} = \frac{b_z (\sqrt{s})^z + b_{z-1} (\sqrt{s})^{z-1} + \dots + b_0}{a_p (\sqrt{s})^p + a_{p-1} (\sqrt{s})^{p-1} + \dots + a_0} \quad (7.63)$$

This \sqrt{s} -representation originates from the fact that diffusion processes, such as thermal diffusion, result in a \sqrt{s} -representation in the Laplace domain. In the time domain, this gives rise to a fractional order differential equation. The domain of 'fractional order control' (FOC) deals with the design of PI-controllers for these kind of systems [see e.g. 113]. Implementation of the \sqrt{s} -models in an optimization framework requires fitting a higher-order s -model in the control frequency range. The latter is not investigated in this work.

System identification The coefficients a_i and b_i are fitted in the frequency domain, using the Matlab FDIDENT toolbox [99]. The procedure does not require an initial guess for the a_i or b_i , only the steady state system response to a multisine excitation. The software allows to user to vary the number of zeros z and poles p between any range. For each combination of z and p , FDIDENT optimizes the a_i and b_i coefficients. For the entire range of z and p , the cost function $V(z, p)$ (evaluated in terms of the model error) is graphically represented. The user can select the best model as the one with the lowest cost function evaluation, or as the one with the lowest AIC-value (see Eq.(2.14) on p.20). For each ID set, only the model with the lowest AIC value is retained.

7.4.3 Results

This section evaluates the three modeling approaches. The models are validated in the time domain (Val1, Val2 and Val3) and in the frequency domain. A first evaluation of the models is based on a graphical representation of the time constants of the different models obtained.

Time constants

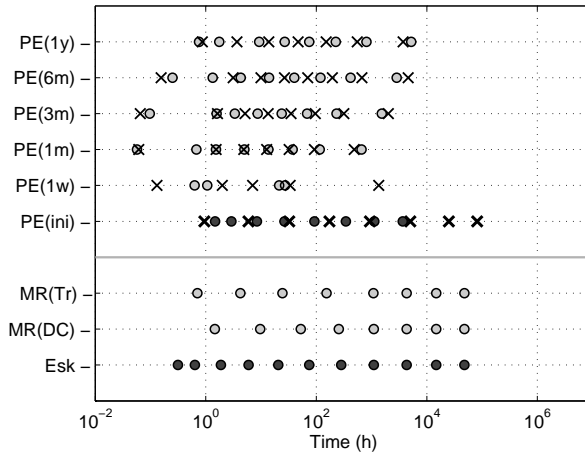
Heat diffusion is characterized by an infinite number of time constants with a continuous distribution. Simulation of heat diffusion by a numerical model limits the number of time constants or nodes to a finite number, equal to the model order N .

Figure 7.19(a) and Figure 7.19(b) depict the time constants of the models obtained by MR and by PE for respectively $N = 8$ and $N = 4$ on a logarithmic scale. The time constants of the 11th order model obtained when following Eskilson's grid generation guidelines and used as initial model for MR (MR(ini)), range from 1 h, related to the inner node, to 10^5 h, related to the outer node. The 'matchDC' MR method (MR(DC)) only keeps the N largest time constants. The 'Truncate' method (MR(Tr)) puts one of the time constants more towards the left in order to describe also the faster dynamics. For the models obtained by PE the location of the time constants depends on the identification data set. The shorter the time length of the identification data set (ID1 (1 week) < ID2 (1 month) < ID3 (3 months) < ID4 (6 months) < ID5 (1 year)), the smaller the time constants of the resulting model. The degrees of freedom are used to describe as accurately as possible the frequency range contained in the excitation signal.

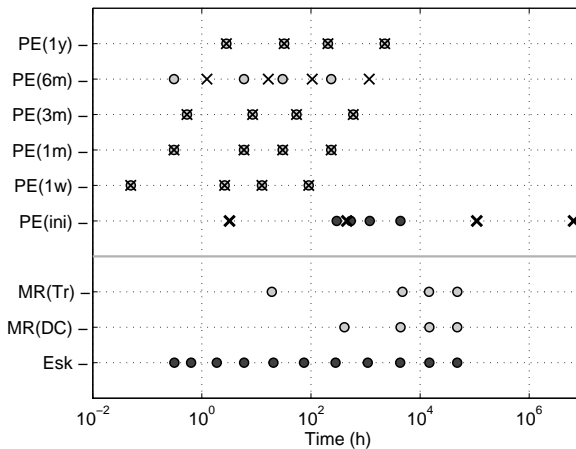
The influence of the initial guess on the optimization result is investigated by using two different starting models for PE (see PE(ini)). In Figure 7.19 they are indicated by respectively a circle ('o') and a cross ('x'). For $N = 4$, the position of the time constants is unique for the majority of identification data sets, i.e. independent of the initial guess for the parameters. For $N = 8$, on the contrary, the solution depends on the initial parameter values. This means that there are local minima if the model order is high.

Figure 7.20 depicts the time constants of the s -models obtained by black-box system identification. For each ID set only the result for the best model (defined as the model with the lowest AIC value, see Chapter 2) is shown. The time constants are nicely spread over the entire frequency range covered by the ID sets. Note however that the smallest time constant, located at the left end and circled in red, for all investigated cases corresponds to a pair of complex poles.

The \sqrt{s} -models can not be characterized by time constants.



(a)



(b)

Figure 7.19: Comparison of the time constants of the BHE-models obtained with MR and PE of order $N = 8$ (a) and $N=4$ (b). Below the horizontal grey line: Models obtained by MR using the 'Match DC' option (MR(DC)) and the 'Truncate' option (MR(Tr)) of the 11th order 1D-FDM obtained with Eskilson's guidelines (Esk). Above the horizontal grey line: Two starting models for PE (PE(ini)), marked by respectively 'o'(bold) and 'x'(bold) and the corresponding models found by PE with the identification data sets ID1 (PE(1w)), ID2 (PE(1m)), ID3 (PE(3m)), ID4 (PE(6m)) and ID5 (PE(1y)).

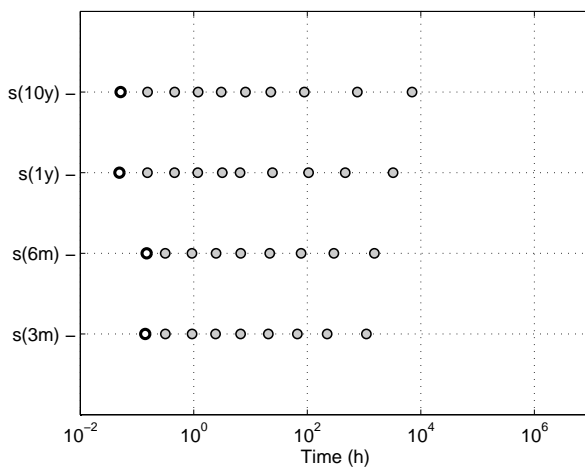


Figure 7.20: Comparison of the time constants of the black-box s -models obtained with an identification data set length of respectively 3 months, 6 months, 1 year and 10 year ($s(\text{ID}3)$, $s(\text{ID}4)$, $s(\text{ID}6)$, $s(\text{ID}7)$). The first markers, circled in black, denote time constants related to a pair of complex poles.

Validation in the time domain

The model accuracy is evaluated for 3 distinct validation data sets, presented in Figure 7.14: Val1, which corresponds to a typical balanced annual heat injection and extraction profile, Val2, which corresponds to a typical imbalanced heat profile (extraction only) and Val3, being a step heat input. The model accuracy for Val1 and Val2 is quantified in terms of the RMSE ($^{\circ}\text{C}$), the accuracy for Val3 in terms of the relative model error (Rel.Error)(%) evaluated after 10 years.

This section is structured as follows. First, the validation results obtained with the MR and the PE approach are presented, with focus on the influence of the model order N . The RMSE for the Val1, Val2 and Val3 is graphically presented as a function of N (see Figure 7.21). For the MR method (see left hand side of Figure 7.21), the influence of the model reduction method ('MatchDC' versus 'Truncate') is analyzed, while for the PE method (see right hand side of Figure 7.21), the influence of the ID set is quantified. For the black-box approach the influence of N is *not* analyzed: for each ID set, only the model yielding the lowest AIC value is retained. The first part of this section therefore only deals with the MR and PE approach. In the second part, the difference between the black-box and the grey-box models is evaluated and discussed.

White-box (MR) and grey-box (PE): validation as a function of the model order N

The validation results for the MR and the PE approach are presented in Figure 7.21. The plots at the left-hand side contain the results for the models obtained by MR, the plots at the right-hand side show the results for the models obtained by PE. Figure 7.21(a) and Figure 7.21(b) show the RMSE as a function of the model order N . For both approaches, the model accuracy hardly changes when the model order is reduced from the initial order of 11 down to model order 6. However, the validation results for N lower than 5 differ substantially. For the models obtained by MR, the RMSE strongly increases for $N < 5$ whereas the increase is far more moderate (but still significant) in case of PE. As an illustration, the RMSE values for validation set 1 (representing a balanced load profile) amount to 4.6°C , 1.2°C and 0.6°C for the reduced models of order N respectively 2, 4 and 6. For the models identified with the identification set of 3 months, the RMSE is a factor 5 to 2 lower, respectively 1.0°C , 0.4°C and 0.3°C . For $N < 6$ the absolute error of the models obtained by PE is almost a factor 4 lower than for the ones obtained by MR, namely 3°C , 2°C and 1.2°C compared to 9°C , 5°C and 0.6°C . Given the amplitude of the T_f signal of 35°C (depicted in Figure 7.14(b)), the maximum relative error of the former equals 10% for $N = 2$, 6% for $N = 4$ and 4% for $N = 6$. Increasing the time span covered by the identification data set, further improves

the model accuracy. Further increasing the model order, however, does not. On the contrary, it was found that for $N > 6$ the PE procedure sometimes yields unstable models, depending on both the choice of the initial guess and on the identification data set. This indicates that for $N > 6$ there are too many degrees of freedom compared to the information contained in the identification data set.

The results for Val1 clearly show that PE is more adequate than MR for obtaining low-order models able to describe the dynamics excited by a typical balanced load profile. The impact of load imbalance on the prediction quality is quantified by validating the models for Val2. The validation results for the models obtained by MR and PE are shown in respectively Figure 7.21(c) and 7.21(d). Comparison of these two graphs reveals that for $N < 6$, PE still performs better than MR. For $N > 6$, the MR technique discards fewer modes related to the faster dynamics, resulting in a better performance than the models obtained by PE.

The ability to describe the slow dynamics is investigated by applying a step heat input and evaluating the relative error on the mean fluid temperature T_f after one year. The validation results for the models obtained by MR and PE are presented in respectively Figure 7.21(e) and Figure 7.21(f). Two conclusions can be drawn. First, the low order models obtained by MR accurately describe the slow dynamics, at least if the 'MatchDC' option is used. Given the results for Val1, (see Figure 7.21(a)) it can be concluded that the 'Truncate' method, which tries to achieve a fit for the entire frequency range, is inadequate since neither the fast (excited by Val1) nor the slow dynamics (excited by the step heat input) are well described. Second, the models obtained by PE, result in larger relative errors. This is explained by the fact that the model parameters have been optimized for the given, restricted time frame covered by the identification data which do not capture the long-term dynamics excited by the step heat input.

The RMSE for this 10-year evaluation is shown in Figure 7.22. As for the 1-year-simulations, for lower values of N the RMSE is by far the smallest for the models obtained by PE. For higher values of N the MR method yields more accurate models.

Comparison of the grey-box (PE) and the black-box (s and \sqrt{s}) results

The difference between the grey-box and the black-box models is summarized in Table 7.3. For the black-box models in s and \sqrt{s} , the tabulated values

Table 7.3: RMSE for validation data sets Val1 (1 year) and Val3 (10 years) of the BHE-models obtained with the grey-box modeling approach (RC) and the black-box system identification approach (s and \sqrt{s}). For each model, the number of zeros z and poles p is given, the latter corresponding to the model order N . Identification data sets ID6 and ID7 could only be used within the black-box system identification framework in the frequency domain.

	ID3			ID4			ID6		ID7	
	RC	s	\sqrt{s}	RC	s	\sqrt{s}	s	\sqrt{s}	s	\sqrt{s}
z/p	8/8	8/8	2/5	8/8	8/8	2/5	11/11	2/5	11/11	7/7
Val1	0.002	0.010	0.018	0.003	0.079	0.057	0.038	0.046	0.066	0.024
Val3	0.63	0.83	0.33	0.37	0.67	0.29	0.49	0.17	0.30	0.06

correspond to the best model, based on the AIC value, for the given ID set. For the s -models these are the 8th order model (ID3, ID4) and the 11th order model (ID6, ID7). For the \sqrt{s} -models, these are the 5th order model (ID3, ID4, ID6) and the 7th order model (ID7), which shows that the model order of \sqrt{s} -models tend to be smaller than for s -models.

In general, very high model accuracies are achieved with all model types. The RC-models are the most accurate for the validation set Val1 (1year), while \sqrt{s} -models perform best for the extrapolation set represented by Val3 (10 year). The quality of the s -models found is inferior to that of the RC-models. However, as the grey-box model structures are RC-networks which belong to the s -model set, the global optimum of the s -model set should be at least as good as the one for the RC-model set. This suggests that the s -model identification in the frequency domain got stuck in a local minimum. The results for ID6 and ID7 show that the wider range covered by the identification data effectively results in both an improved short-term and long-term prediction.

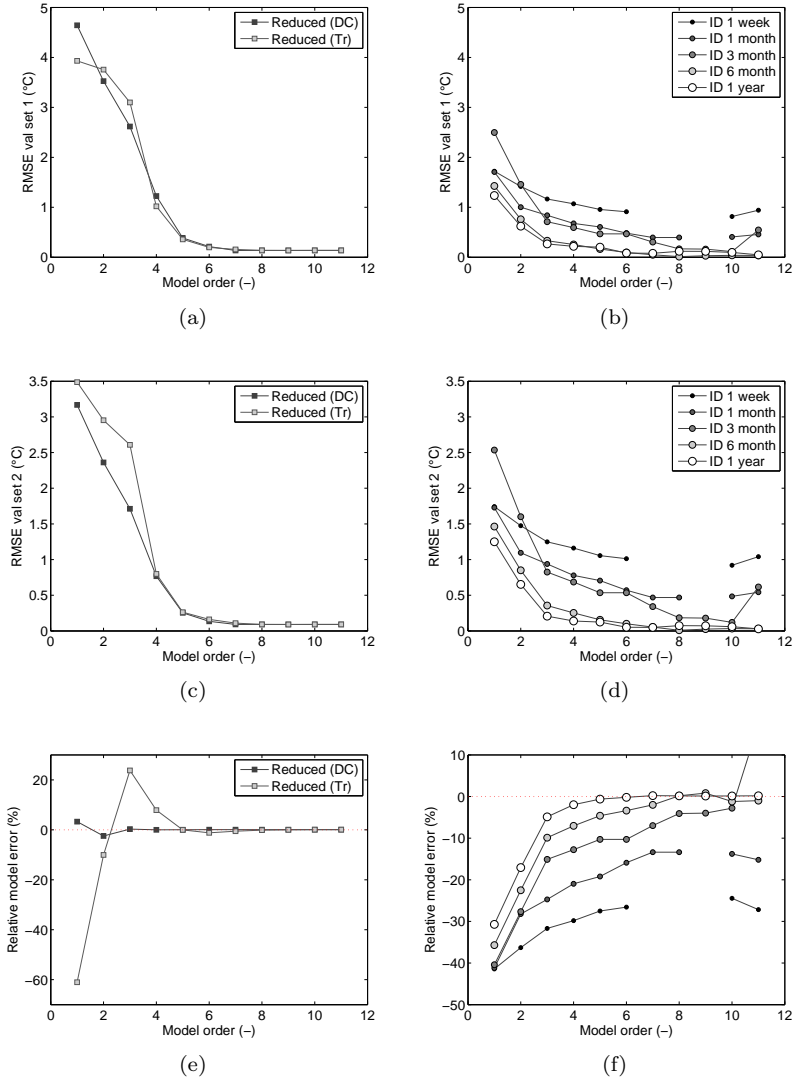


Figure 7.21: Validation results for the models obtained by MR ('MatchDC') (left) and for the models obtained by PE (right) for model order N ranging from 1 to 11. Unstable models, which yield very high RMSE values, are not displayed. Top: RMSE for Val1 (balanced annual load profile), Middle: RMSE for Val2 (imbalanced annual load profile), Bottom: Relative model error for Val3 (step heat input) at time step $t = 8760h$ (1 year).

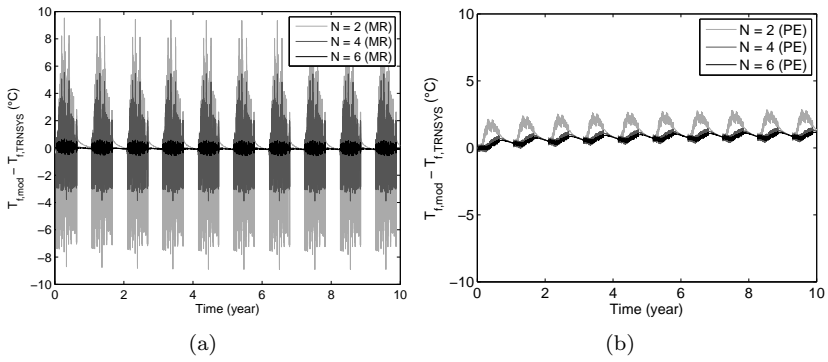


Figure 7.22: Absolute error on T_f for validation set 2 - repeated for 10 years - for the models obtained by MR (Truncate) (left) and for the models obtained by PE (ID 3 months) (right).

Validation in the frequency domain

Figure 7.23 and Figure 7.24 compare the frequency response of the low-order BHE models to the frequency response determined from the DST-model simulation results. The frequency range displayed corresponds to periods ranging from 1 hour to 100 years.

The magnitude plots on the left show that the grey-box models (PE) and the black-box models (s and \sqrt{s}) are accurate within the frequency band of the ID set. For lower frequencies outside this band, the fit of the \sqrt{s} -models is better than that of the RC- and s -models. This indicates that the \sqrt{s} -models are better suited for long-term extrapolation.

The phase plots on the right show a more pronounced difference between the 4 model types. The phase of the frequency response of the models obtained by MR (Figure 7.23(b)) does not properly fit the TRNSYS-simulation results. The models obtained by PE (Figure 7.23(d)) and black-box system identification (Figure 7.24(b,d)) are accurate in the frequency band of the ID set. Outside this band all models deviate from the TRNSYS-data. The deviation is again the smallest for the \sqrt{s} -models. Theoretically, analytical solutions are functions of the square root of the time variable, so the low frequent diffusion behavior of the borehole is predictably better described by the \sqrt{s} -models, even with a smaller model order compared to the s -model.

Note The graphs reveal that the frequency response obtained from the TRNSYS DST-model has a number of local discontinuities. These are located at the frequencies where the response of different sets of multisines (5 in total) are concatenated. These numerical artefacts probably explain the inferior performance of the s -models compared to the RC-models. A new set of TRNSYS simulations data, to obtain a smoother frequency response signal for the frequency domain system identification, could alleviate this problem. This result however clearly shows that care should be taken when using numerical models as a reference.

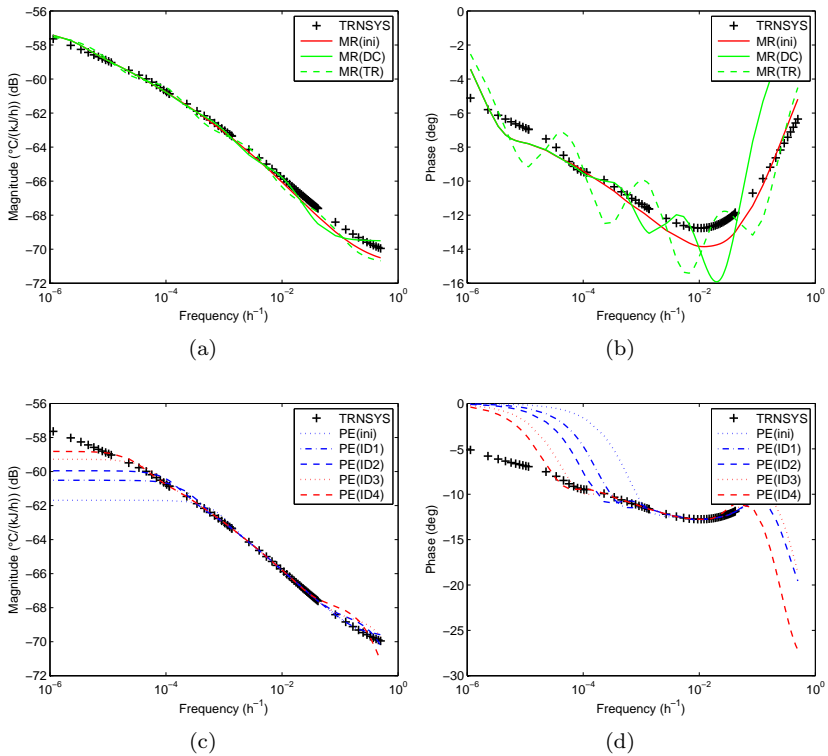


Figure 7.23: Magnitude (left) and phase (right) of the 6th-order BHE-models obtained by (above) model reduction (MR) of a first-principles initial model (MR(ini)) with respectively the 'Match-DC' method (MR(DC)) and the 'Truncate' method (MR(Tr)) and by (below) parameter estimation (PE) with identification data sets covering different time scales (ID1, ID2, ID3, ID4, ID5).

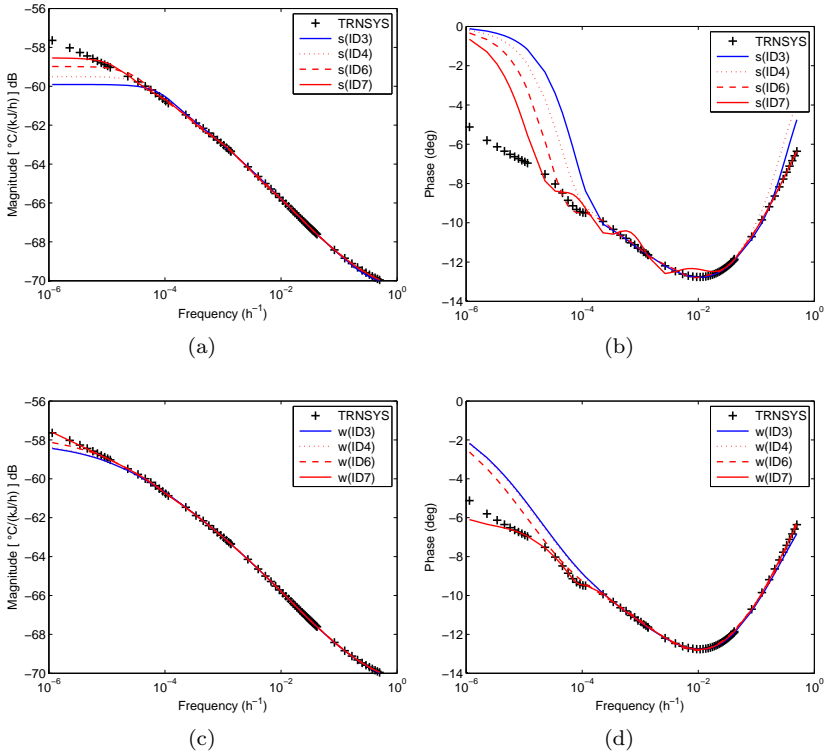


Figure 7.24: Magnitude (left) and phase (right) of the best-fit rational models in the Laplace-variable s (above) and in \sqrt{s} (below, legend (w)) obtained by black-box system identification with identification data sets covering different time scales (ID3, ID4, ID6, ID7).

7.4.4 Sensitivity to non-idealities

The results presented above are obtained under some assumptions, which do not necessarily hold in practice:

- The values for the ground thermal properties and borehole resistance used to set up the 1D-FDM - which is subsequently used for MR - are identical to the values used in the TRNSYS DST-model. In practice, the accuracy of the values determined from a TRT is limited by the quality of the measurement set up. Moreover, the ground thermal properties are not homogeneous. Both factors will affect the quality of the 1D-FDM and, as a consequence, the quality of the reduced models.
- The grey-box and black-box models are based on simulation data for multisine load profiles without measurement noise. In practice measurement data from the borefield in operation will be used. Those are prone to measurement noise and missing data. Moreover, typical building loads will not excite all frequencies equally.

In this section a sensitivity study is performed to investigate the impact of these non-idealities. The influence of the ID set on the model quality is only performed for the grey-box models (PE). Assessing the impact of non-idealities for the black-box SI approach fits within in the scope of the ongoing FWO project 'Black-box model based predictive control of ground coupled heat-pump systems'.

White-box with MR: Impact of uncertainty on the physical parameters

The ground thermal conductivity k_g and the borehole thermal resistance R_b can be obtained from a TRT with an uncertainty of respectively 10% [7, 61, 188] and 10 to 20% [60]. The ground thermal capacity ρc_g is known with an uncertainty of typically 20% Wagner and Clauser [180]. To analyze the impact of these uncertainties on the accuracy of the 1D-FDM and the models derived by MR, the values for R_b and k_g have been perturbed with -10% and +10% of their nominal value (used in the TRNSYS DST-model) and the value for ρc_g with -20% and +20%. The results are depicted in Figure 7.25. Figure 7.25(a) shows the RMSE for validation set 1, Figure 7.25(b) shows the relative model error to a step heat input after one year. It is observed that *a bad estimate of the k_g substantially decreases the model accuracy.*

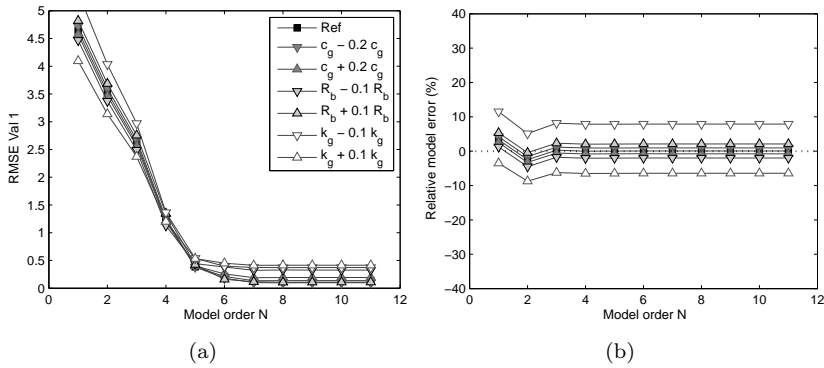


Figure 7.25: RMSE in the case of validation set 1 (left) and relative error to a step heat input after 1 year (right) for the models obtained by MR of a 1D-FDM and this in the case of an estimation error on the values for the physical parameters ρc_g , R_b and k_g .

The RMSE for validation set 1, see Figure 7.25(a), and the relative model error to a step heat input, see Figure 7.25(b), both increase by almost 10% for an error on k_g of 10%. The impact of an error on the estimate for R_b is smaller. The relative error to a step heat input is only about 2%. The impact of an estimation error on the parameter ρc_g of 20% is found to be negligible.

Grey-box with PE: Impact of excitation signal and measurement noise

The PE procedure is repeated with a heat injection and extraction profile for an office building with CCA as excitation signal. Note that this excitation signal differs from the load profiles used for validation, depicted in Figure 7.14. The excitation signal is applied to the TRNSYS DST-model to obtain the simulation results for the fluid water temperature T_f . For PE, white noise is added to both the input \dot{Q} and the output T_f . In this study, the standard deviation of the measurement error on \dot{Q} is varied between 0% and 20%, based on the value of 10% reported by Gentry et al. [61]. The measurement error on T_f is varied between 0°C and 0.3°C, based on the value $\pm 0.11^\circ\text{C}$ reported by Hern [79]. The results for an identification time length of 3 months are presented in Figure 7.26. For comparison, also the results obtained for the reference identification data set, i.e. a multisine excitation signal and no measurement noise, are shown. Figure 7.26(a) and Figure 7.26(b) at the top and Figure 7.26(c) and Figure 7.26(d) at the bottom show the validation results for various

amplitudes of the temperature measurement error for respectively the case without and with measurement noise on the input \dot{Q} .

These figures show that *the main impact of measurement noise is the reduction of the maximum model order yielding a stable model*. Without noise, a stable model is found up to $N = 11$. In the presence of noise, the maximum model order is 5 or 4, depending on the magnitude of the measurement noise. However, if a stable model is obtained, the validation results are improved compared to the reference case (i.e. multisine, no measurement noise). This improvement holds for both validation set 1 and step heat input. The same trends are observed for the shorter and longer identification time lengths, not displayed here. From these observations it is concluded that the use of measurement data of a heat pump system in operation on the one hand impose an upper bound on the model order (due to the presence of measurement noise), but may on the other hand result in a model which enables to accurately predict the fluid temperature (due to the fact that the identification data set contains the relevant information needed for PE). With measurement data covering 3 months, a fifth order model is obtained characterized by an RMSE of about 0.6°C for validation data set 1, which, given the temperature amplitude of 35°C (see Figure 7.14(b)), corresponds to a relative model error of less than 2%.

7.4.5 Summary and conclusions

Three distinct approaches are investigated to obtain a low-order dynamic borefield model for control purposes: white-box modeling with model reduction (MR), grey-box modeling with parameter estimation (PE) and black-box system identification in the Laplace variable s and the Warburg variable \sqrt{s} .

The validation results showed an inferior model quality obtained with the black-box modeling approach. This inferior performance could however be attributed to discontinuities in the frequency response signal used as input.

Table 7.4 summarizes the results for MR and PE. First, it is found that an 11th order 1D-FDM, based on the guidelines of Eskilson (1987), predicts the fluid temperature output from the TRNSYS-DST-model for various hourly load profiles (i.e. Val1, Val2 and Val3) with a relative error of 0.6% for a time horizon of 1 year, and with a relative error of less than 2% for a time horizon of 10 years (see column 1D-FDM). Second, the results have proven that the order of this 1D-FDM can be reduced down to a sixth order model with the 'Match DC' method without a major loss in accuracy (see column MR(DC)). The validation error remains below 1% for the time frame of 1 year and hardly

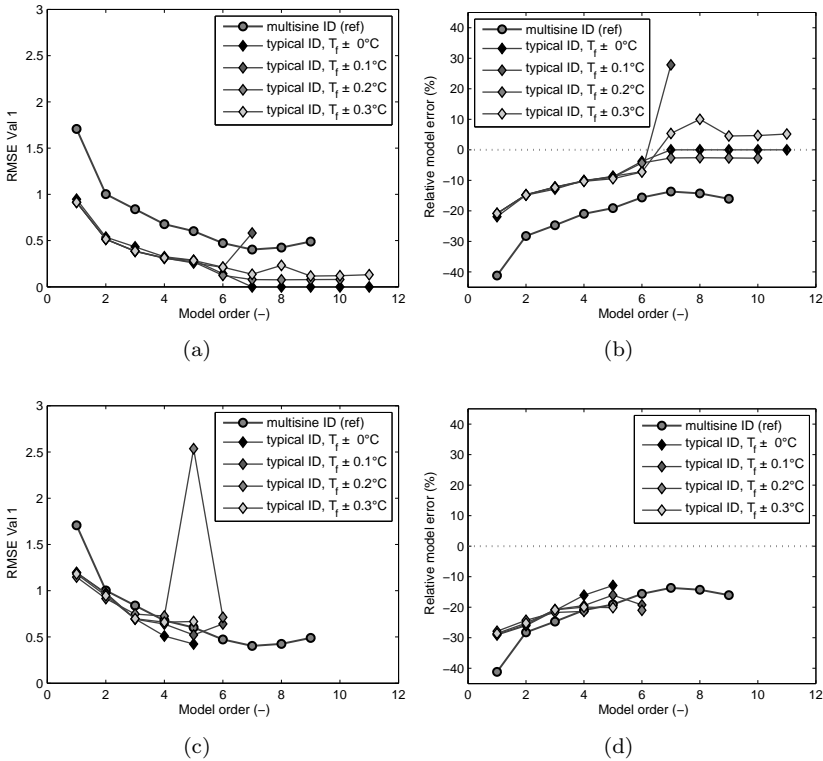


Figure 7.26: Validation results for the models obtained by PE with a multisine excitation signal ('multisine ID') and with typical data of a system in operation ('typical ID'). For the 'typical ID' case, the influence of white noise on the measurement of T_f and of \dot{Q} are shown: (a,b) standard deviation of the measurement error on $\dot{Q} = 0\%$ (c,d) standard deviation of the measurement error on $\dot{Q} = 20\%$. The validation results for the unstable models are not displayed.

increases for the time horizon of 10 years compared to the initial 1D-FDM. Third, the models obtained by PE based on simulation data resulting from the TRNSYS-DST-model, are able to predict the fluid temperature for Val1 with a relative error of 4% for ID1 (1 week), down to 0.4% for ID4 (6 months). The models found by PE are less accurate in predicting the response to a step heat input. The relative error obtained with ID1 amounts to 50%. With ID4, this error is reduced to the acceptable level of 0.2%. However, the relative errors for an unbalanced load profile (Val2) applied during 10 consecutive years, are

small for both the models obtained with ID1 and with ID4, respectively 6% and 2%. This shows that PE, even based on a limited time span covered by the identification data, is able to yield models which can accurately predict the control relevant dynamics.

Next, the influence of non-idealities is investigated. For the MR approach, the sensitivity to the estimation error of k_g , ρc_g and R_b , used to set up the initial model (1D-FDM), is investigated. The validation results listed in Table 7.4 in column 1D-FDM', printed in grey, are found by perturbing the values for k_g , ρc_g and R_b with respectively +10% , +10% and -10%. Those are typical uncertainties, as reported in the literature, and the chosen combination yields the worst case scenario (i.e. a strong underestimation of the fluid temperature as a response to a step heat input). The validation errors increase up to 3% for validation set 1 and up to 9% for the step responses. The same holds for the derived models obtained by MR (listed in column MR(DC)', grey).

Values in black correspond to the ideal scenario: (a) for the white-box modeling approach followed by MR, this means perfect knowledge of k_g , ρc_g and R_b to define the 1D-FDM initial model; (b) for the grey-box modeling approach this means a multisine excitation signal and no measurement errors (ID1, ID3, ID4). Values in grey correspond to a more realistic scenario: (a) Estimation error on k_g , ρc_g and R_b of respectively +10% , +10% and -10%, yielding a slightly modified initial model 1D-FDM'; (b) Typical load profile as excitation signal with white measurement noise on \dot{Q} and T_f of respectively 10% and 0.3°C, denoted by ID1', ID3' and ID4' corresponding to a measurement time of respectively 1 week, 3 months and 6 months.

Table 7.4: Comparison of models based on relative model error (%) (*).

Model order N	Model reduction from 1D-FDM (MR)				Parameter estimation (PE)					
	1D-FDM	1D-FDM'	MR(DC)	MR(DC)'	ID1	ID1'	ID3	ID3'	ID4	ID4'
	11	11	6	6	6	4	6	5	6	5
Val1 (1 year)	0.6	3	0.9	3	4	17	1.3	2	0.4	2
Val3 (1 year)	0.1	-9	0.1	-9	-27	51	-10	-17	-0.2	7
Val2 (10 years)	0.5	2	0.6	2	6	13	3	4	2	2
Val3 (10 years)	1.7	-8	1.7	-8	-37	29	-23	-29	-12	-8

(*) Values in black correspond to the ideal scenario: (a) for the white-box modeling approach followed by MR, this means perfect knowledge of k_g , ρc_g and R_b to define the 1D-FDM initial model; (b) for the grey-box modeling approach this means a multisine excitation signal and no measurement errors (ID1, ID3, ID4). Values in grey correspond to a more realistic scenario: (a) Estimation error on k_g , ρc_g and R_b of respectively +10% , +10% and -10%, yielding a slightly modified initial model 1D-FDM'; (b) Typical load profile as excitation signal with white measurement noise on \dot{Q} and T_f of respectively 10% and 0.3°C, denoted by ID1', ID3' and ID4' corresponding to a measurement time of respectively 1 week, 3 months and 6 months.

Also the influence of non-idealities on the PE procedure is investigated. Two aspects are considered: (1) the fact that in practice the identification data result from measurements of a system in operation, i.e. the excitation signal is

determined by the real load profile, and (2) the presence of measurement noise. The validation results for the models identified under these non-ideal conditions are printed in grey in the columns for ID1', ID3' and ID4'. The errors remain acceptable, at least if the measurement period is long enough. The validation error for the models identified based on a measurement period of 6 months (ID4') is about 2% for Val1 (1 year) and Val2 (10 years). The main impact of the presence of measurement noise is that the maximum model order (for stable models) is reduced. Identifying models with $N > 5$ in the presence of high levels of measurement noise, gives rise to unstable models.

The suitability of the models for incorporation in an optimal control problem formulation, as introduced in Section 7.2, depends on three factors: first, the model accuracy to predict the control relevant dynamics, second, the complexity to develop or identify the model and, third, the impact of the model structure and order on the computation time. The complexity to develop the model depends on the modeling approach and its sensitivity to non-idealities, while the computation time depends on the model structure and order. This study has analyzed the model accuracy for two distinct modeling approaches, i.e. model reduction and parameter estimation, as a function of the model order and the level of non-idealities. The results suggest that, if measurement data are available, parameter estimation is well suited to obtain very-low order models for control purposes. Even in the presence of measurement errors, the prediction error of a fifth order model based on in-situ measurement data, is less than 2% for a typical annual load profile, corresponding to an RMSE of less than 1°C. The model order can be further reduced to a second or even a first order model, with the RMSE amounting to respectively 1°C and 1.2°C (see Figure 7.26(c)). If no measurement data are available, model reduction is a good alternative. In that case, a fifth order model is required. Compared to parameter estimation, the model reduction approach is intrinsically better suited to describe the long term dynamics.

Here, we want to incorporate the controller model into an optimal control problem formulation which allows to optimally distribute the building heating and cooling loads over the different heating and cooling devices, while guaranteeing long term borefield thermal balance. The first objective requires description of the short term time scale, the latter of the long term time scale. The prediction accuracy required for these time scales, depends on the sensitivity of the optimal solution to these effects (i.e. the short term dynamics around the BHE and the long term dynamics near the far field). This evaluation will be performed in Section 7.5. The relatively high model accuracies obtained with the PE method for very low-order models, suggests that a model order between one and six will suffice.

7.5 Control performance evaluation

A selection of the developed BHE models is now used within the OCP, presented in Section 7.2, which aims at defining the optimal distribution of the annual heating and cooling load profiles over the 4 different devices (namely the heat pump (HP), the gas boiler (GB), the passive cooling heat exchanger (PC) and the chiller (CH)). The OCP problem is formulated such that the obtained solution is at steady state, which means, it could be repeated unaltered year after year if the same annual building load is being applied.

The optimal solution is analyzed as a function of:

1. the level of imbalance between the building heating and cooling loads,
2. the time scale over which the building loads are lumped: hourly load profiles versus weekly load values.

Additionally, the sensitivity of the optimal distribution on the following OCP variables is analyzed:

1. constant COP_{HP} -representation versus source temperature dependent COP_{HP} -representation,
2. constant COP_{PC} -representation versus source temperature dependent COP_{PC} -representation,
3. the incorporated BHE model

From this analysis, insight will be gained in the factors driving the optimization.

7.5.1 Settings

The OCP, given by the set of equations Eq.(7.1a)-Eq.(7.10), is solved with the following settings.

Building heating and cooling loads The heating and cooling loads, given as input to the optimization and denoted by respectively \dot{Q}_h and \dot{Q}_c , are to be delivered by the installation (see Eq.(7.1a)-(7.1b)):

$$\dot{Q}_h = \dot{Q}_{HP} + \dot{Q}_{GB}$$

$$\dot{Q}_c = \dot{Q}_{PC} + \dot{Q}_{CH}$$

Table 7.5: Results building load calculation

	Thermal comfort		Specific loads				δQ_b
	$Kh_{tot,N}$ (Kh)	$Kh_{tot,S}$ (Kh)	$Q_{h,tot}$ ($\frac{kWh}{m^2a}$)	$Q_{c,tot}$ ($\frac{kWh}{m^2a}$)	$\dot{Q}_{h,max}$ ($\frac{W}{m^2}$)	$\dot{Q}_{c,max}$ ($\frac{W}{m^2}$)	
HC/CC	35	27	13	-27	54	-51	-0.33
MPC	24	65	13	-25	36	-22	-0.34

Two load profiles, both obtained from the study performed in Chapter 5 for the two zone office building, are evaluated and compared. The first one, presented in Figure 7.27(a), corresponds to the load profile obtained with the best performing heating curve/cooling curve (HC/CC) control strategy, i.e., based on feedback of the CCA surface temperature $T_{c,s}$. The second load profile, presented in Figure 7.27(b), is the one obtained with the best performing MPC strategy, i.e., using the controller building model `nx2-DS3`, prediction correction method c_2 and perfect disturbance predictions (see Section 5.5.1). In what follows, they are simply denoted by 'HC/CC', respectively 'MPC'. Note that the loads, depicted in Figure 7.27, represent the loads for the entire office building (i.e., 3600 m² conditioned floor area, see Chapter 4).

Figures 7.27(a) and (b) show that the hourly load profiles strongly differ: the HC/CC-control strategy requires much higher peak powers than the MPC strategy. The weekly averaged loads, by contrast, shown in Figure 7.27(c) and (d), are almost identical. In terms of net annual heating and cooling energy demand (kWh), see Table 7.5, the two demand profiles indeed hardly differ. We will evaluate the impact of the power content of the load profile, i.e. with high power peaks (HC/CC) and with a flat power profile (MPC), on the optimal HyGCHP operation and on the required borefield size.

Heat pump coefficient of performance COP_{HP} The optimization is solved for 2 representations of COP_{HP} :

$$COP_{HP}(T_f) = 6 + 0.07(T_f - T_{ws,h}) \quad \text{with } T_{ws,h} = 25^\circ\text{C} \quad (7.65)$$

$$COP_{HP}(constant) = 4.45 \quad (7.66)$$

The first presentation takes the source temperature dependency of the heat pump COP into account. The COP is represented by a linear function of the mean fluid temperature T_f ($^\circ\text{C}$), i.e. the output of the controller borefield model, and the heating supply water temperature $T_{ws,h}$ ($^\circ\text{C}$). The coefficients are obtained by a fit through the catalogue data of a water-to-water heat pump [33].

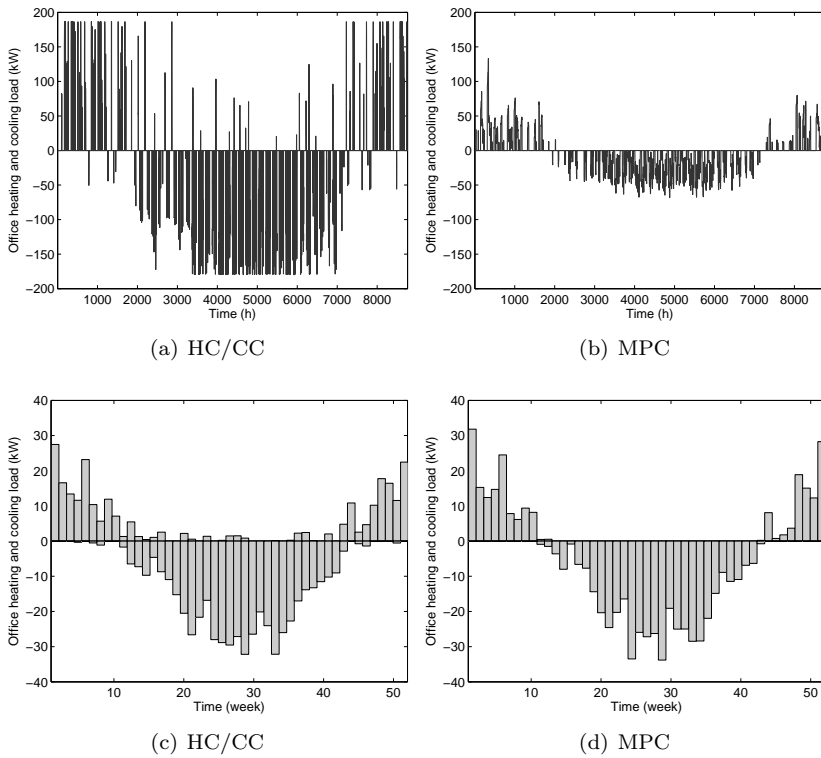


Figure 7.27: Heating (>0) and cooling (<0) load profiles, \dot{Q}_h and \dot{Q}_c , derived for the office building with (left) heating curve/cooling curve (HC/CC) control and (right) MPC. Top: Hourly load values. Bottom: Weekly averaged load values.

As in this chapter abstraction is made of the building level, a constant supply water temperature of 25°C is assumed, corresponding to the annual mean supply water temperature in heating mode obtained from the case for which the building loads have been calculated. Similarly to the optimization problem considered in Chapter 6, the cost function with $COP_{HP}(T_f)$ is nonlinear. The second representation, by contrast, - in absence of other nonlinear terms - results in a convex problem.

Passive cooling coefficient of performance COP_{PC} The optimization is solved for 2 representations of COP_{PC} :

$$COP_{PC}(T_f) = 50 - 2.5T_f \quad (7.67)$$

$$COP_{PC}(constant) = 20 \quad (7.68)$$

The first presentation takes the source temperature dependency of the passive cooling efficiency into account. The COP is represented by a linear function of T_f with COP_{PC} corresponding to 20 for T_f equal to 12 °C and to 0 for T_f equal to 20 °C. The latter expresses that there is no passive cooling capacity when T_f approaches the supply water temperature for cooling at building side, $T_{ws,c}$. While this T_f -dependent COP_{PC} -formulation gives rise to a nonlinear OCP, the second representation with a constant COP_{PC} -value can be used within a convex OCP formulation.

Chiller coefficient of performance COP_{CH} The COP of the chiller is represented by a linear function of the ambient air temperature T_{amb} and the cooling supply water temperature $T_{ws,c}$. Again, making abstraction of the building level, a constant value for $T_{ws,c}$ is taken to evaluate COP_{CH} , corresponding to the annual mean supply water temperature in cooling mode obtained from the case for which the building loads have been calculated.

$$COP_{CH}(T_{amb}) = 5 + 0.07T_{ws,c} - 0.08T_{amb} \quad \text{with } T_{ws,c} = 20^\circ\text{C} \quad (7.69)$$

Gas boiler efficiency η_{GB} The gas boiler efficiency is taken equal to 0.85.

Electricity price c_{el} and gas price c_{gas} The peak electricity price amounts to 0.15 €/kWh, the off-peak electricity price to 0.09 €/kWh and the gas price to 0.06 €/kWh. The peak electricity price period extends from 7AM to 10PM.

Controller borefield models One of the aims of this study is to determine the minimal model order N required to accurately solve the OCP. For very low model orders ($N < 6$), the BHE models obtained with parameter estimation (PE) were found to yield better predictions of T_f compared to the models obtained with model reduction (MR) of the initial model representing the radial heat transfer around the BHE (1D-FDM). For this aim, the models found with PE (obtained with ID set 1 covering a period of 1 year) of order N from 3 to 6, are incorporated in the OCP.

A second aim is to gain insight in the optimal ground temperature distribution. While very-low order models may well describe T_f , they do not provide sufficient

information on the temperature distribution around the BHE. To evaluate the radial temperature distribution around the BHE, the 1D-FDM derived from the discretization of the radial heat transfer around the BHE, is used.

7.5.2 Computational limitations

Ideally, the OCP is solved for the hourly building load profile, depicted in Figure 7.27. This way the short term dynamics and the long term dynamics are both taken into account in the optimization. This however requires to determine the optimal values for \dot{Q}_{HP} , \dot{Q}_{GB} , \dot{Q}_{PC} and \dot{Q}_{CH} for each hour of the year, resulting in a problem with 8760 by 4 optimization variables. This is a large optimization problem and by consequence hard to solve. On a computer with a 32-bit dual core processor (Intel(R) Core(TM)2 Duo CPU P9700 @ 2.80GHz), even a powerful solver such as CPLEX [29] can not solve this problem due to memory restrictions. On a 64-bit processor this problem *can* be solved, at least with the CPLEX solver. With non-commercial convex solvers this problem is hardly solvable and for nonlinear optimization solvers, such as incorporated in ACADO, the problem is far too large. Therefore, the OCP will first be solved with a control time step of 182.5 h (approximately 1 week), resulting in a control problem of 48 by 4 optimization variables. In a second approach the OCP will be solved for a control time step of 1 h (8760 by 4 optimization variables, assuming constant COP values). Each approach will enable to focus on a particular aspect of the OCP:

1. weekly control time step

Assumption: week-averaged load profiles

Focus: What drives the optimization on the long term?

- (a) influence of $COP_{HP}(T_f(t))$ (nonlinear OCP)
- (b) influence of $COP_{PC}(T_f(t))$ (nonlinear OCP)
- (c) influence of $COP_{CH}(T_{amb}(t))$ (seasonal variation)
- (d) influence of the long term borefield thermal balance condition

2. hourly control time step

Assumption: constant COP_{HP} and COP_{PC} (convex OCP)

Focus: What drives the optimization on the long + short term?

- (a) influence of the peak loads
- (b) influence of $COP_{CH}(T_{amb}(t))$ (seasonal + diurnal variation)
- (c) influence of the electricity price $c_{el}(t)$ (diurnal variation)
- (d) influence of the long term borefield thermal balance condition

Nonlinear OCP with a weekly control time step To solve the nonlinear optimization problem, resulting from the T_f -dependency of COP_{HP} and COP_{PC} , the number of control intervals has to be reduced. To this end, the 8760 hourly **building load** values, see Figure 7.27(a,b), are **lumped** into 48 time-averaged values, see Figure 7.27(c,d). The latter corresponds to a control time step of 182.5 h or approximately one week (a control time step of exactly one week, i.e. 168 h, would not yield an integer number of control intervals). Note the different scaling of the y-axis: by lumping the loads over larger time frames, the load profile is flattened. For the short term response, this lumping introduces an inconsistency: *information on the actual peak heat injection and extraction rates is lost*. As a consequence, only the *weekly average* mean brine temperature, here denoted by $T_{f,av}$, can be evaluated. This implies that COP_{HP} and COP_{PC} , which are both function of the *actual* mean brine temperature T_f , can only be approximately assessed. This may be problematic, especially for the cooling dominated cases because of the strong dependency of COP_{PC} on T_f . Therefore, to guarantee that the solution effectively enables the use of passive cooling, an additional constraint on $T_{f,av}$ is imposed. While the actual T_f should remain below $T_{ws,c}$ to have passive cooling capacity (see Eq.(7.70)), with ΔT_{lm} ($^{\circ}\text{C}$) the logarithmic mean temperature difference over the PC heat exchanger (see Eq.(7.72)), the $T_{f,av}$ -value obtained with the weekly load profile should remain even lower, as expressed in Eq.(7.71)). This temperature margin, $\Delta T_{f,av}$ ($^{\circ}\text{C}$), see Eq.(7.73), is proportional to the effective borehole thermal resistance, R_b (K/W) and the difference between the actual heat injection rate $\dot{Q}_{bf,in}$ (W) and its weekly-averaged value $\dot{Q}_{bf,in,av}$ (W)).

$$T_f \leq T_{f,max} = T_{ws,c} - \Delta T_{lm} \quad (7.70)$$

$$T_{f,av} \leq T_{f,max} = T_{ws,c} - \Delta T_{lm} - \Delta T_{f,av} \quad (7.71)$$

with

$$\Delta T_{lm} = (UA)_{PC}^{-1} \dot{Q}_{bf,in} \quad (7.72)$$

$$\Delta T_{f,av} = R_b (\dot{Q}_{bf,in} - \dot{Q}_{bf,in,av}) \quad (7.73)$$

The weekly averaged building load values for the office load profile depicted in Figure 7.27(c,d), are about a factor 6 smaller than the actual peak loads (depicted in Figure 7.27(a,b)). Therefore, the term $\dot{Q}_{bf,in,av}$ in Eq.(7.73) can almost be neglected. For a realistic heat injection rate of 40 – 50 W/m BHE length and a specific borehole thermal resistance R'_b of 0.1 mK/W, $\Delta T_{f,av}$ amounts to about 3 $^{\circ}\text{C}$. Assuming $T_{ws,c}$ equal to 20 $^{\circ}\text{C}$ and ΔT_{lm} of 1.5 $^{\circ}\text{C}$, this yields an upper bound $T_{f,av,max} \approx 15$ $^{\circ}\text{C}$. For the same reason, the lower temperature bound of 0 $^{\circ}\text{C}$ on T_f to prevent frost formation, is translated to a lower bound $T_{f,av,min} \approx$ of 3 $^{\circ}\text{C}$.

One could wonder what can be learned from solving this lumped-load-case scenario. While the physical information content of the results is effectively reduced, the long term response can be evaluated, since the latter does not depend on the hourly load variations. On this time scale, we are able to analyze the optimal annual mean brine temperature, being a result of the optimization thanks to the free periodic boundary conditions on the ground temperatures $T_{g,i}$ (see Eq.(7.8)). If the incorporated BHE model is a first-principles model, the optimization additionally yields the optimal annual mean ground temperature distribution around the BHE. The question addressed for the long term time scale, is what determines the optimal value of the annual mean brine temperature and the corresponding ground temperature distribution. Two conflicting objectives come into play, as visualized in Figure 7.28: maximizing the efficiency (COP_{HP} or COP_{PC}) on the one hand versus maximizing the heat exchange with the borefield ($\int \dot{Q}_{bf,ex} dt$ or $\int \dot{Q}_{bf,in} dt$), on the other hand. If *maximizing the efficiency* is the driving factor, one should observe that the optimal borefield temperature is higher for the heating dominated case than for the cooling dominated case, since COP_{HP} rises with rising source temperature while \dot{Q}_{PC} - and thus COP_{PC} - increases with decreasing heat sink temperatures (see Eq.(7.6c)).

If maximizing the total *amount of heat exchanged* with the borefield is the driving factor, by contrast, the optimal borefield temperature should be higher for the cooling dominated case than for the heating dominated case. The condition for long term borefield thermal balance, expressed by the periodic boundary conditions on $T_{g,i}$ (see Eq.(4.31)), can namely be written in terms of energy flows:

$$\int_0^{1y} (\dot{Q}_{bf,in} - \dot{Q}_{bf,ex} - \dot{Q}_{bf,\infty}) dt = 0, \quad (7.74)$$

with

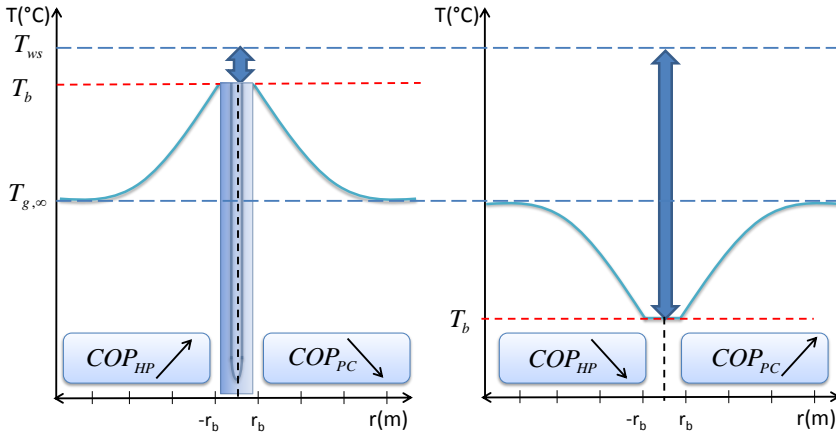
$$\begin{aligned} \dot{Q}_{bf,in} &= \frac{COP_{PC} + 1}{COP_{PC}} |\dot{Q}_{PC}|, \\ \dot{Q}_{bf,ex} &= \frac{COP_{HP} - 1}{COP_{HP}} \dot{Q}_{HP}, \end{aligned}$$

$\dot{Q}_{bf,\infty}$ (W) denotes the heat flow from the borefield to the surroundings, i.e. the sum of the heat exchange with the ambient air at the borefield surface and the heat exchange with the ground far field. Since the presented borefield controller models only describe the radial heat transfer, only the latter term is taken into account. For the discussion here, this heat loss term is assumed to be proportional to the difference between the mean borefield temperature T_{bf} and the undisturbed ground temperature $T_{g,\infty}$:

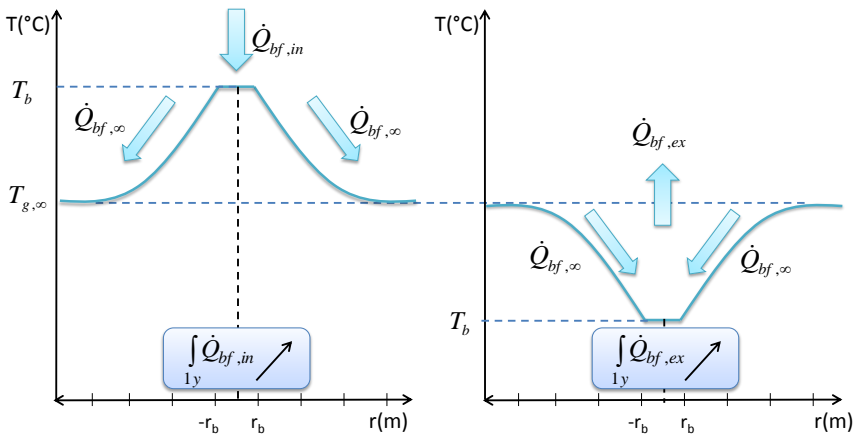
$$\dot{Q}_{bf,\infty} \sim T_{bf} - T_{g,\infty}.$$

The larger the heat loss from the borefield to the surroundings ($\int_0^{1y} (\dot{Q}_{bf,\infty}) dt > 0$) the more heat can be injected to the ground through passive cooling. The larger the heat gains from the surroundings to the borefield ($\int_0^{1y} (\dot{Q}_{bf,\infty}) dt < 0$), the more heat can be extracted for heat pump operation. The annual net heat exchange between the borefield and the surrounding ground depends on the borefield temperature distribution, as visualized in Figure 7.28: if the mean borefield temperature T_{bf} is higher than $T_{g,\infty}$, there will be a net heat loss from the borefield to the surrounding ground. If T_{bf} is lower than $T_{g,\infty}$, there will be a net heat flux from the surrounding to the borefield. The optimal value of T_{bf} is therefore based on a trade-off between increasing the *efficiency* of the heat and cold production with the GCHP system, on the one hand, and of the *share* of the GCHP in the total heat and cold production, i.e. $\int_0^{1y} \dot{Q}_h dt$ and $\int_0^{1y} |\dot{Q}_c| dt$, on the other hand. This trade-off will depend on the building loads (heating versus cooling dominated) and on the sensitivity of the terms COP_{HP} , COP_{PC} and $\dot{Q}_{bf,\infty}$ on T_{bf} (and thus on the borefield dynamics).

As a variable COP formulation gives rise to a non-convex optimization problem, we are interested to know how much the result obtained with a constant COP approximation deviates from the original solution. The constant COP formulation gives rise to a convex problem which allows solving the OCP much faster (using CPLEX) and for much smaller control time steps (down to 1 hour for a 8760 h-optimization), as stated above.



(a) Temperature difference between the supply water at building side, T_{ws} , and the borehole wall, T_b , determines COP_{HP} and COP_{PC} .



(b) Temperature profile around BHE determines the net heat exchange $\dot{Q}_{bf,\infty}$ with the surroundings at the undisturbed ground temperature $T_{g,\infty}$. In the case of borefield thermal balance, this heat exchange is compensated by an annual net heat injection $\dot{Q}_{bf,in}$ (left) or by an annual net heat extraction $\dot{Q}_{bf,ex}$ from the borefield.

Figure 7.28: Influence of the radial ground temperature profile around a BHE on the heat pump coefficient of performance, COP_{HP} and on the passive cooling coefficient of performance, COP_{PC} (top) and on the heat exchange with the surrounding ground and the GCHP system (bottom).

Convex OCP with hourly control time step The CPLEX solver is able to solve the convex optimization problem (using constant COP values) with 8760 by 4 optimization variables, enabling to capture both the short and the long term borefield dynamics in the optimization. With the hourly load values, also the short term response of T_f will be accurately predicted. Consequently, we are able to effectively impose constraints on T_f and thus accurately determine *when* to use passive cooling and *at which rate*. Compared to the weekly time scale, the hourly time scale additionally allows to take the time dependency of the electricity price $c_{el}(t)$ into account, as well as the dependency of $COP_{CH}(T_{amb})$ on the diurnal variation of the ambient air temperature, two factors that may influence the choice of passive versus active cooling. As the long term thermal balance condition is also incorporated, the distribution of the cooling loads will also take this aspect into account. The only drawback is that the CPLEX solver requires a constant COP_{HP} and COP_{PC} representation. From the insights gained from (1) the influence of the T_f -dependency of COP_{HP} and COP_{PC} on the long term time scale (see Section 7.5.3) and (2) the influence of the T_{ws} -dependency of COP_{HP} on the short term time scale (see Chapter 6), we will be able to assess the impact of this approximation.

7.5.3 What drives the optimization in the long term?

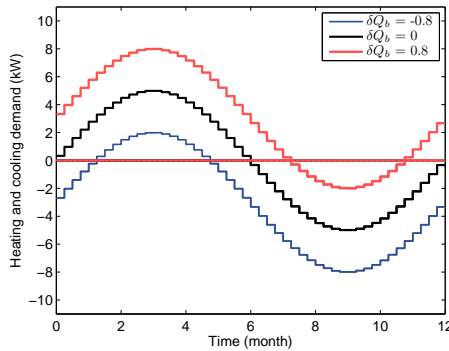


Figure 7.29: Idealized building load profiles, characterized by the relative level of load imbalance δQ_b : $\delta Q_b > 0$: heating dominated building (red), $\delta Q_b < 0$: cooling dominated building (blue) and $\delta Q_b = 0$ building with balanced heating and cooling load (black).

Influence of COP_{HP} and COP_{PC} First, we analyze the impact of the COP-formulation on the optimal borefield temperature. To this end, the nonlinear and convex OCP formulations are solved for a set of idealized building load profiles, depicted in Figure 7.29. Each of these building loads is characterized by the absolute and relative imbalance between the building heating and cooling demand, denoted by respectively ΔQ_b (kWh) and δQ_b (-). The values ΔQ_b and δQ_b , defined by Eq.(7.75)-Eq.(7.76), are positive for a heating dominated building and negative for a cooling dominated building.

$$\Delta Q_b = \int_{1y} \dot{Q}_h dt - \int_{1y} |\dot{Q}_c| dt \quad (7.75)$$

$$\delta Q_b = \frac{\int_{1y} \dot{Q}_h dt - \int_{1y} |\dot{Q}_c| dt}{\int_{1y} \dot{Q}_h dt + \int_{1y} |\dot{Q}_c| dt} \quad (7.76)$$

For each of these building loads, the OCP formulations yield an optimal profile for the control variables \dot{Q}_{HP} , \dot{Q}_{GB} , \dot{Q}_{PC} and \dot{Q}_{CH} which satisfies the imposed building load profile, as illustrated in Figure 7.30 for both a cooling and a heating dominated building with a relative building load imbalance δQ_b of respectively -0.6 and +0.6). For each case, both the control profiles obtained with the nonlinear OCP and the convex OCP are displayed. For the investigated weekly building load profiles, the two OCP formulations yield almost identical results and this despite the very different profiles for $COP_{HP}(T_f)$ and $COP_{PC}(T_f)$ used for the nonlinear and convex OCP.

Figure 7.31(a) and Figure 7.31(c) compare the profiles for $COP_{HP}(T_f)$ and $COP_{PC}(T_f)$ obtained with the nonlinear OCP to the constant ones assumed in the convex OCP. The fact that the 2 OCP formulations, despite their significant different values for COP_{HP} and COP_{PC} , yield almost identical control profiles (see Figure 7.30, indicates that maximizing the COPs is not the driving factor for the optimization. Otherwise we would observe a fundamentally different operation strategy for the two OCP formulations. For the cooling dominated case, the nonlinear OCP could for instance have constrained the use of PC to a certain extent, to keep the T_f low and thus $COP_{PC}(T_f(t))$ high. Similarly, for the heating dominated case, the use of the HP could have been constrained to keep T_f high and thus $COP_{HP}(T_f(t))$ high. This is however not the case.

Figure 7.32 presents the optimal profiles for $\dot{Q}_{bf}(t)$ and $\dot{T}_{f,av}(t)$ and this for different levels of building load imbalance. The constraints on the average brine temperature $T_{f,av}$ are active. For the theoretical demand profiles depicted in Figure 7.29, which are rather large for the considered BHE, the constraints are not only 'hit', but they remain active for a long period. This indicates that the

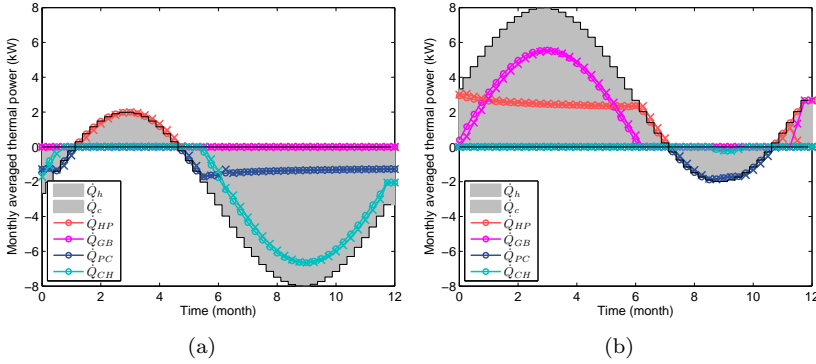


Figure 7.30: Optimal distribution of the building heating load $\dot{Q}_h(t)$ and building cooling load $\dot{Q}_c(t)$ over respectively the heat pump $\dot{Q}_{HP}(t)$, the gas boiler $\dot{Q}_{GB}(t)$, the passive cooling $\dot{Q}_{PC}(t)$ and the chiller $\dot{Q}_{CH}(t)$ for respectively a cooling dominated building ($\delta Q_b = -0.8$) (left) and a heating dominated building ($\delta Q_b = +0.8$) (right). The results for the nonlinear OCP (-x-) and those for the convex OCP (-o-) almost coincide.

optimal control, at least for the considered control time step of 1 week, is of the bang-bang control type, i.e. operating at the constraints. By consequence, the operation is very sensitive to the actual value of the upper and lower bound on $T_{f,av}$.

Figure 7.33 depicts the optimal ground temperatures $T_{g,i}$ for the incorporated BHE model, which corresponds to a 6th order model obtained with PE. This choice is motivated by the sensitivity analysis of the optimal solution with respect to the model order N , treated further in this section. Figure 7.33(a) shows the $T_{g,i}(t)$ -profile as a function of time for a heating dominated building load. For each of the temperature nodes, the annual mean value is calculated. The resulting values are depicted in Figure 7.33(b) and this for the different building loads. The heating dominated cases are plotted in red, the cooling dominated in blue and the balanced load case in black. For each case, both the profiles obtained with the nonlinear OCP and the convex OCP are displayed. As noted previously, the two OCP formulations yield almost identical results. This confirms again that maximizing the COPs is not the driving factor for the optimization. On the contrary, the higher the heating demand/cooling demand ratio, the lower the optimal borefield temperature; the lower the heating demand/cooling demand ratio, the higher the optimal borefield temperature. From this we can conclude that maximizing the heat exchange with the borefield

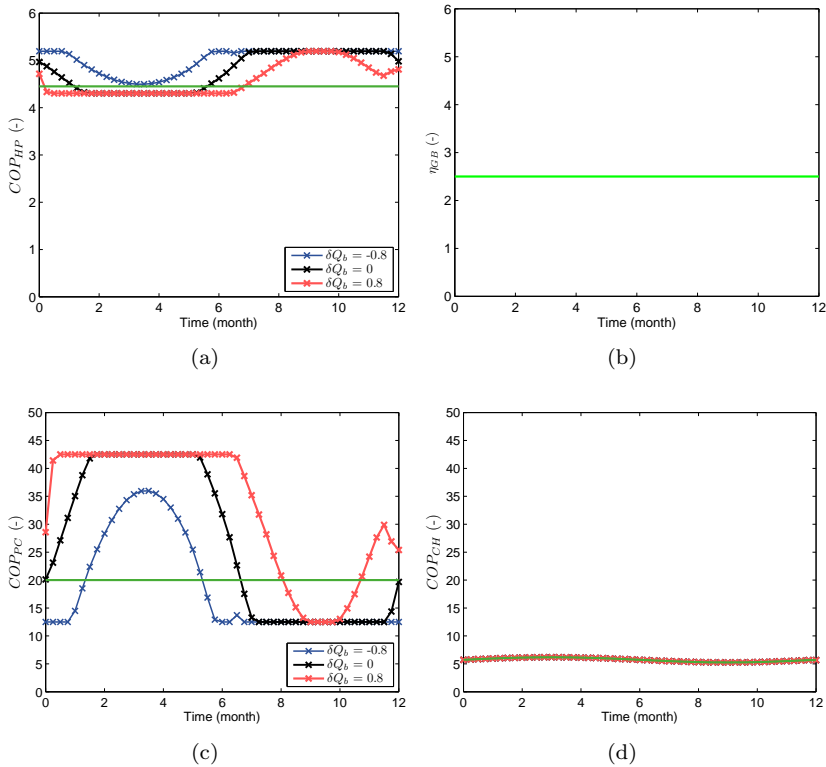


Figure 7.31: (a) The green line represents the constant COP_{HP} value for the convex OCP, the markers the $COP_{HP}(T_f)$ -profiles obtained with the nonlinear OCP for different load imbalances, (b) Gas boiler efficiency η_{GB} , scaled with the electricity-to-gas price ratio c_{el}/c_{gas} (-) to compare the GB energy cost with the HP energy cost, (c) The green line represents the constant COP_{PC} value for the convex OCP, the markers the $COP_{PC}(T_{f_f})$ -profiles obtained with the nonlinear OCP for different load imbalances, (d) $COP_{CH}(T_{amb})$ -profile for both the nonlinear and convex OCP.

is the driving factor. For the heating dominated case, the optimal operation maximizes the use of the borefield as a heat source. In order to do this, while meeting the periodic boundary conditions, there is only one way: maximize the heat gains from the surroundings for the heating dominated case and maximize the heat loss to the surroundings for the cooling dominated case, as depicted in Figure 7.28(b). The temperature profiles presented in Figure 7.33(b)

confirm that the higher the heating demand/cooling demand ratio, the lower the optimal borefield temperature; and vice versa. The small deviation between the nonlinear and the convex OCP formulation is caused by the difference in the calculated heat extraction rates (which weakly depend on COP_{HP} and COP_{PC}), rather than by a different evaluation of the cost function.

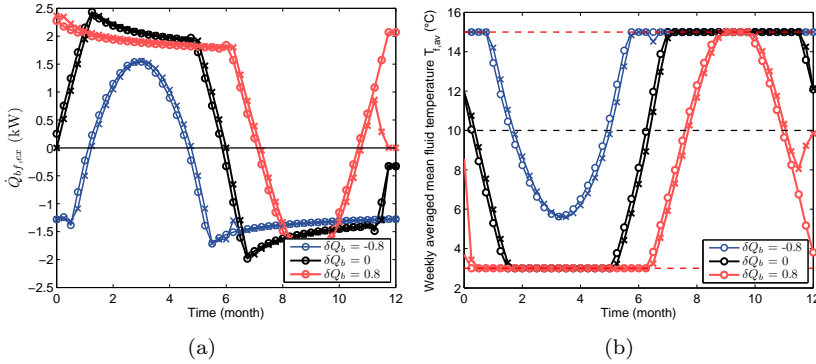


Figure 7.32: Optimal profiles for the weekly averaged borefield heat extraction power $\dot{Q}_{bf}(t)$ (left) and the brine fluid temperature $T_{f,avr}(t)$ (right) for the building load profiles depicted in Figure 7.29, characterized by their level of building load imbalance δQ_b . The results for the nonlinear OCP (-x-) and those for the convex OCP (-o-) almost coincide. The horizontal line at 10°C on the right figure indicates the undisturbed ground temperature $T_{g,\infty}$.

This result can be explained by the knowledge that it is more interesting to use the HP instead of the GB as long as the related energy cost, $c_{el}COP_{HP}(t)$ versus $c_{gas}\eta_{GB}$, is lower. Comparison of the $COP_{HP}(t)$ -profiles, presented in Figure 7.31(a), and the $c_{el}/c_{gas}\eta_{GB}$ -profile, presented in Figure 7.31(b), shows that - for the adopted c_{el}/c_{gas} -ratio ($=3.75$), this is always the case. As a consequence, in the heating dominated case, annual minimization of the energy cost is achieved by maximizing the use of the borefield for heating, i.e. maximizing the ratio of the GCHP for heating, denoted here by GEO_h :

$$GEO_h = \frac{\int_0^{1y} \dot{Q}_{HP} dt}{\int_0^{1y} \dot{Q}_h dt} \quad (7.77)$$

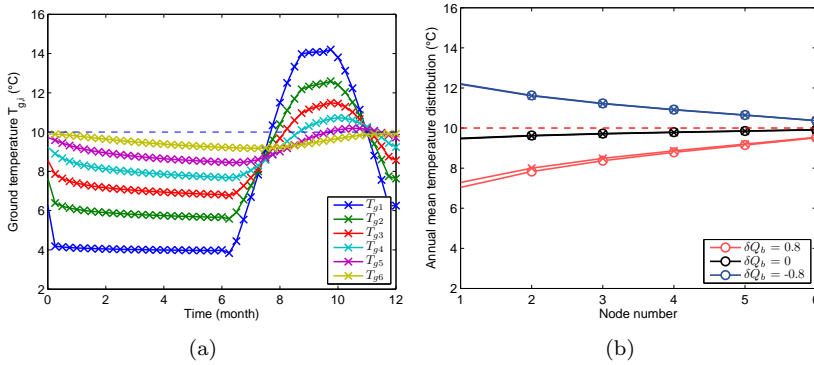


Figure 7.33: Left: Optimal profiles for the ground temperatures $T_{g,i}(t)$ for the case of a heating dominated building load profile ($\delta Q_b = 0.8$). $T_{g,1}$ represents the temperature near the BHE, $T_{g,6}$ the temperature near the undisturbed ground at a temperature $T_{g,\infty}$ of 10°C . Right: Annual mean temperature of the different model nodes $T_{g,i}$ for different building load profiles. The first node corresponds to $T_{g,1}$, the last node to $T_{g,6}$. The results for the nonlinear OCP (-x-) and those for the convex OCP (-o-) almost coincide.

Similarly, as long as COP_{PC} is higher than COP_{CH} , the optimization will maximize the ratio of the passive cooling, denoted by GEO_c :

$$GEO_c = \frac{\int_0^{1y} |\dot{Q}_{PC}| dt}{\int_0^{1y} |\dot{Q}_c| dt} \quad (7.78)$$

Note that maximizing GEO_h for the heating dominated case also results in lower energy costs for cooling thanks to the relatively low borefield temperature which increases the average COP_{PC} . Similarly, maximizing GEO_c for the cooling dominated case results in a higher COP_{HP} and thus in lower energy costs for heating.

The load imbalance at borefield level is - analogously to the load imbalance at building level - expressed in both absolute terms, denoted by ΔQ_{bf} (kWh), and in relative terms, denoted by δQ_{bf} (-), see respectively Eq.(7.79) and Eq.(7.80).

$$\Delta Q_{bf} = \int_{1y} (\dot{Q}_{bf,ex} - \dot{Q}_{bf,in}) dt \quad (7.79)$$

$$\delta Q_{bf} = \frac{\int_{1y} (\dot{Q}_{bf,ex} - \dot{Q}_{bf,in}) dt}{\int_{1y} (\dot{Q}_{bf,ex} + \dot{Q}_{bf,in}) dt} \quad (7.80)$$

Figure 7.34 shows the load imbalance at borefield level as a function of the load imbalance at building level. Figure 7.34 (a) reveals that ΔQ_{bf} scales approximately linearly with ΔQ_b . Figure 7.34 (b) shows that for a relative load imbalance at building level δQ_b between -50% and +50% the resulting imbalance at borefield level δQ_{bf} amounts to -20% to 20%. Obviously, for buildings with only a heating or a cooling demand (i.e. $|\delta Q_b| = 1$), the borefield thermal imbalance $|\delta Q_{bf}|$ also equals 1.

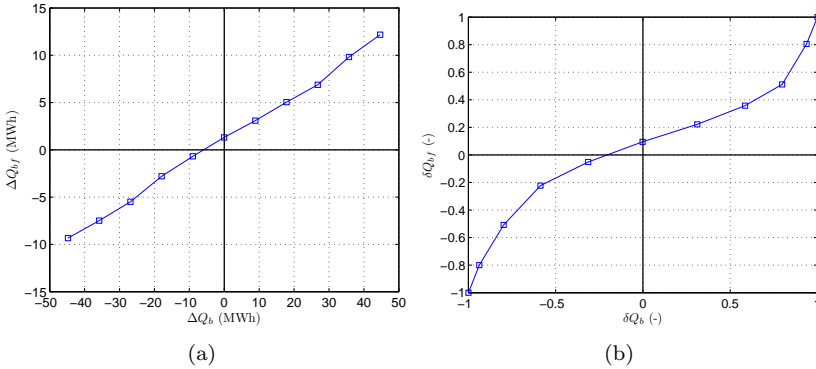


Figure 7.34: Annual imbalance at borefield level as a function of the annual imbalance at building level, expressed in absolute values (left) and relative values (right).

Following conclusions are derived: first, the optimization shows that achieving a sustainable operation - represented by the condition of periodicity for ground temperatures $T_{g,i}$ - does not necessarily mean that the total amount of injected and extracted heat (at borefield level) should be equal. By contrast, a certain amount of imbalance is tolerated. This finding is consistent with recent research results [31]. For the heating dominated case, a limited thermal depletion is even beneficial, while for the cooling dominated case a limited thermal build-up is allowed. Once the optimal T_{bf} is reached, however, the operation should guarantee no further deviation from this optimal point. A very first proposal of how this can be accomplished within an MPC-framework, is discussed in Chapter 8. However, this topic remains to be explored further. Second, the optimization yields interesting information for the design of HyGCHP systems. According to current design practice, the borefield is sized for the smallest of the two loads, with the remaining fraction of the largest of the two loads being covered by the backup system. The optimization problem discussed here, actually shows that balancing all the loads at borefield level does not necessarily

require the injected and extracted heat to be equal. Depending on the ground thermal properties and on the borefield configuration, an optimal annual amount of imbalance between the injected and extracted heat is found as a result of the optimization. A third conclusion, interesting from computational point of view, is that a convex OCP formulation is allowed.

Influence of the BHE model order The observations indicate that the controller borefield model should capture both short and long term dynamics. The former are required to accurately predict the brine temperature since - for a well-designed borefield - the constraints on this variable are active. The latter determine the heat loss from the borefield to the surroundings, being a driving factor in the optimization. The lower the model order N , the more information is lost. For the models obtained with PE, decreasing the model order was found to affect the description of the long term dynamics while for the models obtained with MR, the description of the short term dynamics is affected. In general, for very low order models (i.e. $N < 6$), which are interesting to limit the computational requirements to solve the nonlinear OCP, the validation results for the models obtained by PE were better than for the ones obtained with MR.

To assess the influence of the model accuracy on the optimization result, both the nonlinear OCP and the convex OCP are solved with the BHE models obtained with PE, with N ranging from 3 to 6, and with the initial model of order $N = 11$, based on Eskilson's guidelines. Figure 7.35 depicts the results of the optimization for the optimal borefield heat extraction rate $\dot{Q}_{bf,ex}$ and the weekly average mean brine temperature profile $T_{f,av}$, evaluated for the weekly building load profile with $\delta Q_b = 0$. For the convex OCP, depicted on the right hand side, no significant impact of N is observed. For the nonlinear OCP, on the contrary, the model order does influence the result. For $N < 6$ and $N = 11$ the solutions for $T_{f,av}$ and $\dot{Q}_{bf,ex}$ are found to oscillate. For $N < 6$, this oscillation is probably caused by an attempt of the optimization to maximize the efficiency of passive cooling COP_{PC} at the start of the cooling season. However, if the model order is increased up to $N = 6$, this oscillation disappears, suggesting that the solutions found for $N < 6$ do not correspond to a physically meaningful optimal solution. The Eskilson model with $N = 11$, however, does describe the physics of the ground accurately. The oscillatory behavior observed here is probably attributed to numerical problems due to the very large range of time constants involved. This hypothesis gains strength as comparison of the solutions obtained by the nonlinear OCP and the convex OCP match for $N = 6$. The observations for $N < 6$ show that the nonlinear OCP is more sensitive to the model quality than the convex OCP. The results for $N = 11$ additionally suggest that the nonlinear OCP is more prone to convergence problems. Only

for $N = 6$ the nonlinear OCP was able to find a good result. This emphasizes the importance that, in order to perform this kind of theoretical investigations, the BHE model should not only be accurate, but also have a low order in order to prevent numerical problems.

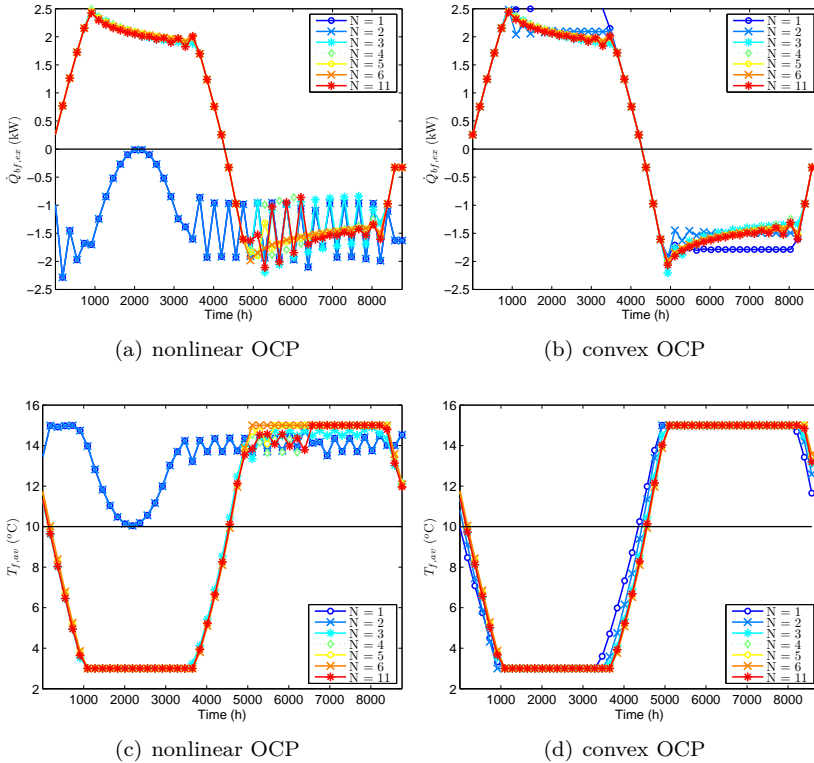


Figure 7.35: Influence of the controller borefield model order N on the optimal borefield heat extraction rate \dot{Q}_{bf} (top) and on the optimal weekly average mean brine fluid temperature profile $T_{f,av}$ (bottom). The figures on the left and right hand side show the results obtained with respectively the nonlinear and the convex OCP formulation.

Results for the office building load profiles The optimization of the HyGCHP operation is now performed for the weekly averaged office building loads presented in Figure 7.27(c) and Figure 7.27(d), i.e. the loads obtained with an

advanced HC/CC-control strategy on the one hand, and an MPC strategy on the other hand. For these two load profiles, we will analyze the impact of the GHE length on the optimal solution, i.e. on the distribution of the building heating and cooling loads over the HP, GB, PC and CH. Assuming a fixed BHE depth H and no BHE thermal interference, the GHE length scales linearly with the number of BHEs n_b . The impact of the GHE length will here be evaluated by varying n_b .

In Chapter 4, the borefield size has been determined for the office loads obtained with the HC/CC-control strategy. Applying the current HyGCHP design guidelines (i.e., borefield sized for the smallest of both loads and balancing the loads at borefield level), resulted in 26 BHEs, each of 125 m depth and spaced with 5 m distance. The current controller borefield model, however, represents a single BHE. We will analyze the optimal operation of the HyGCHP system assuming that there is no thermal interaction between the BHEs, an assumption that will be evaluated after performing the optimization. This means that the borefield loads, $\dot{Q}_{bf,in}$ and $\dot{Q}_{bf,ex}$, are simply divided by the number of BHE n_b in the borefield. The OCP is solved for the convex formulation incorporating the 11th order BHE model (Eskilson). This way, information on the radial distribution of the ground temperatures $T_{g,i}$ is obtained, enabling to evaluate the neglect of the thermal interaction between the BHEs.

Figure 7.36 shows the optimal distribution of the weekly averaged heating and cooling load profile over the HP, the GB, the PC and the CH for the different values of n_b (26-15-11). The figures at the left hand side present the results of the optimization for the office loads obtained with the HC/CC-control strategy, the figures at the right hand side the results for the office loads obtained with the MPC strategy. Figure 7.36(a) and Figure 7.36(b) show that the borefield with 26 BHEs is able to cover the entire heating and cooling load with the HP and the PC alone. If n_b is reduced to 15, see Figure 7.36(c) and Figure 7.36(d), the weekly averaged heating loads can still entirely be covered by the HP, but now CH operation is required to help covering the high cooling loads in summer. Figure 7.36(e) and Figure 7.36(f) show that a borefield with 11 BHEs is still able to cover the entire weekly averaged heating load. The share of the CH is further increased. PC provides base load cooling, while the CH helps to cover the higher cooling loads in summer.

The profiles for \dot{Q}_{bf} and $T_{f,av}$ as a function of n_b , shown in Figure 7.37, confirm these observations. n_b is varied between 38 and 6. Figure 7.37(a) and Figure 7.37(b) show that GEO_h remains 100% when reducing n_b from 38 to 11; only the fraction of the building cooling load covered by PC, i.e. GEO_{PC} , decreases. Only when n_b is further reduced down to 7 or 6, GEO_h decreases

Table 7.6: Influence of the borefield size, represented by the number of BHEs n_b , on the fraction of the office heating load covered by the HP ($GEO_h(-)$), the fraction of the office cooling load covered by PC ($GEO_c(-)$) and the resulting relative thermal imbalance at borefield level (δQ_{bf} (-)). The building heating and cooling loads are the *weekly averaged values* of the office loads obtained with a HC/CC-control strategy (left) and an MPC control strategy (right), and are characterized by the relative imbalance between the building heating and cooling demand (δQ_b).

n_b	Office loads HC/CC				Office loads MPC			
	GEO_h	GEO_c	δQ_b	δQ_{bf}	GEO_h	GEO_c	δQ_b	δQ_{bf}
25	1.00	1.00	-0.33	-0.48	1.00	1.00	-0.34	-0.44
15	1.00	0.86	-0.33	-0.41	1.00	0.85	-0.34	-0.38
11	1.00	0.70	-0.33	-0.32	1.00	0.69	-0.34	-0.28
8	1.00	0.60	-0.33	-0.24	1.00	0.58	-0.34	-0.20
7	0.99	0.52	-0.33	-0.17	0.95	0.50	-0.34	-0.15
6	0.95	0.47	-0.33	-0.13	0.88	0.43	-0.34	-0.12

as well, requiring the GB to help covering the heating load of the first month. Figure 7.37(c) and Figure 7.37(d) reveal that the GB is required when the lower limit on $T_{f,av}$ of 3 °C is active, which is only the case for these very small borefields. Also the fact that a borefield with 26 BHEs may be too large is confirmed: neither the upper, nor the lower limit on $T_{f,av}$ is active.

Figure 7.37(d) and Figure 7.37(e) plot the annual mean ground temperature as a function of the radial distance to the BHE, obtained with the 11th-order model. Two phases are distinguished. In a first phase, when n_b is reduced from 38 to 15, the borefield temperature increases with decreasing n_b . For this range of n_b , \dot{Q}_h and \dot{Q}_c can be (almost) entirely covered by respectively the HP and PC, i.e. $GEO_h = 1$ and $GEO_c \approx 1$ (see Table 7.6). While the relative and absolute imbalance at borefield level, $\|\delta Q_{bf}\|$ and $\|\Delta Q_{bf}\|$, remains almost the same, the imbalance *per BHE* increases, with an increase in $T_{g,i}$ as a result. Further reducing n_b , i.e. from 15 to 6, however, yields a decrease in GEO_c due to the active constraint on $T_{f,av}$. As the amount of heat extracted from the borefield by the HP remains the same while the amount of heat injected to the borefield by PC decreases, both $\|\delta Q_{bf}\|$ and $\|\Delta Q_{bf}\|$ decrease. As a consequence, further thermal build-up is counter-acted and in this second phase, $T_{g,i}$ decreases with decreasing n_b . The influence of n_b on GEO_h , GEO_c and δQ_{bf} is summarized in Table 7.6 for both office loads, i.e. obtained with the HC/CC-control strategy on the one hand, and with the MPC strategy on the other hand. The figures clearly show the decrease in GEO_c from 100% for 26

BHEs to about 40% for 6 BHEs. GEO_h remains 100% until 8 BHEs.

Figure 7.37(d) and Figure 7.37(e) also allow to evaluate the assumption made that there is no thermal interaction between the BHEs. The ground temperature increase relative to the $T_{g,\infty}$ at a distance of 2.5 m of the BHE (which corresponds to half the BHE spacing assumed at the borefield design stage) ranges from 0.3 °C to 0.5 °C, depending on the number of BHEs. While in absolute terms this seems to be quite small, in relative terms the impact may not be negligible. To incorporate the impact of thermal interaction for a given borefield configuration, the borefield loads could be distributed over a number of 'central' BHEs, with adiabatic boundary conditions at half of the BHE spacing, and a number of 'outer' BHEs, with the undisturbed ground temperature connected to the outer node. The relative number of 'insulated' versus 'outer' BHEs would then reflect the compactness or volume-to-surface ratio of the borefield. For densely packed BHEs, the allowed level of thermal buildup or thermal depletion will probably be lower than observed here for the single BHE case, imposing a smaller imbalance between injected and extracted heat (i.e., smaller ΔQ_{bf}). This investigation is however left for future research.

Following qualitative conclusions can be drawn: first, there is no significant difference between the optimal solution for the weekly averaged loads obtained with the HC/CC-controller on the one hand, and with the MPC on the other hand. This indicates that with this large control time step, only the influence of the loads expressed in terms of energy (kWh) matter, which, as listed in Table 4.7, are almost equal for the two control strategies. Second, the number of BHEs required to cover the entire heating load could be significantly reduced compared to the number obtained at the design stage (i.e. n_b 8 in stead of 26). This suggests that the *peak* heating loads have determined the borefield size at design stage. Note that the numerical results depend on the choice of the lower and upper limit for $T_{f,av}$, since this directly constraints the amount of heat injected or extracted from the borefield. The values presented here, are obtained for $T_{f,av,min}$ and $T_{f,av,max}$ equal to respectively 3 °C and 15 °C. These limits were chosen more stringent than the limits of 0 °C and 20 °C on the actual T_f to account for the temperature change of T_f due to a peak heat injection or extraction power (see Eq.(7.71) on p.202). In the next section, the OCP will be solved for the hourly load data. In that case, no assumptions on the required temperature margins have to be made, and the actual constraints for T_f (0 °C and 20 °C) are imposed.

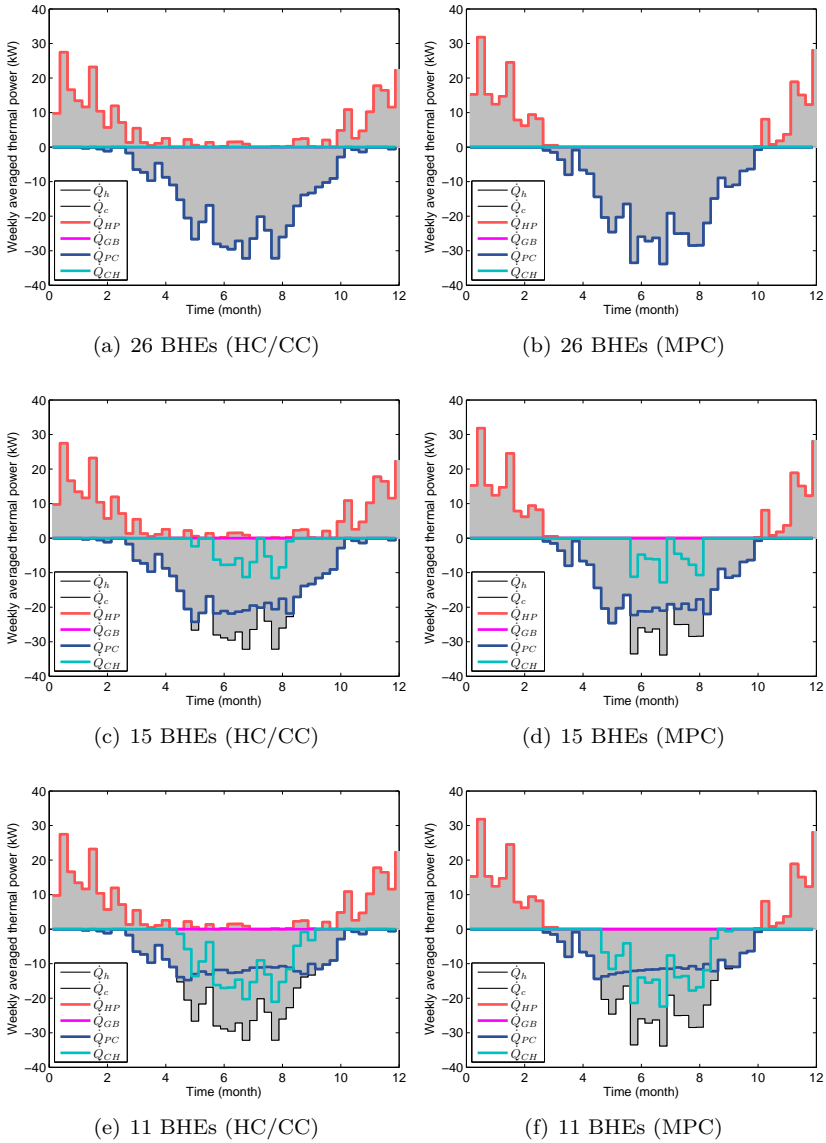


Figure 7.36: Optimal distribution of the weekly averaged heating load $\dot{Q}_h(t)$ and cooling load $\dot{Q}_c(t)$ over respectively the heat pump $\dot{Q}_{HP}(t)$, the gas boiler $\dot{Q}_{GB}(t)$, the passive cooling $\dot{Q}_{PC}(t)$ and the chiller $\dot{Q}_{CH}(t)$ for different borefield sizes ((top) 26 BHEs, (middle) 15 BHEs, (bottom) 11 BHEs), and this for the office (3600 m²) load profiles obtained with the HC/CC-control strategy HC/CC (left) and with MPC (right).

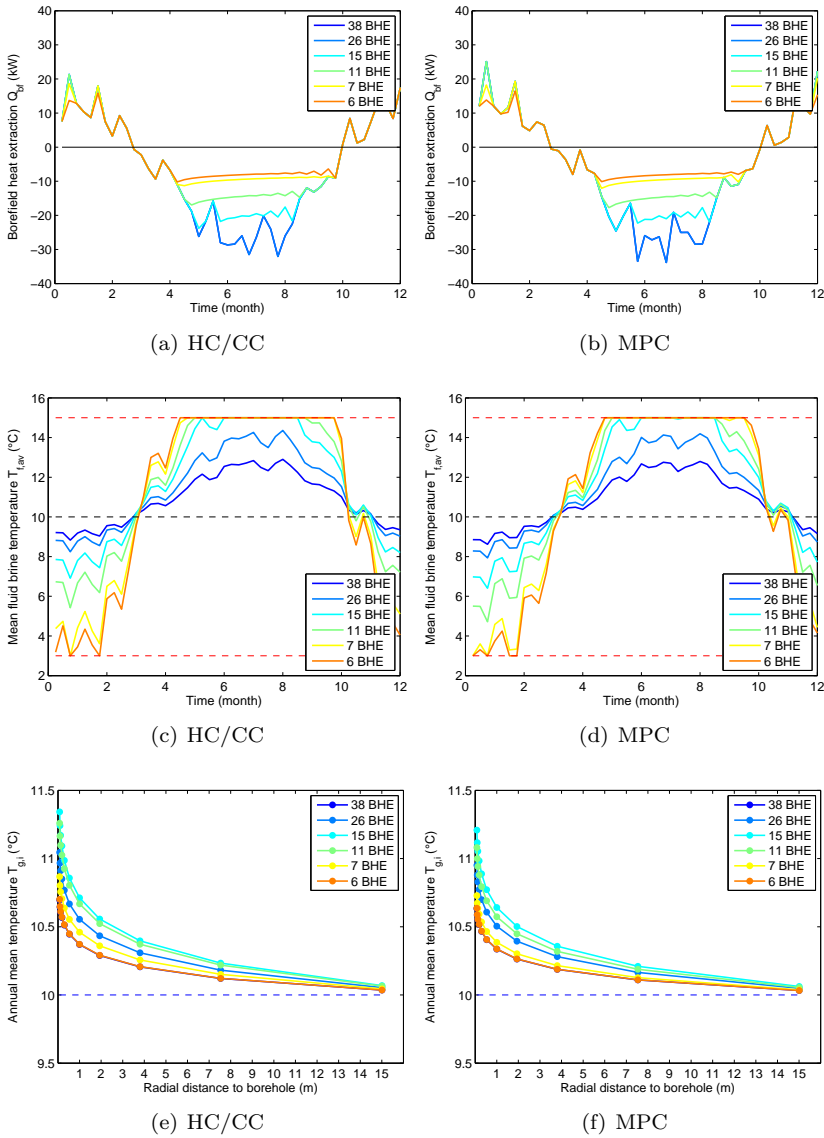


Figure 7.37: Optimal profile for the thermal power extracted per BHE $\dot{Q}_{bf}(t)$ (top), the week-averaged mean fluid temperature $T_{f,av}(t)$ (middle) and the annual mean ground temperature distribution around a single BHE (bottom), for different borefield sizes (6 till 38 BHEs), and this for the load profiles of the office building (3600 m²) obtained with (left) a HC/CC-control strategy, see Figure 7.27(a) and (right) with MPC see Figure 7.27(b).

7.5.4 What drives the optimization in the short term?

As shown in Subsection 7.5.3, there is no fundamental difference between the results obtained with the original nonlinear OCP (with COP_{HP} and COP_{PC} both expressed as a function of T_f) and those obtained with the convex OCP (with COP_{HP} and COP_{PC} being approximated by well-chosen constant values). Compared to nonlinear problems, convex problems can be solved for a significantly larger number of optimization variables. This advantage is exploited to analyze the optimal HyGCHP operation considering both the short and the long term time scale, ranging from 1 h to 1 year. Compared to the OCP with the weekly time step, discussed before, the extension towards the hourly time scale allows to accurately predict the actual brine temperature value T_f instead of the week-averaged one, $T_{f,av}$. Additionally, the impact of the time-of-day electricity price and the diurnal variation of COP_{CH} can be assessed.

The solution of the OCP for the weekly load profiles suggested that the borefield with 26 BHEs (sized to cover 98% of the heating load obtained with the HC/CC control strategy) is too large for the investigated office building. This result can now be verified using the hourly load profiles. Figure 7.38 shows the distribution of \dot{Q}_h and \dot{Q}_c over the HP, the GB, the PC and the CH. While the HP covers the entire heating load, a small fraction of the cooling demand is covered by the CH. Figure 7.39(a) reveals that in summer, T_f indeed reaches the maximum value. In winter, T_f also hits the lower bound $T_{f,min}$. The latter indicates that the borefield size of 26 BHEs, which was obtained following the design guidelines described in Chapter 4, is indeed required to cover 98% of the heating load. The values for GEO_h , GEO_c and δQ_{bf} , based on the hourly load values, are listed in Table 7.7. For 26 BHEs, the optimization yields a GEO_c fraction of 95% and a relative borefield thermal imbalance δQ_{bf} of 43%. These latter values significantly differ from the values assumed at the design stage. There, we imposed thermal balance of the annual amount of heat injected and extracted, i.e. $\delta Q_{bf} = 0$, with a limited GEO_c of only 42% as a result. The optimization indicates that, while respecting (1) the requirement for a long term sustainable borefield operation, and (2) the temperature limits on T_f , a considerable amount of thermal imbalance between injected and extracted heat is tolerated, with a significant increase of the share of PC as a result. The chiller is only operated to cover a few peaks in the cooling demand. Withdrawing the chiller would cause an increase in thermal discomfort during only a few hours of the year. This means that this borefield size corresponds to a GCHP system, not to a HyGCHP system. To analyze the operation of a HyGCHP, which is more cost efficient from life cycle cost point of view, the number of

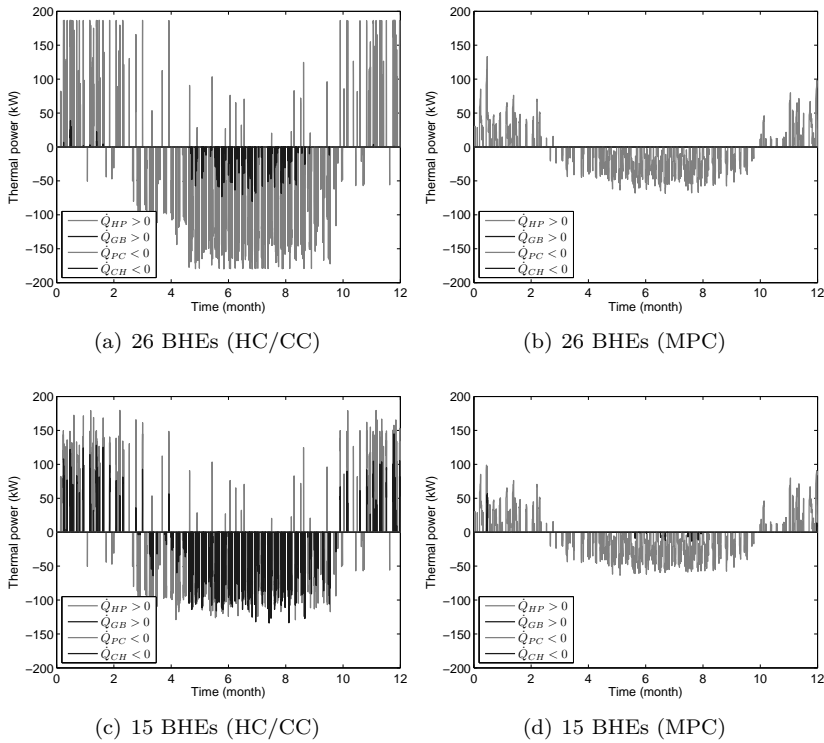


Figure 7.38: Optimal distribution of the hourly heating load $\dot{Q}_h(t)$ and cooling load $\dot{Q}_c(t)$ over respectively the heat pump $\dot{Q}_{HP}(t)$, the gas boiler $\dot{Q}_{GB}(t)$, the passive cooling $\dot{Q}_{PC}(t)$ and the chiller $\dot{Q}_{CH}(t)$ for different borefield sizes ((top) 26 BHEs, (bottom) 15 BHEs), and this for the hourly office load profiles obtained with the HC/CC-control strategy HC/CC (left) and with MPC (right).

BHEs will need to be reduced, as was also suggested by the results obtained with the week-averaged load profiles. The optimization results for the office loads obtained with the HC/CC control strategy for a borefield with 15 BHEs are depicted in Figure 7.38(c) and Figure 7.39(c), and listed in Table 7.7. For GEO_h and GEO_c the optimization yields respectively 77% and 71%. Recall that, based on the week-averaged load profiles these values (for the same n_b) amounted to respectively 100% and 86%. *The difference between the hourly and the weekly optimization is an indicator of the performance loss caused by the peak power demands.*

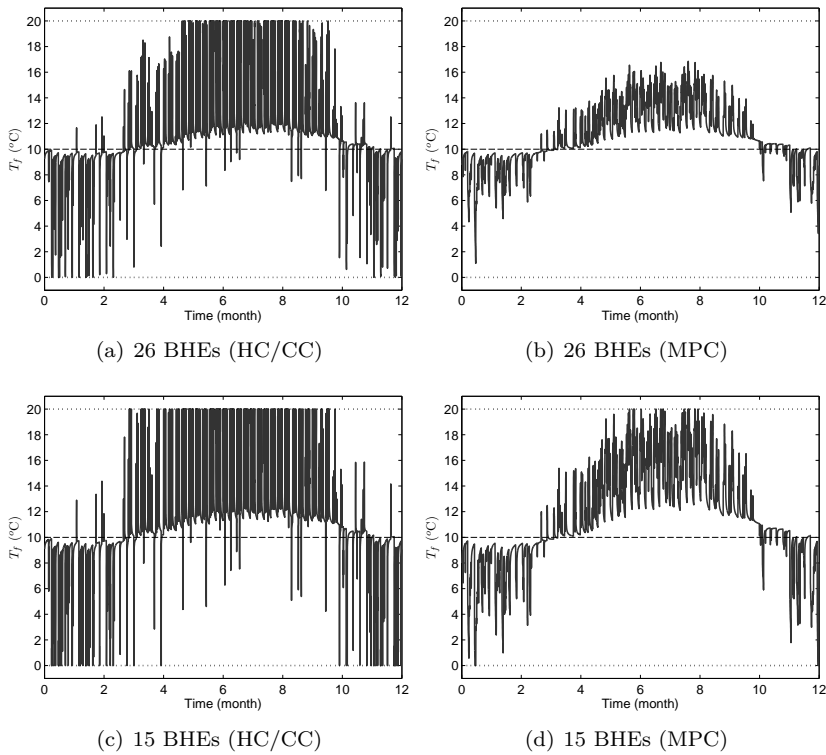


Figure 7.39: Optimal mean fluid temperature $T_f(t)$ for different borefield sizes ((top) 26 BHEs, (bottom) 15 BHEs), and this for the office hourly load profiles obtained with the HC/CC-control strategy (left) and with MPC (right). The dashed horizontal line at 10 ° indicates the undisturbed ground temperature $T_{g,\infty}$, the dotted lines the upper and lower limits on T_f .

Figure 7.38(b) and (d) show the optimal \dot{Q}_{HP} , \dot{Q}_{GB} , \dot{Q}_{PC} and \dot{Q}_{AC} -profiles for the hourly office loads obtained with the MPC controller and Figure 7.39(b) and (d) show the corresponding T_f -profiles. A significant difference with the results for the loads obtained with the HC/CC-control strategy is observed. The borefield with 26 BHEs is by far too large which, as listed in Table 7.7, results in 100% coverage of the heating and cooling loads by the HP and the PC respectively. Even with 15 BHEs, GEO_h and GEO_c remain close to 100%, namely 98% for GEO_h and 100% for GEO_c . While in terms of energy the heating load is the smallest of both ($Q_{h,tot}$ equals 13 kWh/m², $Q_{c,tot}$ equals 25 kWh/m²), the peak heating demand is larger than the peak cooling demand

($\dot{Q}_{h,max}$ equals 36 W/m^2 , $\dot{Q}_{c,max}$ equals 22 W/m^2 , see Table 4.7), and it is the latter factor that dominates the result. Hackel and Pertzborn [70] also emphasized that care should be taken that the peak load of a cooling dominated building is *not* defined by the heating load. This is especially important for borefield design according to current practice, with the borefield size being calculated to meet the smallest of the two loads (in this case heating) entirely, since the required GHE length scales almost linearly with the imposed peak heat injection or extraction power.

With respect to the time-of-day variation of c_{el} and the T_{amb} -dependency of COP_{CH} , none of these factors have an impact on the optimal distribution of \dot{Q}_h and \dot{Q}_c over the 4 devices. The reason for this is the same as for the sinusoidal building loads profiles, discussed in the previous section, where the insensitivity of the optimal solution on the T_f -dependency of $COP_{HP}(t)$ and $COP_{PC}(t)$ was explained: as it will always be cheaper to operate the HP instead of the GB, and PC instead of the CH, the optimization will just strive to maximize GEO_h and GEO_c . This means that the GB and the CH are only used when the HP, respectively the PC, are not able to meet the *imposed* heating and cooling loads. Of course, if the loads could be shifted in time, the optimization could shift the heating and cooling loads towards the night to make better use of the low energy price tariff and of the higher COP_{CH} performance. This flexibility was not provided here. Including both the building and borefield dynamics in the OCP is proposed as a topic for further research. Note that in Chapter 8, where the HyGCHP operation is optimized including the building dynamics (but not the borefield dynamics), the opportunity for peak shaving and load shifting can be exploited.

Following conclusions are derived from the results obtained for the hourly building load profiles. First, the results confirm the observation made for the OCP with the weekly load profiles, namely that the result of the optimization is determined by the constraints on T_f . The second conclusion is a direct result of the first one: it is not the *energy* content of the heating and cooling loads (kWh), but their *power* rates (kW) which limit the use of the borefield in covering the heating and cooling demand. For instance, while the total annual heating and cooling demand with the HC/CC-control strategy is close to the one with the MPC-control strategy, the former requires a borefield with 26 BHEs to cover the entire heating demand, while the latter only requires 15 BHEs. This also explains why *both* GEO_h and GEO_c decrease with decreasing n_b . If the net energy demand (kWh) was the restricting factor, we would initially only observe a decrease of GEO_c when reducing n_b for this cooling dominated office building. The third conclusion is also linked with the fact that the T_f -constraints determine the solution: the fraction of the heating and cooling demand covered by the HP, respectively PC, is maximized within these limits,

Table 7.7: Influence of the borefield size, represented by the number of BHEs n_b , on the fraction of the office heating load covered by the HP ($GEO_h(-)$), the fraction of the office cooling load covered by PC ($GEO_c(-)$) and the resulting relative imbalance of the borefield loads ($\delta Q_{bf} (-)$). The building heating and cooling loads are the *hourly values* of the office loads obtained with a HC/CC-control strategy (left) and an MPC control strategy (right), and are characterized by the relative imbalance between the building heating and cooling demand (δQ_b).

n_b	HC/CC				MPC			
	GEO_h	GEO_c	δQ_b	δQ_{bf}	GEO_h	GEO_c	δQ_b	δQ_{bf}
38	1.00	0.99	-0.33	-0.43	1.00	1.00	-0.34	-0.44
26	1.00	0.95	-0.33	-0.42	1.00	1.00	-0.34	-0.44
19	0.89	0.82	-0.33	-0.40	1.00	1.00	-0.34	-0.44
15	0.77	0.71	-0.33	-0.40	0.98	1.00	-0.34	-0.44

and this maximization can result in a significant amount of thermal imbalance between the injected and extracted heat. For the office loads obtained with the HC/CC-control strategy and the MPC strategy, δQ_{bf} amounts to respectively 40% and 44%. To conclude, the OCP results differ from the assumptions made at the design phase on two points: first, balance of the injected and extracted heat (i.e. $\delta Q_{bf} = 0$) is not required. On the contrary, large imbalances allow higher values for GEO_h and GEO_c . Second, it is not necessarily optimal to size the borefield for the smallest of the two loads (expressed in terms of energy), also the peak loads should be considered. For the office loads obtained with MPC, for instance, the optimal GEO_h decreases with n_b before GEO_c starts decreasing.

7.5.5 Comparison of weekly versus hourly optimization

Current borefield design practice often starts from predefined building loads, i.e. \dot{Q}_h and \dot{Q}_c , as well as predefined values for GEO_h and GEO_c . For a traditional GCHP system, for instance, both GEO_h and GEO_c are imposed to be close to 100%, while for an HyGCHP system only GEO_h or GEO_c (depending which of the loads is the smallest) is imposed to be 100%. The investigated OCP, presented in Section 7.2, showed to be interesting to assist in the choice for GEO_h and GEO_c . The OCP yields an optimal value for GEO_h and GEO_c for a given heating and cooling load profile as a function of the number of BHEs. The OCP was solved both for week-averaged loads and for hourly loads. The latter requires much more computational power, while the former requires tuning of the constraints set with respect to $T_{f,av}$. In this section, we briefly discuss the differences in the results obtained for the weekly and hourly optimization, and what can be learned from this.

Figure 7.40(a) and Figure 7.40(b) summarize the influence of n_b on GEO_h and GEO_c for the two office loads ('HC/CC' and 'MPC'), for respectively the week-averaged loads and the hourly values.

Figure 7.40(a) illustrates that the results obtained for the HC/CC loads and for the MPC loads are almost the same if abstraction of the actual peak powers is made. In this case, the optimization only considers the heating and cooling loads expressed in terms of *energy* (kWh). To cover the entire heating load ($GEO_h = 100\%$), 7 BHEs are found to be enough. To additionally cover the entire cooling load ($GEO_c = 100\%$), 15 BHEs are required.

Based on the hourly heating and cooling load values, which include the impact of the *power* demand (kW), the results for the loads with the HC/CC on the one hand and with MPC on the other hand, significantly differ. The loads obtained with the HC/CC-control strategy require 26 BHEs to cover the entire heating load, while for the MPC loads only 15 BHEs are required. For the MPC loads, further reduction of n_b causes a larger drop in GEO_h than in GEO_c , while for the HC/CC loads the opposite holds. This is explained by the fact that for the considered MPC the peak heating demand is much larger than the peak cooling demand (36 versus 22 W/m²), while this is not the case for the considered HC/CC control (53 versus 51 W/m²).

The difference between the results shown in Figure 7.40(a) and Figure 7.40(b) illustrates that the optimization based on hourly loads, is entirely determined by the peak powers. The same is true for current borefield design practice. The impact on the required GHE length of something so 'random' is alarming. The results obtained with the week-averaged loads seem to be more 'robust'. For weekly-averaged loads the borefield size is not so sensitive to the required peak

powers (only indirectly, through the choice for the $T_{f,av}$ temperature limits) and thus to the control strategy used to determine the loads. Moreover, the sensitivity of GEO_h and GEO_c to n_b corresponds better to what we would expect for a cooling dominated building.

It is observed that the required n_b obtained for the week-averaged loads is significantly smaller than what results from the hourly optimization. The difference between both is a function of the peak loads, which, as stated before, is more sensitive to the controller used to determine the load profiles, than to the building considered. The question arises how the HyGCHP would operate if the borefield was sized based on the results of the OCP with the week-averaged building loads. The impact of the the GHE length (through n_b) on the investment costs and the energy costs, evaluated over a time frame of 10 years for both a HC/CC-control strategy and an MPC strategy, is evaluated in Chapter 8.

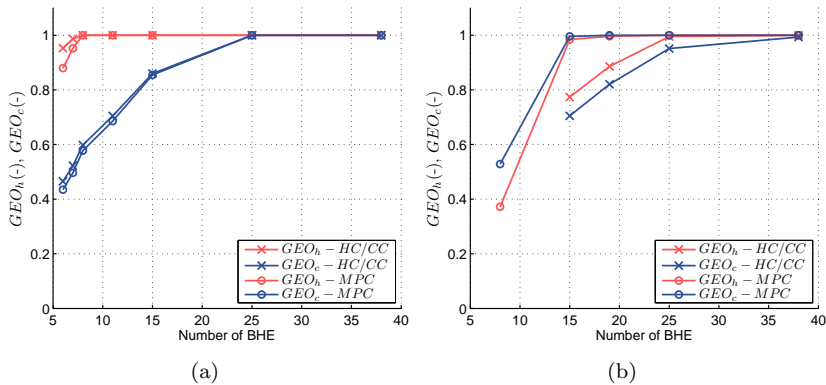


Figure 7.40: Fraction of the annual heating demand covered by the HP (GEO_h) and of the annual cooling demand covered by PC (GEO_c) as a function of the number of BHEs, and this for the weekly (left) and hourly (right) office building loads obtained with the HC/CC-control strategy ('HC/CC') and MPC strategy ('MPC').

Figure 7.41 summarizes the results obtained for the OCP with respect to the thermal imbalance between the injected heat by PC and the extracted heat by the HP. We recall that all results correspond to a steady-state optimal solution for the borefield given the defined building loads, i.e. the borefield is in thermal balance as imposed by the periodic boundary conditions on the ground temperatures $T_{g,i}$. Both for the weekly and hourly control time steps, and for

the HC/CC and MPC load profiles, a heat injection surplus of more than 40% is found, at least for borefields with more than 15 BHEs. For smaller borefields, the hourly and weekly optimization results contradict each other. While the imbalance drops to 10% in the case of the weekly OCP (due to the decreased GEO_c , see Figure 7.41(a)), the imbalance increases up to 60% in the case of the hourly OCP.

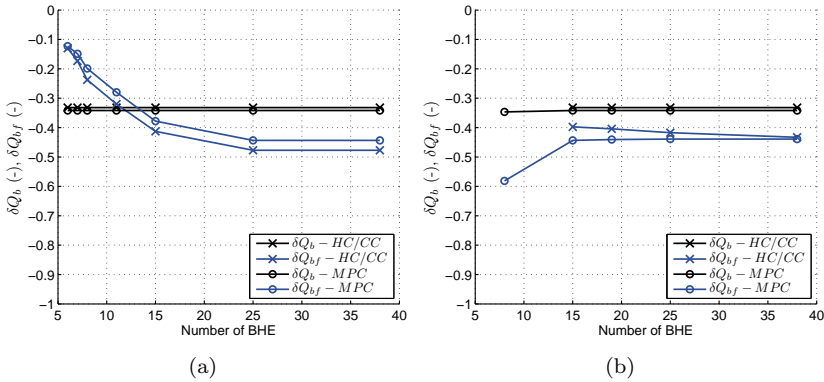


Figure 7.41: Relative imbalance between heating and cooling loads at building level (δQ_b) and imbalance between heat injection and extraction at borefield level (δQ_{bf}) as a function of the borefield size (characterized by the number of BHE), and this for the weekly (left) and hourly (right) office building loads obtained with the HC/CC-control strategy ('HC/CC') and MPC strategy ('MPC').

7.5.6 Computation time

Table 7.8 evaluates the computation time (CPU) as a function of the following factors:

- convex versus nonlinear OCP,
- the number of control time steps N_c ,
- the order of the BHE model N .

The values illustrate the computational benefit of a convex optimization problem compared to a nonlinear one. With the CPLEX and QPOasis solvers used, the

Table 7.8: Computation time for solving the OCP as a function of the optimization problem, the number of control time steps N_c and the BHE model order N . If a range is given, this corresponds to a range of borefield sizes.

Δt_c	N_c	convex OCP (CPLEX)			nonlinear OCP ACADO (QPOasis)		
		$N=3$	$N=6$	$N=11$	$N=3$	$N=6$	$N=11$
1 month	12	<1s	<1s	<1s	20s	x	300s
1 week	48	<1s	<1s	<1s	200s	x	1500s
1 day	365	$\approx 1s$	$\approx 1s$	$\approx 1s$	-	-	-
1 hour	8760	3min	5-60min	23min - >1h	-	-	-

CPU time differs with a factor 100 or more. Moreover, the nonlinear solver sometimes has convergence problems, while the convex solver always find a solution. Additionally, the convex OCP allows us to increase the number of control time steps N_c to 8760. For this large N_c value, the CPU time to solve the OCP with a BHE model of $N=3$ is 10 times less than for $N=11$. The tabulated spread in CPU time depends on the physics of the OCP solved. The lower CPU is found for the case with a large borefield, the higher CPU for the case with a small borefield. In the former case the constraint on T_f are rarely active. In the latter case, the constraint on T_f is active during a large fraction of the time and this makes the problem harder to solve.

7.5.7 Optimization from a system's perspective

It is important to frame the observations made, i.e. the influence of the number of BHEs on GEO_h , GEO_c and the related borefield temperature, within the context of the presented OCP. As is the case for standard borefield design calculations, the *building heating and cooling loads* \dot{Q}_h and \dot{Q}_c are predefined. This means that the optimization has no flexibility to increase the share of the HP, i.e. GEO_h , or the share of PC, i.e. GEO_c , by shifting the loads in time. An optimization from a system's perspective, including both the building dynamics and the borefield dynamics in one single optimization, would therefore enable even larger shares of the HP and the PC. Load shifting at building level, made possible thanks to the thermal mass of CCA, could be directly exploited for this purpose. As the optimization has to run over a time horizon of 8760 h, a low-order building model is required which accurately predicts the operative temperature T_{op} for the entire year, including the response to the solar gains and the internal gains. The validation results for the low-order building models obtained by parameter estimation in Chapter 5, Section 5.4, however, indicate

that this requirement is not easy to fulfill. The models were found to yield satisfactory prediction of T_{op} only within the MPC framework, as the latter enables to improve the predictions of T_{op} based on the actual T_{op} measured (see Section 5.5.1). This optimization from an integrated system's perspective which can be used at design level, is therefore left for future research.

7.6 Summary and conclusions

The operation of HyGCHP systems requires a strategy for switching between the GCHP system and the backup system. Optimally, the building heating and cooling demand are satisfied at a minimal energy cost. The formulation of the corresponding OCP requires a dynamic BHE model which captures both the short and long term borefield dynamics. The small time scale, related to the brine temperature response to the borefield loads, determines the heat pump COP and the passive cooling efficiency. The large time scale is required to assure a long term sustainable solution.

Existing borefield models have been developed for design purposes, being too complex for incorporation in an optimization framework. The following questions arise: (1) Is it possible to describe the control relevant dynamics by a low-order state space model? (2) How to obtain such a model? (3) What is the minimal model order?

Three approaches have been studied: black-box, grey-box and white-box modeling. The black-box models were obtained by system identification in the frequency domain using the FDIDENT Matlab toolbox. Both rational functions in the Laplace variable s and in \sqrt{s} were put forward, with the latter being based on the analytical solution for radial heat diffusion. The grey-box models were obtained by parameter estimation of a resistance-capacitance network representing the radial heat transfer in the ground. The white-box models were obtained by applying the modeling guidelines formulated by Eskilson, followed by model reduction to decrease the model order. The data for system identification, parameter estimation and model validation are simulation data obtained with the detailed TRNSYS DST-model.

The validation results revealed that the grey-box and white-box approaches are able to predict the brine water temperature for the long term time scale with a relative model error of less than 1% and this with very low-order models, respectively order 3 and order 6. The black-box models in the variable s , on the contrary, required large model orders to predict the brine water temperature. Moreover, these models could not be used outside the frequency range covered by the identification data. This inferior model performance could possibly be

explained by numerical artefacts in the identification data set. The black-box models in the variable \sqrt{s} were shown to have good extrapolation capabilities and this with lower model orders. This confirms that a description in \sqrt{s} better matches the physics of the heat diffusion process.

Next, a selection of the borefield models were incorporated in the investigated optimal control problem (OCP). The OCP has as objective optimizing the distribution of the building heating and cooling loads over the heat pump (HP) and the gas boiler (GB) on the one hand, and passive cooling (PC) and active cooling (CH) on the other hand, such that long term sustainable borefield operation is guaranteed. The results show that the optimization maximizes the share of the HP and the PC in covering the heating and cooling demand. As a natural consequence, the optimal mean borefield temperature at equilibrium is *higher* than $T_{g,\infty}$ for cooling dominated buildings. This way, the net annual heat loss from the borefield to the surroundings compensates the excess heat injection to the borefield. The benefit of an increased PC/CH ratio thus outweighs the deterioration of the COP_{PC} caused by the increased source temperature. For heating dominated cases, the opposite holds: the optimal mean borefield temperature at equilibrium is *below* $T_{g,\infty}$. This way, the net heat gain from the surroundings to the borefield compensates for the net heat extraction from the borefield. The benefit of an increased HP/GB ratio thus outweighs the deterioration of COP_{HP} caused by the lower borefield temperature. The PC/CH ratio, respectively HP/GB ratio are constrained by the limits on the brine fluid temperature. The temperature difference between the brine fluid and the surrounding ground is proportional to the heat injection or extraction rate. Therefore, the flatter (or lower) the thermal power demand profile, the larger the PC/CH ratio and HP/GB ratio can be.

The analysis of the optimal solution for the envisaged time scales shows that a crucial requirement for the borefield control model is the accurate description of the heat exchange between the borefield and the far field. This net heat exchange constitutes an important term in the heat balance equation and determines the optimal mean borefield temperature. A second requirement to the controller model is a good prediction of the brine temperature as the constraint on this variable is active. A final conclusion is that maximization of the heat pump COP or the passive cooling efficiency as such, is not the driving force in the optimization. A good estimate of the heat pump COP is only needed to determine the borefield heat extraction rate for a given heat pump power. The results of the OCP were also analyzed as a function of the BHE model accuracy. For a control time step of one week, a sixth order model was found to yield the best result for the nonlinear OCP. The convex OCP showed to be less sensitive to the model order, with a minimal required model order of 3. The convex OCP, shown to be a valid approximation of the original nonlinear

OCP, has been used to solve the optimization problem over a time frame of 8760h and a control time step of 1 h. This way, both the short and long term dynamics are included in one single optimization. The results obtained with this hourly control time step confirmed the results obtained with the weekly control time step, namely that the optimization maximizes the share of the borefield in covering the heating loads, GEO_h (-), and in covering the cooling loads, GEO_c (-), within the constraints imposed on the mean fluid brine temperature T_f . Comparison of the optimal values of GEO_h and GEO_c obtained with the week-averaged building load values on the one hand, and with the hourly load values on the other hand, highlights the significant impact of the peak power demand on these performance indicators. This in turn illustrates the impact of the peak power demands on the required borefield size to fulfill a predefined fraction for GEO_h and/or GEO_c . The insights gained from this optimization, i.e. (1) the tolerance towards imbalance between the injected and extracted heat from the borefield, (2) the active constraints on the brine fluid temperature T_f , and (3) the impact of the peak power demands on the required BHE length, are incorporated in Chapter 8, which has as objective to optimize the control of the office building with CCA and a HyGCHP system from an integrated system's perspective.

7.7 Chapter highlights

- Three approaches to obtain a low-order BHE-model have been investigated and compared against the TRNSYS DST-model. The model accuracy is determined for the time scale ranging from 1 h to 10 years.
- Model reduction of a simple white-box model (1D-FDM), yields accurate models of model order down to $N = 6$. Grey box modeling with parameter estimation, yields accurate models of model order down to $N = 3$. The black-box approach for rational functions in \sqrt{s} have good extrapolation performance for the long term dynamics.
- A set of these BHE-models is incorporated in an OCP formulation which optimizes HyGCHP operation for a given building load profile. The total annual energy cost is minimized under the condition of long term borefield thermal balance (sustainability).
- The optimization maximizes the share of the HP for heating and the share of PC for cooling. For cooling-dominated buildings, this results in an excess heat injection to the borefield. At equilibrium borefield temperature this excess heat injection is compensated by the heat exchange with the surrounding ground. Therefore, the borefield should be a good

heat dissipater rather than a good thermal storage medium. The active constraints are found to be the brine fluid temperature limits.

- The required BHE length to cover the building loads is currently determined by the peak power demand and, as a consequence, very sensitive to the building load calculation step. Peak shaving at building level allows significant reduction of the required BHE length, which in turn yields significant investment cost savings.

Chapter 8

MPC of a HyGCHP system

8.1 Introduction

The study presented in this chapter aims first at contributing to the development of an MPC strategy to optimize the operation of a CCA-HyGCHP system from an integrated system's perspective. Second, this chapter addresses the objective to integrate the use of MPC in both the design and operation phase of HyGCHP systems. The benefit with respect to the life cycle cost compared to conventional design and control strategies is assessed.

In Chapter 5 the operation of the office building with CCA was optimized from a building level perspective with abstraction being made of the installation level. There it was found that, with an ideal boiler/chiller enabling to perfectly track the supply water temperature setpoint, MPC has the potential to reduce the annual energy cost for space heating and cooling by 15% compared to a well-tuned HC/CC controller. The control of a HyGCHP is however far more complex than the control of an ideal boiler/chiller, especially if on/off-controlled devices are considered. As described in Chapter 4, Section 4.5, currently used rule-based control strategies for a HyGCHP system require tuning of a large number of control parameters. Since the control performance is found to be very sensitive to the choice of these control parameters, both in terms of thermal comfort and in terms of energy cost, the development of a more generic approach to guarantee an efficient operation of these HyGCHP systems is strongly advocated [70].

In Chapter 7 the operation of the HyGCHP system was optimized from the installation perspective with abstraction being made of the building level. There

it was found that an optimal operation of the HyGCHP system allows a certain amount of load imbalance of the borefield heat injection and extraction loads, such that the total amount of heat exchanged with the borefield is maximized under the given constraints on the brine fluid temperature and the periodic boundary condition on the ground temperatures in the borefield. The MPC formulation presented in this chapter extends the MPC formulation developed for the building level in Chapter 5 towards the installation level, including these insights.

The results of Chapter 7 also illustrated the dominant impact of the peak power demands on the total ground heat exchanger (GHE) length required to cover the entire heating and/or cooling demand by respectively the HP and passive cooling (PC). For the investigated office building, the results suggested that the number of BHEs n_b required to cover the entire heating load, could be reduced from 26 BHEs (of each 125 m depth) to 15 BHEs if the building load calculation is performed with the MPC strategy presented in Chapter 5 instead of a HC/CC-based control strategy, as the MPC strategy requires smaller peak powers. If thermal power peaks would be flattened out further, n_b could be even further decreased, down to 7. Given the fact that the borefield cost dominates the investment cost, the potential to reduce the GHE length by improving the control strategy at building level, is investigated. The Net Present Value (NPV), evaluated over a time horizon of 20 years, is assessed as a function of the borefield size and as a function of the control strategy (HC/CC-based control versus MPC). The assessment is based on extrapolation of 10-year simulation results of the CCA-HyGCHP system in TRNSYS.

Section 8.2 presents the proposed methodology to tackle the combination of the short term and the long term control objectives as well as the evaluated design cases. Section 8.3 presents the corresponding optimal control problem (OCP) formulation, Section 8.4 the results and Section 8.5 the conclusions.

8.2 Methodology

This chapter tackles two issues. The first issue, being the main focus of this work, is how to optimize the operation of a CCA-HyGCHP system, illustrated in Figure 8.1, from an integrated system's perspective. As stated in Chapter 1, this objective is motivated by experiences from practice which show that those systems are difficult to operate. A first reason is the large thermal capacity of the CCA and a second reason is the presence of different heat and cold production devices. The number of control parameters for this kind of systems is high, and an adequate tuning of the settings proves to be a complex task. As

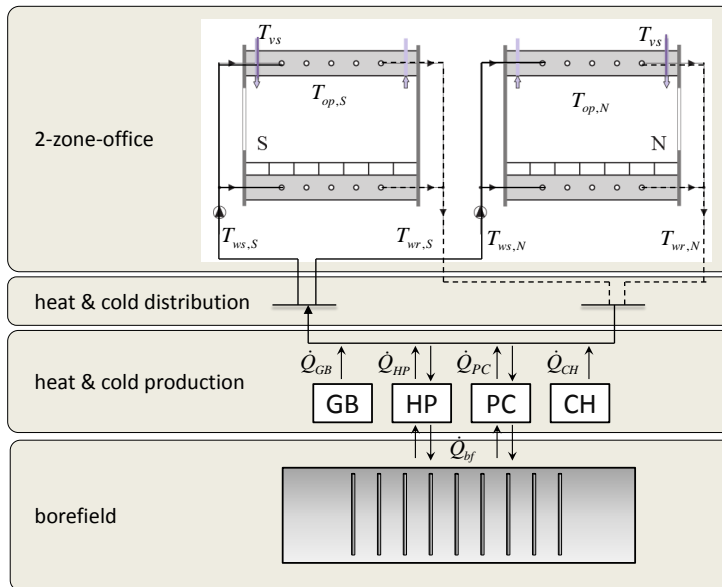


Figure 8.1: Schematic presentation of the system with indication of the two zone office, the heat and cold distribution, the heat and cold production and the borefield. $T_{op,S}$ and $T_{op,N}$ denote the zone operative temperature in respectively the South and North zone, $T_{ws,S}$ and $T_{ws,N}$ the corresponding supply water temperatures and $T_{wr,S}$ and $T_{wr,N}$ the corresponding return water temperatures. The heat and cold production system comprises a gas boiler (GB), a heat pump (HP), a heat exchanger for passive cooling (PC) and a chiller (CH). The heating power $\dot{Q}_h = \dot{Q}_{HP} + \dot{Q}_{GB}$ and the cooling power $\dot{Q}_c = \dot{Q}_{PC} + \dot{Q}_{CH}$. \dot{Q}_{bf} represent the thermal power extracted or injected from the borefield by means of the HP and PC.

a consequence, the energy saving potential of these systems, which in theory is very promising, is in practice not fully harnessed. The objective of the developed MPC strategy is to facilitate the control task by replacing the large number of control settings by one single optimization. The MPC strategy defines the status of each heat and cold production device, based on knowledge of the building dynamics on the one hand, and of the heat and cold production power capacities and performances on the other hand. To this end, the MPC requires a simple but accurate representation of the building dynamics. In Chapter 5 such a controller building model has been derived for the investigated office building.

Additionally, the MPC requires knowledge of the installation characteristics. Catalogue data can be used for this purpose, or, as proposed in this chapter, this information can be obtained from on line measurements. The main question that has to be dealt with, for the case of a HyGCHP system, is how to guarantee long term sustainable operation of the HyGCHP system. At the start of this study, this objective was directly translated to the question: *'How to prevent thermal build-up or thermal depletion of the borefield?'*. The latter is namely assumed to affect the global system's performance as it results in a gradual decrease of the amount of cold available for passive cooling, respectively the amount of heat available for heat pump operation. This wide-spread idea is also reflected in current design guidelines for HyGCHP systems, which suggest to balance the heat injection and extraction loads at borefield level to obtain an optimal borefield size:

$$\int_0^{1y} \dot{Q}_{bf,in} dt - \int_0^{1y} \dot{Q}_{bf,ex} dt = 0 \quad (8.1)$$

This would imply that the optimal operation of a HyGCHP system should not only consider the short-term control objectives, i.e. minimizing thermal discomfort cost and energy cost, but also explicitly incorporate the long term condition reflected in Eq.(8.1). In other words, the MPC should assure that the annual amount of injected and extracted heat are in balance. For a cooling dominated building, as considered here, the MPC should then guarantee that the total amount of heat injected into the borefield by PC does not exceed the amount of heat extracted by the HP. A computationally efficient way to realize this, as suggested by Patteeuw [135], is to allocate for each day of the year a certain 'budget' for passive cooling $CB(t)$ (kWh/day), defined off line for the design reference year. The distribution of the total annual passive cooling budget CB_{tot} (kWh), which equals the annual amount of heat extracted by the HP, over the year could be defined through an off-line optimization as presented in Chapter 7, or simply by rules of thumb, e.g. 'use PC in base load'. $CB(t)$ serves as a reference in the short term optimization ($H_c = 48$ h) incorporated in an on-line MPC framework. This way, the MPC has the flexibility to operate the system on a day-by-day basis where the objectives of maximal thermal comfort and minimal energy cost prevail, while the constraint on the use of passive cooling allows to guarantee the condition expressed by Eq.(8.1). The objective function, expressed by Eq.(8.2), then not only includes the energy cost J_e (€) and the thermal discomfort J_d (K²h), but also the long term cost J_{LT} ((kWh)²), defined by Eqs.(8.3)-(8.4) for a control horizon H_c of 48 h. With this definition of J_{LT} , exceeding the passive cooling budget allocated for the 2 days in the control horizon H_c (48 h), denoted by respectively $CB(d)$ and $CB(d + 1)$ in Eq.(8.4), is penalized. The weighting factors α (-), β (€/K²h)

and γ ($\text{€}/(\text{kWh})^2$) in Eq.(8.2) determine the weight of each objective in the cost function.

$$\min_{\dot{Q}_{HP}, \dot{Q}_{GB}, \dot{Q}_{PC}, \dot{Q}_{CH}} (\alpha J_e + \beta J_d + \gamma J_{LT}) \quad (8.2)$$

$$J_{LT} = \epsilon_{LT}^2 \quad \text{with} \quad \epsilon_{LT} = \begin{cases} 0 & \text{if } \Delta Q_{CB} \leq 0 \\ \Delta Q_{CB} & \text{if } \Delta Q_{CB} > 0 \end{cases} \quad (8.3)$$

with

$$\Delta Q_{CB} = \sum_0^{H_c} \dot{Q}_{PC}(t)dt - (CB(d) + CB(d+1)) \quad (8.4)$$

Based on the results obtained in Chapter 7, however, the requirement to balance the amount of injected and extracted heat by the HP/PC (see Eq.(8.1)), is questioned. The optimal distribution of the building heating and cooling loads over the HP, the GB, the PC and the CH was analyzed for different building load profiles and borefield sizes, with annual borefield thermal balance as constraint. The results indicated that the optimization aims at maximizing the fraction of the heating demand covered by the heat pump, denoted by GEO_h (-), as well as the fraction of the cooling demand covered by passive cooling, denoted by GEO_c (-). For a cooling dominated building, the steady state optimal solution (i.e., the solution which can be repeated year by year and therefore represents a long term sustainable solution) is characterized by a significant surplus of injected versus extracted heat. For the considered office building, the relative thermal imbalance δQ_{bf} (-) between the extracted and injected heat, was found to amount to -44% for a borefield with 26 BHEs. Based on the design condition $\delta Q_{bf} = 0$, GEO_c would only amount to 47%. With $\delta Q_{bf} = -0.44$, however, as suggested by the optimization, GEO_c can be as high as 95%. Further increase of GEO_c is hampered by the upper limit on the mean brine fluid temperature T_f , as the latter should remain below about 20 °C for PC. Obviously, the surplus of injected heat results in a mean borefield temperature T_{bf} which is higher than the undisturbed ground temperature $T_{g,\infty}$. This in turn results in a net heat dissipation $\dot{Q}_{bf,\infty}$ from the borefield to the surrounding ground which compensates for the excess heat injection by passive cooling. This way, the optimal solution effectively complies with the long term sustainability requirement, expressed by Eq.(8.5).

$$\int_0^{1y} \dot{Q}_{bf,in} dt - \int_0^{1y} \dot{Q}_{bf,ex} dt - \int_0^{1y} \dot{Q}_{bf,\infty} dt = 0 \quad (8.5)$$

The concept of a passive cooling budget $CB(t)$, introduced above to satisfy Eq.(8.1) within an on-line MPC framework, can also be used to satisfy the

'improved' thermal balance condition expressed in Eq.(8.5). The total annual cooling budget CB_{tot} should then be increased with the term $\int_0^{1y} \dot{Q}_{bf,\infty} dt$ resulting from the off-line optimization. The results obtained in Chapter 7, however, suggest that Eq.(8.5) is automatically satisfied. The optimization just tries to maximize GEO_h and GEO_c for the given constraints on T_f . Further increase of GEO_c , and thus of the steady state mean borefield temperature T_{bf} , is prevented by the constraint on T_f . Therefore, it could be possible that an MPC strategy which only takes the short term objectives into account may also evolve towards this optimal steady state solution, just by respecting the constraints on T_f . For the considered cooling dominated office building, the borefield temperature would then rise during the first years of operation and eventually stabilize at a certain equilibrium temperature. This hypothesis is investigated in this chapter. The MPC formulation is presented in Section 8.3.

A second issue tackled in this chapter, is the relation between control and design. It is generally known that the design influences the control. In the extreme case of a very large borefield, for instance, the heating and cooling loads can be entirely covered by the HP, respectively by PC. In the other extreme, i.e. no borefield at all, the heating and cooling loads are entirely covered by the GB, respectively the CH. For both extremes, the control task is simpler than for a HyGCHP system, where the controller needs to determine when to switch between the different heat and cold production devices. This is a first example of how the design affects the control. A second example is the impact of the installed heating and cooling capacity on the control settings. Larger installed capacities can reach the supply water temperature setpoint faster, and thus also the zone temperature setpoint, compared to less powerful devices. Therefore, smaller installed capacities require earlier start-up. How much earlier, is again a challenge for the controller. It is therefore important to evaluate the performance of the developed MPC and of the HC/CC-based control strategy as a function of the borefield size and of the installed capacities. As stated in Chapter 1 the control also influences the design, especially for cases with (a) CCA [173] and (b) a GCHP system [70] (and thus even more for the combined system CCA-GCHP). The impact of control on design is in practice often underestimated. For conventional heating and cooling systems (with GB and CH only), this is not so problematic as for GCHP systems due to the absence of large borefield investment costs. Current design practice is to size the borefield for a given building load profile. The required total BHE length is, however, extremely sensitive to this building load profile, as illustrated in Chapter 7. For the load profile obtained for the investigated (cooling dominated) office building with the reference HC/CC-control strategy, the optimization results showed that 26 BHEs are required to cover 100% of the heating load ($GEO_h = 1$). This number corresponds to the one found when following the HyGCHP design guidelines in combination with the borefield

design software GLHEPRO [166], described in Chapter 4. The optimization however also suggested that only 15 BHEs are required to cover 100% of the heating demand for the load profile obtained with the MPC strategy, the latter being characterized by far smaller peak heating demands than the HC/CC-control strategy. To validate this result, the required number of BHE for the MPC load profile has been determined with the design software GLHEPRO, following the procedure described in Chapter 4. This yields 14 BHEs, which is close to the result obtained by the optimization. This result confirms the potential to decrease the investment costs of a HyGCHP system, following the current HyGCHP design guidelines, by *incorporating MPC already in the design phase*. The strength of the use of MPC, with the objective function penalizing the square of the heating and cooling power (see Section 5.3.3, Eq.(5.9)), is that the peak heating and cooling demand, and thus the required BHE length, are drastically reduced compared to current HC/CC-based strategies. We will even go a step further and investigate how the system performs if the number of BHEs is reduced to 7. This number was found by optimization based on the week-averaged loads, discussed in Chapter 7, Section 7.5. In this chapter it will be investigated whether this result makes sense for the actual operation of a HyGCHP system, i.e., taking the dynamics at building level into account. Finally, also a system without a borefield, i.e. a conventional system with only a GB and a CH, will be evaluated. To summarize, 4 design cases will be evaluated:

1. DC1 - 26 BHEs: HyGCHP sized for the office loads obtained with the HC/CC-strategy,
2. DC2 - 14 BHEs: HyGCHP sized for the office loads obtained with the MPC-strategy,
3. DC3 - 7 BHEs: HyGCHP sized for the office loads obtained with the MPC-strategy, with the borefield size based on the OCP result for the week-averaged loads,
4. DC4 - 0 BHEs: gas boiler/chiller (GB-CH) system sized for the office loads obtained with the HC/CC-strategy

The corresponding installed capacities of the HP, the GB, the PC and the CH are listed in Table 8.1.

It should be noted that this study does not provide a methodology to optimize the design and the control of a HyGCHP *simultaneously*. This task was recently undertaken by Hackel [71], who optimized the control settings of a rule-based control strategy simultaneously with the main design parameters

Table 8.1: Evaluated design cases

Design case	Installed power			$\dot{Q}_{CH,nom}$ (kW)
	$\dot{Q}_{HP,nom}$ (kW)	$\dot{Q}_{PC,nom}$ (kW)	$\dot{Q}_{GB,max}$ (kW)	
DC1-26 BHEs	179	124	8	51
DC2-14 BHEs	85	71	33	21
DC3-7 BHEs	48	40	16	27
DC4-0 BHEs	-	-	193	183

(BHE length and cooling tower size). This was achieved by coupling the TRNSYS simulation environment, in which the HyGCHP installation was modelled, with the GENOPT optimization software [184]. The building loads are given as input. The approach evaluated here, by contrast, is to optimize the control from an integrated system's perspective, which, as shown in Figure 8.1, not only comprises the installation level with the borefield, but the heat and cold distribution level and the building zone level as well. Moreover, the MPC framework allows to effectively reduce the peak power demands which determine the installation size. Optimizing design and control simultaneously, with incorporation of the MPC strategy evaluated here, is an interesting topic for further research.

8.3 MPC strategy

The MPC strategy comprises of 2 steps. In a first step, the optimal control problem (OCP), presented below, is solved for the next 48 h, based on the dynamic controller building model, building and installation measurement data and future weather predictions. The solution of the OCP yields a 48 h-profile for $\dot{Q}_{HP}(t)$, \dot{Q}_{GB} , $\dot{Q}_{PC}(t)$ and $\dot{Q}_{CH}(t)$, with hourly values fluctuating between 0 and the maximal thermal power. In a second step, a post-processing step, these profiles are translated into on-off-signals for the corresponding devices. The first 24 h of this on/off-profile are actually applied. After 24 h, the optimization is repeated, using updated system measurements. The optimization is performed each day at 0AM, as this time of the day is (1) characterized by few disturbances and (2) far from the transient periods of the morning start-up and the loads during occupancy, two factors which are known to affect the quality of the measurements.

Note that, in contrast to the hydraulic lay-out of the system considered in Chapter 5, there are no 3-way mixing valves, and by consequence, there is no zone level control: both the mass flow rate \dot{m}_w and the supply water temperature

T_{ws} are equal for the North and the South zone. This simplification is made to simplify the control problem for the HyGCHP system. For the ideal boiler/ideal chiller in Chapter 5, the control signal is the heating or cooling supply water setpoint temperature, which can easily be determined from the setpoints for the individual zones, i.e. $T_{ws,N}$ and $T_{ws,S}$. In the case of a HyGCHP system, however, 4 control signals are required at installation level, i.e. the on-off-status of each of the devices. Additionally optimizing the supply water temperatures for the North and South oriented office zones, i.e. zone-level MPC, would result in a nonlinear optimization problem. Alternatively, the control could be a combination of MPC as high-level controller, determining the total energy flow to the building, with a rule-based low-level control strategy, determining the distribution of the produced heat and cold over the different zones. The MPC then treats the building as a whole, without distinguishing between the loads of the different zones. Here, neither of these two options, i.e. zone-level MPC, nor high-level MPC combined with low-level rule-based control, is implemented. The impact of this simplification on the control performance has been assessed in Chapter 5. In order to meet the thermal comfort requirements in both zones, it was found that the optimization should be performed for the most demanding of the two zones. For the investigated office building with automated solar shading at the South side, the North zone was found to be the most demanding, both for heating and for cooling. The price for this conservativeness showed to be an energy cost increase of about 5%.

OCP formulation The optimization aims at defining the optimal heating or cooling power delivered by each device as a function of time, in order to minimize the weighted sum of the energy cost J_e (€) and the thermal discomfort J_d (K²h), both evaluated over a time horizon H_c of 48 h, see Eq.(8.6). The weighting factors α_e (-) and α_d (€/K²h) define the relative weight of these conflicting objectives.

$$\min_{\dot{Q}_{HP}, \dot{Q}_{GB}, \dot{Q}_{PC}, \dot{Q}_{CH}} (\alpha_e J_e + \alpha_d J_d) \quad (8.6)$$

The definition of J_d remains unaltered (see Eq. (5.10)), penalizing operative temperatures T_{op} exceeding the lower or upper temperature limit denoted by respectively $T_{comf,min}$ and $T_{comf,max}$:

$$J_d = \sum_0^{H_c} (\epsilon_h(k)^2 + \epsilon_c(k)^2) \Delta t_c \quad \text{with} \quad \begin{cases} \epsilon_h(k) & \geq T_z(k) - T_{comf,max}(k) \\ \epsilon_c(k) & \geq T_{comf,min}(k) - T_z(k) \end{cases}$$

The energy cost term, J_e is now defined by Eq. (8.7). J_e penalizes the sum of the *absolute* values of the predicted energy costs, with COP_{HP} and COP_{CH}

assumed constant for the entire control horizon H_c . Penalizing power peaks by minimizing the *square* of the predicted power, found to yield close to optimal operation for the modulating air-to-water HP investigated in Chapter 6, is now not useful as we are dealing with on/off-controlled devices. The values for COP_{HP} , COP_{PC} and COP_{CH} , are updated prior to the MPC-call, based on the measured values for the delivered thermal powers and the corresponding electricity consumptions. This way, no model for the installation devices or the borefield outlet temperature $T_{f,o}$ is needed. On the other hand, it requires additional installation of calorimeters. $c_e(k)$ (€/kWh) denotes the time-of-day electricity price and c_{gas} (€/kWh) the gas price. Peak electricity price amounts to 0.15 €/kWh (from 7AM to 22AM), off-peak electricity price 0.09 €/kWh and the gas price 0.06 €/kWh .

$$J_e = \sum_0^{H_c} (c_{el}(k) \left(\frac{\dot{Q}_{HP}(k)}{COP_{HP}} + \frac{\dot{Q}_{PC}(k)}{COP_{PC}} + \frac{\dot{Q}_{CH}(k)}{COP_{CH}} \right) + c_{gas} \frac{\dot{Q}_{GB}(k)}{\eta_{GB}}) \Delta t_c \quad (8.7)$$

The incorporated controller building model is the 2nd order model **nx2-DS3** in combination with the prediction error correction method c_2 (see Eq.(5.30)), obtained from parameter estimation as described in Chapter 5. This combination was found to yield a very good control performance for the investigated office building. The building model equations (see Eq.(5.27)) are repeated here:

$$\begin{bmatrix} T_c(k+1) \\ T_z(k+1) \end{bmatrix} = \mathbf{A} \begin{bmatrix} T_c(k) \\ T_z(k) \end{bmatrix} + \mathbf{B}_T \begin{bmatrix} T_{ws}(k) \\ T_{vs}(k) \\ T_{amb}(k) \end{bmatrix} + \mathbf{B}_Q \begin{bmatrix} \dot{Q}_{int}(k) \\ \dot{Q}_{sol}(k) \end{bmatrix} + \begin{bmatrix} 0 \\ \Delta T_z(k) \end{bmatrix}$$

The input of the building model, $T_{ws}(t)$ has to be related to the controlled variables $\dot{Q}_{HP}(t)$, $\dot{Q}_{GB}(t)$, $\dot{Q}_{PC}(t)$ and $\dot{Q}_{CH}(t)$. The expression for T_{ws} which links the building dynamics to the installation is given by Eq.(8.8).

$$(UA)_{wf} (T_{ws} - T_c) = \dot{Q}_{HP} + \dot{Q}_{GB} - \dot{Q}_{PC} - \dot{Q}_{CH} \quad (8.8)$$

with $(UA)_{wf}$ (W/K) representing the lumped heat exchange coefficient between the supply water at temperature T_{ws} and the concrete core at temperature T_c .

Input constraints The heating and cooling devices are on/off-controlled. The OCP, however, determines the hourly averaged values of the thermal power delivered by each device. By consequence, the OCP formulation allows the

powers to take any value between zero and the maximal heating or cooling capacity, as indicated by Eqs. (8.9) - (8.12).

$$0 \leq \dot{Q}_{HP} \leq \dot{Q}_{HP,max} \quad (8.9)$$

$$0 \leq \dot{Q}_{GB} \leq \dot{Q}_{GB,max} \quad (8.10)$$

$$0 \leq \dot{Q}_{PC} \leq \dot{Q}_{PC,max} \quad (8.11)$$

$$0 \leq \dot{Q}_{CH} \leq \dot{Q}_{CH,max} \quad (8.12)$$

The maximal thermal power of the gas boiler, denoted by $\dot{Q}_{GB,max}$ (W), is constant, i.e. equal to $\dot{Q}_{GB,max}$ listed in Table 8.1. The heating capacity of the heat pump and the cooling capacity of the PC heat exchanger, denoted by respectively $\dot{Q}_{HP,max}(t)$ (W), $\dot{Q}_{PC,max}(t)$ (W), depend on the brine temperature leaving the borefield, $T_{f,o}(t)$ (°C) and the supply water temperature at building level $T_{ws}(t)$. The cooling capacity of the chiller, $\dot{Q}_{CH,max}(t)$ (W), depends on the ambient air temperature $T_{amb}(t)$ and on the supply water temperature $T_{ws}(t)$.

$$\dot{Q}_{HP,max}(t) = f_1(T_{bf,o}(t), T_{ws}(t)) \quad (8.13)$$

$$\dot{Q}_{PC,max}(t) = f_2(T_{bf,o}(t), T_{ws}(t)) \quad (8.14)$$

$$\dot{Q}_{CH,max}(t) = f_3(T_{amb}(t), T_{ws}(t)) \quad (8.15)$$

These temperature dependencies can be explicitly taken into account by setting up correlations for f_1 , f_2 and f_3 , as was done by Verhelst et al. [179]. In this study, a more pragmatic approach is used. The values for $\dot{Q}_{HP,max}$, $\dot{Q}_{PC,max}$ and $\dot{Q}_{CH,max}$ are determined prior to the MPC-call, namely equal to the thermal power the last time the device was operating, determined through measurements of the delivered heat/cold. This avoids the need for a controller model of the installation, but - as stated previously - it requires installation of calorimeters. The choice whether to use catalogue data or measurement data is important from practical point of view, but not from theoretical one. Note that in the current OCP formulation, the input constraints are held constant for the entire control horizon H_c of 48 h.

Post-processing The MPC yields a 48 h-profile for $\dot{Q}_{HP}(t)$, $\dot{Q}_{GB}(t)$, $\dot{Q}_{PC}(t)$ and $\dot{Q}_{CH}(t)$. By means of Pulse Width Modulation (PWM) each profile is translated into an on/off-signal for the corresponding device. The minimal pulse width is equal to the TRNSYS simulation time step of 0.2 h (=12 minutes).

For the heat pump a minimal on-time of 20 min is ensured to avoid cycling. A sensitivity analysis of the actual control performance on this post-processing step showed that the impact of this post-processing step, for which different solutions exist, is limited, as also observed by Wimmer [186]. The difference between two distinct implementations on the total annual energy cost is found to be smaller than 5%. The influence on the thermal discomfort cost is slightly higher (30 Kh - 50 Kh for the same choice of the weighting factors α_e and α_d).

8.4 Results

The control performance obtained with the MPC strategy and with the HC/CC-based control strategy are evaluated over a time horizon of 10 years. This long time horizon is required to evaluate the degradation of the control performance due to borefield thermal build-up. In general, we want to assess (1) the improvement potential of MPC compared to a HC/CC-based strategy and (2) the potential to decrease the borefield size in order to reduce investment costs. Specifically, following questions are answered:

1. With respect to **thermal comfort**:
 - How does MPC compare to the HC/CC-based control strategy?
 - What is the sensitivity of thermal comfort to the installation size, in case of MPC?
 - What is the sensitivity of thermal comfort to the installation size, in case of a HC/CC-control?
2. With respect to **energy cost**:
 - How does MPC compare to the HC/CC-based control strategy?
 - What is the sensitivity of the energy cost to the installation size, in case of MPC?
 - What is the sensitivity of the energy cost to the installation size, in case of a HC/CC-control?
3. With respect to the **long term sustainability** of the borefield operation:
 - To what extent does borefield thermal-build up affect the annual energy cost?
 - How does the borefield size relates to the level of borefield thermal build-up?

Table 8.2: Evaluation of MPC versus a HC/CC-control strategy for different HyGCHP designs (DC1, DC2, DC3) and a conventional GB/CH system (DC4). The NPV and PBT are evaluated for 2 energy price scenarios.

Performance indicator			DC1	DC2	DC3	DC4
IC	(k€)		74	100	151	233
Kh_{tot}	(Kh/y)	HC/CC	85	68	80	84
		MPC	23	30	34	31
GEO_h	(%)	HC/CC	93	90	91	0
		MPC	99	98	98	0
GEO_c	(%)	HC/CC	83	75	57	0
		MPC	97	90	69	0
E_{prim}	(kWh/m ² /y)	HC/CC	9.4	13.5	18.2	32.9
		MPC	7.5	9.0	14.2	31.5
C_e	(€/m ² /y)	HC/CC	0.44	0.63	0.88	1.93
		MPC	0.29	0.37	0.62	1.53
NPV	(k€)	HC/CC	142-213	130-160	170-189	244-256
		MPC	129-185	116-133	159-169	241-250
PBT	(y)	HC/CC	ref	>20	17 - >20	8 - 11
		MPC	-	>20	14 - >20	6 - 8

4. With respect to the **life cycle cost**:

- What is the pay-back time (PBT) of the evaluated HyGCHP design cases compared to a GB-CH system ?
- What is the Net Present Value (NPV) of each case, evaluated over a time horizon of 20 years?

8.4.1 Overview

Table 8.2 summarizes the results. The first row tabulates the investment cost (IC) for the different design cases. Next, annual thermal discomfort (Kh_{tot}), GEO_h and GEO_c , primary energy consumption E_{prim} (kWh/m²/y) and energy cost C_e (€/m²/y) - evaluated after 10 years of operation, are tabulated as a function of the control strategy. The two last rows present the NPV evaluated over a time frame of 20 years and the PBT for two energy price scenarios. The following sections discuss these performance indicators one by one in more detail.

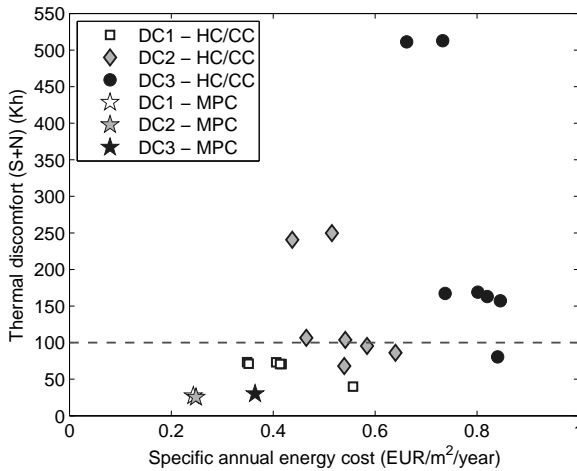


Figure 8.2: Performance cloud of the HC/CC-control strategies for the different HyGCHP design cases (DC1, DC2 and DC3) obtained by varying the HC/CC-control settings. The performance of the MPC strategy for each design case is added as a reference. The thermal comfort limit of 100 Kh is indicated by the dashed line.

8.4.2 Tuning of the control parameters

The results for the reference control strategy presented correspond to the best HC/CC-based control strategy found, based on a manual, iterative optimization of the control settings. The values tuned for DC1 are listed in Table 4.5 on p.49. Using the same settings for DC2 and DC3, which have smaller installed capacity, yields unsatisfactory thermal comfort. Therefore, the manual tuning has been repeated for both DC2 and DC3. Figure 8.2 shows the performance cloud obtained when varying the HC/CC-control settings. For each design, the selected HC/CC-control strategy is the one which satisfies the thermal comfort requirement ($Kh_{tot} < 100$ Kh) at the lowest energy cost. The performance obtained with MPC is added as a reference. The sensitivity of the control performance of the HC/CC-control strategy to the control settings illustrates one of its weaknesses: a HC/CC-based control strategy requires to be fine-tuned for each individual case, not only as a function of the building characteristics, but also as a function of the installation size. The MPC strategy, on the contrary, automatically adjusts the control action as a function of the installed capacities. MPC namely explicitly accounts for the available heating and cooling capacity (see Eq.(8.9)-(8.12)). The tuning variables of the MPC, i.e. the weighting

factors α_e en α_d in the cost function, can be kept constant for the different design cases.

Figure 8.2 also reveals that the HC/CC-control strategy has more difficulty to achieve good control performance for the smaller design cases (DC2 and DC3) than for the larger ones. The control performance of MPC, by contrast, is less sensitive to the installation size. On the other hand, as indicated in Chapter 5, MPC requires a suitable controller building model and good disturbance predictions to achieve good control performance.

8.4.3 Thermal comfort

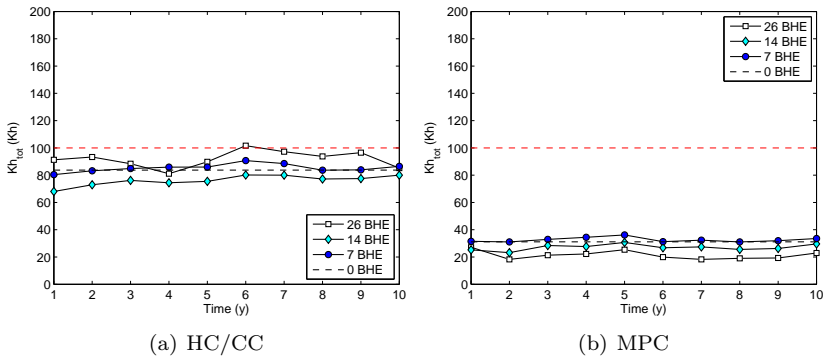


Figure 8.3: Thermal discomfort, expressed in terms of annual number of temperature exceeding hours Kh_{tot} , as a function of time for the HC/CC-control strategy (left) and for MPC (right) for different borefield sizes (26 BHEs, 14 BHEs 7 BHEs and 0 BHEs (GB and CH only)). The thermal comfort limit of 100 Kh is indicated by the dashed line.

Figure 8.3 shows that it is possible to satisfy the thermal comfort requirement for building class B with both the HC/CC-control strategy and MPC. However, the thermal comfort level obtained with MPC is better than for the HC/CC-control strategy. Note that the weighting factors α_e en α_d in the cost function of the MPC, reflecting the relative weight of the energy cost versus the thermal discomfort cost, are kept constant for the different design cases. This explains why the thermal discomfort cost slightly increases with decreasing number of BHEs, see Figure 8.3(b), as the energy cost increases with decreasing number of BHEs.

8.4.4 Primary energy consumption

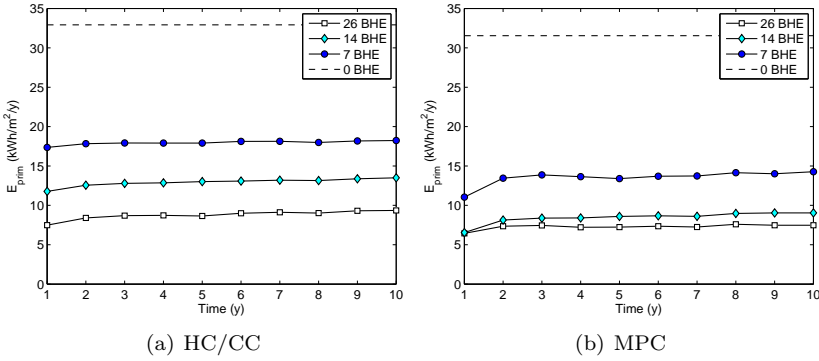


Figure 8.4: Annual primary energy consumption E_{prim} as a function of time for the HC/CC-control strategy (left) and with MPC (right) for different borefield sizes (26 BHEs, 14 BHEs, 7 BHEs and 0 BHEs (GB and CH only)), assuming an efficiency for the electricity production η_{el} of 40%.

The results for the annual primary energy consumption E_{prim} (kWh/m²/y), based on an electricity production efficiency η_{el} of 40%, are shown in Figure 8.4. The primary energy savings potential of a (Hy)GCHP system compared to a conventional GB-CH-system (0 BHEs) is clearly illustrated. With the HC/CC-control strategy, the primary energy consumption for the office building with a HyGCHP system with DC1 (26 BHEs) is 9 kWh/m²/y. Compared to a GB-CH system, where E_{prim} amounts to 33 kWh/m²/y, this is a reduction of more than 70%. For DC2 and DC3 E_{prim} amounts to respectively 13.5 kWh/m²/y and 18 kWh/m²/y. With MPC, the increase of E_{prim} when reducing the number of BHEs is significantly smaller. For DC2 and DC3 E_{prim} amounts to respectively 9 kWh/m²/y and 14 kWh/m²/y compared to 7.5 kWh/m²/y for DC1. This indicates that the relative benefit of MPC is larger for the compact design cases (DC2 and DC3), than for the larger ones (DC1 and DC4). To achieve the thermal comfort requirements with a smaller capacity at an acceptable cost, requires a more intelligent control strategy.

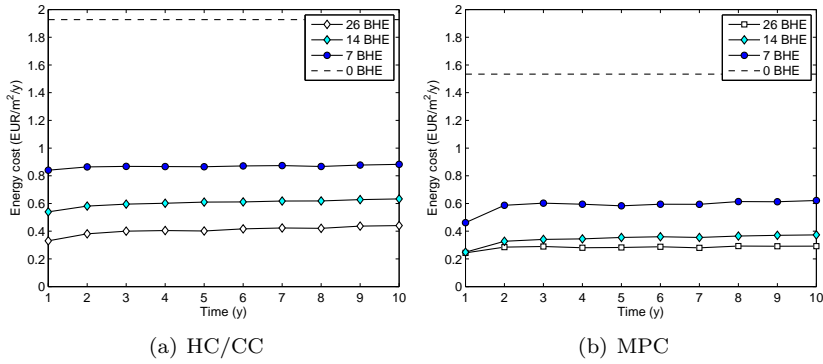


Figure 8.5: Annual energy cost C_e as a function of time for the HC/CC-control strategy (left) and with MPC (right) for different borefield sizes (26 BHEs, 14 BHEs, 7 BHEs and 0 BHEs (GB and CH only)), assuming an efficiency for electricity production η_{el} of 45%.

8.4.5 Energy cost

The annual energy costs (€/m²) are depicted in Figure 8.5. The energy cost reduction obtained with the HyGCHP systems (DC1, DC2, DC3) compared to the conventional system (DC4), tabulated in Table 8.3, is outspoken. The reduction in annual energy cost of a HyGCHP system compared to a conventional system, evaluated at the 10th year of operation, amounts to 82%, 72% and 56% for respectively the DC1 (26 BHEs), DC2 (14 BHEs) and DC3 (7 BHEs) in case of HC/CC-control (see first column in Table 8.3). With MPC, the energy cost savings (which is actually aimed at with the current definition of the energy cost term in the cost function of the OCP formulation (see Eq.(8.7)), even amounts to respectively 88%, 87% and 76% (see second column). The last column shows the energy cost reduction potential of MPC compared to HC/CC-control. For DC1 (26 BHEs), MPC realizes an energy cost reduction of 26% compared to the (well-tuned) HC/CC-controller (and at the same time a better thermal comfort, namely $Kh_{tot} = 23$ Kh per year per zones, instead of 85 Kh), see Table 8.2). For DC4 (GB-CH only), the energy cost reduction amounts to 20% (with Kh_{tot} equal to 31 Kh instead of 84 Kh). For DC2 (14 BHEs) and DC3 (7 BHEs), the energy cost reduction is even higher, respectively 41% and 29%. To conclude, for the same design, and even better thermal comfort, MPC allows to reduce the energy costs compared to a HC/CC-control strategy by 20% up to 40% compared a HC/CC-based control strategy. The cost reduction potential is larger for the (more complex) HyGCHP system than for the (more simple)

GB-CH system. Note that the numerical values in the latter comparison, i.e. the cost reduction potential of MPC compared to HC/CC-control for a given design case, are very sensitive to the HC/CC-controller taken as a reference.

Table 8.3: Annual energy cost reduction of the evaluated HyGCHP systems (DC1, DC2 and DC3) relative to the conventional GB-CH system (DC4). The cost reduction potential is evaluated for both HC/CC-control and MPC. The last column tabulates the energy cost reduction potential (%) of MPC compared to a HC/CC-control strategy.

Reference	DC4 (HC/CC)	DC4 (HC/CC)	HC/CC
Control	HC/CC	MPC	MPC
DC1	-77%	-85%	-26%
DC2	-67%	-81%	-41%
DC3	-54%	-68%	-29%
DC4	0	-20%	-20%

8.4.6 Long term sustainability of borefield use

The profiles of the annual primary energy consumption E_{prim} and of the annual energy cost C_e as a function of time, depicted in Figure 8.4 and Figure 8.5, appear to be rather constant in time. Only between the first year of operation and the second one, a significant degradation of the control performance, i.e. an increase in the primary energy consumption and the related energy cost, is observed. This is especially the case for the HyGCHP design with 7 BHEs operated with the MPC strategy. The impact of the operation on the mean borefield temperature T_{bf} and the correlated fractions of the heating and cooling demand covered by the HP, i.e. GEO_h , respectively PC, i.e. GEO_c , is shown in Figure 8.6. Comparison of Figure 8.6(a) and Figure 8.6(b) shows that the thermal buildup for the design with 26 BHEs is almost the same for the two operation strategies, while for the smaller designs, the thermal buildup with the MPC is clearly more outspoken. After 10 years of operation the borefield with 7 BHEs, T_{bf} has reached 14 °C, i.e. a temperature difference of 4 °C compared to the undisturbed ground temperature $T_{g,\infty}$ of 10 °C. Also for the borefield with 14 BHEs the rise is significant. A longer simulation horizon would be required to determine the actual equilibrium temperature, but the curvature of the graph suggest that the borefield should achieve an equilibrium temperature below 15 °C. The profiles for GEO_c , shown in Figure 8.6(e) and 8.6(f) confirm that the larger temperature rise of T_{bf} for MPC compared to the HC/CC-control, is a direct result of the higher fraction of PC. However,

also GEO_h is larger with MPC than with the HC/CC-control, as depicted in Figure 8.6(c) and 8.6(d), but the relative difference is smaller. The reduction of the energy costs, discussed above, can thus be attributed to two factors. First, MPC realizes a reduction of the total energy demand, through an improved prediction of the actual heating and cooling loads in the presence of internal and solar gains. Second, because of this prediction potential the MPC is able to better spread the heat and cold production in time, this way obtaining a flatter demand profile. This flatter profile in turn enables to make more use of the borefield as the temperature rise of the brine fluid temperature T_f is kept small. With the the HC/CC-control strategy, on the contrary, the lack of anticipative control action will require more often higher power rates (compared to MPC), which necessarily have to be partially covered by the backup GB and CH. The anticipatory character of the MPC strategy is therefore crucial, as illustrated by the result, to satisfy both thermal comfort and to harness the energy saving potential of HP operation and PC in the case of a small sized borefield.

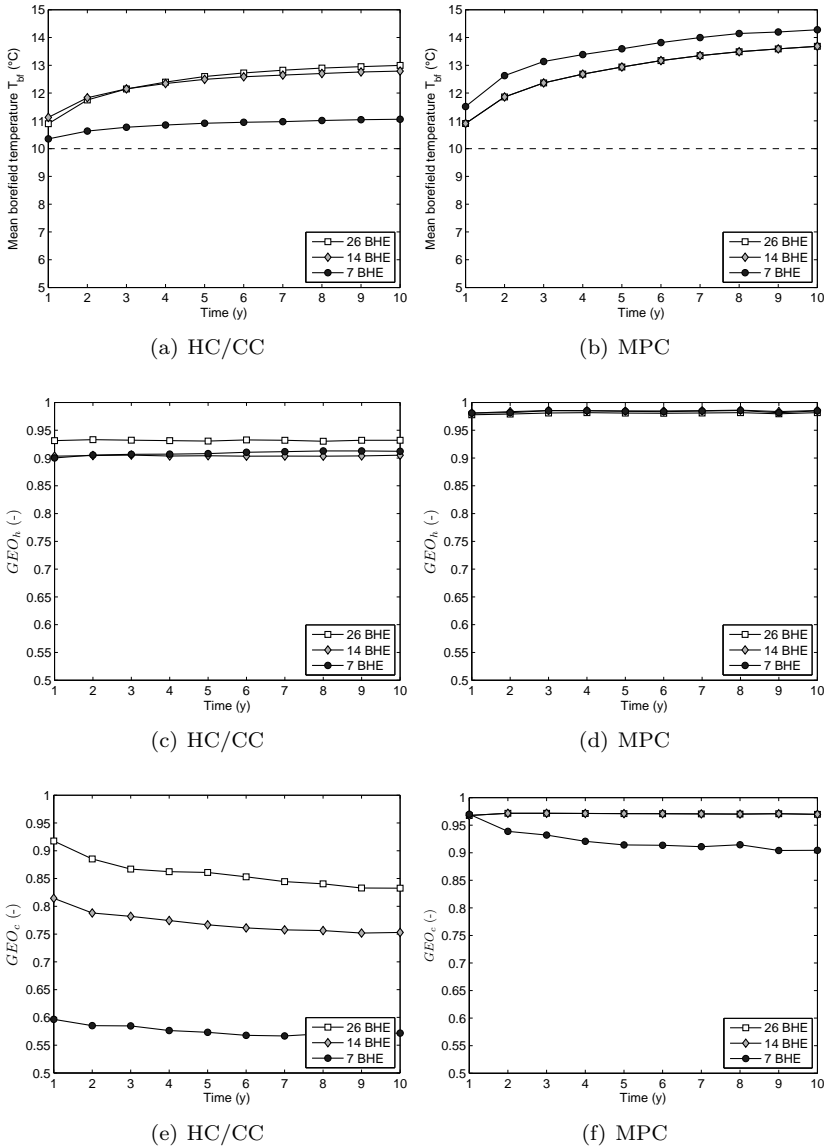


Figure 8.6: Top: Mean borefield temperature T_{bf} as a function of time for the HC/CC-control strategy (left) and with MPC (right) for different borefield sizes (26 BHEs, 14 BHEs and 7 BHEs). Middle and bottom: Corresponding fractions of the annual heating demand covered by the HP, GEO_h , respectively the annual cooling demand covered by the PC, GEO_c .

8.4.7 Economic evaluation

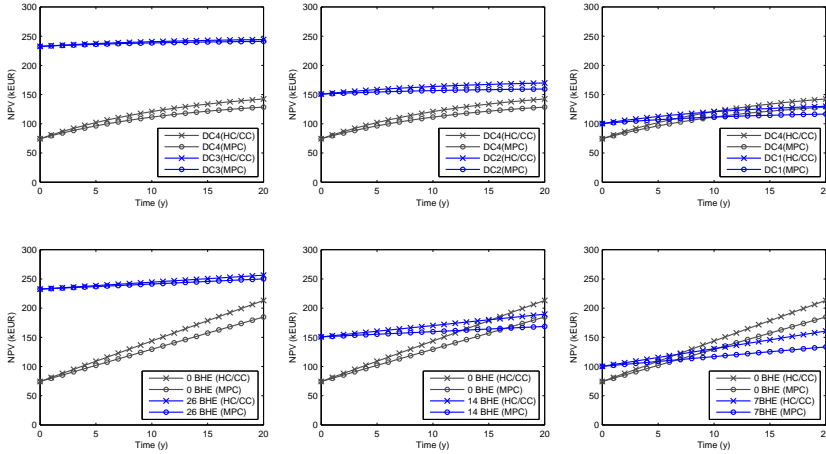


Figure 8.7: NPV cost path with the total costs (investment costs + energy costs) incurred over the given time horizon: (left) DC1 (26 BHE), (middle) DC2 (14 BHEs), (right) DC3 (7 BHEs), each time compared to the NPV cost path of DC4 (0 BHEs). Top: Scenario with an energy price inflation E_r equal to 2%. Bottom: Scenario with E_r equal to 10%. The results with MPC are marked by the circles ('o'), the ones with HC/CC-control by crosses ('x').

The asset of MPC to maximize the use of the borefield, irrespective of its size, opens the path towards economically competitive HyGCHP designs, as is clearly illustrated in Figure 8.7. The horizontal axis has the time horizon (number of years considered) and the vertical axis has the Net Present Value (NPV) cost path with the total costs incurred over that horizon. Figure 8.7(a), (b) and (c) compare the NPV for respectively DC1, DC2 and DC3 to the NPV for DC4 (conventional GB/CH-system). The crossing gives the payback-time. The NPV discounts the monetary value in the future and translates it into today's terms as illustrated by Eq.(8.16), with y_n (year) the considered time horizon, d_r (-) the nominal discount rate, E_r (-) the nominal energy inflation, IC (€) the nominal investment cost, $C_e(i)$ (€/m²) the specific annual electricity cost at year i and A_{tot} (3600 m²) the total conditioned surface.

$$NPV(y_n) = IC + A_{tot} \left(\frac{C_e(y_1)(1 + E_r)}{(1 + d_r)} + \frac{C_e(y_2)(1 + E_r)^2}{(1 + d_r)^2} + \dots + \frac{C_e(y_n)(1 + E_r)^{y_n}}{(1 + d_r)^{y_n}} \right) \quad (8.16)$$

The values used for the investment cost analysis are listed in Table 8.4. Note that we make abstraction of operation costs other than the energy costs. The result for the 4 design cases are shown in Table 8.5. Bf_{fix} (€) comprises the cost of the TRT and the additional costs for the engineering study and the control and monitoring equipment. Bf_{var} (€) comprises the costs which scale with the borefield size, i.e. the cost of the BHEs, the horizontal piping and the collectors.

Table 8.4: Values used for the investment cost evaluation [2]

<i>HP</i>	420	€/kW	collector (max. 10 BHEs)	7260	€
<i>HE</i>	56	€/kW	circulation pump	760	€
<i>GB</i>	100	€/kW	TRT	8500	€
<i>CH</i>	197	€/kW	borefield engineering study	20000	€
<i>CT</i>	104	€/kW	borefield control	8250	€
<i>GHE</i>	30	€/m	energy cost rise E_r	2 - 10 [46]	%/y
hor. piping	50	€/m	cost of capital d_r	10 [122]	%/y

Figure 8.7(a) shows that the designs with 26 BHEs and 14 BHEs are not economically attractive. For the scenario with an energy price rise E_r of 2% (being the mean value for the period 1996 - 2011 [46]), the PBT is more than 20 years for both designs. Only for the scenario with large energy price rise, i.e. E_r 10%, DC2 becomes economically viable. The design with 7 BHEs, on the contrary, has a pay-back time of less than 10 years for both energy price scenarios: it is already economically interesting for conservative estimates of E_r . This clearly illustrates the potential for such a compact HyGCHP system, not only to reduce the primary energy consumption related to space heating and cooling (shown to amount up to 50%, compared to a GB-CH system, see Figure 8.4), but also to reduce the related energy cost with a comparable investment cost. The latter two factors are also illustrated in Figure 8.8 which presents the NPV evaluated over a time horizon of 20 years for a nominal discount rate d_r of 10%, a nominal energy price inflation E_r of 2%, and assuming that the annual energy cost C_e for year 11 to year 20 equals the one for year 10. The relatively small difference between the depicted NPV values and the depicted investment

Table 8.5: Investment costs for the 4 design cases (€)

	<i>HP</i>	<i>HE</i>	<i>GB</i>	<i>CH</i>	Bf_{var}	Bf_{fix}	Total
DC1	0	0	19 300	55 080	0	0	74 380
DC2	14 450	1 490	1 600	8 130	37 970	36 750	100 390
DC3	26 490	2 740	2 550	6 320	75 940	36 750	150 790
DC4	53 880	5 570	1 600	13 850	120 940	36 750	232 590

costs (IC), again illustrates the enormous impact of the IC on the economic feasibility of the installation. *From economic point of view, the benefit of MPC is therefore in the first place that it enables a smaller design.* As this smaller design in turn makes HyGCHP competitive with conventional systems, a widespread implementation of these compact HyGCHP systems could contribute to significant savings in the primary energy consumption for buildings with both space heating and cooling demand.

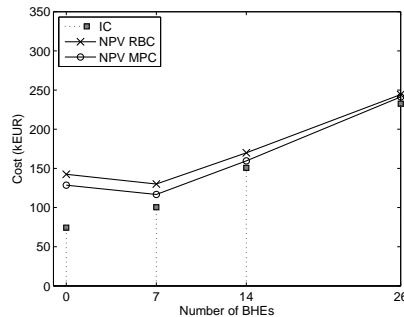


Figure 8.8: Investment cost ('IC') and Net Present Value ('NPV') as a function of the number of BHEs. The results with MPC are marked by the circles ('o'), the ones with HC/CC-control by crosses ('x').

8.5 Summary and conclusions

A first objective of this chapter was to evaluate the benefits of MPC compared to a HC/CC-based control strategy for the operation of HyGCHP-CCA systems in cooling dominated office buildings. A second objective addressed, was quantifying the impact of a smaller borefield size (resulting from a different design strategy) on investment costs and energy costs. The results show a significant potential of the use of MPC for HyGCHP-CCA systems, in terms of thermal comfort, energy cost and investment cost.

For the same design, and significantly better thermal comfort, MPC realizes an energy cost reduction of 20% up to 40% compared to a HC/CC-based control strategy. The cost reduction potential is larger for the (more complex) HyGCHP system than for the (more simple) GB-CH system. Arguably more important, is that MPC is able to guarantee good thermal comfort with smaller HyGCHP installations than what is currently common. The impact on the

investment costs and the net present value (NPV) (evaluated over a time span of 20 years) is considerable. Three HyGCHP designs, with different borefield size, were evaluated and compared to a conventional gas boiler/chiller (GB-CH) installation. The NPV of the first HyGCHP installation (26 BHEs), evaluated after 20 years and assuming an energy price rise of 2%, amounts to 241 000 €. Compared to the NPV of the GB-CH installation, approximately 130 000 €, this design is not economical. The NPV of the second HyGCHP installation (14 BHEs) operated with MPC, amounts to 159 000 €. The pay-back time ranges from 14 years to more than 20 years, depending on the energy price scenario. For the third HyGCHP design, with the borefield size based on an optimization for the week-averaged building loads (see Chapter 7, Section 7.5) (7 BHEs), the NPV with MPC amounts to 113 000 €, being economically very attractive. Moreover, this third HyGCHP design realizes a primary energy consumption reduction of more than 50% compared to the GB-CH installation (the specific annual primary energy consumption is reduced from 32 kWh/m²/y to 14 kWh/m²/y). This way, this compact HyGCHP design is very attractive from both economic and ecological perspective.

These results are possible thanks to the specific combination of the HyGCHP with CCA on the one hand, and the use of MPC on the other hand. The thermal capacity of CCA allows load shifting and peak power reduction, which in turn allows to reduce the installation and borefield size. The anticipatory character of MPC allows to effectively exploit this potential: prediction of the building loads, given the thermal capacity of the CCA, allows to maximize the share of the heat pump in heating mode, and the share of passive cooling in cooling mode. This way, even if the borefield is small, the share of the heat pump and the passive cooling are large. With HC/CC-control strategies, however, the lack of anticipation results in peak power demands which can not be covered by the (small) heat pump or the (small) passive cooling power capacity, which automatically results in a less efficient use of the borefield compared to MPC.

Finally, the results indicate that the strong interdependence between building dynamics, borefield dynamics and control, should already be taken into account at the borefield design phase. A first step is to integrate an MPC strategy, which penalizes peak thermal power demand, in the building load calculation phase (here represented by HyGCHP DC2). A second step is to determine the borefield size based on an optimization with the week-averaged building load values as input. The advantage of this optimization-based approach, compared to current design guidelines, is that, first, the condition to balance the borefield heat injection and extraction loads is relaxed (instead, the condition for long term thermal balance is imposed) and, second, that the required borefield size to cover the smallest of the two loads is determined by the loads (in terms of energy) instead of by the peak power demands (which very much depend on

the way the building load calculation is performed, cfr HyGCHP DC1). The feasibility of the resulting HyGCHP design (represented by HyGCHP DC3) to satisfy thermal comfort at a low energy cost by means of MPC, was shown in this Chapter.

8.6 Chapter highlights

- MPC guarantees high thermal comfort for all design cases, irrespective of the installation size.
- MPC exploits the thermal capacity of CCA for load shifting and peak shaving to maximize the use of the borefield in covering the heating and cooling demand.
- For a same design, and even better thermal comfort, MPC realizes an energy cost reduction between 20% and 40% compared to HC/CC-control.
- For CCA-HyGCHP systems, MPC allows a borefield size reduction of more than 50% compared to current HyGCHP design and control practice.
- For compact borefields, operated with MPC, thermal build-up is significant ($+4^{\circ}\text{C}$), however:
 - the thermal build-up levels are constrained by the the borefield fluid outlet temperature limit,
 - the thermal build-up levels do not jeopardize the long-term system performance.
- An integrated approach for design and operation of these systems seems recommended.

Chapter 9

Conclusions

This study aimed at contributing to the development of MPC to optimize the operation of CCA-HyGCHP systems from an integrated system level approach. A step-wise approach was adopted to achieve this objective. Motivation for this research and an introduction of the key concepts of the proposed methodology, were given in Chapter 1, Chapter 2 and Chapter 3. Chapter 4 described the investigated case, the boundary conditions and the reference control and design. Chapter 5 focused on the optimization at building level, Chapter 6 on the optimization at heat pump level and Chapter 7 on the optimization at borefield level. In Chapter 8, MPC is evaluated from an integrated system perspective. The insights gained from these last 4 chapters can be summarized as follows:

Chapter 5, dealing with the development of a controller building model for the investigated office building with CCA, reveals a significant impact of the identification data (ID) set used for parameter estimation of the grey-box model structures, on the model accuracy. The model structure itself is shown to have a smaller impact. A simple 2nd order model, with the parameters identified with a data set with step excitation of all model inputs, yields the most accurate predictions of the operative temperature T_{op} . Within the MPC framework, fortunately, the impact of model mismatch on the MPC performance can be reduced by compensating for the measured prediction errors. The main benefit of MPC compared to an advanced HC/CC-control strategy, is found to be the reduction in peak power demand, both for heating and for cooling.

Chapter 6, evaluating the impact of the controller heat pump model for the case of a modulating air-to-water heat pump connected to a residential floor heating system, showed that optimal operation is characterized by a continuous and smooth operation at part load, in the case of a constant electricity price

scenario, or a combination of full load operation at night and part load operation during the day, in the case of a day-night electricity price tariff structure. This optimal profile is found with the nonlinear optimal control problem (OCP) formulation which explicitly takes the dependency of the heat pump COP on the source temperature, supply temperature and compressor frequency into account. If the COP is assumed constant, yielding a convex OCP, the same result is found if the cost function penalizes power peaks. The main conclusion of this chapter is that, for modulating heat pumps, power peaks and on/off-cycling should be avoided since these largely affect the COP. For on/off-controlled heat pumps, this result emphasizes the benefit of small HP sizes.

Chapter 7, dealing with the development of a low-order BHE model for incorporation in a HyGCHP control optimization framework, shows that very low-order models ($N < 6$) can be surprisingly accurate in describing both the short and the long term BHE dynamics. The BHE-models have been validated through comparison with the TRNSYS DST-model. The most simple approach, being model reduction (MR) of a white-box BHE-model, yields accurate models down to model order $N = 6$. With parameter estimation (PE) N can be reduced down to 3. The model performance obtained with black box system identification (SI) of rational transfer functions in the Laplace variable s (frequency domain identification) is found to be inferior than for the other approaches, while the transfer functions in the Warburg variable \sqrt{s} , adequate for modeling diffusion phenomena, accurately describe the long term BHE-dynamics. This indicates that BHE-modeling requires incorporation of some form of physical knowledge (i.e., initial model for MR, initial guess for PE and \sqrt{s} -format for SI).

The subsequent analysis of the optimal operation of a HyGCHP system, effectuated for various building load profiles and borefield sizes, indicate that - contrary to what is often suggested - sustainable HyGCHP system operation does not require annual balance of the borefield heat injection and extraction loads (as was recently also observed by Hackel and Pertzborn [70]). On the contrary, the optimization aims at maximizing both the share of HP operation in covering the heating loads (GEO_h) and the share of PC in covering the cooling loads (GEO_c). For cooling dominated buildings, this results in an excess heat injection to the ground which in turn is compensated by higher heat losses to the surrounding ground. As a consequence, an optimal *and* sustainable HyGCHP operation allows thermal build-up during the first years of operation, until equilibrium is reached. The amount of borefield thermal build-up (and thus the value of GEO_c), is limited by the constraint on the brine fluid temperature T_f , since the latter must remain below the cooling water temperature at building side to enable PC. For the formulation of an MPC strategy which aims at optimizing the CCA-HyGCHP system from an integrated systems perspective, this result suggests that incorporation of the annual time scale in the MPC

formulation (which is needed if the condition for annual borefield load thermal balance is imposed) is not required, implicating that MPC of a HyGCHP system is allowed to focus on the short time scale only.

The performed sensitivity analysis of the optimal HyGCHP operation on the borefield size showed a significant impact of the building peak power demand on the borefield size required to cover the (smallest of) the loads. This in turn highlights the impact of the building load calculation. For instance, the required borefield size for the building loads obtained with MPC (14 BHEs) is also 50% smaller than for the loads obtained with the HC/CC-control strategy (26 BHEs). This reduction can entirely be attributed to the reduction in peak power demand since, in terms of total annual heating and cooling demand, these two load profiles hardly differ. The borefield size required to meet the week-average load, is another 50% smaller (7 BHEs) and, due to the time-averaging, less sensitive to the building load calculation. The difference in borefield size required to cover the week-averaged versus the hourly loads is indicative for the investment cost reduction which can be achieved by peak load reduction.

Chapter 8 evaluates these three design cases, DC1 (26 BHEs), DC2 (14 BHEs) and DC3 (7 BHEs), for both an MPC and a HC/CC-control strategy. For a CCA-HyGCHP system, the benefits of MPC compared to a HC/CC-control strategy are:

- Significantly better thermal comfort: a reduction of the amount of temperature exceeding hours from 85-100 Kh/zone/year (depending on the design case) to 40-25 Kh/zone/year.
- Significant energy cost savings: a reduction of the annual energy cost of 20 up to 40%.

The results indicate that MPC is better suited than HC/CC-based control strategies for efficiently operating CCA-HyGCHP systems in general (due to the large number of decision variables), and compact, cost-efficient CCA-HyGCHP systems in particular. For the small HyGCHP designs (DC2 and DC3), the HC/CC-control strategy makes less efficiently use of the borefield than the MPC. Due to the lack of anticipation of the future building loads, the HC/CC-control strategies require relatively higher powers to satisfy the thermal comfort requirements. Since the installed capacity of the HP and the PC for these designs is limited, this means a more frequent use of the GB/CH. For the small HyGCHP designs, the share of the heating and cooling demand covered by the HP, respectively PC, is 10% to 20% higher with MPC than with the HC/CC-control. Contrary to the HC/CC-control strategy used as a reference, MPC optimally exploits the thermal capacity of CCA for load shifting and peak shaving to maximize the use of the (limited) HP and PC capacity.

This way, MPC in combination with CCA facilitates the operation of economically competitive HyGCHP systems: the NPV for DC1, DC2 and DC3, evaluated over a time span of 20 years, amounts to respectively 241 000 €, 159 000 € and 113 000 €, compared to 130 000 € for a conventional gas boiler/chiller system. The primary energy cost reduction of these HyGCHP systems, compared to the conventional system, amounts to respectively 76%, 72% and 56%. This means that DC3, which has a pay back time of 6 to 8 years, is interesting both from economical as from ecological point of view.

Future research The following paths for further research, related to the presented work, are identified:

- **Chapter 5**

- Design of experiments for defining the optimal set of excitation signals for building control model identification,
- evaluating the proposed building grey-box model and parameter estimation approach in the presence of unmeasured internal and solar gains,
- elaborating on improved error-correction methods to extract a maximal amount of information from the recorded prediction errors,
- improving the robustness of MPC with respect to model mismatch, measurement noise and prediction errors,
- experimental validation.

- **Chapter 6**

- evaluate the potential for MPC in the case of varying occupancy profiles.

- **Chapter 7**

- extending the study of controller models for single BHE towards borefields with BHE thermal interaction,
- evaluating the optimal HyGCHP performance including both the building and the borefield dynamics in one single optimization.

- **Chapter 8**

- optimizing the HyGCHP performance for modulating instead of on/off-controlled devices,

- optimizing the HyGCHP performance for buildings requiring simultaneous heating and cooling,
- taking the hydraulics into account to optimize the use of the circulation pumps,
- experimental validation.

Bibliography

- [1] Energy efficiency and renewable energy (EERE) homepage. Technical Report 15 December, US Department of Energy EERE, www.energysavers.gov, 2011. pages 2
- [2] Figures obtained from investment cost analysis for a Belgian office building installed in 2010. pages 255
- [3] B. C. Ahn and J. W. Mitchell. Optimal control development for chilled water plants using a quadratic representation. *Energy and Buildings*, 33(4):371–378, 2001. pages 27
- [4] F. Allgöwer, R. Findeisen, and Z. K. Nagy. Nonlinear Model Predictive Control: From Theory to Application. *Chinese Institute for Chemical Engineers*, 35(3), 2004. pages 12
- [5] M. Anderson and P. Whitcomb. *Design of experiments*. Wiley Online Library, 1974. pages 108
- [6] ANSI/ASHRAE. Standard 55-2004:thermal environmental conditions for human occupancy. *American Society of Heating, Refrigerating and Air-Conditioning Engineers, Atlanta, GA*, 2004. pages 42
- [7] W. A. Austin and J. D. Spitler. Development of an in situ system for measuring ground thermal properties. Master’s thesis, Oklahoma State University, Oklahoma, 1998. pages 160, 191
- [8] H. Awbi and A. Hatton. Natural convection from heated room surfaces. *Energy and Buildings*, 30:233–244, 1999. pages 78
- [9] P. Bacher and H. Madsen. Identifying suitable models for the heat dynamics of buildings. *Energy and Buildings*, 43(7):1511–1522, 2011. pages 16, 25, 68

- [10] V. Badescu. Model of a space heating system integrating a heat pump, photothermal collectors and solar cells. *Renewable energy*, 27(4):489–505, 2002. pages 114
- [11] R. Balan, J. Cooper, K.-M. Chao, S. Stan, and R. Donca. Parameter identification and model based predictive control of temperature inside a house. *Energy and Buildings*, 43(2-3):748–758, 2011. pages 25
- [12] E. Balsa-Canto, A. A. Alonso, and J. R. Banga. An iterative identification procedure for dynamic modeling of biochemical networks. *BMC Systems Biology*, 4(11), 2010. pages 18
- [13] P. Bax and Y. Krishnasing. *Notarisgebouw in Wellen: modellering, experimentele validatie en ontwikkeling MPC-regeling*. PhD thesis, KU Leuven, 2010. pages 72, 109
- [14] R. A. Beier, M. D. Smith, and J. D. Spitler. Reference data sets for vertical borehole ground heat exchanger models and thermal response test analysis. *Geothermics*, In Press,. pages 160
- [15] R. Bellmann. *Dynamic Programming*. University Press, Princeton, 1957. pages 11, 161
- [16] H. Berberich, N. Fisch, and E. Hahne. Field experiments with a single duct in water saturated claystone. In *Proceedings of 6 th International Conference on Thermal Energy Storage, Calorstock*, volume 94, pages 22–25. pages 159
- [17] M. Bernier. Closed-loop ground-coupled heat pump systems. *ASHRAE Journal*, 48(9):12—19, 2006. pages 56, 142
- [18] M. Bernier, M. Kummert, and S. Bertagnolio. Development and application of test cases for comparing vertical ground heat exchanger models. In *10th International IBPSA Conference*, pages 1462–1469, Beijing, China, 2007. Tsinghua University Press. pages 160, 165, 170
- [19] D. Bertsekas. Dynamic programming and suboptimal control: A survey from ADP to MPC. In *CDC*, 2005. pages 11
- [20] M. Bianchi. *Adaptive Modellbasierte Prädiktive Regelung einer Kleinwärmepumpenanlage*. PhD thesis, ETH Zürich, 2006. pages 19, 25, 26, 28, 31, 65, 66, 68, 105, 108, 116, 131, 133, 161
- [21] J. Bjornberg and M. Diehl. Approximate robust dynamic programming and robustly stable MPC. *Automatica*, 42(5):777–782, May 2006. pages 12

- [22] H. G. Bock and K. Plitt. A multiple shooting algorithm for direct solution of optimal control problems. In *9th IFAC World Congress, Budapest*, page 7. Pergamon Press, 1983. pages 123
- [23] S. Boyd and L. Vandenberghe. *Convex optimization*. Cambridge University Press, 2004. pages 10
- [24] H. Carslaw and J. Jaeger. Conduction of heat in solids. *Oxford: Clarendon Press, 1959, 2nd ed.*, 1, 1959. pages 150, 156
- [25] CEN, European Committee for Standardisation. EN12831 : Heating systems in buildings - Method for calculation of the design heat load, 2003. pages 35, 52
- [26] CEN, European Committee for Standardisation. EN15251:2007, Indoor environmental input parameters for design and assessment of energy performance of buildings addressing indoor air quality, thermal environment, lighting and acoustics, 2007. pages 43
- [27] S. H. Cho and M. Zaheer-uddin. Predictive control of intermittently operated radiant floor heating systems. *Energy Conversion and Management*, 44(8):1333–1342, 2003. pages 24, 25
- [28] B. Coffey, F. Haghighat, E. Morofsky, and E. Kutrowski. A software framework for model predictive control with GenOpt. *Energy and Buildings*, 42(7):1084–1092, 2011. pages 25, 67
- [29] CPLEX. 11.0 users manual. *ILOG SA, Gentilly, France*, 2008. pages 11, 201
- [30] D. Crawley, L. Lawrie, C. Pedersen, and F. Winkelmann. Energy plus: energy simulation program. *ASHRAE journal*, 42(4):49–56, 2000. pages 5
- [31] J. Cullin and J. D. Spitler. Comparison of simulation-based design procedures for hybrid ground source heat pump systems. In *Proceedings of the 8th International Conference on System Simulation in Buildings, Liège, Belgium*, 2010. pages 28, 29, 55, 212
- [32] Daikin Europe N.V. Altherma. In *Technical data Heat Pump: Altherma ERYQ007.*, 2006. pages 118, 119, 120, 121, 128
- [33] Daikin Europe N.V. Daikin. In *Technical data Water-to-Water Heat Pump (personal communication).*, 2006. pages 198
- [34] P. Dalin, J. Nilsson, and A. Rubenhag. The European cold market. *Ecoheatcool, work package, 2*, 2006. pages 2

- [35] F. De Ridder, M. Diehl, G. Mulder, J. Desmedt, and J. Van Bael. An optimal control algorithm for borehole thermal energy storage systems. *Energy and Buildings*, 2011. pages 4, 29, 30, 161
- [36] J. Deerman and S. Kavanaugh. Simulation of vertical U-tube ground coupled heat pump systems using the cylindrical heat source solution. *ASHRAE Transactions*, 1991. pages 156
- [37] N. R. Diao, H. Y. Zeng, and Z. H. Fang. Improvement in modeling of heat transfer in vertical ground heat exchangers. *HVAC&R research*, 10(4):459 – 470, 2004. pages 154, 155, 157
- [38] M. Diehl, H. Ferreau, and N. Haverbeke. Efficient numerical methods for nonlinear mpc and moving horizon estimation. *Nonlinear Model Predictive Control*, pages 391–417, 2009. pages 12
- [39] M. Diehl. Optimal control - an overview. In *Athens Course, KULeuven, March 19-23, 2007*. pages 10
- [40] M. Diehl. *Direct Multiple Shooting*. KULeuven (course material), 2007. pages 11
- [41] A. Dounis and C. Caraiscos. Advanced control systems engineering for energy and comfort management in a building environment - a review. *Renewable and Sustainable Energy Reviews*, 13(6):1246–1261, August 2009. pages 25
- [42] EED. Earth Energy Designer, Software for dimensioning of BHE, 2000. pages 57, 142, 157
- [43] P. Eskilson. *Thermal analysis of heat extraction boreholes*. PhD thesis, Lund University, Department of Mathematical Physics, 1987. pages 143, 149, 150, 152, 154, 157, 164, 173, 174
- [44] P. Eskilson and J. Claesson. SIMULATION-MODEL FOR THERMALLY INTERACTING HEAT EXTRACTION BOREHOLES. *Numerical Heat Transfer*, 13(2):149–165, 1988. pages 58
- [45] P. Eskilson. Superposition borehole model Manual for computer code, 1984. pages 146, 150, 155, 157
- [46] European Commission. Eurostat, harmonized indices of consumer prices (hicp) database: <http://epp.eurostat.ec.europa.eu> last accessed on 20.03.2012. pages 255
- [47] P. Fanger. *Thermal comfort: analysis and applications in environmental engineering*. Danish Technical Press Copenhagen, 1970. pages 26, 40

- [48] L. Ferkl, C. Verhelst, L. Helsen, A. Ciller, and J. Komárek. Energy Savings Potential of a Model-Based Controller for Heating: A Feasibility Study. In *IEEE International Conference on Control Applications (CCA)*, Denver, USA, September 2011. pages 116
- [49] L. Ferkl. Ceiling radiant cooling: Comparison of ARMAX and subspace identification modelling methods. *Building and Environment*, 45(1):205–212, January 2010. pages 25, 67
- [50] R. Findeisen and F. Allgöwer. An introduction to nonlinear model predictive control. In *21st Benelux Meeting on Systems and Control*, Veldhoven, Netherlands, 2002. pages 12
- [51] R. Fisher. *The design of experiments*. Oliver & Boyd, 1935. pages 20
- [52] W. Fisk and O. Seppanen. Providing better indoor environmental quality brings economic benefits, wellbeing indoors: key-note lecture,. In *9th REHVA World Congress for Building Technologies - CLIMA, Helsinki, Finland*, 2007. pages 66
- [53] G. Fraisse, C. Viardot, O. Lafabrie, and G. Achard. Development of a simplified and accurate building model based on electrical analogy. *Energy and Buildings*, 34(10):1017–1031, 2002. pages 25, 67
- [54] R. Franke. *Integrierte dynamische Modellierung und Optimierung von Systemen mit saisonaler Wärmespeicherung*. VDI Verlag, Düsseldorf, 1998. pages 29, 161, 172
- [55] R. Z. Freire, G. H. C. Oliveira, and N. Mendes. Development of regression equations for predicting energy and hygrothermal performance of buildings. *Energy and Buildings*, 40(5):810–820, 2008. pages 65
- [56] R. Z. Freire, G. H. C. Oliveira, and N. Mendes. Predictive controllers for thermal comfort optimization and energy savings. *Energy and Buildings*, 40(7):1353–1365, 2008. pages 65
- [57] N. T. Gayeski, P. R. Armstrong, and L. K. Norford. Predictive Pre-cooling of Thermo-Active Building Systems with Low-Lift Chillers. Part 2: Experiment. *ASHRAE Journal*, 2004. pages 31
- [58] N. T. Gayeski, P. R. Armstrong, and L. K. Norford. Predictive Pre-cooling of Thermo-Active Building Systems with Low-Lift Chillers. Part 1: Control Algorithm. *ASHRAE Journal*, 2011. pages 1, 3, 25, 27, 31, 112
- [59] N. T. Gayeski. *Predictive Pre-Cooling Control for Low Lift Radiant Cooling using Building Thermal Mass*. Doctor of philosophy in building

- technology dissertation., Massachusetts Institute of Technology., 2010. pages 64, 68, 114, 116
- [60] S. Gehlin. *Thermal Response Test Method development and evaluation*. PhD thesis, Luleå University of Technology, Department of Environmental Engineering, 2002. pages 28, 159, 160, 191
- [61] J. E. Gentry, J. D. Spitler, D. E. Fisher, and X. Xu. Simulation of hybrid ground source heat pump systems and experimental validation. In *7th International Conference on System Simulation in Buildings, Liège, Belgium*, 2006. pages 191, 192
- [62] GEOTRAINET. *Training manual for designers of shallow geothermal systems, EFG, Brussels*. GEOTRAINET, EFG, Brussels, efg, brussels edition, 2011. pages 61
- [63] D. Goldberg. *Genetic algorithms in search, optimization, and machine learning*. Addison-wesley, 1989. pages 5
- [64] P. Gruber, M. Gwerder, and J. Tödtli. Predictive control for heating applications. In *7th REHVA World Congress for Building Technologies - CLIMA, Napoli, Italy*, Napoli, 2000. pages 24
- [65] M. Gwerder, J. Tödtli, B. Lehmann, F. Renggli, and V. Dorer. Control of thermally activated building systems. In *8th REHVA World Congress for Building Technologies - CLIMA, Lausanne, Switzerland*, 2007. pages 3
- [66] M. Gwerder and J. Tödtli. Predictive control for integrated room automation. In *8th REHVA World Congress for Building Technologies - CLIMA, Lausanne, Switzerland*, 2005. pages 24
- [67] D. Gyalistras and T. O. Team. Use of weather and occupancy forecasts for optimal building climate control (OptiControl) - final report. Technical report, ETH Zürich, 2010. pages 65, 108
- [68] D. Gyalistras, M. Gwerder, F. Oldewurtel, C. N. Jones, M. Morari, B. Lehmann, K. Wirth, and V. Stauch. Analysis of Energy Savings Potentials for Integrated Room Automation. In *10th REHVA World Congress for Building Technologies - CLIMA, Antalya, Turkey*, 2010. pages 24
- [69] S. Hackel and G. Nellis. Optimization of hybrid geothermal heat pump systems. In *9th International IEA Heat Pump Conference, Züürich, Switzerland*, 2008. pages 29, 32

- [70] S. Hackel and A. Pertzborn. Effective design and operation of hybrid ground-source heat pumps: Three case studies. *Energy and Buildings*, 43(12):3497 – 3504, 2011. pages 52, 55, 223, 234, 239, 260
- [71] S. Hackel. *Development of Design Guidelines for Hybrid Ground-coupled Heat Pump Systems*. PhD thesis, University of Wisconsin, Solar Energy lab, Madison, 2008. pages 29, 55, 240
- [72] A. Handbook. Fundamentals, chapter 18. *American Society of Heating, Refrigerating and Air Conditioning Engineers, Atlanta*, 2009. pages 37
- [73] A. Handbook-Fundamentals. Chapter 8: Thermal comfort. *American Society of Heating Refrigeration and Air-Conditioning Engineers, Atlanta*, 1997. pages 41
- [74] G. Hellström. DST Duct ground storage model, Manual for Computer Code, 1989. pages 157, 161, 164, 165
- [75] G. Hellström. *Ground Heat Storage, Thermal Analyses of Duct Storage Systems*. PhD thesis, University of Lund, Department of Mathematical Physics, 1991. pages 136, 158
- [76] H. Hens. *Toegepaste bouwfysic en installaties: Gebouw, energie, verwarming, ventilatie*. ACCO, Leuven, 2002. pages 42
- [77] H. Hens. Personal communication. March 2012. pages 44
- [78] G. P. Henze, C. Felsmann, D. E. Kalz, and S. Herkel. Primary energy and comfort performance of ventilation assisted thermo-active building systems in continental climates. *Energy and Buildings*, 40(2):99–111, 2008. pages 31
- [79] S. A. Hern. *Design of an experimental facility for hybrid ground source heat pump systems*. PhD thesis, Department of Mechanical Engineering, Oklahoma State University, Stillwater, Oklahoma, 2004. pages 192
- [80] B. Houska, H. J. Ferreau, and M. Diehl. Acado toolkit: An open-source framework for automatic control and dynamic optimization. *Optimal control applications & methods*, 32(3):298–312, 2011. pages 11, 19, 123
- [81] S. Hovland, K. Willcox, and J. T. Gravdahl. MPC for large-scale systems via model reduction and multiparametric quadratic programming. In IEEE, editor, *Decision and Control, 2006 45th IEEE Conference on*, pages 3418–3423, 2006. pages 160
- [82] A. Huber and O. Schuler. Berechnungsmodul für erdwärmesonden. *Forschungsprogramm Umgebungs-und Abwärme, Wärmekraftkopplung. Bundesamt für Energie, Bern*, 1997. pages 151, 158, 160

- [83] A. Huber, J. Good, P. Widmer, T. Nussbaumer, D. Trüssel, and C. Schmid. Gekoppelte kälte-und Wärme-erzeugung mit Erdwärmesonden, 2001. pages 151
- [84] L. Ingersoll, F. Adler, H. Plass, and A. Ingersoll. Theory of earth heat exchangers for the heat pump. *ASHRAE Transactions*, 56:167–188, 1950. pages 154
- [85] International Organisation for Standardization. ISO 7730:2005, Ergonomics of the thermal environment: Analytical determination and interpretation of thermal comfort using calculation of the PMV and PPD indices and local thermal comfort criteria, 2005. pages 44, 107
- [86] S. Javed and J. Claesson. New analytical and numerical solutions for the short-term analysis of vertical ground heat exchangers. In *ASHRAE Transactions. Winter Conference of the American-Society-of-Heating-Refrigerating-and-Air-Conditioning-Engineers (ASHRAE), Las Vegas, 2011*, volume 117, page 3, 2011. pages 143, 150, 160
- [87] H. Jin and J. D. Spitler. A Parameter Estimation Based Model of Water-to-Water Heat Pumps for Use in Energy Calculation Programs. *ASHRAE Transactions*, 108(1), 2002. pages 114
- [88] X. Jin, H. Ren, and X. Xiao. Prediction-based online optimal control of outdoor air of multi-zone VAV air conditioning systems. *Energy and Buildings*, 37(9):939–944, 2005. pages 27
- [89] F. Karlsson and P. Fahlén. Impact of design and thermal inertia on the energy saving potential of capacity controlled heat pump heating systems. *International Journal of Refrigeration*, 31(6):1094–1103, 2008. pages 128
- [90] H. Karlsson and C.-E. Hagentoft. Application of model based predictive control for water-based floor heating in low energy residential buildings. *Building and Environment*, 46(3):556–569, 2011. pages 24, 26, 64, 66, 105
- [91] S. Kavanaugh. Field tests for ground thermal properties—methods and impact on ground-source heat pump design. Technical report, Univ. of Alabama, Tuscaloosa, AL (US), 2000. pages 160
- [92] S. Kavanaugh and K. Rafferty. Ground-source heat pumps—design of geothermal systems for commercial and institutional buildings. *ASHRAE, Atlanta*, 1997. pages 56, 142, 156
- [93] J. Kennedy and R. Eberhart. Particle swarm optimization. In *Neural Networks, 1995. Proceedings., IEEE International Conference on*, volume 4, pages 1942–1948. IEEE, 1995. pages 5

- [94] E.-j. Kim, J.-J. Roux, M. Bernier, and O. Cauret. A new borehole heat exchanger (bhe) model based on state model reduction techniques analysis. In *10th REHVA World Congress for Building Technologies - CLIMA*, Antalya, Turkey, 2010. pages 161, 165
- [95] M. Kintner-Meyer and A. F. Emery. Optimal control of an HVAC system using cold storage and building thermal capacitance. *Energy and Buildings*, 23(1):19–31, 1995. pages 27
- [96] D. E. Kirk. *Optimal Control Theory, An introduction*. Englewood Cliffs, New Jersey, 1970. pages 9, 28
- [97] T. Kohl and R. Hopkirk. FRACure — a simulation code for forced fluid flow and transport in fractured, porous rock. *Geothermics*, 24(3):333 – 343, 1995. <ce:title>Hot Dry Rock (HDR) Reservoir Modelling Activities within Europe</ce:title>. pages 158
- [98] T. G. Kolda, R. M. Lewis, and V. Torczon. Optimization by direct search: New perspectives and some classical and modern methods. *Society for industrial and applied mathematics*, 45(3):97, 2003. pages 5
- [99] I. Kollár. Frequency Domain System Identificaton Toolbox V3.3 for Matlab. pages 164, 166, 179
- [100] M. Koschenz and B. Lehmann. *Thermoaktive Bauteilsysteme TABS*. EMPA Energiesysteme/Haustechnik, Duebendorf (Switzerland), 2000. pages 38, 78
- [101] M. Kummert. *Contribution to the application of modern control techniques to solar buildings. Simulation-based approach and experimental validation*. PhD thesis, Fondation Université Luxembourgeoise, Liège, 2001. pages 25, 40, 42, 64, 65, 66, 67, 99, 108, 161
- [102] M. Kummert. Performance comparison of heating control strategies combining simulation and experimental results, 2005. pages 25, 26
- [103] M. Kummert and P. André. Simulation of a model-based optimal controller for heating systems under realistic hypotheses. In *9th International IBPSA Conference*, Montréal, Canada, 2005. pages 24, 65, 66
- [104] L. Lamarche and B. Beauchamp. A fast algorithm for the simulation of GCHP systems. *ASHRAE Transactions*, 2007. pages 150
- [105] L. Lamarche and B. Beauchamp. A new contribution to the finite line-source model for geothermal boreholes. *Energy and Buildings*, 39(2): 188–198, 2007. pages 143, 154, 155, 156, 157, 158, 160, 173

- [106] C. K. Lee and H. N. Lam. Computer simulation of borehole ground heat exchangers for geothermal heat pump systems. *Renewable Energy*, In Press, :163, 2007. pages 151
- [107] K.-h. Lee and J. E. Braun. Model-based demand-limiting control of building thermal mass. *Building and Environment*, 43(10):1633–1646, 2008. pages 31
- [108] X. Li, Z. Chen, and J. Zhao. Simulation and experiment on the thermal performance of u-vertical ground coupled heat exchanger. *Applied thermal engineering*, 26(14):1564–1571, 2006. pages 29
- [109] Z. Liao and A. L. Dexter. A simplified physical model for estimating the average air temperature in multi-zone heating systems. *Building and Environment*, 39(9):1013–1022, 2004. pages 161
- [110] L. Ljung. *System identification*. Wiley Online Library, 1999. pages 13, 15, 18
- [111] J. Löfberg. Yalmip wiki: Solvers, <http://users.isy.liu.se/johanl/yalmip> , last accessed on 29.03.2012, 2012. pages 11
- [112] J. Lund, B. Sanner, L. Rybach, R. Curtis, and G. Hellström. Geothermal (ground-source) heat pumps - A world overview . *Renewable Energy*, 2003. pages 2
- [113] C. Ma and Y. Hori. An introduction of fractional order control and its applications in motion control. In *Proceedings of 23rd Chinese Control Conference*, Wuxi, China, 2004. pages 179
- [114] Y. Ma, F. Borrelli, B. Hancey, A. Packard, and S. Bortoff. Model Predictive Control of Thermal Energy Storage in Building Cooling Systems. In *48th IEEE Conference on Decision and Control*, Shanghai, China, 2009. pages 27
- [115] Z. Ma and S. Wang. An optimal control strategy for complex building central chilled water systems for practical and real-time applications. *Building and Environment*, 44(6):1188–1198, 2009. pages 27
- [116] J. Maciejowski. *Predictive control: with constraints*. Pearson education, 2002. pages 11, 25, 160
- [117] G. Masy. *Definition and validation of a simplified multizone dynamic building model connected to heating system and HVAC unit*. PhD thesis, Université de Liège, 2008. pages 67, 78
- [118] MathWorks. Matlab, 2006. pages 12, 176

- [119] M. Morari and J. H. Lee. Model predictive control: past, present and future. *Computers & Chemical Engineering*, 23(4-5):667–682, 1999. pages 12
- [120] A. Murugappan. Implementing ground source heat pump and ground loop heat exchanger models in the EnergyPlus simulation environment. Master’s thesis, Oklahoma State University, 2002. pages 143
- [121] M. Nani, M. Stalder, A. Schweizer, and T. Baumgartner. Wpcalc. *Rechenprogramm zur Auslegung von WP-Anlagen. Bundesamt für Energiewirtschaft, Bern*, 1994. pages 158
- [122] National Action Plan for Energy Efficiency. Understanding cost-effectiveness of energy efficiency programs: Best practices, technical methods, and emerging issues for policy-makers. energy and environmental economics, inc. and regulatory assistance project., 2008. pages 255
- [123] J. Nelder and R. Mead. A simplex method for function minimization. *The computer journal*, 7(4):308, 1965. pages 5
- [124] P. Ngendakumana. *Modélisation simplifiée du comportement thermique d’un bâtiment et vérification expérimentale*. PhD thesis, Faculté des Sciences appliquées de l’Université de Liège, 1991. pages 67
- [125] J. Nocedal and S. J. Wright. *Numerical optimization*. Springer verlag, 2 edition, 2000. pages 5, 10, 19, 28, 123
- [126] S. E. L. U. of Wisconsin. HYGCHP:Hybrid Ground-Coupled Heat Pump Design Program. pages 29
- [127] F. Oldewurtel, C. N. Jones, and M. Morari. A Tractable Approximation of Chance Constrained Stochastic MPC based on Affine Disturbance Feedback. In *Proc. 47th IEEE Conference on Decision and Control*, Cancun, Mexico, 2008. December 9-11. pages 12
- [128] F. Oldewurtel, D. Gyalistras, M. Gwerder, C. N. Jones, A. Parisio, V. Stauch, B. Lehmann, and M. Morari. Increasing Energy Efficiency in Building Climate Control using Weather Forecasts and Model Predictive Control. In *10th REHVA World Congress for Building Technologies - CLIMA*, Antalya, Turkey, 2010. pages 66
- [129] B. W. Olesen. Heating and cooling systems for better energy efficiency. *Indoor Environment*, pages 45–60, 2007. pages 1, 3
- [130] D. Pahud, F. A., and H. J.D. *The superposition borehole model for TRNSYS User Manual for the November 1996 version*, 1996. pages 158

- [131] E. Palomo Del Barrio, G. Lefebvre, P. Behar, and N. Bailly. Using model size reduction techniques for thermal control applications in buildings. *Energy and Buildings*, 33(1):1–14, 2000. pages 25
- [132] V. Partenay, P. Riederer, E. Wurtz, and S. Pincemin. A new model for BTES systems: model development, comparison and application to an office building. In *10th REHVA World Congress for Building Technologies - CLIMA*, Antalya, Turkey, 2010. pages 165
- [133] S. Patankar. *Numerical heat transfer and fluid flow*. Hemisphere Pub New York, 1980. pages 150
- [134] S. Patankar. *Computation of conduction and duct flow heat transfer*. Maple Grove Innovative Research Inc., 1991. pages 150
- [135] D. Patteeuw. Ontwikkeling van een modelgebaseerde predictieve regeling van een grondgekoppeld warmtepompsysteem (Dutch). Master's thesis, KULeuven, Department of Mechanical Engineering, Leuven, 2011. pages 237
- [136] N. Paul. *The effect of grout thermal conductivity on vertical geothermal heat exchanger design and performance*. PhD thesis, Mechanical Engineering Dept., South Dakota State University, 1996. pages 149
- [137] L. Peeters, L. Helsen, and D'haeseleer. Prediction of next day's heat demand to minimise heat-pump heating costs. In *8th REHVA World Congress for Building Technologies - CLIMA*, page 6, Lausanne, Switzerland, 2005. pages 26
- [138] A. Pertzborn, S. Hackel, G. Nellis, and S. Klein. Experimental validation of a ground heat exchanger model in a hybrid ground source heat pump. *HVAC&R Research*, 17(6):1101–1114, 2011. pages 158
- [139] M. Philippe, M. Bernier, P. Eng, and D. Marchio. Vertical geothermal borefields. *ASHRAE*, 2010. pages 52, 56, 142
- [140] R. Pintelon and J. Schoukens. *System identification: a frequency domain approach*. Wiley-IEEE Press, 2001. pages 13
- [141] R. Pintelon, J. Schoukens, L. Pauwels, and E. Van Gheem. Diffusion systems: Stability, modeling, and identification. In *Instrumentation and Measurement Technology Conference, 2005. IMTC 2005. Proceedings of the IEEE*, volume 2, pages 894–899. IEEE, 2005. pages 164
- [142] W. B. Powell. *Approximate Dynamic Programming: Solving the curses of dimensionality*. Wiley-Blackwell, 2007. pages 11, 160

- [143] S. Prívará, J. Siroký, L. Ferkl, and J. Cigler. Model predictive control of a building heating system: The first experience. *Energy and Buildings*, 43(2-3):564–572, 2010. pages 66
- [144] S. J. Qin and T. A. Badgwell. A survey of industrial model predictive control technology. *Control Engineering Practice*, 11(7):733–764, 2003. pages 5
- [145] A. Rabl. Parameter Estimation in Buildings: Methods for Dynamic Analysis of Measured Energy Use. *Journal of Solar Energy Engineering*, 110(1):15, 1988. pages 67
- [146] M. Ramamoorthy, A. D. Chiasson, and J. D. Spitler. Optimal Sizing of Hybrid Ground-Source Heat Pump Systems That Use a Cooling Pond as a Supplemental Heat Rejecter: A System Simulation Approach. *ASHRAE Transactions*, pages 1–12, 2001. pages 29
- [147] M. Reuss and B. Sanner. Planung und Auslegung von Erdwärmesondenanlagen: Basis einer nachhaltigen Erdwärmenutzung, VDI-Richtlinie 4640 und Berechnungsverfahren, 2000. pages 159
- [148] D. Rijksen, C. Wisse, and A. van Schijndel. Reducing peak requirements for cooling by using thermally activated building systems. *Energy and Buildings*, 42(3):298–304, March 2010. pages 32
- [149] R. E. Rink, V. Gourishankar, and M. Zaheeruddin. Optimal Control of Heat-Pump/Heat-Storage Systems with Time-of-Day Energy Price Incentive. *Journal of Optimization Theory and Applications*, 58(July), 1988. pages 27, 116
- [150] D. Sakellari, M. Forsen, and P. Lundqvist. Investigating control strategies for a domestic low-temperature heat pump heating system. *International Journal of Refrigeration*, 29(4):547–555, 2006. pages 25
- [151] B. Sanner, C. Karytsas, D. Mendrinós, and L. Rybach. Current status of ground source heat pumps and underground thermal energy storage in Europe. *Geothermics*, 32(4-6):579–588, 2003. pages 2
- [152] B. Sanner, G. Hellström, J. D. Spitler, and S. Gehlin. Thermal Response Test : Current Status and World-Wide Application. In *Proceedings World Geothermal Congress*, pages 24–29, Antalya, Turkey, 2005. pages 28, 160
- [153] B. Sanner, E. Mands, M. Sauer, and E. Grundmann. Technology, development status, and routine application of Thermal Response Test. In P. E. G. C. 2007, editor, *European Geothermal Congress 2007*, Unterhaching, Germany, 2007. 30 May-1 June 2007. pages 160

- [154] R. W. H. Sargent. Optimal control. *Journal of Computational and Applied Mathematics*, 124(1-2):361–371, 2000. pages 11
- [155] SEL-University of Wisconsin-USA and TRANSOLAR-Stuttgart. TRNSYS 16, Transient System Simulation Program. At: <http://www.trnsys.com>, 2005. pages 5, 38, 41
- [156] O. Seppanen, W. Fisk, and Q. Lei. Effect of temperature on task performance in office environment. In *5th International Conference on Cold Climate Heating, Ventilating, and Air Conditioning*, Moscow, Russia, November 2005. pages 66
- [157] S. Shao, W. Shi, X. Li, and H. Chen. Performance representation of variable-speed compressor for inverter air conditioners based on experimental data. *International Journal of Refrigeration*, 27(8):805–815, 2004. pages 114
- [158] J. A. Shonder and A. E. Beck. A New Method to Determine the Thermal Properties of Soil Formations from In Situ Field Tests. Technical report, Oak Ridge National Laboratory, Rept. ORNL/TM-2000, 2000. pages 28, 159, 160, 165
- [159] S. Signorelli, T. Kohl, and W. Rogg. Validieren das programms ews und optimieren der erdwärmesondenlänge. *Bundesamt für Energie, Schlussbericht*, 2002. pages 158
- [160] S. Signorelli, S. Bassetti, D. Pahud, and T. Kohl. Numerical evaluation of thermal response tests. *Geothermics*, 36(2):141 – 166, 2007. pages 160
- [161] J. Siroký, F. Oldewurtel, J. Cigler, and S. Prívará. Experimental analysis of model predictive control for an energy efficient building heating system. *Applied Energy*, 88(9):3079–3087, 2011. pages 24, 25
- [162] M. Sourbron and L. Helsen. Identifying appropriate thermal comfort criteria for buildings equipped with thermally active building systems (tabs). In *10th REHVA World Congress for Building Technologies - CLIMA*, Antalya, Turkey, 2010. pages 48, 53
- [163] M. Sourbron, R. De Herdt, T. Van Reet, W. Van Passel, M. Baelmans, and L. Helsen. Efficiently produced heat and cold is squandered by inappropriate control strategies: A case study. *Energy and Buildings*, 41(10):1091–1098, October 2009. pages 3
- [164] M. Sourbron. *Dynamic behaviour of buildings with thermally activated building systems (TABS)*. PhD thesis, KU Leuven, 2012. pages 36, 37, 45, 52, 77

- [165] J. D. Spitler. Ground-source heat pump system research - Past, present, future. *International Journal of HVAC&R research*, 11(2):165–167, 2005. pages 29
- [166] J. D. Spitler. GLHEPRO-a design tool for commercial building ground loop heat exchangers. In *Proceedings of the fourth international heat pumps in cold climates conference*, Aylmer, Québec, 2000. pages 57, 60, 142, 157, 240
- [167] J. D. Spitler, D. Fisher, and C. Pedersen. The radiant time series cooling load calculation procedure. *ASHRAE Transactions*, 103:503–518, 1997. pages 52
- [168] J. D. Spitler, X. Liu, S. J. Rees, and C. Yavuzturk. Simulation and optimization of ground source heat pump systems, 2005. pages 29
- [169] P. Sprecher and F. Tillenkamp. Optimisation of control parameters for concrete core activated systems. In *8th REHVA World Congress for Building Technologies CLIMA*, Lausanne, Switzerland, 2005. pages 3
- [170] J. Sun and A. Reddy. Optimal control of building HVAC&R systems using complete simulation-based sequential quadratic programming (CSB-SQP). *Building and Environment*, 40(5):657–669, 2005. pages 25, 27
- [171] J. Swevers and J. De Schutter. *Aanvullingen bij de cursus Regeltechniek (deel C)*. KULeuven (course material), 2006. pages 15, 19
- [172] TESS. TESS component library General description, 2007. pages 136, 158, 161, 164, 165
- [173] J. Tödtli, M. Gwerder, B. Lehmann, F. Renggli, and V. Dorer. Integrated design of thermally activated building systems and their control. In *9th REHVA World Congress for Building Technologies - CLIMA, Helsinki, Finland*, Helsinki, 2007. pages 32, 239
- [174] V. Torczon et al. On the convergence of pattern search algorithms. *SIAM Journal on optimization*, 7(1):1–25, 1997. pages 27
- [175] E. Van den Bulck. *Warmteoverdracht*. 2004. pages 145
- [176] J. Vandewalle and J. Schoukens. *Systeemidentificatie, Cursusmateriaal*. ACCO Leuven, 2008. pages 20
- [177] D. Vanhoudt, F. De Ridder, J. Desmedt, and J. Van Bael. Controller for Optimal Cost Operation of a Borehole Thermal Energy Storage System. In *10th REHVA World Congress for Building Technologies - CLIMA*, Antalya, Turkey, 2010. pages 4, 161

- [178] Verein Deutscher Ingenieure. *VDI 2078 : Berechnung der Kühllast klimatisierter Räume (VDI-Kühllastregeln)*. VDI-Handbuch Raumluftechnik. Beuth Verlag GmbH, Berlin, 1996. pages 36, 52
- [179] C. Verhelst, F. Logist, J. V. Impe, and L. Helsen. Study of the optimal control problem formulation for modulating air-to-water heat pumps connected to a residential floor heating system. *Energy and Buildings*, 45(0):43–46, 2011. pages 66, 244
- [180] R. Wagner and C. Clauser. Evaluating thermal response tests using parameter estimation for thermal conductivity and thermal capacity. *Journal of Geophysics and Engineering*, 2:349–356, 2005. pages 191
- [181] V. Wagner, P. Bayer, M. Kübert, and P. Blum. Numerical sensitivity study of thermal response tests. *Renewable Energy*, 41(0):245 – 253, 2012. pages 160
- [182] G. Welch and G. Bishop. An Introduction to the Kalman Filter. *University of North Carolina at Chapel Hill Chapel Hill NC*, 95(TR 95-041):1–16, 1995. pages 72
- [183] G. Werner, M. Gwerder, H. Anne, L. Beat, R. Franz, and J. Tödtli. Control of concrete core conditioning systems. In *8th REHVA World Congress for Building Technologies - CLIMA*, Lausanne, Switzerland, 2005. pages 3
- [184] M. Wetter. Genopt®, generic optimization program. In *Seventh International IBPSA Conference*, pages 601–608, 2001. pages 241
- [185] M. Wetter and T. Afjei. TRNSYS TYPE 401: Compression heat pumps including frost and cycling losses , 1997. pages 158
- [186] R. W. Wimmer. *Regelung einer Wärmepumpenanlage mit Model Predictive Control*. PhD thesis, Eidgenössischen Technischen Hochschule ZÜRICH, Zürich, 2004. pages 25, 26, 28, 31, 65, 66, 99, 116, 131, 161, 245
- [187] H. Witte. Advances in geothermal response testing. In S. Netherlands, editor, *Thermal Energy Storage for Sustainable Energy Consumption*, volume Volume 234. 2007. pages 28, 160, 165
- [188] H. J. L. Witte. Geothermal response tests with heat extraction and heat injection: Examples of Application in Research and Design of Geothermal Ground Heat Exchangers, 2001. pages 191
- [189] X. Xiaowei. *Simulation and Optimal Control of Hybrid Ground Source Heat Pump Systems*. Doctoral thesis, Oklahoma State University, 2007. pages 29

- [190] H. Yang, P. Cui, and Z. Fang. Vertical-borehole ground-coupled heat pumps: A review of models and systems. *Applied energy*, 87(1):16–27, 2010. pages 143, 150
- [191] C. Yavuzturk and D. Spitler. Comparative study of operating and control strategies for hybrid ground-source heat pump systems using a short time step simulation model. *ASHRAE Transactions*, 106(2), 2000. pages 29
- [192] C. Yavuzturk and J. D. Spitler. A short time step response factor model for vertical ground loop heat exchangers. *ASHRAE Transactions*, 105(2), 1999. pages 143, 146, 148, 157
- [193] C. Yavuzturk, J. D. Spitler, and S. J. Rees. A transient two-dimensional finite volume model for the simulation of vertical u-tube ground heat exchangers. *ASHRAE Transactions*, 105(2), 1999. pages 150, 158, 160
- [194] Z. Yu, X. Yuan, and B. Wang. Optimal design for a hybrid ground-source heat pump. 2006. pages 28
- [195] M. Zaheer-Uddin. Optimal control of a single zone environmental space. *Building and Environment*, 27(1):93–103, 1992. pages 24
- [196] M. Zaheer-uddin and G. R. Zheng. Optimal control of time-scheduled heating, ventilating and air conditioning processes in buildings. *Energy Conversion and Management*, 41(1):49–60, 2000. pages
- [197] M. Zaheer-Uddin, G. R. Zheng, and S.-H. Cho. Optimal operation of an embedded-piping floor heating system with control input constraints. *Energy Conversion and Management*, 38(7):713–725, 1997. pages 24, 25, 127
- [198] M. Zaheeruddin, V. Gourishankar, and R. E. Rink. Dynamic suboptimal control of a heat pump/heat storage system. *Optimal control applications & methods*, 9(341-255), 1988. pages 27
- [199] H. Y. Zeng, N. R. Diao, and Z. H. Fang. A finite line-source model for boreholes in geothermal heat exchangers. *Heat Transfer-Asian Research*, 31(7):558–567, 2002. pages 157
- [200] H. Zeng, D. Nairen, and F. Zhaohong. Heat transfer analysis of boreholes in vertical ground heat exchangers. *International Journal of Heat and Mass Transfer*, 46(23):4467–4481, 2003. pages 151

Curriculum Vitae

Clara Verhelst was born in Alagoinhas (Brazil) in 1983. She graduated as Master in Mechanical-Electrical Engineering with specialisation Energy at the Katholieke Universiteit Leuven in 2006. Her Master thesis was on the integration of solid oxid fuel cells (SOFC) in integrated gasification combined cycles (IGCC) coal power plants. For her Master thesis, she was Laureate of the KVIV Engineering prizes 2007 and received the European Talent Award for Innovative Energy Systems by the EFPE.

In October 2006 she started her PhD at the Division of Applied Mechanics and Energy Conversion (TME) of the Mechanical Engineering Department at the Katholieke Universiteit Leuven. The PhD was supervised by Prof. dr. ir. Lieve Helsen. The research was funded by a PhD grant of the Institute for the Promotion of Innovation through Science and Technology in Flanders (IWT Vlaanderen). In September 2009 - February 2010 she was a research visitor at the Automatic Control Laboratory of ETH Zürich. She was one of the main authors of the project 'Black-box model based predictive control of ground coupled heat pump systems' (2010 - 2014), approved by the Research Foundation - Flanders (FWO). From January 2012 she is working on this project.

List of Publications

Articles in international journals

- [1] C. Verhelst, F. Logist, J. Van Impe, L. Helsen. Study of the optimal control problem formulation for air-to-water heat pump systems. *Energy and Buildings*, 45: 43–46, 2011.
- [2] C. Verhelst, L. Helsen. Low-order state space models for borehole heat exchangers. *HVAC & R Research*, 17(6): 928–947.
- [3] C. Verhelst, D. Degrauwe, F. Logist, J. Van Impe, L. Helsen. Multi-objective optimal control of an air-to-water heat pump for residential heating. *Building Simulation*, accepted 2011. doi: 10.1007/s12273-012-0061-z
- [4] M. Sourbron, C. Verhelst, L. Helsen. Building models for model predictive control of office buildings with concrete core activation. *Journal of Building Performance Simulation*, accepted 2012. doi: 10.1080/19401493.2012.680497

Articles in national journals

- [1] C. Verhelst. Op hete kolen. *Het ingenieursblad*, (4): 22–27 April 2007.

Articles in international conference proceedings

- [1] C. Verhelst, H. Nolens, K. Schoovaerts, and L. Helsen. Performance of an air-to-water heat pump system in a low energy residential building: modelling and experimental results. In *Proceedings of the 9th IEA Heat Pump Conference*, Zürich, Switzerland, May 2008.

- [2] C. Verhelst, F. De Ridder, and L. Helsen. System identification of a borehole thermal energy storage system for application in optimal control. In *Heat Pump Platform Symposium*, Sint-Katelijne-Waver, Belgium, September 2008.
- [3] C. Verhelst, G. Vandersteen, J. Schoukens, and L. Helsen. A linear dynamic borehole model for use in model based predictive control. In *Proceedings of the 11th International Conference on Thermal Energy Storage - Effstock*, Stockholm, Sweden, June 2009.
- [4] D. Degrauwe, C. Verhelst, F. Logist, J. Van Impe, and L. Helsen. Multi-objective optimal control of an air-to-water heat pump for residential heating. In *8th International Conference on System Simulation in Buildings*, Liège, Belgium, December 2010.
- [5] C. Verhelst, D. Axehill, C. N. Jones, and L. Helsen. Impact of the cost function in the optimal control formulation for an air-to-water heat pump system. In *8th International Conference on System Simulation in Buildings*, Liège, Belgium, December 2010.
- [6] G. Monteyne, G. Vandersteen, C. Verhelst, and L. Helsen. On the use of laplace and warburg variables for heat diffusion modeling. In *10th International Conference on Environment and Electrical Engineering (EEEIC)*, Rome, Italy, May 2011.
- [7] L. Ferkl, C. Verhelst, L. Helsen, A. Ciller, and J. Komárek. Energy Savings Potential of a Model-Based Controller for Heating: A Feasibility Study. In *IEEE International Conference on Control Applications (CCA)*, Denver, USA, September 2011.
- [8] S. Antonov, C. Verhelst, and L. Helsen. Control of ground coupled heat pump systems in offices to optimally exploit ground thermal storage on the long term. In *Proceedings of the 12th International Conference on Energy Storage, Innostock 2012*, Lleida, Spain, May 2012.

Arenberg Doctoral School of Science,

Department
Applied Mech
Ce